Investigating gastrointestinal function at macro and micro scales : Insights from fluid dynamics models

Faisal Ahmad

To cite this version:

Faisal Ahmad. Investigating gastrointestinal function at macro and micro scales : Insights from fluid dynamics models. Materials Science [cond-mat.mtrl-sci]. Université Grenoble Alpes [2020-..], 2023. English. NNT : 2023GRALI057 . tel-04249402

HAL Id: tel-04249402
https://theses.hal.science/tel-04249402v1

Submitted on 19 Oct 2023

THÈSE

Pour obtenir le grade de

DOCTEUR DE L'UNIVERSITÉ GRENOBLE ALPES

École doctorale : I-MEP2 - Ingénierie - Matériaux, Mécanique, Environnement, Energétique, Procédés, Production
Spécialité : MEP - Mécanique des fluides Energétique, Procédés
Unité de recherche : Laboratoire Rhéologie et Procédés

Etude de la fonction gastro-intestinale aux échelles macroscopiques et microscopiques : perspectives offertes par des modèles de dynamique des fluides

Investigating gastrointestinal function at macro and micro scales: Insights from fluid dynamics models

Présentée par :

Faisal AHMAD

Direction de thèse :

Clément DE LOUBENS CHARGE DE RECHERCHE, Université Grenoble Alpes	Directeur de thèse
Stéphane TANGUY MAITRE DE CONFERENCE HDR, Université Grenoble Alpes	Co-encadrant de thèse

Rapporteurs :

Valérie DEPLANO
DIRECTRICE DE RECHERCHE, CNRS délégation Provence et Corse
Aline BEL-BRUNON
MAITRE DE CONFERENCES HDR, INSA Lyon

Thèse soutenue publiquement le **29 septembre 2023**, devant le jury composé de :

Clément DE LOUBENS CHARGE DE RECHERCHE HDR, CNRS délégation Alpes	Directeur de thèse
Philippe PEYLA PROFESSEUR DES UNIVERSITES, Université Grenoble Alpes	Président
Valérie DEPLANO DIRECTRICE DE RECHERCHE, CNRS délégation Provence et Corse	Rapporteure
Aline BEL-BRUNON MAITRE DE CONFERENCES HDR, INSA Lyon	Rapporteure
Guillaume DELAPLACE DIRECTEUR DE RECHERCHE, INRAE centre Hauts-de-France	Examinateur

Invités :

Stéphane TANGUY
MAITRE DE CONFERENCES HDR, Université Grenoble Alpes

“*And that there is not for man/woman except that for which he/she strives.*”

Al Quran 53:39

Acknowledgements

Taking inspiration from the emerging interaction of fluid dynamics technique and physiology, this thesis stems from a complex web of interactions with those around me who have supported me on scientific, technical, and emotional levels. I would like to express my heartfelt gratitude to my parents and my lovely wife *Rushda*, for their unwavering love and understanding throughout my Ph.D. journey. Their support has been instrumental in overcoming the challenges and reaching this stage of completing my thesis. I would like to extend a big thank you to the École doctorale Ingénierie - Matériaux, Mécanique, Environnement, Énergétique, Procédés, Production (ED I-MEP2) for its financial support, which made this incredible journey possible.

I express my sincerest appreciation to my Ph.D. mentors, **Clément de Loubens** and **Stéphane Tanguy**, for providing me with the invaluable opportunity to embark on this journey. Their guidance, continuous support, and insightful feedback have shaped my research work and instilled in me a sense of scientific rigor. They were greatly helpful in realizing a new experimental set-up, and thanks to **Stéphane Tanguy** for his support in doing the ex-vivo experiments. They not only guided me in completing my thesis but also helped me develop an analytical mindset. I am truly grateful for their advice and encouragement during times when I needed it. I am also greatly thankful to our collaborators, **Dr. Alain Dubreuil** and Prof. **Jean-Luc Faucheron** for their support in providing raw materials and in interpreting the results obtained from the fluid dynamics rectal model has been invaluable.

I would like to acknowledge the technical team at LRP, including Mohamed Karrouch, Didier Blésès, Frédéric Hugenel, and others, for their invaluable insights, assistance, and collaboration in developing the experimental setup. Their expertise has contributed to the success of my research.

Furthermore, I want to express my gratitude to the incredible Ph.D. students Dácil, Brian, and Nisrine, as well as the PostDoc candidates Rohan and Lorenzo. Our discussions over coffee, their assistance, and the shared moments of laughter during breaks have been immensely enjoyable and intellectually stimulating. Thank you, **Rohan**, for all the discussions we have had regarding the CFD models and for helping me bring my thesis to fruition.

Lastly, I would like to thank all my colleagues at the research institutes, the LRP and TIMC labs, for their constant encouragement and support throughout the writing phase of my Ph.D. Their presence has created a nurturing environment that has fostered my growth as a researcher.

I am truly fortunate to have such amazing individuals by my side, and I am grateful for the impact they have had on my Ph.D. journey.

Abstract

The gastrointestinal (GI) tract plays a crucial role in the digestion and absorption of nutrients. The complex motility of the GI tract is driven by its own motor activity. Smooth muscle motility is essential for food breakdown, mixing with secretions, nutrient absorption, and the transport of digesta along the GI tract. Despite its importance, many aspects of its biomechanics are not well understood. Therefore, mechanistic models are required to gain more insights into the function of the GI tract. In this thesis, we focus on two main aspects by coupling computational fluid dynamics (CFD) with experimental imaging techniques. The first one is related to the flow of complex fluids, the feces, in the rectum. The second one involves flow phenomena at microscopic scales due to the presence of small-scale active structures in the small intestine, the villi.

Firstly, we develop a patient-specific two-dimensional (2D) CFD model of rectal evacuation by combining video-defecography and a lattice-Boltzmann flow solver. The video-defecographies are carried out with a neo-stool with a soft feces-like rheology which was modelled as a yield stress fluid. In normal defecation, the simulated pressure field demonstrates near homogeneity within the rectal cavity, with a gradient observed from the anorectal junction to the anal canal. Consequently, the pressure loss is attributed to the flow of feces through the anorectal junction and anal canal. The pressure gradient is controlled by the shear-thinning properties of the neo-stool rather than its yield stress, resulting in strongly non-linear pressure-flow rate relationships. Pressure fields for patients showing impaired defecation are also simulated. Comparisons with normal patients reveal potential dysfunction in rectal wall contractility for certain individuals.

Secondly, we investigate fluid flow phenomena at microscopic scales driven by the motility of small intestine villi. Using spatiotemporal motility data of the rat duodenum, we simulate the flow induced by the motion of these villi by lattice-Boltzmann methods for Newtonian fluids. We hypothesize that the villi's motion is induced by fast phasic contractions of the longitudinal smooth muscles. The 2D model represents an infinite array of rigid villi with leaf-like structures, where each villus oscillates longitudinally with a fixed phase lag from neighboring villi. This results in pulsatile radial and axial fluxes. Importantly, the motion of the villi induces a permanent flow in regions where the flow would otherwise be stagnant, due to the phase lag and inertia effects. This motion also leads to irreversible axial pumping in the lumen. These induced fluxes are expected to significantly enhance mass transfer and promote mixing toward the villi.

Finally, we present the development of an original experimental set-up aimed at studying small intestine motility and flow at the scale of the villi. The uniqueness of this setup lies in its ability to observe small intestine villi under iso-tonic conditions. In order to validate the physiological relevance of the device, we quantified the motility of the duodenum under various loads. The data obtained aided in the analysis of duodenal motility at the macroscopic scale using parameters such as amplitude and frequency of contractions, as well as strain rate maps at the microscopic scale. Looking ahead, the future scope of the device involves observing fluid flow patterns around the villi in the open duodenum and utilizing the data in CFD models.

In conclusion, this thesis integrates imaging techniques and fluid dynamics models, exploring transport phenomena in the GI at macro and micro scales. By providing valuable information, this thesis enhances GI biomechanics comprehension and holds clinical promise.

Résumé

Le tractus gastro-intestinal (GI) joue un rôle crucial dans l'absorption des nutriments. Sa motilité est induite par son activité motrice et est essentielle pour la décomposition des aliments, leur mélange avec les sécrétions, l'absorption des nutriments et le transport du digesta. De nombreux aspects de sa biomécanique ne sont pas bien compris. Des modèles mécanistiques sont nécessaires pour mieux appréhender son fonctionnement. Dans cette thèse, nous nous concentrons sur deux aspects principaux en combinant la dynamique des fluides computationnelle (CFD) avec des techniques expérimentales d'imagerie. Le premier concerne l'écoulement de fluides complexes, les feces, dans le rectum. Le deuxième concerne les phénomènes d'écoulement à l'échelle microscopique dus à la présence de structures actives à petite échelle dans l'intestin grêle, les villosités.

Nous développons un modèle CFD bidimensionnel (2D) spécifique au patient de l'évacuation rectale en combinant la vidéo-défécographie et les méthodes de lattice-Boltzmann. Les vidéo-défécographies sont réalisées avec un substitut ayant une rhéologie similaire aux selles molles et qui est modélisé comme un fluide à seuil d'écoulement. Dans une défécation normale, le champ de pression simulé est homogène dans la cavité rectale, avec un gradient de la jonction anorectale vers le canal anal. Par conséquent, la perte de pression est attribuée à l'écoulement des selles à travers la jonction anorectale et le canal anal. Ce gradient est contrôlé par les propriétés rhéofluidiantes du fluide plutôt que par son seuil d'écoulement, ce qui entraîne des relations pression-débit fortement non linéaires. Des champs de pression pour des patients présentant une défécation altérée sont également simulés. Les comparaisons avec des patients normaux révèlent une dysfonction potentielle de la contractilité de la paroi rectale chez certaines personnes.

Nous simulons les phénomènes d'écoulement induits par les villosités de l'intestin à des échelles microscopiques grâce à des données de motilité du duodénum du rat. Nous faisons l'hypothèse que le mouvement des villosités est induit par les contractions des muscles lisses longitudinaux. Le modèle 2D représente un ensemble infini de villosités rigides avec des structures en forme de feuilles, où chaque villosité oscille longitudinalement avec un décalage de phase fixe par rapport aux villosités voisines. Cela entraîne des flux radiaux et axiaux pulsés. Le mouvement des villosités induit un écoulement permanent dans les régions où l'écoulement serait autrement stagnant, du fait du déphasage et de l'inertie. Ce mouvement entraîne également un pompage axial irréversible dans la lumière intestinale. Ces flux améliorent probablement le transfert de masse et favorise le mélange auprès des villosités.

Enfin, nous présentons le développement d'un dispositif expérimental visant à étudier la motilité et l'écoulement de l'intestin grêle à l'échelle des villosités. Sa particularité réside dans sa capacité à observer les villosités dans des conditions isotoniques. Afin de valider le dispositif, nous avons quantifié la motilité du duodénum sous différentes charges. Les données obtenues permettent de caractériser la motilité duodénale en utilisant des paramètres tels que l'amplitude et la fréquence des contractions, ainsi que des cartes de taux de déformation. Le dispositif offre des perspectives prometteuses pour observer les écoulements des fluides autour des villosités dans le duodénum.

En conclusion, cette thèse vise à intégrer des techniques d'imagerie à des échelles macro et micro dans des modèles de dynamique des fluides complexes afin de mieux comprendre les phénomènes de transport dans le tractus gastro-intestinal (GI). Cette thèse fournit des

informations physiques précieuses qui contribuent à une compréhension plus approfondie de la biomécanique du tractus GI et présente un potentiel d'applications cliniques.

Contents

General Introduction

The motivation for pursuing a Ph.D., particularly in the field of Biomechanics, originated when I got admission to the Master 2 program in Biomechanical Engineering at École Polytechnique. During my master's studies, as part of the required internship, I had the privilege of collaborating with Clément de Loubens at Laboratoire Rhéologie et Procédés, who played a pivotal role as the director of my thesis. This experience further solidified my interest in the field.

Subsequently, towards the end of my M2 internship, I was awarded a scholarship from the École doctorale Ingénierie - Matériaux, Mécanique, Environnement, Énergétique, Procédés, Production (ED I-MEP2), which opened the path for me to pursue a Ph.D. in Biomechanical Engineering. This Ph.D. program was conducted jointly between two laboratories: Laboratoire Rhéologie et Procédés (LRP) and Translationnelle et Innovation en Médecine et Complexité (TIMC). In the LRP lab, with the guidance of Clément de Loubens, I acquired proficiency in utilizing advanced numerical methods such as the Lattice Boltzmann Method, and CFD models. These methods were applied to study fluid dynamics models of two distinct organs within the gastrointestinal tract. In the TIMC lab, under the supervision of Stéphane Tanguy, my second supervisor, I delved into the physiology of rats and its relevance to human physiology. I also had the opportunity to conduct ex-vivo experiments on small rats with Stéphane Tanguy. This work was a part of the TransportGut ANR (Agence nationale de la recherche) project, was dedicated to develop mathematical and experimental tools to model transport phenomena in the GI tract.

This thesis presents a comprehensive investigation into the multi-scale fluid mechanics of gastrointestinal tract motility using computational fluid dynamics (CFD) models, focusing specifically on the rectum and small intestine with villi. The study encompasses the active involvement of muscles and accounts for the varying rheological properties of digesta in the small intestine and feces in the rectum. We utilized video defecography of several individuals in the patient-specific 2D CFD to assess rectal function. X-ray defecography is a classic method used to diagnose defecation disorders, which is performed under physiological conditions by inserting neostool inside the rectum until the patient feels the urge to defecate. The videos used in our study were provided by one of our collaborators, Dr. Alain Dubreuil from Clinique du Mail, Grenoble, France. Another collaborator, Prof. Jean-Luc Faucheron from the Department of Surgery, Colorectal Unit, CHU Grenoble Alpes, France, provided valuable insights in interpreting the results obtained from the CFD rectal model. Their contributions were instrumental in the publication of two papers.

Moreover, we have developed a new ex−vivo experimental set−up to observe and record small intestinal motility at both macro and micro levels.

The gastrointestinal system, with its intricate network of organs and processes, plays a vital role in maintaining controlled passage and digestion of food. The process of digestion is both biochemical and biomechanical which involves active boundaries (smooth muscles, mucosa, vascular system), structures at both organ and villi scales, and complex rheological properties of digesta, muscles, and mucus. Disorders resulting from impaired motility of the gastrointestinal (GI) tract, such as gastroparesis, intestinal pseudo-obstruction, and Irritable bowel syndrome (IBS) can have profound effects on human health. These conditions involve the disruption of normal muscle contractions, leading to slowed or ineffective movement of food through the digestive system. Effective management of these disorders often requires a combination of medication, dietary modifications, and specialized medical interventions to restore proper GI motility and improve patient well-being.

Understanding the underlying mechanisms of gastrointestinal function is not only crucial for comprehending the complexities of our own bodies but also holds significance in fields such as multi-scale fluid mechanics, and biomedical sciences. Our approach in this thesis is mechanistic which will be focused on the study of fluid dynamics of motility within the gastrointestinal system. For instance, in the context of unraveling the intricacies of fluid flow with complex rheology, mixing of food, absorption, and transport of nutrients in the GI tract. The principles and insights gained from investigating GI motility can be applied to areas such as bio−reactors, drug delivery, and even the design of fluid-based systems.

Contents of the Thesis

This thesis is divided into two main components: macro and micro-scale analysis using fluid dynamics approach. At the macro-scale, we focused on modeling rectal function using physiological data (X-ray defecography), while at the micro-scale, we investigated villi movements in the small intestine. By examining these different scales, we aimed to gain a comprehensive understanding of gastrointestinal transport and mixing phenomena. Additionally, we also developed a new ex-vivo experimental set-up to observe and record small intestinal motility at both macro and micro scales. An overview of this thesis is provided below, outlining the chapters and the studies conducted within each:

Chapter 1: Overview of Gastrointestinal Tract and Literature Review
This chapter serves as an introduction to the research topic, providing an overview of the subject matter and presenting the context in which the research is conducted. Additionally, the objectives of the study are outlined, setting the direction and purpose of the research in relation to the gaps identified in the literature.

Chapter 2: Numerical Methods
The research methodology is described in detail, encompassing the Fluid Dynamics equations, stress-strain constitutive equation, and analysis techniques utilized, such as the lattice Boltzmann Method (LBM) with a two−relaxation−time (TRT) scheme.

Chapter 3: Fluid Mechanical Modelling of Human Defecation
The chapter focuses on the macro-scale analysis of rectal function, presenting the modeling techniques utilized, the data collected, and the results obtained from the study of rectal function. This chapter is divided into three sections. The first section (Section 3.2 − Paper 1) involves the development of a two-dimensional (2D) patient-specific computational fluid dynamics (CFD) model using physiological data (video defecography). The second section (Section 3.3 − Paper 2) applies the model to normal individuals and patients with pathologic defecation. Lastly, the third section (Section 3.4) extends the model to patients with anatomical abnormalities.

Chapter 4: Fluid Mechanical Study of Villi Motility and Development of New Experimental Set-up
This chapter comprises two sections. Section 4.1 entails a 2D CFD model of small intestinal-induced villi movements, examining the impact of duodenal motility on mixing and transport. Section (4.2) focuses on the validation of a new experimental set-up for investigating duodenal motility at the lumen and villi scales.

Chapter 5: Conclusion and Future Directions
The thesis concludes with a summary of the key findings from the multi-scale study, their implications, and suggestions for future research directions in the field.

Chapter 1

Overview of Gastrointestinal Tract and Literature Review

1.1 Gastrointestinal Tract: Processes and Functions

The gastrointestinal tract (GI tract) is a continuous hollow tube within the body, starting from the mouth and extending to the rectum. It includes organs such as the esophagus, stomach, small intestine, and large intestine, where various processes such as digestion, absorption, and elimination of food take place (anatomy of the GI tract shown in Fig. 1.1). This intricate system serves as a vital interface between the body and the external environment, facilitating the consumption and regulation of diverse nutrients [116].

The process of digestion begins in the mouth, where food is broken down and mixed with saliva. Saliva serves multiple functions, including protecting the oral cavity, providing digestive enzymes, and lubricating the passage of food into the stomach. In the stomach, mechanical degradation, liquefaction, enterogastric reflex, and enzymatic hydrolysis further contribute to breaking down the ingested food into a substance called chyme. As the digesta progresses through the small intestine, peristalsis, which is a rhythmic muscular contraction, propels it along the length of the small intestine. This movement, along with segmentation and pendular activities, facilitates the mixing of the digesta with pancreatic enzymes and bile acids, aiding in further digestion and absorption [65, 92, 143]. Finally, the elimination of indigestible wastes (feces) from the digestive tract occurs through rectal motion

During intestinal absorption, the layers of the gastrointestinal tract employ physiological mechanisms to prevent the passage of infectious materials across the GI mucosal surface [19]. The rheology of fluid in the GI tract also plays a role in nutrient absorption. Tharakan et al. (2010) found that the viscosity of luminal contents can influence nutrient absorption [133], while Mackie et al. (2016) hypothesized that increased viscosity of soluble dietary fiber, such as sodium alginate, interacts with intestinal mucus and decreases its permeability [83]. In a recent study, Ruiz et al. (2021) reviewed the significance of mucosal rheology at different pH levels in maintaining the normal function of the stomach and small intestine, with a particular focus on the critical role of mucus in drug delivery [112]. The complex process of drug absorption can be affected by the physiology of the gastrointestinal tract [97].

Moreover, drug delivery in the gastrointestinal (GI) tract is a complex interplay of absorption, mixing, and transport processes. The small intestine plays a crucial role in drug absorption, thanks to the presence of villi that significantly increase the available surface area for drug uptake [20, 35]. Efficient mixing processes, facilitated by peristalsis, pendular motion, and segmentation, ensure proper dispersion of the drug within the luminal contents [65, 68]. Transport mechanisms, including passive diffusion, active transport, and paracellular pathways, allow the drug to cross the intestinal epithelium and enter systemic circulation. Understanding and optimizing these processes is vital for improving drug delivery efficacy in the GI tract.

Further, research can improve therapeutic outcomes and maximize drug bioavailability in this crucial route of administration by customizing drug formulations and delivery systems to

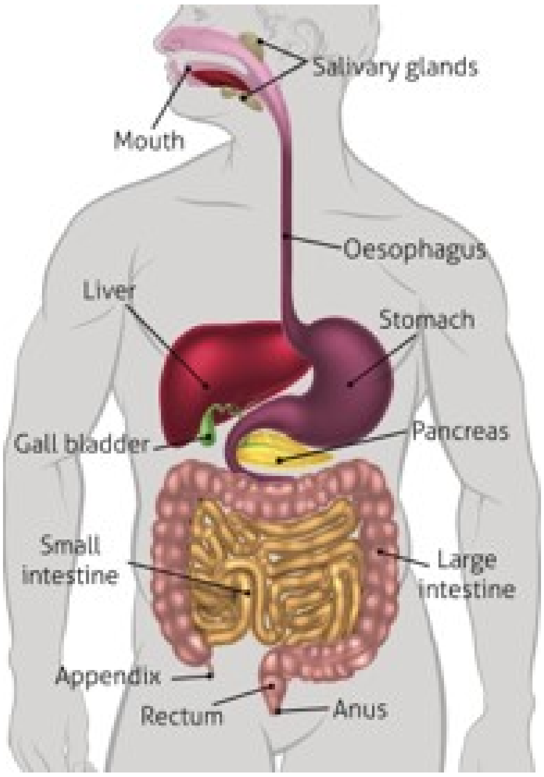

Figure 1.1: Digestive system

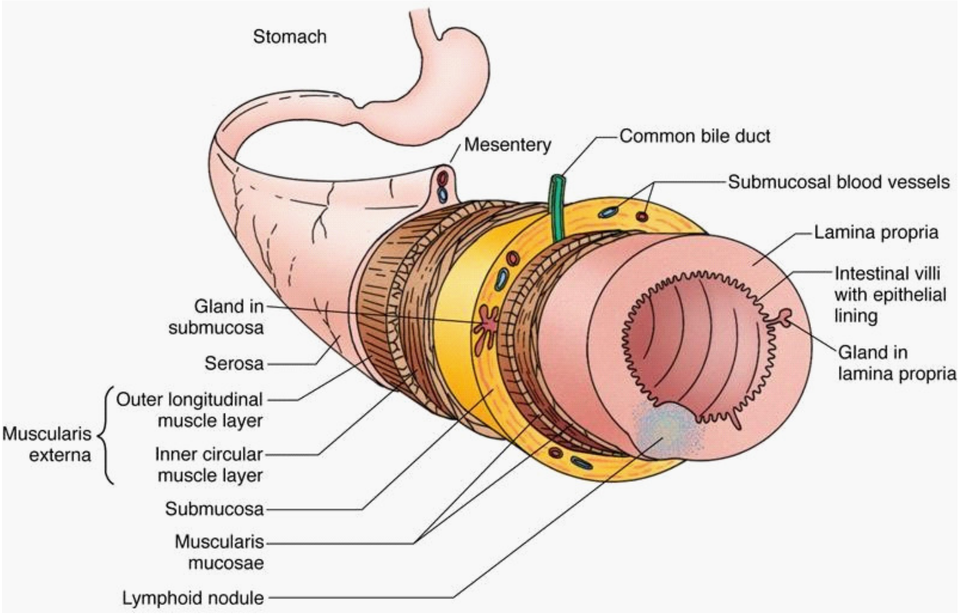

Figure 1.2: Generalized description of the principal layers of the GIT.

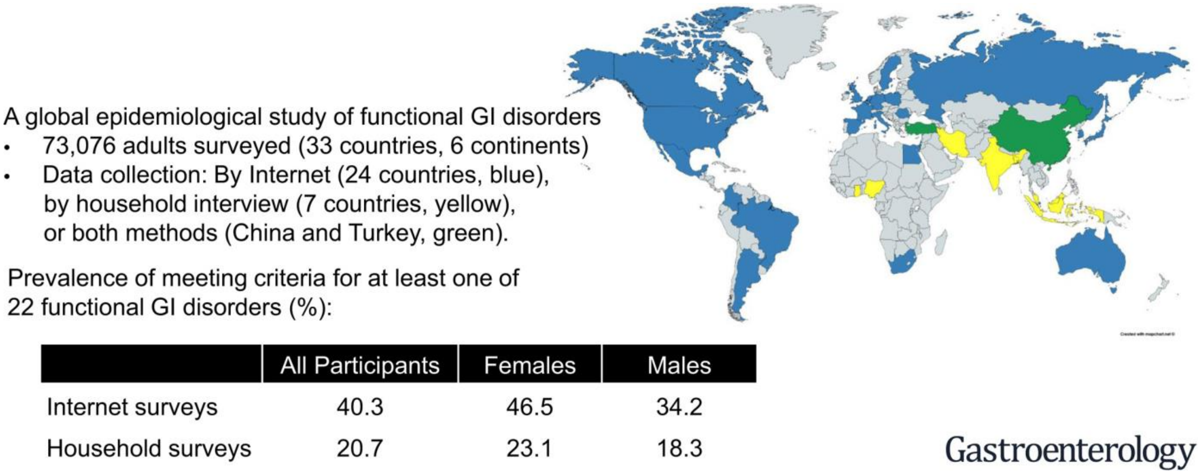

A global epidemiological study of functional GI disorders

- 73,076 adults surveyed (33 countries, 6 continents)
- Data collection: By Internet (24 countries, blue), by household interview (7 countries, yellow), or both methods (China and Turkey, green).

Prevalence of meeting criteria for at least one of 22 functional GI disorders (%):

	All Participants	Females	Males
Internet surveys	40.3	46.5	34.2
Household surveys	20.7	23.1	18.3

Figure 1.3: Worldwide survey on prevalence and distribution of functional GI disorders [123].

leverage the absorption, mixing, and transport mechanisms. By understanding how drugs are absorbed, distributed, and transported within the gastrointestinal tract, new strategies can be developed to optimize drug delivery, leading to enhanced efficacy and better patient outcomes [3, 10].

1.2 Human Health and GI Tract Disorders

The wall of the GIT maintains a similar structure throughout its length but also displays regional specializations and modifications. It consists of four main histological layers, namely the *mucosa, submucosa, muscularis externa, and serosa (or adventitia)*, Fig. 1.2 [42]. Indeed, the proper functioning of the mucosa layers, musculature distention, and neural networks within the gastrointestinal (GI) tract are vital for maintaining the normal functions of the GI tract. However, when these components experience dysfunction, it can lead to various disorders and deteriorate health conditions. Some of the problems that can arise from these malfunctions include inflammation, constipation, ulceration, bleeding, abdominal pain, and irritable bowel syndrome (IBS), among others [32]. Chronic intestinal pseudo-obstruction (CIPO) is characterized by the impaired motility of the small intestine [11]. Sperber et al. conducted a survey on the global population to assess the prevalence and distribution of GI tract disorders. Their findings revealed that more than 40 % of individuals worldwide are affected by functional gastrointestinal disorders (FGIDs), resulting in a substantial impact on their quality of life and healthcare utilization., shown in Fig. 1.3 [123]. Additionally, defecation disorders are also widespread in the worldwide population with prevalence in about 15 % of the population [31] and require medical intervention and management strategies to alleviate symptoms and improve rectal function.

Stress levels, aging, and food quality are some of the common factors responsible for worsening the symptoms of common GI disorders. In fact, high stress or negative emotions can alter the motility and permeability of the gastrointestinal tract (GIT) [44]. The studies based on rodents suggested that aging alters intestinal smooth muscle contractility [93], sensory action [101], and neural interventions of the GI tract [62]. Other symptoms, particularly those related to the upper GI tract, are well-known and can be attributed to three pathophysiological mechanisms: uneven gastric emptying, impaired accommodation, and heightened sensitivity of the muscles [12].

Gastrointestinal tract is also home to the largest population and concentration of microorganisms within the human body. Disturbances in the balance of the gut microbial ecosystem have been linked to a wide range of conditions, including chronic GI diseases like Crohn's disease and ulcerative colitis, as well as metabolic disorders such as type 1 and type 2 diabetes and obesity. Additionally, the use of antibiotics has also been associated with alterations in the gut microbiota (review [119]). Moreover, Saraswati et al. in their [115] review, suggested the need of developing mechanistic models by incorporating information available regarding the diversity of GI tract microbiota in case of aging. The use of animals as research models has been employed to investigate the therapeutic effects associated with manipulating the gut microbiota in various disease states, (review [134]) directed use of different animals (rats, mice, pigs, etc) based on specific research questions.

The following sections are structured into three sections. Firstly, it provides an overview of small intestinal motility, villi movements, and rectal motility, including the rheology of food as it travels through the small intestine and the rheology of feces in the rectum. Secondly, a comprehensive literature survey was conducted to thoroughly analyze prior research in the field, which led to the identification of objectives for this thesis (third section).

1.3 Overview of the GI Tract Motility

The regulation of the GI tract's overall function relies heavily on motility, which is orchestrated by the coordination of myogenic (muscle-related), neural, and hormonal factors. While myogenic parameters initiate the motor patterns, neural and hormonal influences modulate the motor activity by modifying the contractions driven by the myogenic mechanisms. The motor activity ensures proper movement, mixing, and propulsion of the intestinal contents, facilitating digestion, absorption, and overall GI function [20]. The deglutition reflex, also known as the swallowing reflex, is a coordinated sequence of muscular movements and actions that occur during the process of swallowing. It involves the passage of food in solid and liquid from the mouth, through the throat (pharynx), and into the esophagus, ultimately reaching the stomach [135]. GI tract motility provides directions for the flow, mixing, and absorption of food, which are necessary for the functioning of the body and prevent the passage of harmful agents. Consequently, absorption occurs which basically extracts resources for body from the food throughout the GI tract. Its motility varies with respect to the species, organs, the digestive phase, and local mechanical stimuli [72].

In this thesis, the focus will be on investigating the motility of the small intestine and the rectum. Subsequently, the motility patterns and mechanisms specific to these two parts of the gastrointestinal tract will be thoroughly discussed.

1.3.1 Motility of the small intestine

The small intestine is the longest and most intricate part of the gastrointestinal (GI) tract, measuring approximately 5 to 6 meters in length with a diameter of 25 to 30 mm for adult humans. It extends from the pyloric sphincter of the stomach to the ileocecal junction where it connects to the large intestine. The small intestine is a vital component of the gastrointestinal tract, responsible for enzymatic digestion, mucus secretion, and significant absorption of food and nutrients. It comprises the duodenum (25-30 cm), jejunum (3 m), and ileum (3 m). Each segment has different content residence times (40 min, 2-3 hr, 3-4 hr) and absorbing areas (0.09 m^2, 60 m^2, 60 m^2) respectively, crucial for the absorption and mass transport [35, 60]. Moreover, the wall of the small intestine contains rich networks of blood and lymphatic vessels. The lymphatic system is essential for the absorption of fat from the GIT.

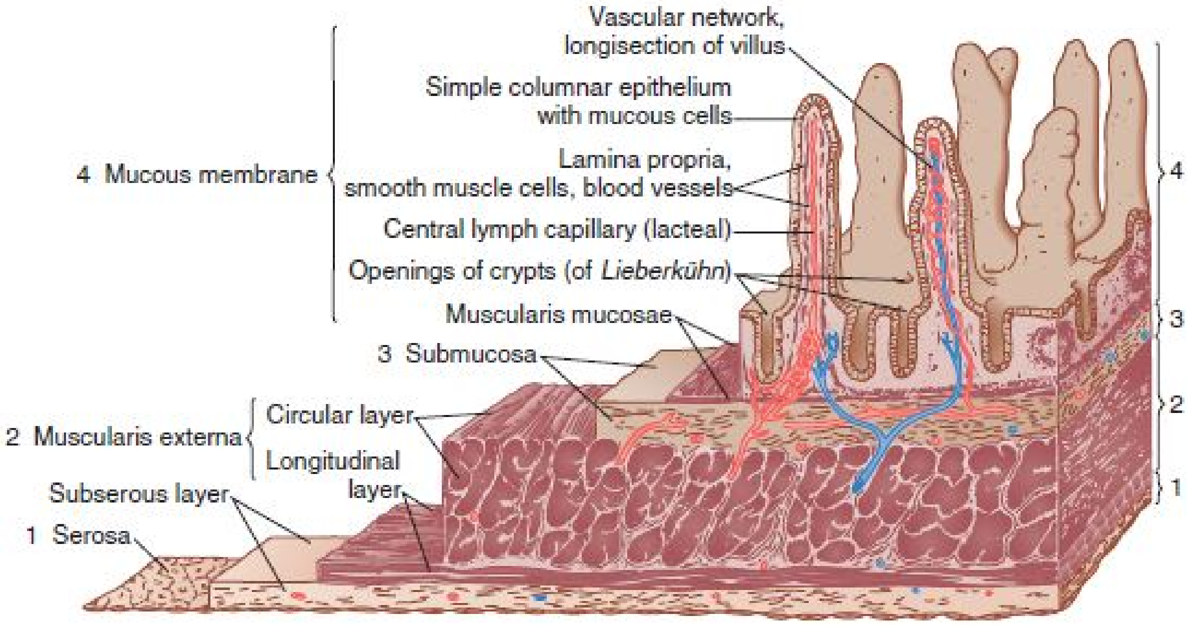

Figure 1.4: There are four main layers of the small intestine. The outermost layer is the serosa followed by the subserosa. Next is the muscularis externa, which is made up of an outer longitudinal and an inner circular layer. The submucosa layer is next and the innermost layer is the mucous membrane, which consists of the intestinal villi. [122].

The larger surface area in small intestine is attributed to the presence of villi and microvilli (Fig.1.4 shows a histological view of the small intestine). In contrast, colon, which is 1.5 meters long, has a surface area of only 0.3 m^2. In humans, the villi, approximately $0.5-1.5$ mm in length (with the longest found in the duodenum) and 0.1 mm in diameter, significantly enhance the surface area by $10-$fold for nutrient absorption. The villi are further covered by microvilli, which are tiny projections measuring 1 μm in length and 0.1 μm in width. These microvilli further contribute to a $20-$fold increase in the surface area [20].

Apart from other places in the GI tract (esophagus, stomach, large intestine), peristalsis movement also occurs in the small intestine, which is a coordinated contraction of longitudinal and circular muscles resulting in the propulsion of food. Small intestinal motility also consists of segmentation motion which involves localized, ringlike, alternating contractions and relaxations of the circular smooth muscles in the intestinal wall. Firstly, it facilitates the mechanical breakdown of the chyme, ensuring thorough mixing with digestive enzymes and maximizing the surface area available for absorption. Additionally, the pendular movements in small intestine involve alternate contractions and relaxations of the longitudinal muscles, resulting in the shortening and lengthening of a portion of the intestine and aiding in the mixing of chyme. These coordinated movements collectively contribute to the overall function of the small intestine in processing and absorbing nutrients from the ingested food and making the SI as most absorptive part of the GI tract [40, 133]. The absorption mainly depends on the health of the mucous membrane and the presence of villi and micro-villi on the mucous layer [87].

1.3.2 Characteristics and movements of the villi

In the previous section, we have mentioned the influence of villi and micro-villi presence in increasing the absorption area in the small intestine. Gruby et al. conducted the initial investigation of villus motility, observing the contraction, expansion, and longitudinal motions of

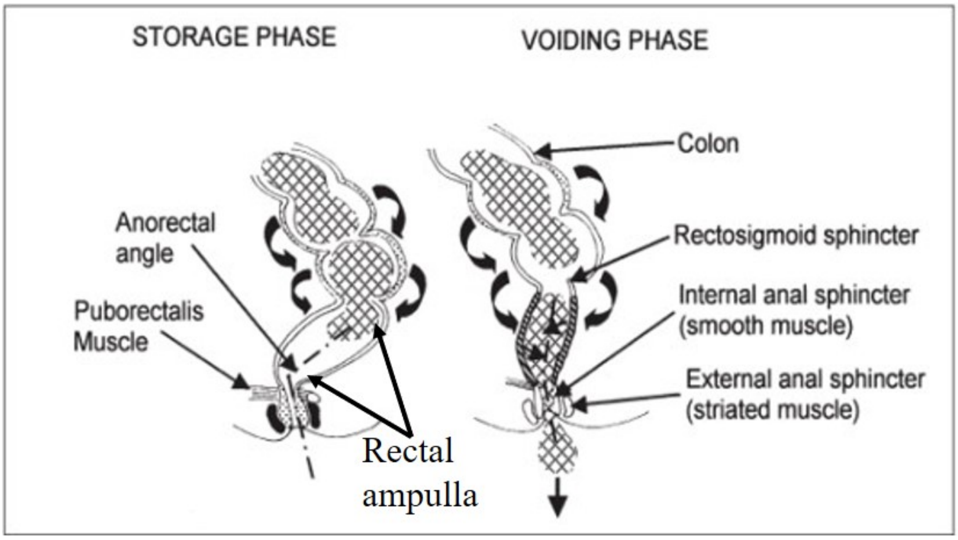

FIGURE 1.5: Rectal evacuation process: Change in anorectal angle during defecation [7].

villi in a gut segment that was taken from a living animal [47]. Kokas et al. [65] wrote an editorial based on their experiments that the rate of contractions and relaxations of villi has great variability, and defects in villous motility could lead to malabsorption and less mass transfer of nutrients. Villous movements (retraction, whipping, and swaying) that are characterized by their frequency and duration of contraction are known to alter the transport of nutrients to the villi. In-silico studies revealed the presence of a micro-mixing layer that interacts with the macroscopic flows to increase the nutrient transit and absorption [78, 137, 139]. Brasseur et al. found that micro-mixing induced by villi and macro-scale motions in the lumen is coupled to enhance absorption [15]. At the micro-scale level, the villi are responsible for the betterment of the immune system, which is key to develop new oral therapeutic strategies [16].

1.3.3 Motility of the rectum

The rectum starts in front of the body of the third sacral vertebra and its geometry complies with the ventral concavity. The middle rectal part of the rectum is the most constant and prominent and is regularly encountered during rigid sigmoidoscopy. The inferior third of the rectum is dilated by the feces and is termed the ampulla (anatomy of rectum is shown in Fig. 1.5). The rectum in adults measures $10 - 14$ cm in length, the anus is 2 to 4 cm long and 3 cm in diameter. The internal anal sphincter measures 3 cm [84]. Rectal motility refers to the contraction and relaxation of muscles of the wall of the rectum, the final section of the large intestine. It acts as a temporary storage area for feces before they are eliminated through defecation, and works in conjunction with the anal canal to maintain continence and evacuation of feces. The physiology of the rectum muscles follows the same properties as in other GI tract parts. The wall of the rectum is also considered a viscoelastic material which allows a significant increase in volume without a significant increase in pressure [51, 95, 96].

Fig. 1.6 shows a series of schematic diagrams depict the normal anatomy and physiology of the pelvic floor in the sagittal plane, both at rest and during defecation, highlighting significant pathophysiological changes observed in individuals with fecal incontinence and dyssynergic defecation [107]. The diagrams demonstrate the resting profile, illustrating the arrangement of the three anal muscles, including the puborectalis muscle. During defecation, normal changes occur: the anal sphincters and puborectalis muscles relax, while the abdominal and rectal

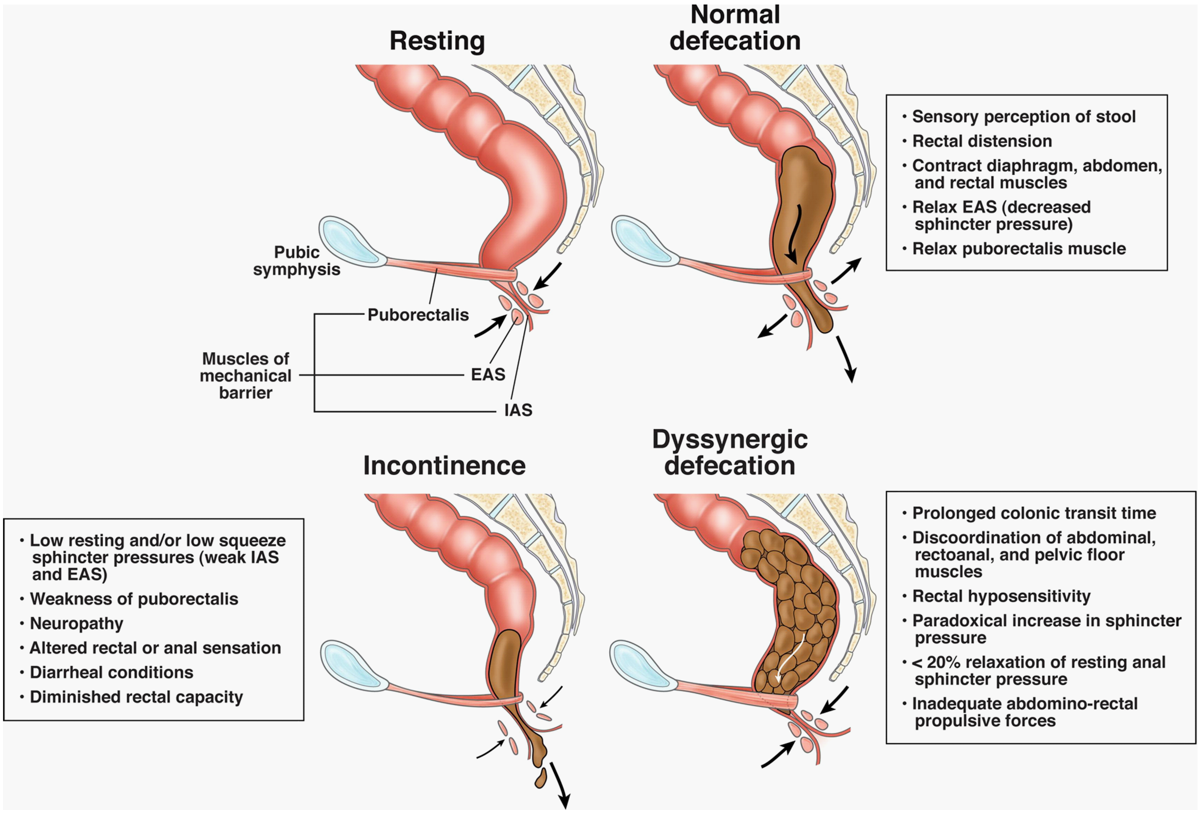

FIGURE 1.6: Anatomy and Physiology of the Pelvic Floor: Exploring Normal Function and Pathophysiologic Changes. internal anal sphincter (IAS), external anal sphincter (EAS) [107].

pushing forces generate the necessary propulsion to empty the rectum and expel stool. In the case of fecal incontinence, weakened anal and puborectalis muscles may lead to stool leakage. Similarly, in individuals with dyssynergia, there may be impaired push effort or anal relaxation, resulting in a lack of coordination (dyssynergia) and stool retention, as the anal sphincters and puborectalis muscles fail to relax during attempted defecation.

Defecation is a complex physiological process, which involves the coordination of neural, muscular, hormonal, and cognitive systems [51]. Rectal motility disorders encompass a range of conditions that can affect the ability to initiate or complete defecation (constipation) or control bowel movements (incontinence). These disorders also include related syndromes such as functional diarrhea and irritable bowel syndrome (IBS). Constipation refers to difficulty in initiating or completing bowel movements, often resulting in infrequent or hard stools. It can be caused by various factors, including decreased rectal motility, inadequate fiber intake, dehydration, certain medications, or underlying medical conditions. Incontinence, on the other hand, refers to the inability to control bowel movements, leading to involuntary leakage of stool. It can be caused by weakened rectal muscles, nerve damage, or other factors affecting anal sphincter control. Functional diarrhea is defined by the occurrence of recurring episodes of loose stools, which do not exhibit any discernible structural or inflammatory abnormalities. This condition is frequently accompanied by changes in rectal motility and heightened bowel frequency. IBS is a chronic functional gastrointestinal disorder characterized by abdominal pain, bloating, and changes in bowel habits. It is believed to involve abnormalities in rectal motility and visceral hypersensitivity. As a result, the classification and identification of defecation disorders (DDs) have proven to be challenging due to the significant overlap in symptoms [94]. In Section 1.4.2, we will discuss the available techniques available to diagnose defecation disorders (DDs).

Phases in defecation

The phenomenon of defecation has been further elucidated by categorizing it into four distinct phases, each characterized by varying pathophysiology and duration of the defecation process. These phases include the basal phase, pre-expulsive phase, expulsive phase, and end phase. The classification is largely taken from a recent review study conducted in 2021 [51].

Basal phase refers to the non-defecatory state of the colon, acting as a reservoir prior to defecation. During this phase, there is synchronous pressure increase throughout the colon, which is particularly prominent after a meal and gradually diminishes afterward [24]. Rectal continence is maintained during this phase. Recent advancements in high-resolution anorectal (HRA) manometry have revealed the presence of periodic and rhythmic rectal contractions known as cyclic rectal motor activity, which may play a functional role in initiating rectal filling [30].

Pre-expulsive phase encompasses colonic propulsion, rectal filling, and the distension of the muscles. As the rectum becomes distended, it triggers a conscious defecatory urge through the stimulation of rectal mechanoreceptors.

Expulsive phase of defecation involves nearly complete emptying of the rectum. It is characterized by increased anorectal pressure, a reduced anorectal angle, and voluntary relaxation of the external anal sphincter (EAS). These factors collectively facilitate the effective expulsion of fecal matter during defecation.

End phase involves a decrease in the pressure gradient across the rectum, accompanied by the contraction of the anal sphincter and pelvic floor muscles, returning the rectum to its resting state.

1.4 Fluid Dynamics of the GI Tract

Different studies employed various models, including in-vivo, ex-vivo, and in-silico models, to observe, assess, and analyze factors influencing gastrointestinal (GI) tract functions. These models play a crucial role in testing new drugs, diagnosing diseases, exploring direct drug delivery methods, creating a favorable environment for the GI tract, and developing new technologies such as micro-capsules and robotic capsules. However, it is important to acknowledge the importance, usefulness, and limitations of these models, which will be discussed in the following sections after discussing the rheology of food found in the GI tract.

1.4.1 Rheology of food throughout GI tract

Rheology is the field of study that focuses on the flow of fluids and the deformation of solids when subjected to an applied force. It involves establishing relationships between stress and strain rate using parameters such as viscosity (μ), flow index (n), and consistency index (k). Viscosity refers to the internal friction experienced by a fluid or soft solid as it flows or deforms under a given strain rate. While Newtonian fluids like water and alcohol exhibit a linear relationship between viscous stress and strain rate, non-Newtonian fluids such as dilatant (shear-thickening) and pseudoplastic (shear-thinning) fluids exhibit more complex rheological behavior. Fig. 1.7 illustrates five different time-independent rheological models, commonly referred to as flow curves, depicting the relationship between shear or viscous stress and strain rate or shear rate [130].

Rheology of digesta in the small intestine

When investigating the rheology of the gastrointestinal (GI) tract, the primary objective is to comprehend the rheological properties of both food and mucus. This understanding plays

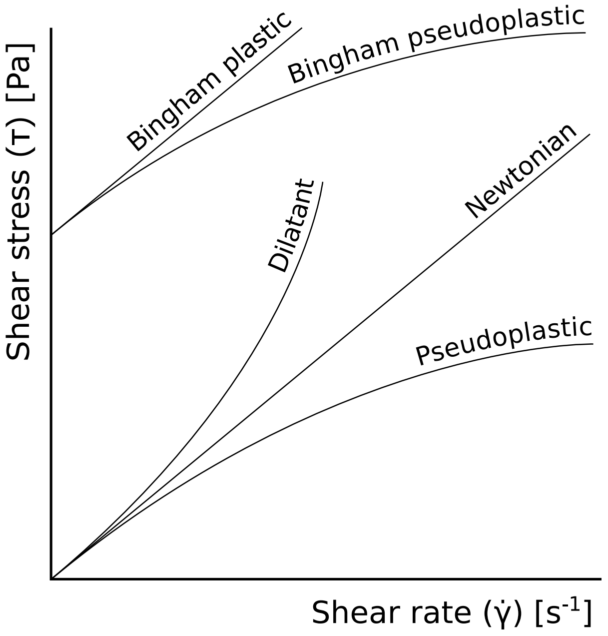

Figure 1.7: Rheological behavior of non-Newtonian fluids.

a crucial role in enhancing nutrition through the incorporation of diverse ingredients. The initial breakdown of food occurs in the oral cavity through a combination of mechanical and biochemical processes, resulting in the formation of a lubricated bolus. Subsequently, in the stomach, antral contractions and chemical factors work together to further break down food particles, reducing them to approximately 1 mm in size before they reach the pyloric opening. [121]. In the small intestine, food exhibits mainly shear-thinning behavior. Experimental data of water-soluble dietary fiber can be fitted into the Cross model to analyze its rheological properties. Additionally, the Carreau model can be used to introduce shear-thinning behavior of the intestinal digesta [110].

Whereas, muscus is a viscoelastic gel that behaves as a non-Newtonian thixotropic gel, where its viscosity decreases with an increase in the shear rate (review - [112]). Moreover, the rheology of mucus can be influenced by factors such as high stress, prolonged shear rate, and changes in pH [136].

Rheology and Bristol scale for the stool

Feces, in general, consist of a heterogeneous suspension of partially or fully digested food particles suspended in an aqueous Newtonian liquid. This mixture exhibits shear thinning (pseudoplastic) behavior, where its viscosity decreases with increasing shear rate. The consistency of feces can vary greatly depending on factors such as diet, water content, and physiological factors. The rheological properties of feces are likely influenced by factors such as particle size, shape, microstructure, as well as the volumes of the solid and liquid phases, and the properties of the continuous liquid phase [72]. Changes in any of these properties can affect the net apparent viscosity and other rheological characteristics of feces, including yield stress [81].

- **Shear yield stress and shear thinning**

The shear yield stress refers to the minimum shear stress required to initiate flow in a fluid. Below this threshold, the fluid behaves like a solid and flows in packets, while above this threshold, it starts to flow continuously. Based on Figures 1.8a and1.8b, feces exhibit behavior

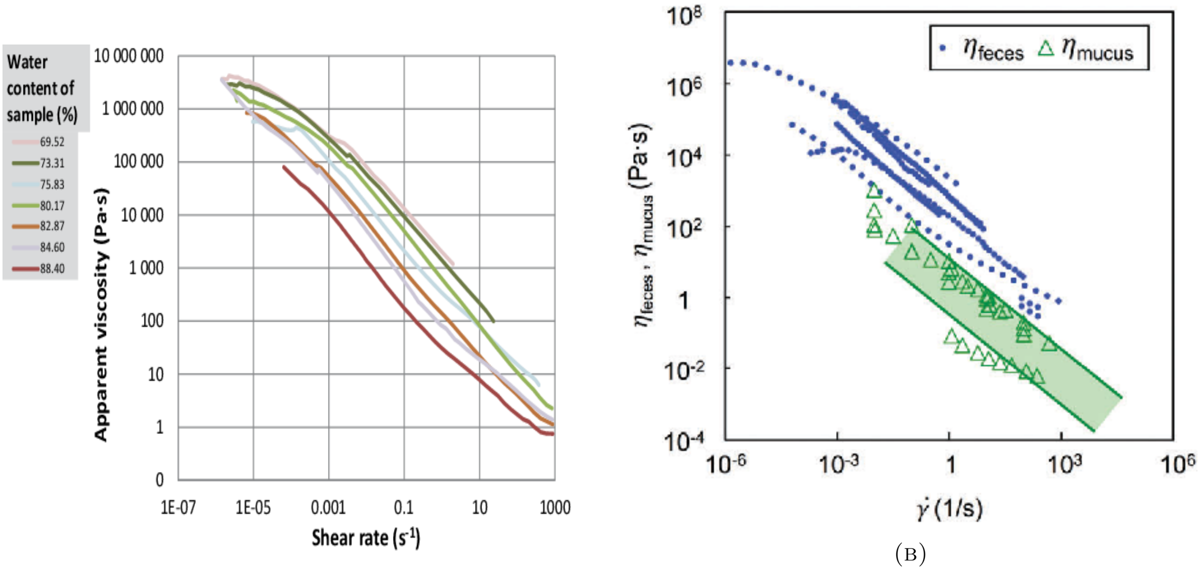

(A)

(B)

FIGURE 1.8: (a) Viscosity flow curves for fresh human feces for different water content relative to the shear rate [144] (b) The relationship between the viscosities of feces and mucus relative to the shear rate [146].

similar to that of a shear-thinning fluid. To describe the rheology of feces, the Herschel-Bulkley model, also known as the modified Bingham model, can be used. The constitutive equation of the Herschel-Bulkley (HB) model, and dynamic viscosity (η) is given by,

$$\begin{cases} \eta = \left(\frac{\tau_0}{|\dot{\gamma}|} + k|\dot{\gamma}|^{n-1}\right), & \text{if } |\tau| > \tau_0 \\ \eta = 0, & \text{if } |\tau| \leq \tau_0 \end{cases} \tag{1.1}$$

where τ is the shear stress, k the consistency index, n is the flow index, $\dot{\gamma}$ is the shear rate, and τ_0 is the yield shear stress. If $\tau < \tau_0$ the Herschel-Bulkley (HB) fluid behaves as a solid, otherwise it behaves as a fluid and in case of the feces $n < 1$ that corresponds to the shear-thinning fluid.

- **Bristol stool scale**

The Bristol Stool Scale is a medical tool designed to categorize human feces into seven different types based on their consistency and liquid content (Fig. 1.9a). It has been widely used in clinical and experimental settings for various purposes. The scale was originally developed at the Bristol Royal Infirmary in 1997 for clinical use and has since become a valuable research tool for assessing the efficacy of treatments for bowel-related conditions. It is also included as part of the diagnostic triad for irritable bowel syndrome, contributing to its clinical significance in gastrointestinal disorders [111].

Recently, de Loubens et al. conducted a study to investigate the shear yield stress of feces and its relationship with water content [81]. They also examined the correlation between the Bristol Stool Scale and the yield stress, as shown in Fig. 1.9b. This research highlights the significance of understanding the rheological properties of stool in the rectum, which can vary in magnitude by threefold across different Bristol scale categories. Consequently, it becomes crucial to consider the impact of stool rheology on rectal performance and related physiological processes.

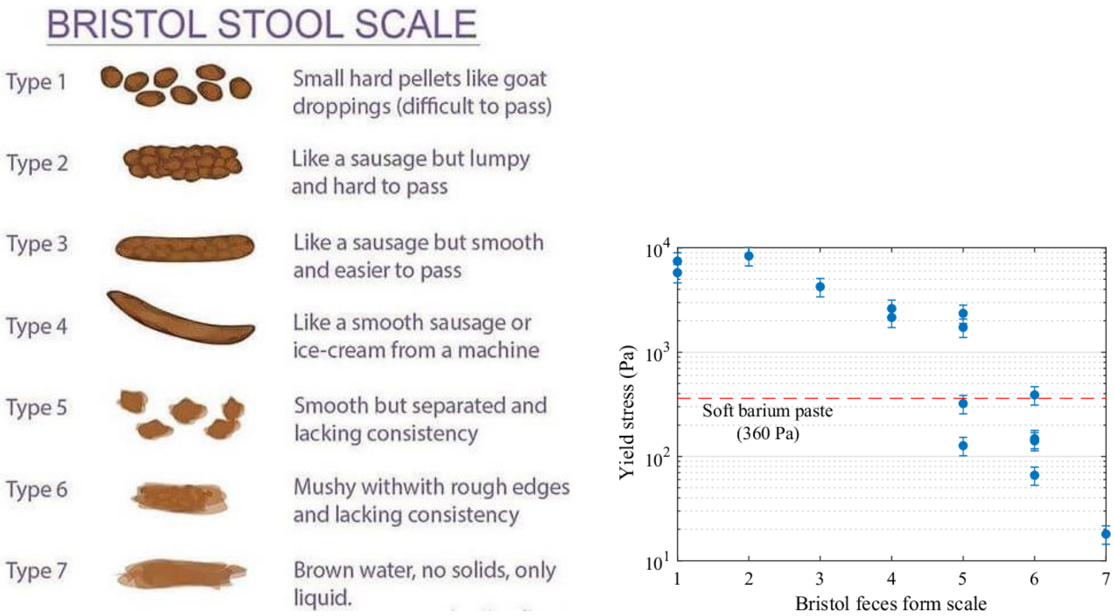

(A) (B)

FIGURE 1.9: **(a)** The Bristol Stool Form Scale **(b)** Left: yield as a function of solid content, Yield stress increases over several orders of magnitude as solid volume content increases. Right: yield stress is correlated with the score on the Bristol feces from the hardest "7" to watery "1" [81].

1.4.2 Models for the rectum motility

Diagnostic methods

These series of schematic diagrams reveal the normal anatomy and physiology of the pelvic floor in the sagittal plane at rest, during defecation, and the key pathophysiologic changes in subjects with fecal incontinence and dyssynergic defecation. The resting profile shows the arrangement of the 3 anal muscles including the puborectalis muscle and the normal changes that occur during defecation: the anal sphincters and the puborectalis relax and the abdominal and rectal pushing forces generate a push force to empty the rectum and stool. In a patient with fecal incontinence, the anal and puborectalis muscle may be weak, causing stool leakage. In subjects with dyssynergia, the push effort or anal relaxation may be impaired or the anal sphincters and puborectalis may not relax during attempted defecation, leading to incoordination (dyssynergia) and stool retention.

Impaired motility of the rectum plays a pivotal role in the development of defecation disorders (DDs). Therefore, it is crucial to have accurate and effective diagnostic methods to identify and assess these conditions. In-vivo methods involve the application of diagnosing techniques such as anorectal manometry (ARM), defecography, magnetic resonance imaging (MRI), balloon expulsion test (BET), etc. The BET helps to diagnose functional defecation disorders (FDDs) which are described by in-consistence contraction or poor relaxation of the pelvic floor muscles and/or insufficient propulsive force during tried defecation. In the BET test, the patients ask to expel a balloon filled with water or air with a volume of 50 ml, and the time to expel the balloon is recorded [88]. While ARM, catheters are the central part of the assessment of DDs, to which many sensors are attached. It measures pressure across the rectum (intra- rectal), anal pressure, rectoanal coordination, and muscle activity or electromyography (EMG) during attempted defecation to diagnose FDDs. The results obtained for patients are sometimes contradictory when compared with the results of asymptomatic individuals. This suggests that ARMs are still in the evolutionary phase. Recently, fecobionics technique has also been used in which a normal stool-shaped tool is inserted in the rectum. This method was developed by Lewis et al. in 1997 [75], they inserted a bag in the rectum and then filled it until the patient feel the urge to defecate with a maximum of 100 ml fluid. The main advantage of this method compared to others such as anorectal manometry, BET, and defecography, is that it incorporates the pressure measurements of the manometry, the evacuation duration of the BET, and the angle measurement of the defecography. Also, it showed consistency with BET and defecography during defecation despite different filling volumes [61].

The mentioned diagnostic technique has the potential to provide insights when there are issues related to muscle health, coordination between the muscles, rectum wall motility, and feces expulsion time. However, pathological structural abnormalities, as well as functional abnormalities, are common in patients with chronic constipation which can only be identified with imaging techniques such as defecography, and MRI. These tests have notable limitations. For instance, high-resolution anorectal manometry (HRAM) lacks the capability to capture dynamic events during actual defecation because it is commonly performed in non-physiological conditions with an empty rectum. Defecography, on the other hand, does not offer insights into anorectal sensation and motility. Balloon expulsion testing (BET) fails to provide physiological information regarding geometric and pressure changes occurring during the passage of simulated stool through the rectum and anal canal. Moreover, there exists substantial disagreement among the results of different anorectal tests, and unsurprisingly, these test outcomes demonstrate poor correlation with symptoms and treatment outcomes [51, 96]. In the following section, we will discuss the studies which involve mechanistic approach to assess rectal function during defecation.

Mechanistic model

The concept of the fluid model of defecation was initially introduced by Farag, who considered feces as a Newtonian fluid and applied the Hagen-Poiseuille law to calculate intra-rectal pressure [36]. Anorectal physiological parameters were compared between normal controls and patients with functional pelvic outlet obstruction and fecal incontinence. The parameters included intrarectal pressure, measured using anorectal manometry at different stages of defecation, and dimensions of the rectum, obtained from lateral defecography videos. These factors were incorporated into the Hagen-Poiseuille law to determine anal canal resistance and flow. In another study, the sensory component was associated with intrarectal pressure, while the reflex component of the rectum was linked to the dynamic viscosity of the bowel contents, anal canal length, and diameter [37, 38]. This approach opened up a new way to incorporate fluid dynamics and physiological data, with Farag's analysis providing fundamental insights into anorectal geometry and the rheology of feces. Building upon this, Bush et al. expanded the fluid model by incorporating a more realistic rectal geometry (Fig. 1.10a) and considering normal feces as a plastic fluid [18]. The idea was to study flow resistance in relation to the anal canal diameter. They discovered that reducing the diameter ratio by 2 times resulted in an 8-fold increase in flow resistance. This finding highlighted the importance of rectal geometry, but the considered geometry was still fundamental as it did not take into account the actual shape of the rectum. On a different note, Yang et al. conducted observations on various animals based on defecation time and proposed that fecal flow was primarily influenced by the rheology of the mucus layer and the mucus lubrication in a straight channel, Fig. 1.10b [146].

Another approach for studying rectal function has emerged through the advancements in Fecobionics, a specialized field within bionics that is at the forefront of medical applications, presents a state-of-the-art method for investigating rectal dynamics [61]. Unlike ingestible capsules, fecobionics employs a simulated stool that closely resembles the shape of normal stool and is inserted into the rectum to take data. Throughout defecation time, this innovative technique captures and measures a range of parameters, including pressures, anorectal angle, flow

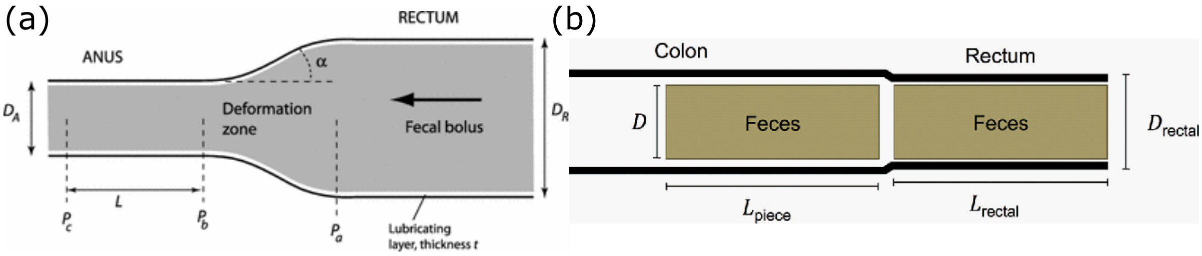

FIGURE 1.10: **(a)** Simplified anorectal representation with lubrication between bolus and duct wall [18], **(b)** Schematic of the dimensions of the rectum and fecal pieces [146].

rate, and changes in shape of rectum. These parameters are commonly evaluated in existing tests and offer valuable insights into rectal function and motility. Although, fecobionics is still in its infancy when it comes to the utilization to a patient and the realization of the defecation disorders [45, 127]. Therefore, developing a more advanced mechanistic model that incorporates a comprehensive understanding of rectal function would be instrumental in simulating defecation in a realistic and physiological manner.

1.4.3 Macroscopic and microscopic models: Flow around villi

Physical models

Quantitatively investigating the processes of mixing, mass transfer, and absorption in the gastrointestinal tract has been a longstanding challenge. One specific example is the determination of intestinal permeability (cm/s). In the past decades, numerous methodologies have been proposed to assess this coefficient, which serves as a reflection of the rate at which substances pass through the intestinal membrane.

Several researchers have conducted in-vivo experiments, although these studies are often limited due to ethical constraints. One commonly employed technique is intestinal perfusion, which involves both in-vivo human intestinal perfusion [27, 70, 90] and in-situ animal intestinal perfusion [2, 76]. While this approach allows for the quantification of intestinal permeability, it does come with inherent challenges. For instance, the technique often necessitates the use of unrealistically high flow rates, which may not accurately represent the natural conditions in the body. Additionally, it is unable to distinguish between the processes of absorption and intestinal metabolism, posing a limitation [106]. Moreover, when it comes to in-vivo experiments, especially those involving humans, it becomes impossible to isolate and accurately assess the individual effects of factors such as intestinal morphology and motility, which further complicates the analysis.

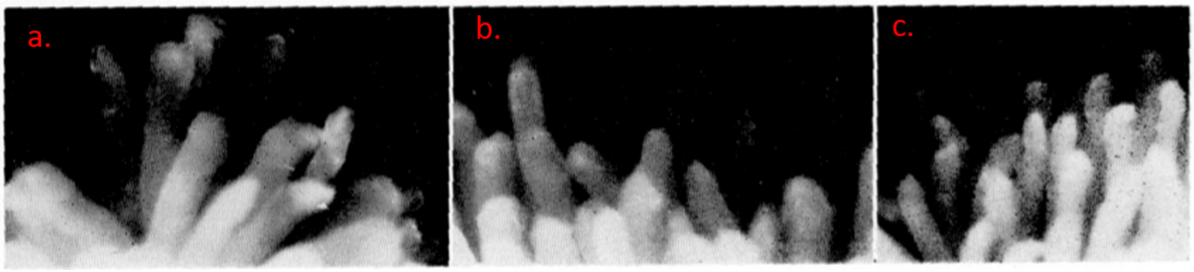

FIGURE 1.11: Villi in the duodenum (a), the jejunum (b), the ileum (c) of a dog [92].

To overcome these limitations, many in-vitro and ex-vivo digestion systems have emerged as a substitute approach in recent years [85, 145]. Nonetheless, majority of these systems mainly study the processes prior to the absorption without taking into account the intricate anatomy of the small intestine such as mixing, gastric emptying, and hydrolysis. Very few studies have tried to mimic the absorption process using a semipermeable membrane that permits the passage of digested products while blocking undigested substrates. However, implementing complex geometric features of the small intestine, such as circular folds and villi, which significantly impact flow patterns and mass transfer, remains challenging in in-vitro systems [147, 150]. Although some research groups have excised animal intestinal tissues, replicating the various movements of the intestinal walls, such as segmentation and peristalsis, proves difficult in these experiments [102, 108].

After that, many studies were conducted regarding the villi motility and their potential contribution to local mixing and formation of "unstirred water layer" (UWL) [49, 142, 143]. Nanba et al. actually recorded the movement of the villi of a dog on a mechanograph [92] (Fig. 1.11 shows villi in the dog's intestine). They observed increased activity in the upper part of the small intestine, specifically at the tip of the villi. These villi underwent rapid shortening and slow extension, occurring approximately $10-28$ times per minute. However, there are still gaps in understanding villi motility, unlike the well-established knowledge on intestinal motility, thanks to advancements in animal ex-vivo models. These models have facilitated the observation of segmentation and peristalsis motions and their effects on absorption and digestion at both micro and macro scales [55, 71]. Moreover, motility of the small intestine has been studied on live ex-vivo tissues using spatiotemporal and contraction data ([8, 71, 73]). These studies involve excised tissue, mounted on the experimental setups to record tissue motility in terms of image data.

Fig. 1.12a shows an example of spatiotemporal map for change in the diameter of the small intestine [8]. The local deformation and strain rate of the tissue can also be seen in this figure. Lim et al. conducted an ex-vivo study on the villi of the brushtail possum's small intestine at both macroscopic and microscopic scales. The study revealed that the villi were rigid structures when the shear stress was in the physiological range and suggested that mixing and absorption were predominantly restricted to the tip of the villi, Fig. 1.12b [79].

Recently, microfluidic devices (concept of "gut-on-chip") have emerged to replicate the invivo intestine microenvironment along with the movements of the villi [26, 58, 63]. Costello et al. developed a porous, synthetic 3D tissue scaffold with villi to mimic the natural microenvironment of the small intestine by culturing epithelial cell types [26]. Although advancement in the concept of "gut-on-chip" helps in drug testing, the study of microbiota in physiological conditions but the systems do not record the movements of the villi in live animal tissue in physiological conditions. Most recently, Kuriu et al. attempted to design a microfluidic setup to observe flow behavior in the vicinity of the villi of small intestinal tissue using microbeads and studied that the flow field near the villi may be crucial for the settlement of gut bacteria [69]. Further, they have developed another device in which intestinal tissue was given motility with the help of pneumatic actuators [68] and found that the mobile tissue led to arresting the microbeads between two villi. The obtained results cannot accurately reflect the absorption and mixing processes in the presence of live tissue since the studies utilized deceased tissue.

Therefore, there was no experimental setup available that can observe the live tissue motility with villi movements at microscopic scales. In the following section, we will discuss the computational fluid dynamics model developed to study small intestinal motility.

In−silico micro-models for the small intestine

Sophisticated computational algorithms applied to in−silico models of the gastrointestinal tract (GIT) leverage powerful computing resources. In−silico models provide higher throughput

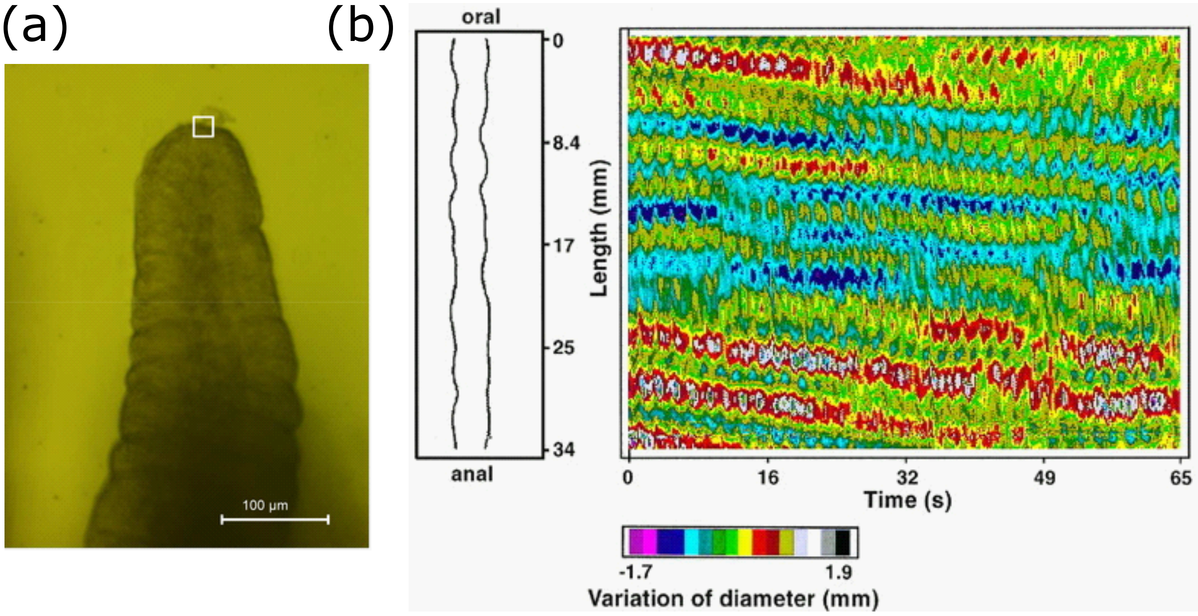

FIGURE 1.12: **(a)** (left) Contour of the small intestine at time 0, (right) time variation of the diameter length with colorbar (bottom) showing the magnitude [8], **(b)** Villus with a white square region to follow its movement [79].

compared to other methods, offering preliminary insights into mixing, absorption, and food flow rates. Experimental techniques provide data related to the chyme flow rate, physiological conditions, layer and villi presence, and gut motility in the small intestine. However, computational models are required to understand flow behavior at the micro or nano scale near the villi, shear strain in the food, and absorption rates. They serve as valuable tools for gaining an inital understanding the GI tract motility.

Nutrient and pharmaceutical absorption, as well as the process of digestion, depend on a tightly interconnected transport and mixing process that occurs across various scales (organ and villi levels), encompassing a wide range of sizes, from the macro scale (approximately 1-2 cm) to the micro scale (villi and micro-villi measuring around 200-500 μ m and 1 μ m). The primary idea behind the presence of villi is to substantially enhance the surface area available for absorption, increasing it by a significant factor (20−folds). This expansion is crucial to compensate for the existence of a commonly known phenomenon called the "unstirred water layer" (UWL) [6], which is a small-velocity layer that nutrients must pass through before diffusing into the luminal surface. The evidence showed that absorption is limited through the UWL into the epithelial surface [113, 140]. The thickness of the UWL (1000 μm) was initially measured in dogs, but it seemed unrealistic at the time [41]. Subsequent researches were conducted on the same animal, which found the thickness to be one order of magnitude lower than the previous values. [74, 124].

Gruby et al. conducted the initial investigation of villus motility in live animals, observing the contraction, expansion, and longitudinal motions of villi in a gut segment [47]. After that, numerous studies were conducted regarding villi motility and their potential contribution to local mixing and the passive formation of the UWL [49, 142, 143]. The belief was to consider the passive involvement of villi in absorption or mixing. A counter study was conducted by Wang et al. to explore the active involvement of villi in enhancing absorption, arrangement of the villi and their motion shown in Fig. 1.13a [139]. In this study, a 2D flow analysis was performed at the macro-scale, driven by lid cavity flow. Additionally, a micro-scale representation of finger-like villi was considered by dividing them into multiple groups. Each group was assigned

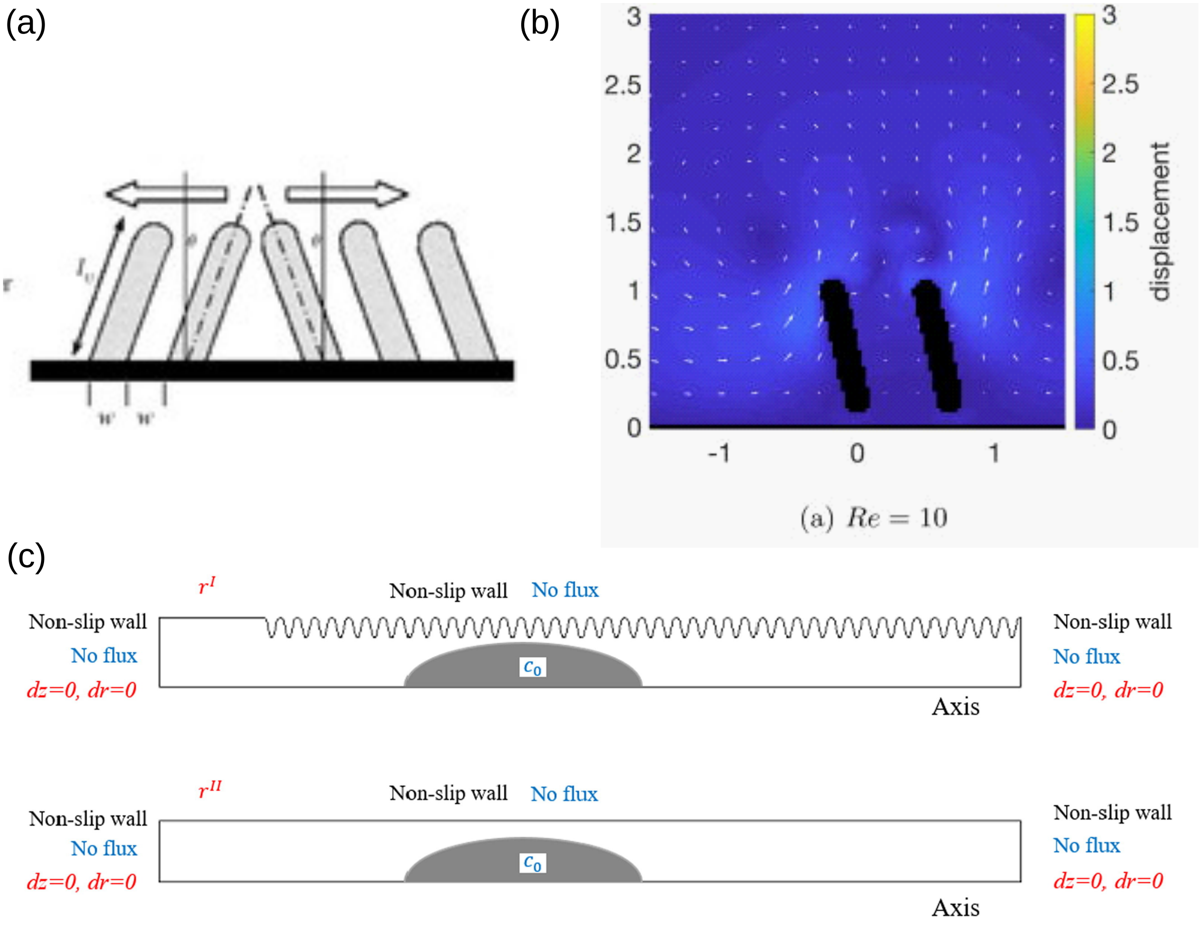

FIGURE 1.13: Villi movements from the bibliography, **(a)** Schematic of villi geometry and motion [138], **(b)** Displacement field at Reynolds number 10 when villi (black) were in-phase [39], **(c)** Initial and boundary conditions for two conditions: (top, with circular folds) Condition 1; and (bottom, without circular folds) Condition 2. The black, blue, and red fonts respectively correspond to momentum transfer, mass transfer, and moving mesh [147].

a pendular motion with a 180° phase difference from its adjacent groups. The study aimed to investigate the formation of a "micro-mixing layer" (MML) resulting from muscle-induced pulsating motions of the villi. The MML was found to enhance absorption and exhibited sensitivity to villus length and oscillation frequency. Further, they extended the 2D model to 3D to study the influence of lateral spacing between the villi groups and their motion with respect to the macroscopic motion at the lumen−scale for better physiological control of intestinal absorption [137].

Moving forward, de Loubens et al. conducted a modeling analysis to investigate the mixing phenomena occurring in the proximal duodenum of rats during longitudinal contractions. Their findings demonstrated that peripheral mixing was more prominent compared to central region mixing when it came to the influence of longitudinal contractions [80]. This study supported the presence of microscale mixing in the periphery of the intestinal lumen, which remained unaffected by an imaginary UWL. Moreover, de Loubens et al. investigated impact of pendular activity, segmentation, and fluid viscosity on flow and mixing in the proximal duodenum, utilizing real-time data obtained from the strain rate map of the rat duodenum. In their study, the duodenum was modeled as a smooth cylinder without villi and found that tissue motility enhanced the absorption, segmentation could be crucial in mixing particulate suspension in the viscous environment [28]. Subsequently, a three-dimensional (3D) model was developed to simulate the movement of villi in non-Newtonian fluid digesta. The findings revealed the formation of laminar eddies in the vicinity of the villi, facilitating radial mixing even in challenging rheological conditions [78]. Zhang et al.in their model incorporated intestinal lumen flow unlike the lid-driven cavity flow [138],[137], along with villi pendular motion to study motility of the duodenum. The results of their investigation indicated that the augmentation of absorption was trivial when considering lumen bulk flow [150]. In another CFD model, Zha et al. aimed to accurately represent geometry of the small intestine by utilizing a cylindrical model with circular folds without villi. Their study focused on examining how the segmentation caused by these circular folds influenced mass transfer within the lumen in laminar flow condition (Fig. 1.13c shows the intestinal wall with and without the folds) [147]. Furthermore, in the context of viscous flow (creeping flow) conditions, the study incorporated a model of symmetric oscillation of the villi. This modeling approach led to the emergence of steady streaming flow over an extended period of time near the villi, thereby enhancing the mixing capabilities specifically at the tip of the villi and supporting the formation "micro-mixing layer" (MML) which depends on both Stokes layer thickness and the lateral confinement between the villi[103].

These studies reveal two important physical phenomena based on the motion of the villi resulting in radial mixing and pumping and based on the inertia of the fluid or Reynolds number resulting in mixing and axial transport. In a recent study, Fishman et al. explored the impact of phasic and anti−phasic oscillations between adjacent villi−like actuators on mixing. They observed the emergence of global behaviors resulting from the cross−coupling interactions among villi. Notably, their research revealed that these interactions augmented transport and mixing processes, particularly at higher Reynolds numbers (100 − 6000) with anti−phasic oscillation which can also be coupled with the MML (Fig. 1.13b shows the displacement field when the villi were in-phase at Re 10) [39]. The range of the Reynolds number could be used e.g. bioinspired artificial villi but physiologically Reynolds in the small intestine is less than 1 [28, 103].

In a different way to analyze mixing and absorption at microscopic scale, the effects of wall structure and motion of bionic reactor were investigated at higher Reynolds number (2-840) by Zhang et al. [149]. The results showed that mixing was enhanced in case of the presence of villi on the bionic reactor's wall with symmetric peristalsis compared to the asymmetric peristalsis. Qin et al. developed a diffusion–convection–reaction model and they checked its capability on rat duodenum consisted of a villus with pendular motion and found that the mass transfer and absorption were influenced by the length of the villus and mass transfer was inhibited in case of higher oscillating frequency [105].

The above-discussed models and their results highlight a significant issue regarding the comparative impact of geometric pumping and inertia of the fluid on transport and mixing within the small intestine in both radial and axial directions. This issue gains particular importance when considering relevant motility data in physiological scenarios.

1.5 Objectives

As we have discussed, the flow in the GI tract or gut is multi-scale with fluid exhibiting complex rheology, induced by active boundaries. The coordination and response of GI motility with digesta are crucial to digestion and the elimination of undigested waste. Therefore, mechanistic models are necessary to gain further insights into the functioning of the GI tract. In this thesis, we concentrated on two main aspects by combining computational fluid dynamics (CFD) with experimental imaging techniques. The first aspect pertained to the flow of complex fluids, specifically feces, in the rectum. The second aspect involved flow phenomena at microscopic scales resulting from the presence of small-scale active structures in the small intestine, namely the villi. We will address it through two different examples: first, defecation, and second, villi motion. The main objectives of this thesis were to develop two-dimensional (2D) computational fluid dynamics (CFD) models for defecation (macroscopic scale) and villi movements (microscopic scale). Moreover, a new experimental set-up was developed to record intestinal motility along with the villi.

In the context of rectal function, there are many tests available currently to study anorectal motility disorders but it is not clear whether the tests identify the precise pathophysiologic abnormality as they provide overlapping results between normal individuals and patients. Therefore, they require more information to diagnose and classify defecation disorders (DDs). While the available models are basic with respect to the fluid rheology and geometry of the rectum. Therefore, we will develop a CFD model and then employ it on different individuals to gain mechanistic insights into the rectal function.

(1) Development of a Patient-specific 2D fluid dynamics model of the rectal function in physiological conditions by coupling video defecography and yield stress fluid flow based on Lattice Boltzmann Method (LBM), Chapter 3.

(2) The utilization of the model on various patients aims to provide insights into different pathologies and structural abnormalities in the rectum.

Despite the available studies on villi movements induced by intestinal motility at the microscopic scale, the literature review revealed that the presence of villi and their pendular movements enhance mixing and absorption. However, little is known about whether the villi oscillate with a constant phase difference from their neighboring villi. Hence, a comparative study was needed to investigate the pumping effect generated by the moving villi and the influence of fluid inertia in the small intestine on transport and mixing.

The detailed objectives are presented below.

(1) Analysis of radial and axial, mixing, and transport phenomena at different modes of the villi movements using a 2D CFD model based on LBM solver, Chapter 4.

(2) Development of an ex-vivo experimental setup to observe and record small intestinal tissue motility at both macro and micro scale.

Chapter 2

Numerical Methods

2.1 Introduction

Apart from developing and validating a new experimental set-up, this thesis is comprised of three papers, two of which focus on rectal function and one on villi movements based on 2D CFD models. In these papers, we utilized the Lattice Boltzmann Method (LBM) as the solver, which is an advanced numerical method. Here, we will provide a systematic and detailed description, starting from the fluid dynamics equations, fluid stress-strain relationship, and boundary conditions. In Section 2.3, we have discussed the Lattice Boltzmann Method (LBM) with the two-relaxation-time (TRT) scheme. We have also performed several simulations on known benchmarks to validate the LBM solver, in Section 2.4.

2.2 Mathematical Model

The computational fluid dynamics (CFD) models of rectal function and villi movements involved different fluid flows, geometries, and the utilization of the Lattice Boltzmann Method (LBM) as the solver. This section presents the fluid dynamics equations and boundary conditions employed in the two-dimensional (2D) model of the rectum during defecation and the 2D model of moving villi in the small intestine. The fluid dynamics of these models are described by the Navier-Stokes equations, which govern the flow of a viscous fluid. These equations account for the conservation of mass and momentum. Furthermore, a constitutive equation is incorporated to accurately represent the yield stress (τ_0) behavior of the fluid during defecation in the case of the rectum model.

The figures illustrate the two-dimensional geometry of the rectum and small intestine with villi, as shown in Fig. 2.1a,b. In the rectum model, the fluid flow representing feces was considered as the yield stress (τ_0) fluid, while in the villi model, the fluid was assumed to be Newtonian. The boundary conditions used in the models are discussed in Section 2.2.5. By employing these fluid dynamics equations and boundary conditions, the behavior of fluid flow in both the rectum and small intestine models can be simulated and analyzed.

2.2.1 Index notations

This section provides an overview of the mathematical symbols and conventions used in the thesis. Bold font letters are used to indicate tensors and vectors in-line within the text, such as the stress tensor $\boldsymbol{\sigma}$ or the velocity vector $\mathbf{u}$. However, in numbered equations, the index notation is preferred for representing tensors of any rank.

The index notation is a useful mathematical notation for denoting tensors and vectors. In this work, a general tensor component is denoted by a subscript indices equal to the rank of the tensor (, e.g. τ_{ij} and u_i). Since the analysis is conducted in 2D Cartesian space with axial coordinates represented by (x, y), tensor components along specific directions are indicated by replacing the index with 1 or 2 (e.g. x-directional stress τ_{1j} or x-directional velocity, u_1).

Symbols or letters with non-indexed subscripts, except for x and y, are not considered as tensor objects.

2.2.2 Einstein summation convention

The index notation has an important advantage when used with the "Einstein summation convention." This convention specifies that if an index appears twice in a term and is not otherwise defined, that term must be summed over all possible values for the repeated index. For example, $u_j\tau_{ij} = u_1\tau_{i1} + u_2\tau_{i2}$ which is a vector. Using this convention, general tensor operations such as dot products, full tensor contractions, and pre/post transpose multiplication become unambiguous and straightforward. The summation convention simplifies the notation and enables concise expressions for complex tensor operations.

2.2.3 Flow model

In this thesis, we employed two distinct 2D models for simulating fluid flow within the rectum and small intestine (including villi). Since the flow is primarily laminar and incompressible, the conservation of mass and momentum equations are used to fully characterize the fluid mechanics of the systems. These two equations are the Navier-Stokes (NS) equations. The mass conservation equation, also known as the continuity equation, for incompressible two-dimensional flow in index notation is given by,

$$\frac{\partial u_i}{\partial x_i} = 0 \tag{2.1}$$

where $\frac{\partial u_i}{\partial x_i}$ represents the divergence of the velocity vector $\mathbf{u}$. This equation states that in incompressible flow, the divergence of the velocity field is zero, implying that the mass flow into or out of a control volume is balanced. The momentum balance equation for the incompressible fluid flow is given by,

$$\frac{\partial u_i}{\partial t} + u_j\frac{\partial u_i}{\partial x_j} = -\frac{1}{\rho}\frac{\partial p}{\partial x_i} + \frac{1}{\rho}\frac{\partial \tau_{ij}}{\partial x_j} + b_i \tag{2.2}$$

where i,j (=1,2), u_i, x_i, τ_{ij}, b_i, and p are the indices of the system of coordinates, the velocity, the position vector, the deviatoric part of the viscous stress tensor, body force vector, and the pressure respectively.

2.2.4 Fluid stress−strain relation

We will consider Newtonian fluid flow while modeling the small intestine of the rat, and non-Newtonian fluid flow for the rectum model. The rheology of food in the duodenum can range from semi-solid to liquid, depending on the stage of digestion and the nature of the food consumed. In many cases, it exhibits Newtonian fluid behavior [50]. On the other hand, human feces behave as a yield stress fluid (viscoplastic) which means it exhibits both viscous (fluid-like) and plastic (solid-like) behavior depending on the applied stress. When the applied stress exceeds the yield stress τ_0, the material flows like a fluid, and when the stress is below the yield stress, the material behaves like a solid. Moreover, video-defecographies were made using a soft neostool which has the same rheology as human feces. So, in the rectum model, we utilize the Herschel-Bulkley (HB) model, along with Papanastasiou regularization, which is a popular constitutive equation used to describe viscoplastic behavior [131]. This gives the

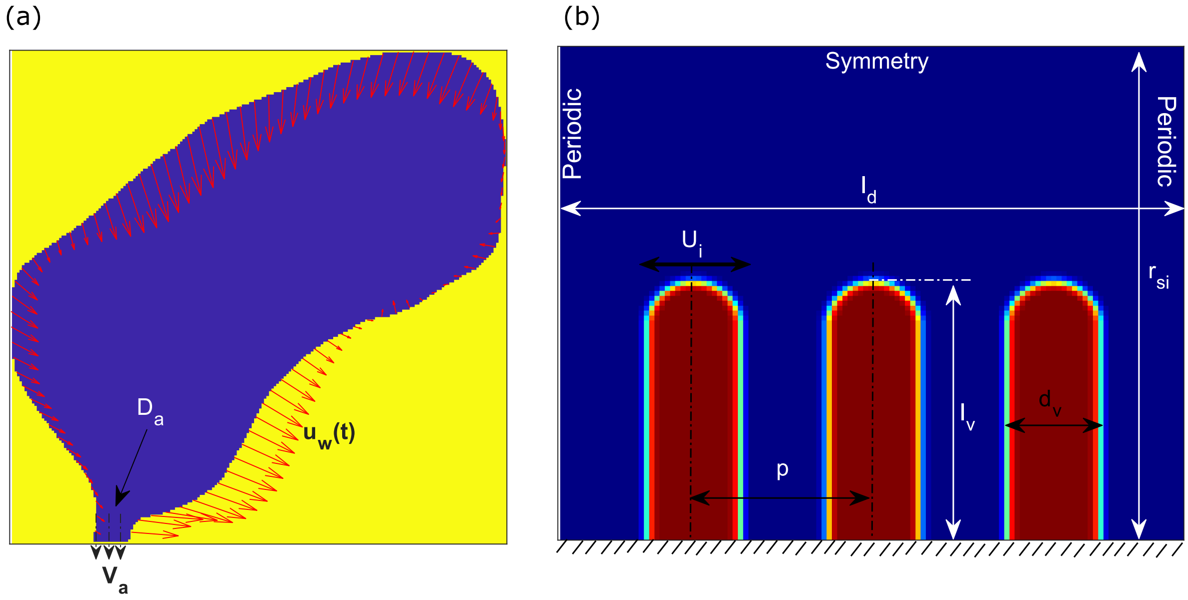

FIGURE 2.1: Domains and their boundary conditions. (a) Rectum with wall velocity vector and imposed velocity boundary condition at the anus. (b) Small intestine (SI) of rat with domain length (l$_d$), oscillation velocity of a villous (U$_i$), distance between the center of the adjacent villi (pitch, p), diameter of the villi (d_v), length of the villi (l$_v$), radius of the SI (r$_{si}$), and boundary conditions

relation between the viscous stress tensor τ_{ij} and the strain rate tensor $\dot{\gamma}_{ij} = \frac{\partial u_i}{\partial x_j}$,

$$\begin{cases} \tau_{ij} = \left(\frac{\tau_0}{|\dot{\gamma}|}\left[1 - \exp\left(-m|\dot{\gamma}|\right)\right] + k|\dot{\gamma}|^{n-1}\right)\dot{\gamma}_{ij}, & \text{if } |\tau| > \tau_0 \\ \tau_{ij} = 0, \text{as}, \dot{\gamma}_{ij} = 0, & \text{if } |\tau| \le \tau_0 \end{cases} \tag{2.3}$$

where $|\dot{\gamma}| = \sqrt{\dot{\gamma}_{ij}\dot{\gamma}_{ij}}$ is the second invariant of the rate-of-strain tensor which is related to the local dynamic viscosity $\left(\eta = \left(\frac{\tau_0}{|\dot{\gamma}|} + k|\dot{\gamma}|^{n-1}\right)\right)$, τ_0 is the yield stress, k the consistency index, n the flow index, and m the regularization coefficient.

2.2.5 Boundary conditions

The boundary conditions for the rectum model included specifying the inlet velocity or pressure, as well as prescribing the wall conditions such as no-slip conditions (Fig. 2.1a). The boundary conditions for the moving villi model involved prescribing the motion and shape of the villi (Fig. 2.1b).

Fig. 2.1a shows the rectal domain with rigid moving walls and fixed velocity boundary conditions at the anus. The red arrows show the imposed boundary velocity vectors at a given time. We have also considered no-slip and moving boundary conditions at the wall which means $u = u_w$, where w is the wall or a solid interface. The fixed or imposed mean outlet velocity (V$_a$) at the anus will be calculated using the known wall velocity ($\mathbf{u_w}$) obtained from the image analysis, given by,

$$V_a = \frac{1}{2R_a}\int\limits_{\mathcal{L}} \mathbf{u_w}.\mathbf{n}\ \mathrm{d}l \tag{2.4}$$

where $\mathbf{n}$ is the normal to the boundary of the rectum, $\mathcal{L}$ is the contour length of the boundary and R_a is the radius of the anus.

The half part of the 2D small intestinal model with villi is shown in Fig. 2.1b. We incorporated symmetry boundary conditions at the top, no-slip conditions at the fixed wall at the bottom, and periodic boundary conditions at the left and right. At the boundary of the villi, the presence of a white gradient can be observed. This is due to the fact that the boundaries of the villi were drawn using the smoothed profile method (SPM), which will be discussed in Section 2.3.5.

2.3 Lattice Boltzmann Method (LBM)

This method has been around us for almost 4 decades, to solve the NS equations using a discretized equation. It is quite popular among computational fluid dynamics (CFD) solvers because of its variability and simplicity. The method was descended from the lattice gas automata (LGA) method and was first introduced in 1988 [86]. Over a period of time, the LBM has evolved remarkably by researchers in different fields. A rich variety of behaviors and fluid flow in vast fields has been realized by the LBM. Such as multi-phase flow in porous medium [77], microfluidic applications [148], GI tract flow [67, 138], heat transfer [120], [89], acoustics [17], etc.

It is evident that the LBM has extensive applications. To accurately address various problems based on the Boltzmann equation, complementary information specific to those problems needs to be incorporated. This thesis will utilize the LBM for low Reynolds number flow ($Re < 1$), specifically to solve yield stress fluid flow with complex moving rectum boundaries, as well as Newtonian fluid flow around oscillating villi. The LBM's performance can be observed in simpler fluid flows like Poiseuille flow, where it demonstrates better adaptability to highly intricate geometries [126] compared to conventional CFD techniques.

One of the key advantages of the Lattice Boltzmann Method is its inherent parallelization capability. The simplicity of parallelizing LBM is due to the local nature of operations on the computational grid, allowing each node to be updated independently of others. The LBM algorithm consists of seven steps (Section 2.3.6) that can be solved independently, resulting in significant time savings for computationally intensive tasks.

However, when dealing with very high Reynolds numbers (turbulent flow) or higher Mach numbers [100], there are certain considerations to keep in mind when using an LBM solver. Careful attention must be given to the selection of discrete space and time steps. These parameters may vary from one simulation to another, although they remain fixed within a specific simulation. Adapting the discretization to the specific flow conditions is crucial to ensure accurate results and reliable simulations in such cases. In the next section, lattice structure (D2Q9 and D2Q19) and equilibrium distribution function (f_α^{eq}) are discussed which are necessary to solve *collision* and *streaming* steps involve in the LBM.

2.3.1 Lattice structure and equilibrium distribution function

When discussing the kinetic theory of gases, we consider a system composed of hard particles or a lattice moving along a regular grid, with a discrete set of possible velocities, denoted as $\vec{e_\alpha}$, for each particle. Instead of referring to microparticles or macroparticles, we introduce an intermediate scale known as the mesoscopic scale, derived from the Latin term meaning 'between'. At this scale, we describe the system using a distribution density function ($f(x_\alpha, e_\alpha, t)$), which provides the probability of finding a particle at a specific position and velocity at a given time. The macroscopic variables can be directly calculated using this distribution function. However, before delving into that, it is beneficial to have a basic understanding of the lattice structure, which aids in comprehending the mesoscopic approach and the computation of macroscopic variables.

A particle with a distribution function has a probability of moving in the discretized space. Therefore, it is necessary to define the probability of movement for all particles. Particle positions are confined to the nodes of the lattice and are reduced to q lattice directions in a d-dimensional space, commonly referred to as the "DdQq lattice", was classified by Qian for the mass of a single particle [104]. Due to the particles having a uniform mass (1 mass unit), the mesoscopic velocities and momenta are always effectively equivalent. These lattice directions provide the particles with the option to move from one lattice point to another during the flow. Another significant parameter is the lattice constants, including the lattice weights (w_α) and the speed of sound (c_s) in the medium. In this thesis, we will utilize the D2Q9 lattice structure for the rectum model and D3Q19 for the SI fluid models. Fig. 2.2 illustrates the directions of the lattice structure.

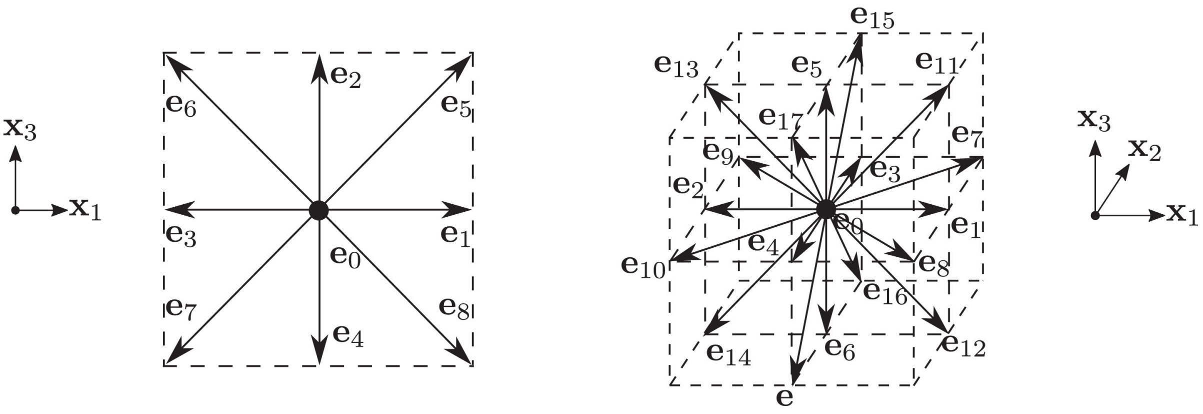

FIGURE 2.2: The D2Q9 and D2Q19 lattice directions of the LBM space discretization for two and three-dimensional models [22].

Another parameter, the lattice directions (e_α) and constants (weight coefficients w_α) will be used to calculate the equilibrium distribution function in case of $D2Q9$ and $D3Q19$ are given by,

D2Q9

$$\boxed{e_\alpha = \begin{cases} (0,0), & \alpha = 0 \\ (1,0),(0,1),(-1,0),(0,-1), & \alpha = 1,2,3,4 \\ (1,1),(-1,1),(-1,-1),(1,-1), & \alpha = 5,6,7,8 \end{cases}}$$

$$\boxed{w_\alpha = \begin{cases} 4/9, & \alpha = 0 \\ 1/9, & \alpha = 1,2,3,4 \\ 1/36, & \alpha = 5,6,7,8, \end{cases}}$$

D3Q19

$$\boxed{e_\alpha = \begin{cases} (0,0,0), & \alpha = 0 \\ (\pm 1,0,0),(0,\pm 1,0),(0,0,\pm 1), & \alpha = 1,2,...,6 \\ (\pm 1,\pm 1,0),(\pm 1,0,\pm 1),(0,\pm 1,\pm 1), & \alpha = 7,8,...,18, \end{cases}}$$

$$\boxed{w_\alpha = \begin{cases} 1/3, & \alpha = 0 \\ 1/8, & \alpha = 1, 2, ..., 6 \\ 1/36, & \alpha = 7, 8, ..., 18, \end{cases}}$$

In this section, we also look at the equation of the equilibrium distribution function. It tells about the probability function of gas particles at equilibrium which is essential for modeling the process of molecular collisions or the first step of the LBM (equation 2.8). f_α^{eq} is defined as

$$f_\alpha^{eq} = \begin{cases} 1 - (1 - \omega_0)\frac{p}{c_s^2} + s_0(u), & \alpha = 0 \\ \omega_\alpha \frac{p}{c_s^2} + s_\alpha(\mathbf{u}), & \alpha = 1 - (q-1) \end{cases} \tag{2.5}$$

where $s_\alpha(\mathbf{u}) = 3\omega_\alpha e_\alpha \cdot \mathbf{u}$, for Stokes flow, $c_s = 1/\sqrt{3}$ is the speed of sound, p is the macroscopic pressure and $\mathbf{u}$ is the macroscopic velocity. q is 9 and 19 for D2Q9 and D3Q19 respectively.

2.3.2 Discreet Boltzmann equation

In a lattice Boltzmann simulation, each node contains a set of q variables f_α ($\alpha = 0$ to q-1) known as the particle distribution functions. These functions carry information from one node to its neighboring nodes. The direction of this neighbor is determined by the vector e_α, which represents the displacement from the current node to the corresponding neighbor node. This vector is inherent to the lattice structure and remains constant throughout space and time. The evolution of a lattice Boltzmann (LB) model follows a general rule that outlines the specific role of the vector, given by,

$$f_\alpha\left(\mathbf{x} + \mathbf{e}_\alpha \Delta t, t + \Delta t\right) - f_\alpha\left(\mathbf{x}, t\right) = \Omega_\alpha \tag{2.6}$$

In LBM, Δt is the lattice time step. These distribution functions evolve in time and interact through a collision operator. The term Ω_α on the right-hand side of Eqn. 2.6 is the collision operator. The macroscopic variables, namely density ρ and velocity $\mathbf{u}$, are defined locally as moments of the distribution functions. The moments are obtained by summing up the distribution functions weighted by certain velocity vectors. Macroscopic variables are given in Section 2.3.4.

2.3.3 Collison operator with single and two-relaxation-time (TRT) scheme

Now, in order to solve the discrete lattice Boltzmann method (LBM) Eqn. 2.6, we require a collision operator. Originally, the collision operator proposed by Boltzmann involved a summation or integration over all possible velocities and momenta, which proved to be complex when incorporated into the LBM equation. However, a significant breakthrough occurred in 1954 when a group of scientists introduced a remarkably simple approach to account for the collision effect in the LBM evolution Eqn. [9].

In our thesis, we are particularly focusing on the rheology of feces in the rectum model and Newtonian fluid flow in the small intestine model. We will describe two different ways to introduce the collision operator. In the case of both the rectal model and the villi model, we will employ the Two-Relaxation-Time (TRT) scheme instead of the traditional Single-Relaxation-Time (SRT) scheme. The TRT-LBM scheme offers superior performance compared to the standard single relaxation time LBM scheme, particularly for non-Newtonian flows with significant variations in viscosity. By adopting the TRT scheme, we can circumvent pronounced numerical errors that may arise in such scenarios, ensuring robust simulations [48, 131].

In TRT, the distribution function will be divided in two (symmetry f_α^+ and anti-symmetry f_α^-) and they will relax towards the symmetry $f_\alpha^{+,eq}$ and anti-symmetry $f_\alpha^{-,eq}$ part of the equilibrium distribution function (f_α^{eq}) respectively over two different relaxation times (τ_+ and τ_-), then the collision parameter is given by, also $f_\alpha\left(\mathbf{x},t\right) = f_\alpha$, throughout this chapter if written

$$\Omega_\alpha = -\frac{1}{\tau_+}\left[f_\alpha^+ - f_\alpha^{+,eq}\right] - \frac{1}{\tau_-}\left[f_\alpha^- - f_\alpha^{-,eq}\right] \tag{2.7}$$

Further, the LB Eqn. 2.6 can be split into two different steps famously adopted in the simulation are *collision* and *streaming.* After splitting, we get,

Collision

$$\boxed{f_\alpha^c\left(\mathbf{x},t\right) = f_\alpha\left(\mathbf{x},t\right) - \frac{1}{\tau_+}\left[f_\alpha^+\left(\mathbf{x},t\right) - f_\alpha^{+,eq}\left(\mathbf{x},t\right)\right] - \frac{1}{\tau_-}\left[f_\alpha^-\left(\mathbf{x},t\right) - f_\alpha^{-,eq}\left(\mathbf{x},t\right)\right]} \tag{2.8}$$

Streaming

$$\boxed{f_\alpha(\mathbf{x} + e_\alpha\Delta t, t + \Delta t) = f_\alpha^c\left(\mathbf{x},t\right)} \tag{2.9}$$

here, f_α^c represents the post-collision distribution function. Equations 2.8 and 2.9 are fundamental components of the LBM algorithm. These two steps are separated due to distinct regions and the ease of performing these operations. In the first step, we only require information about the nodes at time t, regardless of other nodes. In other words, this step occurs locally, facilitating parallelization and the inclusion of multi-scale fluid problems [141]. Next, the distribution function f_α and the equilibrium distribution function f_α^{eq}, along with their respective symmetry and anti-symmetry components, are given by,

$$f_\alpha^+ = \frac{1}{2}\left(f_\alpha + f_{\bar{\alpha}}\right), \; f_\alpha^- = \frac{1}{2}\left(f_\alpha - f_{\bar{\alpha}}\right)$$
$$f_\alpha^{+,eq} = \frac{1}{2}\left(f_\alpha^{eq} + f_{\bar{\alpha}}^{eq}\right), \; f_\alpha^{-,eq} = \frac{1}{2}\left(f_\alpha^{eq} - f_{\bar{\alpha}}^{eq}\right)$$

where, $\bar{\alpha}$ is the opposite direction to α (i.e $\mathbf{e}_\alpha = -\mathbf{e}_{\bar{\alpha}}$). The idea behind multiple relaxation time (MRT) schemes or in our case TRT scheme is that each distribution function can be relaxed at a different rate (τ_+ or τ_-).

The Single-Relaxation-Time (SRT) involves only one relaxation time constant which was purposed by [9], given by,

$$\Omega_\alpha = \frac{1}{\tau}\left[f_\alpha - f_\alpha^{eq}\right], \tag{2.10}$$

Only the *collision* step will be changed a little due to the SRT scheme, given by,
streaming. After splitting, we get,
Collision

$$\boxed{f_\alpha^c = \left(1 - \frac{1}{\tau}\right) f_\alpha + \frac{1}{\tau} f_\alpha^{eq}}, \tag{2.11}$$

To use the LBM solver, we shall need the equilibrium distribution function f_α^{eq}, symmetric and anti-symmetric relaxation times (τ_+ and τ_-), the SRT relaxation time (τ). Finally, we can calculate the macroscopic parameters like velocity and pressure.

2.3.4 Macroscopic variables

The macroscopic variables, the density ρ, the velocity $\mathbf{u}$, and the pressure are given by, q is 9 in case of D2Q9 and 19 in case of D3Q19,

$$\rho = \sum_{\alpha=1}^{q-1} f_\alpha, \qquad \mathbf{u} = \frac{1}{\rho}\sum_{\alpha=1}^{q-1} e_\alpha f_\alpha, \quad \text{and} \quad p = \frac{c_s^2}{1-\omega_0}\left[\sum_{\alpha=1}^{q-1} f_\alpha + s_0(\mathbf{u})\right] \tag{2.12}$$

Further, the rate-of-strain ($\dot{\gamma}_{ij}$) tensor is given by,

$$\dot{\gamma}_{ij} = -\frac{1}{2c_s^2\tau_+\Delta t}\sum_{i=1}^{q-1} \mathbf{e}_{i\alpha}\mathbf{e}_{i\beta}\left[f_i^+(\mathbf{x},t) - f_i^{+,eq}(\mathbf{x},t)\right] \tag{2.13}$$

The local viscosity was calculated with the Papanastasiou regularization of the Herschel-Bulkley constitutive equation by [98, 131],

$$\eta = \frac{\tau_0}{|\dot{\gamma}|}\left[1 - \exp\left(-m|\dot{\gamma}|\right)\right] + k|\dot{\gamma}|^{n-1} \tag{2.14}$$

where $|\dot{\gamma}| = \sqrt{\dot{\gamma}_{ij}\dot{\gamma}_{ij}}$ is the second invariant of the rate-of-strain tensor and m the regularization coefficient. Next, the symmetric relaxation time (τ_+) and the SRT relaxation time (τ) are calculated using,

$$\tau = \tau_+ = \frac{6\eta + 1}{2} \tag{2.15}$$

The anti-symmetric relaxation parameter is given by,

$$\tau_- = \frac{\Lambda}{\tau_+ - 0.5} + 0.5 \tag{2.16}$$

where Λ is the magic collision parameter and taken to $1/4$ in order to optimize the accuracy of the numerical scheme [33]. The TRT-LBM scheme was used as it is superior to the standard single relaxation time LBM scheme because it avoids strong numerical errors for non-Newtonian flows with large variations in viscosity [48, 131]. The relaxation time τ which is very important while using the LBM in the simulations. It easily affects the stability of the LBM and the time required to make the simulation [151]. Therefore, $\tau \geq 0.5$ is a necessary condition for stability when using the BGK collision operator for the LBM from Eqn. 2.15.

2.3.5 LBM boundary and initial conditions

At the boundary of a fluidic system, the boundary conditions consist of either fixed scalar values or a gradient of scalar values acting at specific boundaries of the system. In a physical fluidic system, these conditions are defined at a macroscopic level. However, in the lattice Boltzmann method (LBM), we operate at a mesoscopic scale. Therefore, we need to convert the macroscopic variables into unknown particle populations entering or exiting from the boundaries. It is important to carefully apply these boundary conditions in the LBM to ensure that they produce the same effects as they would at the macroscopic scale.

The same principle applies when prescribing initial conditions. We need to provide an initial particle population that reproduces the macroscopic initial condition. In the lattice Boltzmann method (LBM), prescribing initial conditions is relatively straightforward and easy (Section 2.3.5). In general, the lattice Boltzmann method (LBM) provides a high degree of spatial and temporal flexibility in applying complex boundary conditions. This is one of the many aspects of the LBM that contributes to its reputation as a popular solver.

Wall bounceback: Fixed and moving wall boundary conditions

As already mentioned in the previous section that the fixed (small intestine wall) and moving boundaries (rectum wall) can be explained with the help OF bounceback boundaries. In the LBM, this is considered a kind of miraculous way to simulate fluids in domains characterized by complex geometries such as those found in porous media. Their utility comes just by defining a particular node as a solid obstacle (blue circles in Fig. 2.3) and no special programming treatment is required.

Fig. 2.3 shows the walls which separate the solid and fluid nodes from each other. The isolated solids that do not contact fluid would not involve in the calculation. Consequently, it is possible to eliminate unnecessary computations at inactive nodes, will save a lot of time when it comes to complex and large geometry. The walls are fixed in this Fig. 2.3 with zeros velocity ($\mathbf{u}_w = 0$). In this thesis, we utilized the *half-way bounceback,* scheme. In which, we already defined extra nodes (solid nodes) outside the fluid flow. In reality, these solid nodes do not participate in NS equations but they are helpful to simplify the bounceback scheme.

The yellow arrows in Fig. 2.3 are the velocities direction with solid wall. So, they cannot supply the unknown particle populations in normal streaming step because they are out of the LBM algorithm. To take care of this situation, modification at the streaming happens with the half−way bounceback rule, which is given as,

$$f_{\bar{\alpha}}(\mathbf{x}_i, t + \Delta t) = f_{\alpha}^{bb}(\mathbf{x}_i, t), \tag{2.17}$$

where, the distribution function f_{α}^{bb} donates the post-collision populations (yellow arrows in Fig. 2.3) that would cross the wall and move towards solid nodes and the index $\bar{\alpha}$ denotes a velocity set direction such that $e_{\bar{\alpha}} = e_{\alpha}$. Effectively, with this scheme, the mass is conversed because no particle is go-out or coming−in. Also, the momentum is conserved as the wall is fixed. For a moving wall treatment (rectal wall), using bounceback scheme, certain amount of momentum must be added to the bounced distribution function to reflect the fluid˘solid interaction (i.e. the momentum transfer) at the boundary surfaces. In other words, the distribution function should be formulated in the form as,

$$f_{\bar{\alpha}}(\mathbf{x}_i, t + \Delta t) = f_{\alpha}^{bb}(\mathbf{x}_i, t) + 6 w_{\alpha} \frac{\rho}{c_s^2}(e_{\alpha}.\mathbf{u}_w) \tag{2.18}$$

The half-way bounceback scheme works effectively when applied to linear walls. However, when this scheme is applied to curved boundaries using a Cartesian mesh, it results in a noticeable "staircase" effect, where lines are connected by step changes [43]. As a result, the half-way bounceback scheme is second-order accurate for linear walls, but only first-order accurate for curved walls [14].

Periodic and symmetry boundary conditions

The 'periodic' boundary is one of the simplest boundary conditions, where the system is considered closed by treating the edges as if they were connected to opposite edges. The periodic boundary condition (shown in Fig. 2.1b) also modifies the streaming step of the LBM algorithm (Eqn. 2.9). When simulating flow between two walls, for instance, bounceback boundaries would be applied to the solid walls, while periodic boundaries would be applied to the 'open' ends of the walls. At the corner node shown in Fig. 2.3a, it can be observed that all velocities in the D2Q9 lattice return to the system without changing their directions. We can modify the streaming step of the LBM algorithm using the following equation (Eqn. 2.19). The periodic boundary conditions are similar to bounceback boundaries, with the difference being that the velocities do not change their directions in the case of periodic boundary boundaries.

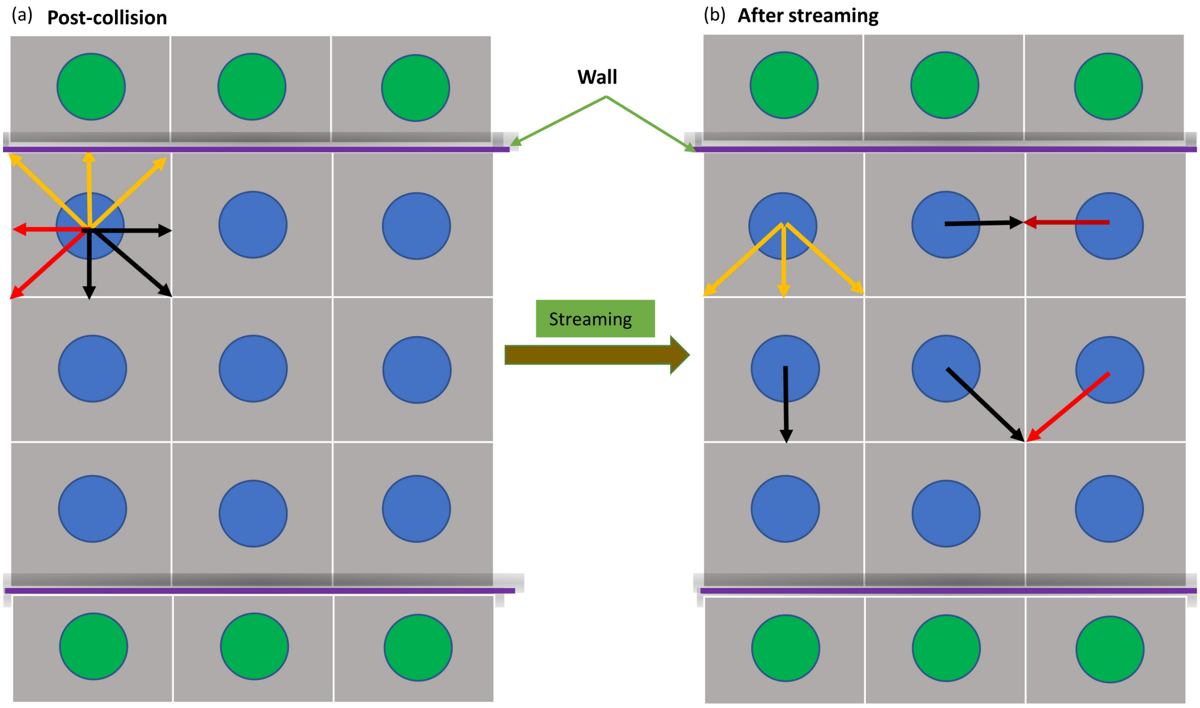

FIGURE 2.3: The periodic and bounce back conditions of a 2D boundary in a $D2Q9$ lattice structure at a corner node with 3×3 nodes. **(a)** Left at time t and **b** right at time $(t + \Delta t)$. Yellow arrows represent the *bounceback* streaming, red arrows represent the *periodic* streaming and black arrows represent simple streaming.

$$f_\alpha(\mathbf{x}_i, t + \Delta t) = f_\alpha^{pr}(\mathbf{x}_j, t), \tag{2.19}$$

where a node at any location $\mathbf{x}_i$ is the periodic neighbor for the fluid node at position $\mathbf{x}_j$, and f_α^{pr} is the particle populations that would leave the fluid domain through a periodic boundary during streaming. Since a certain number of particles goes out from the domain and the same number of particles comes-in in each time step Δt which refers to the conversation of mass and moment during the streaming globally. To apply the periodic boundary condition, it is better to pre−defined the lattice nodes based on the physical geometry. It is generally done similarly to the obstacle nodes with the bounce-back scheme. Now, we have an understanding of both the boundary conditions that we use in this thesis.

On the other hand symmetric boundary condition is like a mirror image. We would just replicate the whole domain at the symmetric boundary as in the case of the small intestine model (Fig. 2.1 b).

Smoothed profile method (SPM)

Moving boundary conditions are commonly encountered in fluid dynamics simulations, especially when studying the interactions of solid particles in multi-body systems. To address this challenge, the smoothed profile method (SPM) was developed. The SPM has been integrated with lattice Boltzmann (LB) methods to investigate the rheology of concentrated suspensions consisting of rigid particles [91]. Moreover, utilizing a continuous and smoothed interface to delineate the boundary between the fluid and the rigid body offers a solution to minimize numerical errors inherent in interpolation and extrapolation methods commonly employed to handle curved and moving boundary conditions in lattice Boltzmann method (LBM) solvers [14, 59].

The profile function of ith villi (from left Fig. 2.1) $\mathbf{\Phi}_{Vi}$ was constructed by stacking disks of diameter d$_v$, thickness Δx, and total length l$_v$. The profile $\mathbf{\Phi}_{Vi}$ of each individual disk can be expressed as follows,

$$\Phi_{Di} = \frac{1}{2}\left[1 + \tanh\frac{d_v/2 - |x - X_{ci}|}{\xi}\right] \tag{2.20}$$

where $\mathbf{x}$ represents the position of lattice nodes, $\mathbf{X}_{ci}$ represents the center of the disk, and ξ represents the interface thickness. The tip of the villi was modeled with a semi-spherical cap. In the fluid region, the profile function $\mathbf{\Phi}_{Vi}$ is set to 0, while in the solid villi region, it is set to 1. The value of $\mathbf{\Phi}_{Vi}$ smoothly transitions in the interfacial region, as depicted in Fig. 2.1b. For this study, a commonly used interface thickness of $\xi = 1\Delta x$ was adopted [56, 91].

To enforce no-slip boundary conditions, the fluid-solid interaction force for ith villus was calculated at each lattice point $\mathbf{x}_i$ by,

$$f_{Vi}(\mathbf{x}, t) = \mathbf{\Phi}_{Vi}(\mathbf{x_i}, t)\left[U_{Vi}(t) - \mathbf{u}(\mathbf{x}, t)\right]/\Delta t \tag{2.21}$$

The translational velocity of the villus U$_{Vi}$, is determined by a sinusoidal function with frequency f and amplitude U$_0$ = 2πfa, where a represents the displacement amplitude and $\mathbf{u}$ is the fluid velocity computed in Eq. (2.12).

$$U_{Vi}(t) = 2\pi f a \sin\left(2\pi f t + i\Delta\phi\right)\mathbf{e}_z \tag{2.22}$$

where, phase difference $\Delta\phi$ between two adjacent villi is constant $\Delta\phi = \phi_i - \phi_{i-1}$. Finally, all the forces at lattice nodes $\mathbf{x}_i$ will be added ($f_V = \sum_{i=1}^{N_v} f_{Vi}$) and contribute in the collision (Eqn. 2.11) step of the LBM as a body force, $b_i = 3w_\alpha f_V e_\alpha$.

Initial conditions

In this thesis, we are not using unsteady conditions where initialization is crucial. In order to start the LBM algorithm (step 2), we shall specify some initial values of macroscopic variables such as ρ and $\mathbf{u}$. We can obtain these variables using the equilibrium distribution function from Eqn. 2.5. Therefore, we simply put all the values of the equilibrium distribution for each node as zeros from there we will have the initial macroscopic velocity $\mathbf{u}_0 = 0$ and macroscopic density $\rho_0 = 0$. It can be more arbitrary as after some time steps, the initial values are completely lost and all the variables shall have new updated values.

2.3.6 Algorithm

Now we have all the necessary elements to write the final LBM algorithm in the following steps,
1. Start at time $t = t_0$ with initialized particle populations at every node in the simulation domain.
2. From the particle populations, compute the macroscopic variables.
3. Then, using the values of p and $\mathbf{u}$, compute the equilibrium distribution function from Eqn. 2.5.
4. The collision step: Modify particle populations at every lattice node using Eqn. 2.8.
5. The streaming step: Move (or stream) the post-collision populations to their neighbor lattice nodes (Eqn. 2.9) with velocities according to the D2Q9 velocity set in case of rectal model and D3Q19 in case of villi model.
6. Increment the time counter by t. This completes one-time step for the LBM.
7. Return to step (2), and repeat the loop until the desired final time-step is reached.

This completes our discussion on the discretization of the Boltzmann equation, leading to the LBM with the BGK-TRT collision operator.

2.4 Validation of the LBM Solver

The numerical methods employed in this study have been extensively validated in the literature [14, 56, 131]. To ensure the accuracy and reliability of the final code, various benchmarks of similar flow problems were utilized for validation. To validate the lattice Boltzmann solver employed in this thesis, two scenarios were considered: the movement of villi and the movement of the rectum. For the villi, a Newtonian fluid was assumed to surround them, while a yield stress fluid was assumed to be expelled during defecation. Three distinct cases were examined to validate the LBM. Firstly, the oscillating or pulsating flow of the villi was analyzed for validation. Secondly, the Smoothed Profile Method (SPM) was employed to shape the villi and assign velocity to them, which was further used for validation. Lastly, the LBM solver utilized in the rectum model was validated through the flow of yield stress fluid.

To assess the accuracy of the LBM, the relative L2$-$norm (ϵ) will be computed in these three cases with respect to the grid resolution. The relative L2-norm is obtained by taking the square root of the sum of the squares of the difference between the LBM and analytical solutions, divided by the sum of the squares of the analytical solution.

$$\epsilon = \sqrt{\frac{\sum(\overline{u}_{LBM} - \overline{u})^2}{\sum \overline{u}^2}} \tag{2.23}$$

2.4.1 Oscillating flow

In order to validate the *Lattice Boltzmann Method (LBM)* solver for simulating the oscillating motion of villi, an unsteady internal Newtonian flow condition between parallel plates was considered. The periodic, symmetry, and fixed wall bounceback boundary conditions were utilized. The flow was driven by an unsteady periodic pressure gradient ($\frac{dp}{dy} = Ae^{j\omega t}$), and the dimensionless velocity ($\overline{u}$, normalized using the maximum velocity of the fluid) was determined using Eqn. 2.24 [82]. Fig. 2.4a depicts the schematic of the fluid flow between the parallel plates, while in Fig. 2.4b, a comparison is presented between the analytical and the LBM solutions at two different times (T/4, T/2) when Womersley number (or modified Reynolds number Re_m) ($\mathrm{Wo} = a\sqrt{\frac{\omega}{\nu}}$) was 5. Additionally, Fig. 2.4c shows the variation of the L2-norm of the velocity (calculated at pseudo-steady state) with respect to different grid resolutions between the plates at Wo = 5. The results indicate that the error decreased with second-order accuracy in space, confirming the reliability of the LBM solver with planar wall condition [43].

$$\overline{u}(y,t) = \frac{A}{j\omega\rho}\left[1 - \frac{\cosh\left(\mathrm{Wo}\sqrt{j}\frac{y}{a}\right)}{\cosh\left(\mathrm{Wo}\sqrt{j}\right)}\right]e^{j\omega t} \tag{2.24}$$

where A is the maximum amplitude of pressure gradient $\frac{dp}{dy}$, ω is the circular frequency, $2a$ is the channel width, kinematic viscosity (ν), ρ is the density, j is $\sqrt{-1}$, and t is time.

2.4.2 Smoothed profile method (SPM) and steady streaming flow (SSF)

To simulate steady streaming flow, we used the 3D code developed by Puthumana and de Loubens [103]. Here we study the accuracy of the code to solve steady flow and steady streaming flow.

First, to validate *the Smoothed Profile Method (SPM)* employed for drawing and assigning velocity to the villi in the 2D model of villi movement in the small intestine (Fig. 2.1b), we

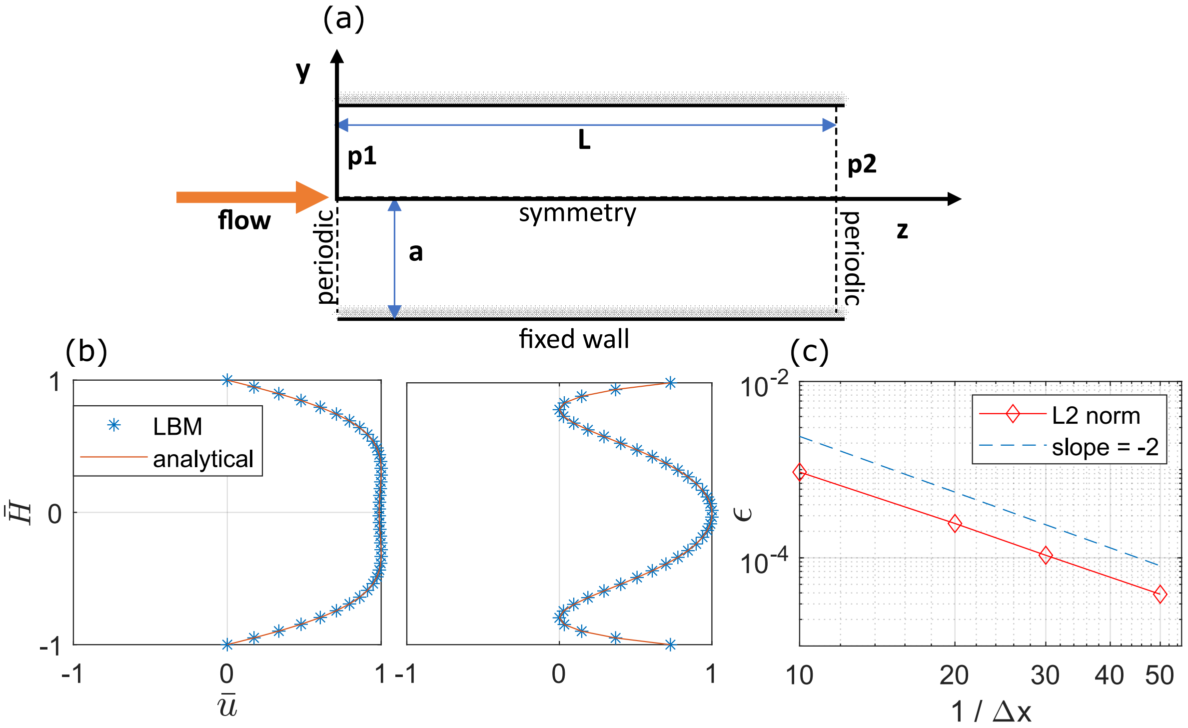

FIGURE 2.4: One-dimensional pulsating flow between two parallel plates, **(a)** Schematic of parallel plates with the Newtonian flow with pressure gradient and boundary conditions, **(b)** Velocity profile at two different times (T/4, T/2), **(c)** Relative error using L2 norm (ϵ, solid red line with diamond marker) of the normalized velocity ($\overline{u}$) with respect to the grid resolution, when Wo = 5, line with slope -2 (blue discontinuous line), $Re = 100$

considered the Newtonian fluid flow in a cylinder [128]. Due to the azimuthal symmetry of the problem, a one-dimensional velocity solution can be obtained. Thus, the velocity can be expressed as follows,

$$\overline{u} = v_{max}\left(1 - \frac{r^2}{R^2}\right), \qquad \text{and} \qquad v_{max} = \frac{R^2}{\eta}\left|\frac{dp}{dz}\right| \tag{2.25}$$

where r is the radial distance from the center, cylinder radius R, v_{max} is the maximum velocity or centerline velocity, dynamic viscosity η, and pressure gradient across the cylinder $\left|\frac{dp}{dz}\right|$.

To solve flow phenomena in the 2D model of the small intestine with villi, we utilized the 3D LBM solver (D3Q19) where we took only one node in the thrid direction. The SPM was utilized to draw the geometries of the cylinders and a constant angular velocity given to the inner cylinder, as depicted in Fig. 2.5d. The D2Q19 LBM solver was used to solve the flow passing through the cylinder. The red part shows the solid region and the blue region shows the fluid. Fig. 2.5e illustrates the comparison of the velocity profiles obtained from the LBM solution and the analytical solution in laminar flow conditions. Moreover, we have calculated the error (ϵ) with respect to the grid resolution, shown in Fig. 2.5f. The error showed first-order accuracy with respect to the space or number of nodes.

The reason behind using the SPM was that, for moving boundary conditions, we could employ interpolated bounceback. However, the interpolation led to a loss of the local character of LBM, making the simulations more computationally demanding [14, 59]. Additionally, we needed an algorithm to refill the fresh nodes, which resulted in a loss of second-order accuracy.

The advantage of the SPM (which is equivalent to immersed boundary methods but for non-deformable solids in motion within a fluid) is that it preserves the locality of the original LBM without requiring the reconstruction of fresh nodes. However, a drawback is that it appears to create a larger slip velocity compared to interpolated bounceback for the same grid resolution. Nonetheless, this slip boundary diminishes as the resolution is increased.

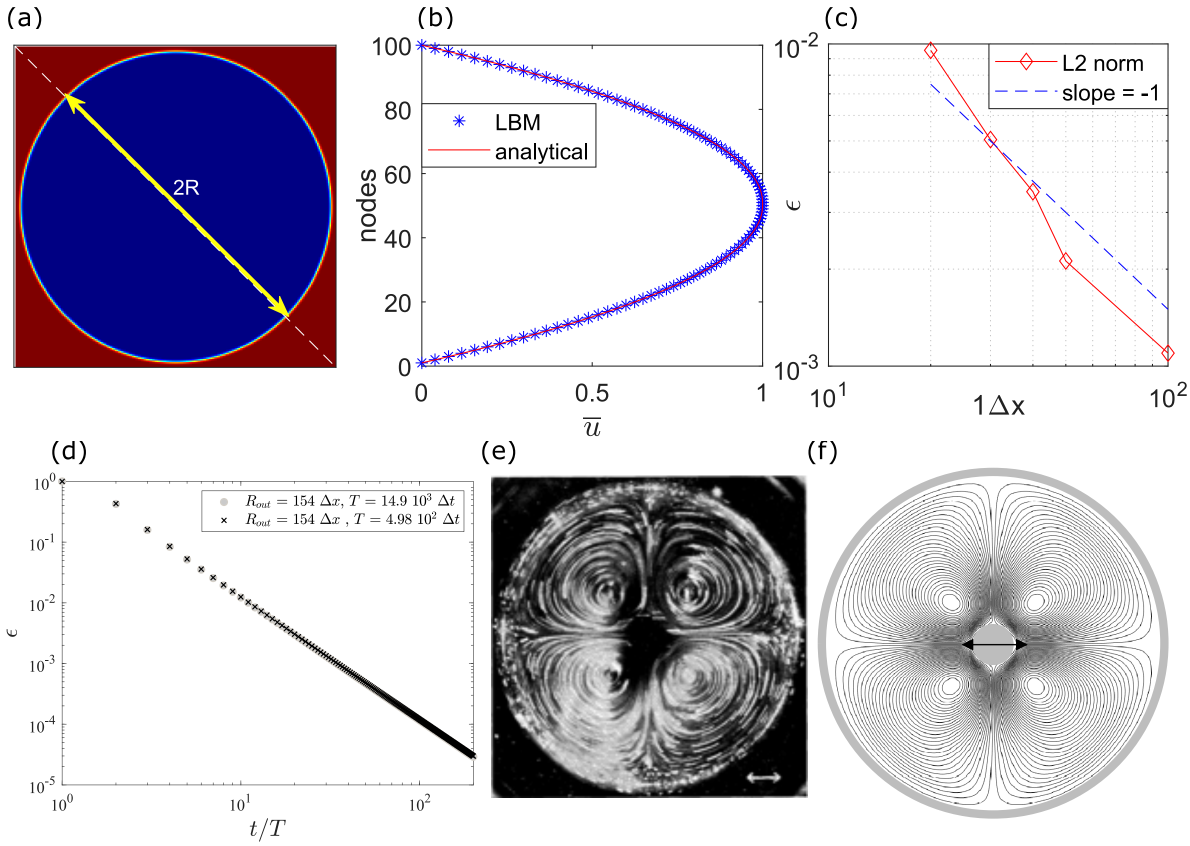

FIGURE 2.5: **(a)** Schematic of the cylinder (gradient of white color at the circumference using SPM), red (solid region), blue (fluid region), **(b)** Velocity profile in the cylinder with respect to the number of nodes, **(C)** Error (ϵ, red solid line with diamond) of the normalized velocity ($\overline{u}$) with respect to the grid resolution, line with slope -1 (blue discontinuous line). **(d)** The relationship between the error ϵ and the number of cycles is examined for different temporal resolutions, **(e)** Tatsuno et al. obtained experimental steady Lagrangian streamlines, where the direction of oscillation of the inner cylinder is indicated by the arrows [132], **(f)** Using our SPM-TRT-LBM algorithm, steady Eulerian streamlines were simulated under the same conditions as in **(d)**,

Second, to observe the SSF phenomenon, we used the D3Q19 TRT-LBM to solve the oscillating flow of the inner cylinder R_{in} inside a fixed cylinder R_{out} when modified Reynolds number Re_m was 0.98, $a/R_{in} = 0.322$, and $R_{out}/R_{in} = 7.69$. We compared the LBM result with the experimental result [132], shown in Fig. 2.5a-c. The error ϵ was decreasing in the same way with the number of time steps in two different cases at $Re_m = 154$ and $T = 4.9 \times 10^2$ or $T = 14 \times 10^3$, Fig. 2.5a. By utilizing stroboscopic light, the displacement of particles was observed in order to obtain the experimental Lagrangian SSF streamlines, Fig. 2.5b [132]. Fig. 2.5c illustrates the Eulerian steady streamlines, which were simulated using our SPM-TRT-LBM algorithm.

2.4.3 Yield stress fluid flow

To validate the Lattice Boltzmann Method (LBM) solver employed in the bi-dimensional (2D) rectum model, where complex geometries and yield stress fluid flow were considered [23], we utilized the Taylor-Couette flow between two concentric cylinders with a yield stress fluid.

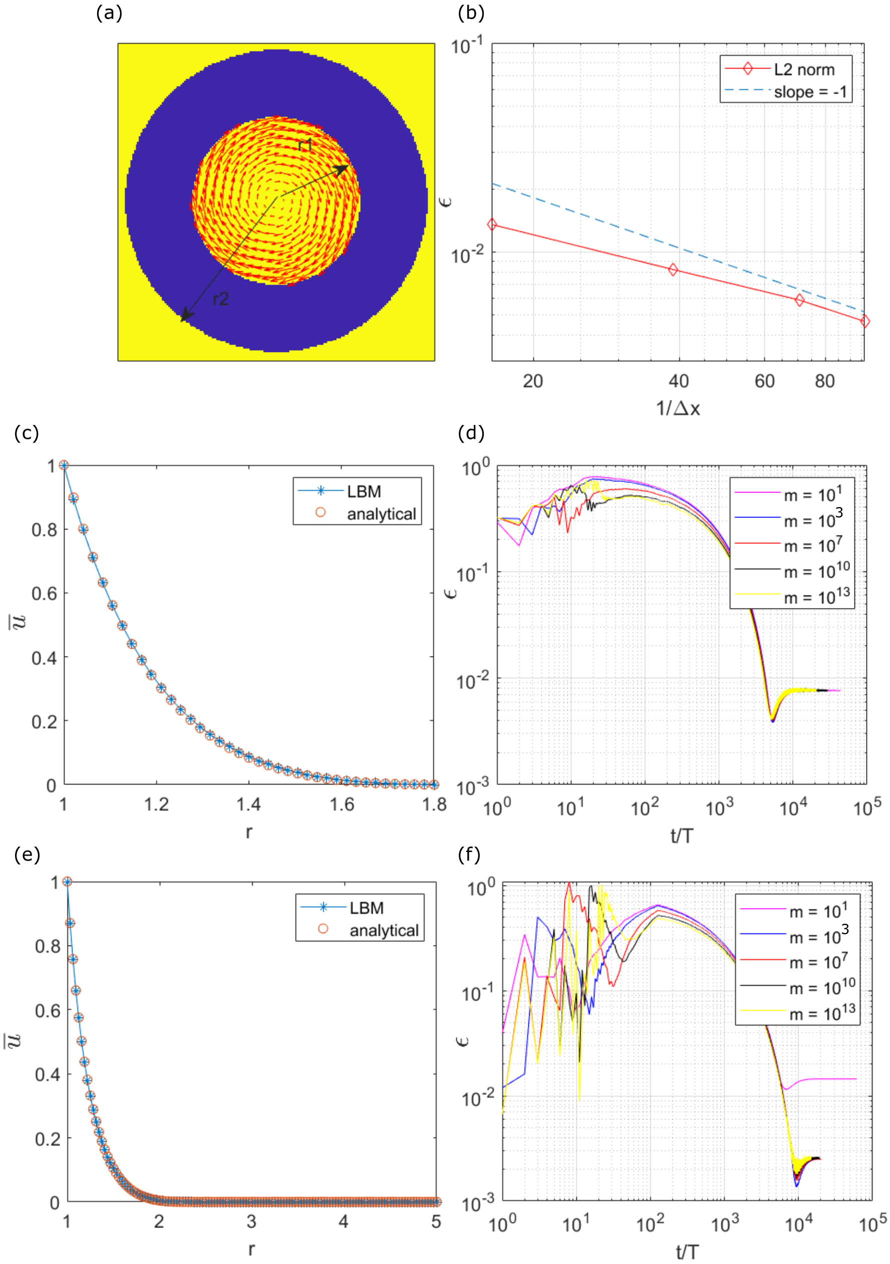

FIGURE 2.6: Yield stress fluid flow between two cylinders, **(a)** Schematic of concentric cylinders, red arrows show the rotation. Fully yielded fluid, when $r2/r1 = 1.8$, $Bn = 0.5$ **(b)** L2 norm error (ϵ, solid red line with diamond marker) of the normalized velocity ($\overline{u}$) with respect to the grid resolution, line with slope -1 (blue discontinuous line), **(c)** Velocity profile between the cylinders with respect to the normalized radial distance. **(d)** L2 norm error versus the number of cycles at different regularization coefficient m. Partially yielded fluid, , when $r2/r1 = 5$, $Bn = 0.5$ **(e)** & **(f)**

The cylinders were modelled using moving wall bounceback boundary conditions. Due to the azimuthal symmetry, a one-dimensional velocity solution can be obtained. Thus, the velocity can be expressed as follows,

$$\overline{u} = \left[1 - Bn^{1/n} \int_{1}^{r} \frac{1}{x} \left(\frac{c}{x^2} - 1 \right)^{1/n} dx \right] \mathbf{r} \tag{2.26}$$

where $\overline{u}$ is the normalized velocity, $\mathbf{r}$ is the normalized radial between two cylinders, c is an arbitrary constant, and Bn is the Bingham number. In the case of Herschel-Bulkley fluid with n = 1/2 with full yielding ($r = r2$), constant c is given by,

$$c = \frac{2r_2^2}{r_2^2 + 1} \left[1 + \sqrt{1 + \frac{1 + r_2^2}{1 - r_2^2} \left(log(r_2) - \frac{1}{Bn^2} \right)} \right] \tag{2.27}$$

In case of partially-yielded fluid, the constant $c = r_o^2$ and $r_o < r_2$.

Fig. 2.6a shows the solid regions (inner and outer cylinder, yellow), and fluid (blue region) and velocity vectors given to the inner cylinder in red arrows. At Bingam number Bn =1 and radius ratio r_2/r_1 =1.8, the error (ϵ) was calculated with respect to the grid resolution (Fig. 2.6b). It can be observed that the error decreases as the resolution increases. This decrease shows a nearly parallel trend to a line (blue dashed line) with a slope of 1, indicating a first-order accuracy. Furthermore, in Fig. 2.6c, the LBM and analytical solutions of $\overline{u}$ are compared at the same Bingham number Bn and radius ratio $r_2/r_1 = 1.8$. We have also compared the error ϵ at different values of the Papanastasiou regularization coefficient m. Fig. 2.6d shows the convergence with respect to the number of cycles. It can also be seen that the effect of m was negligible in the case of fully-yielded fluid flow.

We also compared the LBM and analytical solutions of $\overline{u}$ when Bn =1, r_2/r_1 =5, shown in Fig. 2.6e. In contrast to fully-yielded fluid flow, the partially-yielded fluid shows the error ϵ 10 times higher at the same convergence time (10^4) when $m = 1$ compared to the higher values of m, shown in Fig. 2.6f. The higher error is attributed to the presence of a very small strain rate $\dot{\gamma}$. This occurred between the cylinders, where the shear stress τ was smaller than the yield stress τ_o, leading to a no-flow condition or a region of zero strain rate. Therefore, to avoid the zero strain rate condition, it is necessary to use a sufficiently higher value of m.

The validation results showed that the half-way bounce-back rule was second-order accurate in space for a planar wall (Section 2.4.1) with a unit normal that right-aligns with the Cartesian lattice node mesh. However, in cases where the wall has an arbitrary shape (Section 2.4.2 & 2.4.3), it was found that the scheme reduces to first-order accuracy [43]. This is because the bounce-back scheme when used with a curved wall on a Cartesian mesh, reproduces it inexactly as straight lines connected by step changes. This is referred to as the "staircase" approximation for a curved wall boundary [14]. In case of the rectum model, we considered 200 nodes in both directions and m = 10^8 which was sufficient to maintain non-zero strain−rate in case of negligible deformation. While in case of the villi model, the resolution was varying with respect to the number of villi by keeping the pitch p (distance between the center of two adjacent villi) constant.

Chapter 3

Fluid Mechanical Modelling of Human Defecation

3.1 Evalutaion of Rectal Function by Fluid Mechanical Modelling

In this chapter, we investigated fluid flow in the gastrointestinal (GI) tract at macroscopic scales, where flow is driven by active boundaries and the fluid has complex rheological properties, ranging from watery suspensions to semi-solids with yield stress. Defecation is a complex physiological process, which involves the coordination of neural, muscular, hormonal, and cognitive systems. Rectal motility disorders encompass a range of conditions that can affect the ability to initiate or complete defecation (constipation) or control bowel movements (incontinence). This problem is important for human health and the diagnosis / classification of defecation disorders. One of the limitations in understanding defecatory function is the lack of quantitative assessment tools. Unlike bladder function, where flow and pressure can be measured, there is a lack of such tools for the rectum.

Here, we focused on rectal evacuation or defecation, where the flow was governed by the rectal wall pressure on yield stress fluid, the feces. de Loubens et al. characterized the consistency of human feces with respect to the Bristol scale [80]. Therefore, our fluid mechanical model utilized defecography videos made in physiological conditions by filling neostool in the rectum, which has the same rheology as normal feces. The videos utilized in this study were provided by one of our collaborators, Dr. Alain Dubreuil.

This chapter comprises one conference paper that presents the development of the CFD modeling of rectal evacuation. Additionally, one journal paper is dedicated to the extension of the CFD model to an asymptomatic population and individuals with obstructive defecation. Lastly, the model is applied to individuals with anatomical abnormalities.

3.2 Flow Simulations of Rectal Evacuation: Towards a Quantitative Evaluation from Video Defecography

We developed a two-dimensional (2D) CFD model of the human rectum using the lattice Boltzmann solver. We analyzed the defecography video of a patient without any signs of morphological abnormalities. The objective was to introduce a 2D patient-specific computational fluid dynamic (CFD) model of fecal flow inside the rectum by considering boundary conditions obtained by segmentation of video defecography along with the rheology of the neostool. This work was published for the $44^t h$ annual international conference of the IEEE Engineering in Medicine & Biology Society [5].

My contributions

The first draft of the paper was written by me. I also performed image analysis on the video defecography, developed the model, and prepared all the figures.

Towards an assessment of rectal function by coupling X-ray defecography and fluid mechanical modelling

Faisal Ahmad[1], Clément de Loubens[1], Albert Magnin[1], Alain Dubreuil[2],
Jean-Luc Faucheron[3,4], Stéphane Tanguy[4]

Abstract— **Despite the numerous available clinical investigation tests, the associated alteration of quality of life and the socio-economic cost, it remains difficult for physicians to identify the pathophysiological origins of defecation disorders and therefore to provide the appropriate clinical care.**

Based on standardized dynamic X-ray defecography, we developed a 2D patient-specific computational fluid dynamic model of rectal evacuation. X-ray defecography was carried out in a sitting position with a standardized paste whose yield stress matched that of soft human feces. The flow was simulated with lattice-Boltzmann methods for yield stress fluids and moving boundary conditions.

The model was applied for a patient with a normal recto-anal function. We deduced from the flow field that the main flow resistance during the defecation was due to the extrusion of the paste through the anal canal. We calculated also from pressure and stress fields the spatio-temporal evolution of the wall normal stress. This latter highlighted a gradient from the proximal to the distal part of the rectum.

We discussed how this new set of hydrodynamical and biomechanical parameters could be interpreted to gain new insights on the physiology of defecation and to diagnose underlying evacuation disorders.

Clinical relevance— **If confirmed, our approach should allow clinicians to obtain other parameters from a classic clinical examination and thus better adapt the response of clinicians to the defecation disorders observed in patients.**

I. INTRODUCTION

Human defecation is the voluntary evacuation of faeces coordinated by sensory and motor activity of the rectum. Defecation disorders are worldwide problems observed in a significant part of the population (e.g. 15% in North America) and seriously affect the quality of life with significant socio-economic costs [1]. The health care pathway of these patients remains complex as the symptoms do not permit the physician to identify the pathophysiological origins of those trouble even with in-depth clinical investigations [2].

Moreover, significant disagreements remain between contemporary tests (e.g. manometry, imaging techniques, ballon explusion test) used to assess colonic and anorectal function and then establish a diagnosis and treatment pathway [3]. These diagnostic difficulties are compounded by our incomplete understanding of the normal and pathological process of defecation which has led to the continuing debate over the classification of defecation disorders [4], [5].

For these reasons, some biomechanical models of human defaecation emerged for a few years. By connecting muscle activity, anatomy of the recto-anal junction and the flow and rheology of feces, these models contribute to the renewal of the knowledge on rectal function, [6], [7].

In the present case-study report, based on a standardized dynamic imaging technique of human defecation (X-ray defecography, [8]), we report a 2D patient-specific computational fluid dynamic (CFD) model of rectal evacuation. We describe a model which allows to assess hydrodynamical and biomechanical factors controlling defecation, which could be used to gain new insights on the physiology of defecation and to diagnose underlying evacuation disorders.

II. MATERIALS AND METHOD

A. Videodefecography

The X-ray videodefecography used for CFD modelling was selected among about 2300 examinations performed by Dr. Alain Dubreuil during 28 years of professional medical career [9], [10]. Videodefecogrophy was performed in a sitting position of the patient. The rectum was visualized in the sagittal plane (Fig. 1-a) and filled with a standardized radio-opaque paste until the patient experienced rectal fullness [8].

The paste was prepared by mixing barium sulfate with a suspension of potato starch and cooked to obtain a paste, as described by Mahieu *et al.* [8]. The interest to use barium paste lies in the fact that its rheological properties corresponds to the one of a soft feces. In our previous study [7], we reported that the rheological properties of barium paste can be described by the Herschell-Bulkley constitutive model,

$$\begin{cases} \tau = \tau_0 + k|\dot{\gamma}|^n, & \text{if } |\tau| > \tau_0 \\ \dot{\gamma} = 0, & \text{if } |\tau| \leq \tau_0 \end{cases} \quad (1)$$

where τ_0 is the yield stress, k the consistency index, n the flow index, τ the shear stress and $\dot{\gamma}$ the shear rate. This constitutive equation corresponds to a fluid that can flow only if the stress is larger than the yield stress. For the barium paste, τ_0 = 350 Pa, n = 0.42 and k = 1000 Pa.s^n [7]. CFD simulations were carried out with these rheological parameters.

The videodefecography used in this study was carried out in 2001 on a female patient of 63 years old, who did not present any morphological abnormality. The patient was diagnosed with transit constipation with hard stools and her

---

[1] Univ. Grenoble Alpes, CNRS, Grenoble INP, LRP, 38000 Grenoble, France `clement.de-loubens@univ-grenoble-alpes.fr`

[2] Clinique du Mail, Grenoble, France

[3] Univ. Grenoble Alpes, CHU Grenoble Alpes, Colorectal Unit, Department of Surgery, Grenoble, France

[4] Univ. Grenoble Alpes, CNRS, CHU Grenoble Alpes, Grenoble INP, TIMC, Grenoble, France `stephane.tanguy@univ-grenoble-alpes.fr`

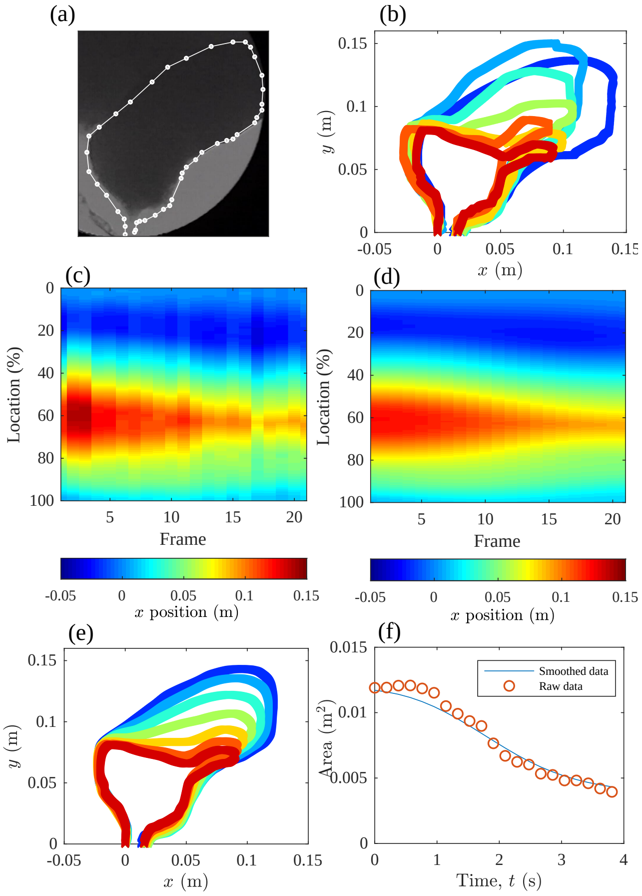

Fig. 1: a: Example of X-ray images segmentation. b: Raw profiles of the rectum after segmentation and interpolation for different time steps (time increasing from blue to red). c: Spatio-temporal map of the x position of the evenly spaced markers. The locations 0 and 100 % correspond to the anterior and posterior part of the anus, respectively. d: ST map after smoothing. e: Smoothed profiles of the rectum. d: Comparison of the area bounded by the raw boundaries (circles) and the smoothed boundaries (plain line).

rectal function was considered to be strictly normal by Dr. Alain Dubreuil. The patient experienced rectal fullness after the administration of 330 g of barium paste. The rectum was emptied at 90% in 4 s. The rectal length (10.2±2.3 cm), ano-rectal angle (120±9°), anal diameter (1.61±0.4 cm), were in accordance with dimensions reported for normal subjects on a large cohort [11].

Patient wa informed that her anonymized data might in the future be the subject of clinical research and could oppose this by informing the doctor. All procedures performed in this study were in accordance with the ethical standards research committee and with the Helsinki declaration. Ethics approval is not required for this retrospective study.

B. Image Analysis

X-ray analog images (HI-8) were first digitized using VLC media player software and process with the Image Processing Toolbox of Matlab R2019b (Mathworks). The boundaries of the rectum and the anus were manually segmented with approximately 40 points; white circles in Fig. 1-a. The selected x and y coordinates of the boundary were interpolated with a Piecewise Cubic Hermite Interpolating Polynomial (PCHIP) method to increase the resolution for all the time steps, Fig. 1-b. For each time step, about 1000 points, evenly spaced along the boundaries, were selected. Fig. 1-c shows the spatio-temporal (ST) map of the x coordinate of these points. ST maps for x and y coordinates were smoothed with a 2D Gaussian filter, Fig. 1-d. Fig1-e shows the profiles of rectum boundaries after the smoothing process. This process allowed to suppress mass movements of the rectum when the patient was moving during the examination. The smoothed set of data was linearly interpolated for subsequent CFD simulations. To validate the image processing algorithm, the variations of the surface area bounded by the smoothed boundaries were compared to the one bounded by the raw data, fig1-f. The averaged outlet velocity of the barium paste in the anal canal V_{out} was given by the ratio of the temporal derivative of the area over the diameter of the anal canal.

C. CFD model

The barium paste flow during the defecation was simulated with D2Q9 lattice-Boltzmann methods (LBM) to solve mass and momentum conservation equations in 2D on a Cartesian mesh [12]. The viscosity at each lattice was calculated with the Papanastasiou's regularization of the Herschel-Bulkley model (Eq. 1) [13], i.e. $\eta = \frac{\tau_0}{|\dot{\gamma}|}[1 - \exp(-m|\dot{\gamma}|)] + k|\dot{\gamma}|^{n-1}$, where η is the viscosity, m is the stress growth exponent, and $|\dot{\gamma}| = \sqrt{\dot{\gamma}_{ij}\dot{\gamma}_{ij}}$ the second invariant of the rate-of-strain tensor. The two relaxation times LBM scheme was used to suppress numerical discrepancies associated to large variations of viscosity in one relaxation time LBM schemes [14], [15].

The moving boundary conditions were calculated by a computationally efficient combination of the bounce-back scheme and the transfer of momentum on the fluid by the moving wall [16]. Similarly, the velocity profile corresponding to the flow of a Herschell-Bulkley fluid of averaged velocity V_{out} was enforced at the outlet of the anal canal. The code was carefully validated with benchmark solutions for flows of yield stress fluids: Poiseuille flow and shear flow with a moving obstacle. The grid to solve the flow consisted in about 4000 lattices.

The stress applied in the normal direction by the fluid over the boundaries of the rectum, i.e the wall normal stress WNS, was calculated by

$$\text{WNS} = (-p\bar{\bar{I}} + \bar{\bar{\tau}}).\vec{n} \tag{2}$$

where p is the pressure on the rectum boundary, $\bar{\bar{I}}$ is the identity normal tensor, $\bar{\bar{\tau}}$ is the deviatoric part of the stress tensor and $\vec{n}$ is the normal unit vector to the boundary.

III. RESULTS & DISCUSSIONS

The patient-specific CFD model of rectal evacuation was used to calculate different hydrodynamical and biomechan-

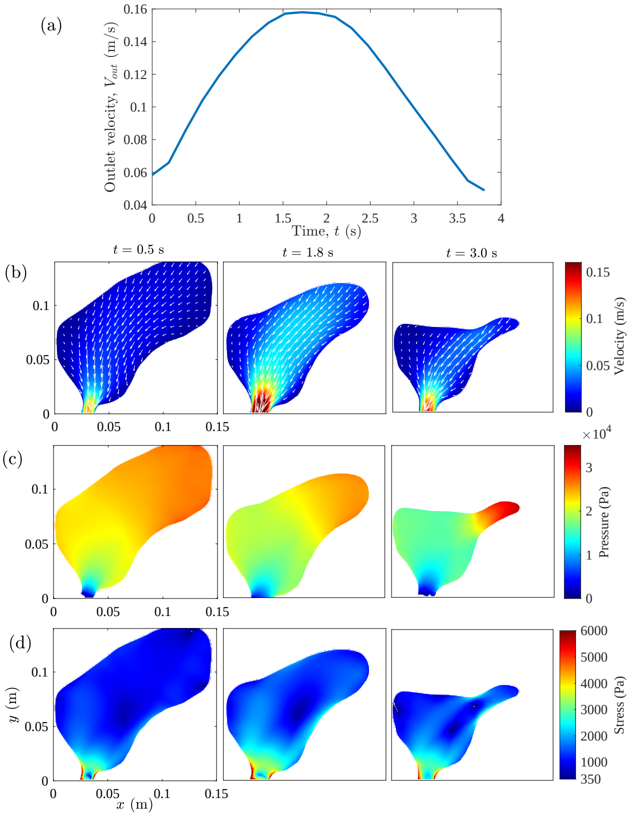

Fig. 2: Average outlet flow velocity V_{out} of the barium paste passing through the anus (a). Velocity (b), pressure (c) and stress (d) fields at 0.5, 1.8 and 3 s during the defecation of the barium paste.

ical parameters during the defecation of the standardised barium paste for a patient who had a normal recto-anal function and anatomy.

A. Hydrodynamics of defecation

The averaged outlet velocity of the barium paste through the anus (V_{out}), calculated from image analysis, and time-sequences of the velocity field in the recto-anal cavity are shown in Fig. 2-a,b. The temporal evolution of V_{out} had a bell-like shape with a maximum of 0.16 m/s after 2 s of the beginning of the defecation. The velocity was oriented from the proximal (colo-rectal part) to the distal (ano-rectal part) parts. Its magnitude was maximal in the anal part and minimal in the cavity forming the anterior part of the rectum.

The pressure field shows a gradient from the proximal to the distal part, and was maximum at the distal part, Fig 2-c. The stress (i.e. second invariant of the stress tensor) was in average 10 times larger than the yield stress of the barium paste (350 Pa), and was maximal at the boundaries of the anus and relatively homogeneous in the rectum (Fig 2-d).

These results illustrated that the main flow resistance was related to the extrusion of the barium paste through the anal sphincter. Moreover, the stress was larger than the yield stress, meaning that all the barium paste was flowing. In pathological situations, the anterior part of the rectum can form a large cavity, called rectocele, in which the feces forms a cluster and accumulates [11]. Rectocele should be identified by regions of low stress and velocity, where the feces does not flow. A question to address in the future is to know if the presence of anatomical abnormalities, such as rectocele or enterocele, can impair the rectum function, i.e. create a supplementary flow resistance that could impair defecation. Also, we could hypothesize that the retention of feces in the rectocele might be the consequence of abnormal properties of the feces. Consequently, our model should help to know whether a surgical procedure is required.

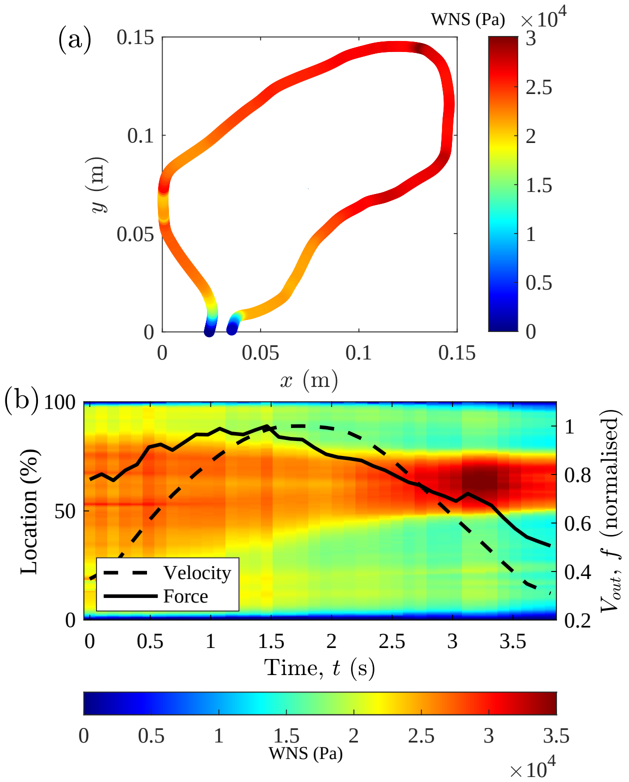

Fig. 3: a: Instantaneous variations of the wall normal stress (WNS) along the boundaries of the rectum at $t = 0.5$ s. The color code corresponds to the magnitude of WNS. b: Spatio-temporal map of WNS along the boundaries of the rectum. The location 0 and 100 % correspond to the anterior and posterior part of the anus, respectively. Plain and dashed lines show respectively the temporal variations of the magnitude of the force $\vec{f}$ and the outlet velocity V_{out}, which are scaled by their maximal value (right y-axis).

B. Muscle activity during defecation

The wall normal stress (WNS), i.e. the normal force per unit of area that is exerted by the boundaries of the rectum over the barium paste, was calculated by projecting the stress field on the rectum boundaries (Fig3-a, Eq. 2). The WNS gradient from the proximal (maximum) to the distal (minimum) part was highlighted in the ST map of WNS

(Fig. 3-b). The gradient was always in a proximal to distal direction, regardless of the time of defecation. The maximum WNS of about 30 kPa observed at 3.2 s is coherent with manometric data, which reported a maximal pressure of about 40.2 kPa [17]. From these results, we can speculate that ST-maps of WNS for patients suffering of evacuations disorders should allow to identify an absence of muscle coordination [10], [18].

By integrating WNS along the rectum boundaries, we calculated the magnitude and the direction of the global force of the boundaries over the barium paste $\vec{f}$. On the ST map (Fig. 3-b), both amplitude of $\vec{f}$ and V_{out} are plotted as a function of time. Note that the amplitude of both variables were divided by their maximum. Both data were not in phase with the evolution of WNS: the temporal evolution of the force showed a bell-like shape, with a maximum almost in phase with V_{out} and preceding the maximum of WNS by 2 s. This phase shift is explained by the reduction over time of the contact surface of the barium paste with the mucosa of the rectum. Consequently, the force decreases for a steady value of WNS. Thus, any relaxation of the muscles would stop the flow. Moreover, the $\vec{f}$ orientation was equal to the recto-anal angle during defecation. In the clinical practice, the magnitude and the direction of the force could be used to detect any weakness of the muscles and/or a desynchronization of the muscles if the orientation of the force was different from the ano-rectal angle.

IV. CONCLUSION

In conclusion, this paper is a first step towards an assessment of the rectal function by coupling a well-established dynamic imaging of human defecation with a CFD model. Our model maps spatially and temporally the action of ano-rectal muscles. This information should be precious to identify problem of muscle strength or loss of coordination. Work is in progress to extend these simulations on a larger cohort of patients showing normal and pathologic defecation.

ACKNOWLEDGMENT

LRP is part of the LabEx Tec21 (ANR-11-LABX-0030) and of the PolyNat Carnot Institute (ANR-11-CARN-007-01). The authors thanks ANR for financial support, TransportGut, ANR-21-CE45-0015.

REFERENCES

[1] Ditah, I., Devaki, P., Luma, H. N., Ditah, C., Njei, B., Jaiyeoba, C., ... & Szarka, L. (2014). Prevalence, trends, and risk factors for fecal incontinence in United States adults, 2005–2010. Clinical Gastroenterology and Hepatology, 12(4), 636-643.

[2] Curtin, B., Jimenez, E., & Rao, S. S. (2020). Clinical evaluation of a patient with symptoms of colonic or anorectal motility disorders. Journal of Neurogastroenterology and Motility, 26(4), 423.

[3] Palit, S., Thin, N., Knowles, C. H., Lunniss, P. J., Bharucha, A. E., & Scott, S. M. (2016). Diagnostic disagreement between tests of evacuatory function: a prospective study of 100 constipated patients. Neurogastroenterology & Motility, 28(10), 1589-1598.

[4] Corsetti, M., Costa, M., Bassotti, G., Bharucha, A. E., Borrelli, O., Dinning, P., ... & Tack, J. (2019). First translational consensus on terminology and definitions of colonic motility in animals and humans studied by manometric and other techniques. Nature Reviews Gastroenterology & Hepatology, 16(9), 559-579.

[5] Corsetti, M., Costa, M., Bassotti, G., Bharucha, A. E., Borrelli, O., Dinning, P., ... & Tack, J. (2019). First translational consensus on terminology and definitions of colonic motility in animals and humans studied by manometric and other techniques. Nature Reviews Gastroenterology & Hepatology, 16(9), 559-579.

[6] Bush, M., Petros, P., Swash, M., Fernandez, M., & Gunnemann, A. (2012). Defecation 2: Internal anorectal resistance is a critical factor in defecatory disorders. Techniques in coloproctology, 16(6), 445-450.

[7] de Loubens, C., Dubreuil, A., Lentle, R. G., Magnin, A., El Kissi, N., & Faucheron, J. L. (2020). Rheology of human faeces and pathophysiology of defaecation. Techniques in coloproctology, 24(4), 323-329.

[8] Mahieu, P., Pringot, J., & Bodart, P. (1984). Defecography: I. Description of a new procedure and results in normal patients. Gastrointestinal radiology, 9(1), 247-251.

[9] Faucheron, J. L., Barot, S., Collomb, D., Hohn, N., Anglade, D., & Dubreuil, A. (2014). Dynamic cystocolpoproctography is superior to functional pelvic MRI in the diagnosis of posterior pelvic floor disorders: results of a prospective study. Colorectal Disease, 16(7), O240-O247.

[10] Faucheron, J. L., & Dubreuil, A. (2000). Rectal akinesia as a new cause of impaired defecation. Diseases of the colon & rectum, 43(11), 1545-1549.

[11] Palit, S., Bhan, C., Lunniss, P. J., Boyle, D. J., Gladman, M. A., Knowles, C. H., & Scott, S. M. (2014). Evacuation proctography: a reappraisal of normal variability. Colorectal Disease, 16(7), 538-546.

[12] Aidun, C. K., & Clausen, J. R. (2010). Lattice-Boltzmann method for complex flows. Annual review of fluid mechanics, 42, 439-472.

[13] Panaseti, P., & Georgiou, G. C. (2017). Viscoplastic flow development in a channel with slip along one wall. Journal of Non-Newtonian Fluid Mechanics, 248, 8-22.

[14] d'Humières, D., & Ginzburg, I. (2009). Viscosity independent numerical errors for Lattice Boltzmann models: From recurrence equations to "magic" collision numbers. Computers & Mathematics with Applications, 58(5), 823-840.

[15] Talon, L., & Bauer, D. (2013). On the determination of a generalized Darcy equation for yield-stress fluid in porous media using a Lattice-Boltzmann TRT scheme. The European Physical Journal E, 36(12), 1-10.

[16] Bouzidi, M. H., Firdaouss, M., & Lallemand, P. (2001). Momentum transfer of a Boltzmann-lattice fluid with boundaries. Physics of fluids, 13(11), 3452-3459.

[17] Carrington, E., Brokjaer, A., Craven, H., Zarate, N., Horrocks, E. J., Palit, S., ... & Scott, S. M. (2014). Traditional measures of normal anal sphincter function using high-resolution anorectal manometry (HRAM) in 115 healthy volunteers. Neurogastroenterology & Motility, 26(5), 625-635.

[18] Lunniss, P. J., Gladman, M. A., Benninga, M. A., & Rao, S. S. (2009). Pathophysiology of evacuation disorders. Neurogastroenterology & Motility, 21, 31-40.

3.3 Extension of the 2D Model to Normal and Pathologic Patients

In previous Section 3.2, a preliminary study of rectal evacuation by modeling dynamic X-ray defecography with complex rheology of the neostool applied to a normal patient. The model gave insights in regard to the rectal function. We expected that ST mapping of the recto-anal pressure and WNS help to identify pathologies.

In this section, we applied the model to multiple patients. Six Patients (4 women and 2 men) with no developed anatomical abnormalities and pathologic conditions were considered and two patients (one woman and one man) with abnormally slow defecation and no anatomical abnormalities were also considered as a case study. The results are presented in the paper published in the special issue of "biological complex fluids" of Interface Focus journal [4].

My contributions

The first draft of the paper was written by me. I also performed image analysis on all the videos, simulations, and prepared all the figures.

Flow simulations of rectal evacuation: towards a quantitative evaluation from video defecography

Faisal Ahmad,[1] Stéphane Tanguy,[2] Alain Dubreuil,[3] Albert Magnin,[1] Jean-Luc Faucheron,[2, 4] and Clément de Loubens[1]

[1] *Univ. Grenoble Alpes, CNRS, Grenoble INP, LRP, 38000 Grenoble, France*
[2] *Univ. Grenoble Alpes, CNRS, CHU Grenoble Alpes, Grenoble INP, TIMC, Grenoble, France*
[3] *Clinique du Mail, Grenoble, France*
[4] *Univ. Grenoble Alpes, CHU Grenoble Alpes, Colorectal Unit, Department of Surgery, Grenoble, France*

Mechanistic understanding of anorectal (patho)physiology is missing to improve the medical care of patients suffering from defecation disorders. Our objective is to show that complex fluid dynamics modeling of video defecography may open new perspectives in the diagnosis of defecation disorders. Based on standard X-ray video defecographies, we developed a bi-dimensional patient-specific simulation of the expulsion of soft materials, the feces, by the rectum. The model quantified velocity, pressure and stress fields during the defecation of a neostool with soft stool-like rheology for patients showing normal and pathological defecatory function. In normal defecation, the proximal-distal pressure gradient resulted from both the anorectal junction which formed a converging channel and the anal canal. The flow of the neostool through these anatomical parts was dominated by its shear-thinning viscous properties, rather than its yield stress. Consequently, the evacuation flow rate was significantly affected by variations in pressure applied by the rectum, and much less by the geometry of the anorectal junction. Lastly, we simulated impaired defecations in absence of obvious obstructive phenomena. Comparison with normal defecation allowed us to discuss critical elements which should lead to effective medical management.

I. INTRODUCTION

Defecation is a complex physiological process, which involves the coordination of neural, muscular, hormonal and cognitive systems [1]. It is triggered by abdominal contractions and thrusts during a Valsalva maneuver. The rectal evacuation is then relayed by the contraction of the rectal muscle that acts similar to the detrusor for bladder emptying [2]. Defecation disorders, which result in constipation or incontinence, are widespread in the worldwide population with prevalence in about 15% of the population [3, 4] and can significantly alter the quality of life of patients [5]. Because of the multi-factorial origins of defecation disorders and gaps in our understanding of normal and pathological defecation, it remains difficult for physicians to clearly distinguish etiologies from symptoms [6].

Defecation is the evacuation of soft materials, the feces, through the anorectal junction and the anal canal. There are many possible etiologies of defecation disorders, including, for example, slow bowel transit associated to hard feces difficult to expel, structural obstructive phenomena, anal sphincter injuries, etc. [1, 7]. It is also worth highlighting that a significant proportion of patients with impaired defecation do not have a well-defined anatomic disorder [8, 9]. Moreover, recent systematic characterization of defecographic abnormalities showed a strong overlap of structural and functional abnormalities in a large cohort of patients [10].

Although many testing tools are available to diagnose the anorectal function (manometry, video defecography, MRI, etc.), there are always some methodologic issues that limit the physicians' understanding of (patho)physiological defecations [11]. Discrepancies between tests are frequent and complicate the medical care of patients [12]. For example, manometry and evacuation are typically measured asynchronously under different conditions. Manometry is generally performed in non physiological conditions with an empty rectum, whereas evacuation is assessed with the expulsion of a balloon [13, 14]. To circumvent these limitations, researchers are developing and validating a soft core with embedded pressure sensors to combine manometry and defecography [15]. Moreover, well established tests are partially processed. For example, video defecographies are currently used to assess structural and functional obstructive phenomena [1], although they contain physical information about the rectal function [8, 16]. All of these elements contribute to 'considerable controversy' in the coloproctology community regarding origins, consequences and treatment of patients [17–19].

In the context of this bleak epidemiology, there is strong agreement that efforts must be directed towards a mechanistic description of the defecatory function [1, 11]. Among the different gaps that have been identified in recent reviews [1, 11, 13], we focused in this paper on the modeling of the anorectal pressure forces generated during evacuation. Indeed, the relationships bettwen the pressure and the flow depends on (i) the anorectal geometry, (ii) the forces applied by the rectal muscles, (iii) the straining of the abdomen and (iv) the rheological properties of the feces. Feces is a yield stress fluid [20]. The yield stress of human feces varies naturally over several order of magnitudes depending on its water content [21]. When the stress applied is larger than the yield stress, feces flows as a shear thinning fluid [22–24]. Consequently, we developed patient-specific simulations of rectal evacuation of yield stress fluids based on X-ray video defecographies with a neostool.

II. METHODS

The two dimensional (2D) patient-specific computational fluid dynamics (CFD) model of rectal evacuation was based on X-ray video defecographies [16]. Examinations were carried out in sitting position with a radio-opaque suspension (neostool) with soft stool-like rheology [8, 21, 25]. Rectal profiles were extracted to impose the kinetics of the rectum walls in the model. The algorithm was based on lattice-Boltzmann methods for yield stress fluids and moving boundary conditions. The CFD model simulated the evolution of velocity, pressure and stress fields in the rectal cavity.

A. Video defecographies

X-ray videodefecographies were carried out with the patient in sitting position, Fig. 1-a. The rectum was filled with a standardized radio-opaque neostool with a silicone gun [8, 25, 26] until the patient experienced rectal fullness, and visualized in the sagittal plane. Consequently, out-of-plane deformations could not be captured. However, such deformations are likely to happen in presence of anatomical abnormalities, which are easily observed in the sagittal plane [27]. As the orientation and z-location of the imaging plane could significantly affect the shape of the rectum, the position of the patient during the radiologic examination has been standardized, as well as the distance between the X-ray machine and the patient [8].

The radio-opaque neostool was prepared by mixing barium sulfate with a suspension of potato starch and cooked to obtain a paste with a yield stress τ_0 [8, 25]. The rheological properties of the neostool was characterized in our previous publication with standard rheometric techniques [21]. The relationships between the shear stress and the shear rate showed that the shear stress tends towards a constant value, the yield stress τ_0, when the shear rate tends towards 0, Fig. 1-b. This means that, as human feces, neostool can only flow if the stress applied is higher than the yield stress. The yield stress of the neostool was 350 Pa, which matched to the yield stress of soft regular human feces [21].

All the patients underwent X-ray defecographies during their health care pathways after they had complained of evacuation disorders, see Appendix A. The movies were selected among the examinations carried out in 2002 by A.D. Six X-ray videodefecographies were considered as representative of a normal evacuation of the neostool: the patients could evacuate the neostool without straining efforts and stool fragmentation, and had the sensation of a complete rectal evacuation. No developed anatomical abnormalities were observed and the function of the rectum and the anus was not considered pathologic after the examination. In agreement with an extensive quantification of normal evacuation in videodefecographies [16], 70 % of the standardised neostool had to be evacuated in one well-defined evacuatory attempt in less than 60 s. The 6 patients included 4 women of 60 to 80 years old and 2 men of 55 and 80 year old. The length of the rectum (12 ± 5.5 cm), the angle between the anal canal

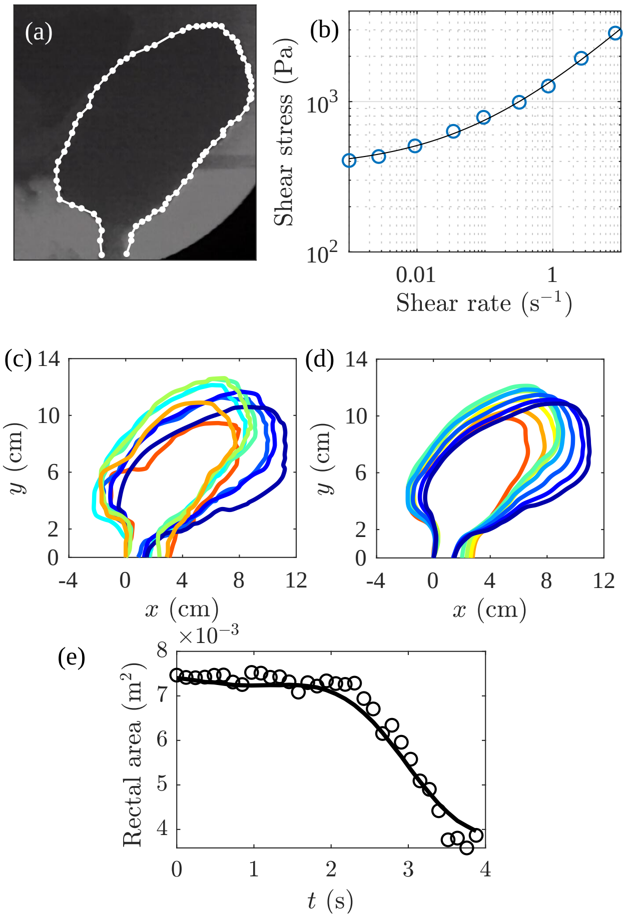

FIG. 1: X-ray defecography and image processing. *(a)* Sagittal view of the rectum filled with standardized radio-opaque neostool. White dots show the segmentation of the rectum. *(b)* Flow curve of the neostool (circles) fitted by the Herschel-Bulkley constitutive model for yield stress and shear-thinning fluids (plain line), from [21]. At low shear rate, the shear stress tends towards the yield stress. At high shear rate, the shear stress increases and the apparent viscosity decreases. *(c)* Raw profiles of the rectum after segmentation and interpolation for different time steps (time increasing from blue to red, patient N3). *(d)* Same profiles after smoothing. *(e)* Comparison of the area bounded by the raw boundaries (circles) and the smoothed boundaries (plain line) as a function of time t.

axis and a tangent line to the posterior edge of the rectal ampulla (i.e. ano-rectal angle) at the beginning of the defecation (130 ± 22°) and the radius of the anal canal (0.95 ± 0.19 cm), were also in agreement with data reported by Palit *et al.* [16]. Data is reported as the mean ± the standard deviation.

As case studies of functional defaecation disorders, two videos (one man and one woman) with abnormally slow rectal evacuation in the absence of visible anatomical abnormality, with the exception of a long anal canal and/or a closed anorectal angle at 90°, were also simulated. The quantity of neostool injected was standard (280 and 220 g).

Patients were informed that their anonymized data might in the future form the subject of clinical research and that they could object to this by informing the doctor. All procedures performed in this study complied with the requirements of the ethical standards research committee and with the Helsinki declaration. Ethics approval is not required for this retrospective study.

B. Flow modeling

The boundaries of the rectum were extracted from each video and processed as detailed in Appendix B. As a result of this process, the smoothed position of boundary nodes with equal arc length along the boundary of the rectum was obtained for each frame of the video (Fig. 1-c, d, e), along with the velocity $\mathbf{u_w}$ of each node. The mean outlet velocity V_a of the neostool through the anus is given by mass conservation, i.e.

$$V_a = \frac{1}{2R_a} \int\limits_{\mathcal{L}} \mathbf{u_w}.\mathbf{n} \, \mathrm{d}l \tag{1}$$

where $\mathbf{n}$ is the normal to the boundary of the rectum, $\mathcal{L}$ is the contour length of the boundary and R_a is the radius of the anus.

As the neostool was very viscous and the Reynolds number very small, the flow was modelled using the incompressible Stokes equations in 2D for Herschel-Bulkley (HB) fluid. Mass and momentum equations are given by

$$\frac{\partial u_i}{\partial x_i} = 0, \; \frac{\partial \tau_{ij}}{\partial x_j} = \frac{\partial p}{\partial x_i} \tag{2}$$

where i,j (=1,2), u_i, x_i, τ_{ij} and p are the indices of the system of coordinates, the velocity, the coordinate, the viscous stress tensor and the pressure respectively. The relation between the viscous stress tensor τ_{ij} and the strain rate tensor $\dot\gamma_{ij} = \frac{\partial u_i}{\partial x_j}$ for the neostool was modelled by the HB constitutive equation

$$\begin{cases} \tau_{ij} = \left(\frac{\tau_0}{|\dot\gamma|} + k|\dot\gamma|^{n-1}\right)\dot\gamma_{ij}, & \text{if } |\tau| > \tau_0 \\ \dot\gamma_{ij} = 0, & \text{if } |\tau| \le \tau_0 \end{cases} \tag{3}$$

where τ_0 is the yield stress, k the consistency index, n the flow index, $|\tau|$ and $|\dot\gamma|$ are the second invariant of each tensor. This set of equations was solved by lattice-Boltzmann methods, see details in Appendix C. The smoothed position of boundary nodes extracted from the video and their velocity $\mathbf{u_w}$ were used as boundary conditions along the moving wall of the rectum. The rheological parameters were fixed and determined by fitting the HB model on the flow curve of the neostool (plain line in Fig. 1-b): $\tau_0 = 350$ Pa, $n = 0.42$ and $k = 1000$ Pa.$s^{0.42}$.

Among the different physical quantities that we analysed, we also computed the stress applied in the normal direction by the fluid over the boundaries of the rectum, i.e the wall normal stress WNS, by

$$\mathrm{WNS} = (-p\mathbb{I} + \tau).\mathbf{n} \tag{4}$$

where $\mathbb{I}$ is the identity tensor. By integrating the WNS along the boundaries of the rectum, we calculated also the effective evacuation force $\mathbf{F}$ and its angle with the horizontal axis. $\mathbf{F}$ and the WNS are the resultant of both abdominal and rectal muscle contractions. We also systemically analyzed velocity, pressure and viscous stress fields. For brevity, the second invariant of the viscous stress tensor $|\tau|$ is refered as the viscous stress throughout this manuscript.

III. RESULTS

A. Normal defecations

For the six patients showing no signs of functional or anatomical pathologies, the outlet velocity of the neostool V_a could be characterized by one or two peaks, in agreement with extensive videodefecography studies [16]. We standardized the period of time during which the flow was simulated. This period of time was included between the two minima that framed the maximal outlet velocity V_a^{max}. The superposition of the profiles of the rectum shows that the proximal part of the rectum was squeezing the neostool through both the anorectal junction and the anal canal, Fig. 2-a. Both of these distal anatomical parts were static during the expulsive phase of defecation. In fact, the diameter of the anal canal showed little variation during the expulsive phase, $D_a = 2.0 \pm 0.4$ cm, whereas V_a^{max} increased up 9 ± 4 cm/s in a few seconds, Fig. 2-b. The color code in Fig.2-b shows the magnitude of the wall normal stress WNS. The WNS was maximal at the moving proximal part and decreased in the static anorectal junction.

Fields of velocity, pressure and viscous stress are shown in Fig. 3 at the time of maximum outflow velocity for each of the six patients. The velocity field was unidirectional and oriented along the mean curvature of the rectum, Fig. 3-a. Its magnitude was maximal in the anus. Some patients presented a small anterior pocket

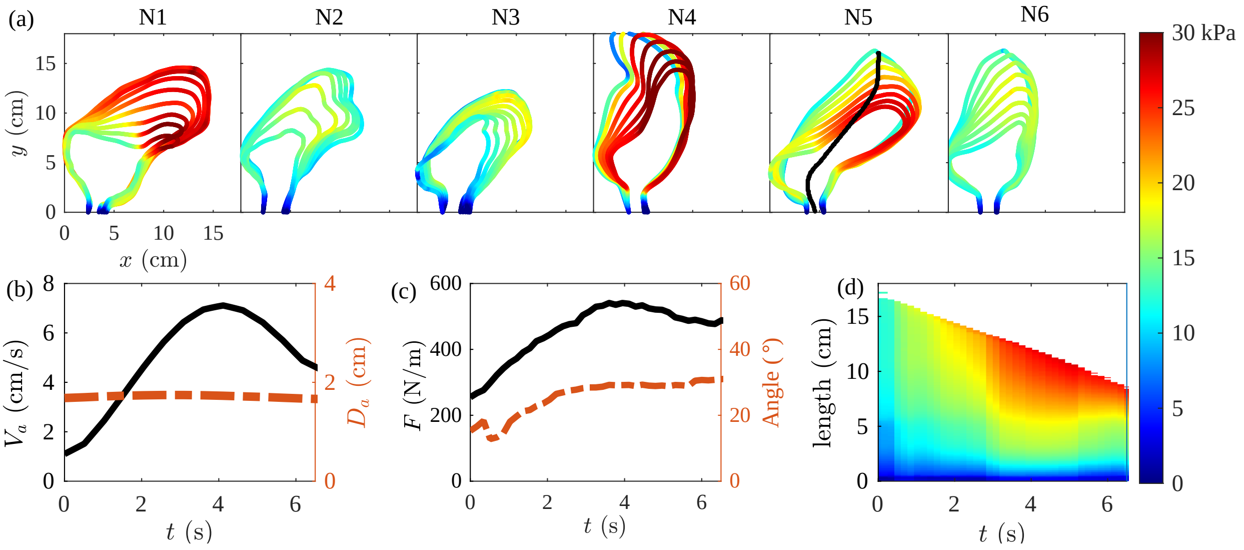

FIG. 2: Simulations of normal rectal evacuations through the open anal canal. *(a)* Evolution of the boundaries of the rectum during the evacuation of the neostool for 6 patients showing a normal rectal function. The color code shows the magnitude of the wall normal stress WNS. *(b)* Example of mean outlet velocity of the neostool through the anal canal V_a (plain lines, left axis) and diameter of the anal canal D_a (dashed lines, right axis) as a function of time (patient N5). *(c)* The evacuation force F (plain lines, left axis) and its angle with the y axis (dashed lines, right axis) as a function of time for patient N5 *(d)* Spatio-temporal map of the pressure variation along the length of a mid-line going from the anal canal (0 cm) to the proximal end at time 0 (black line in a-N5).

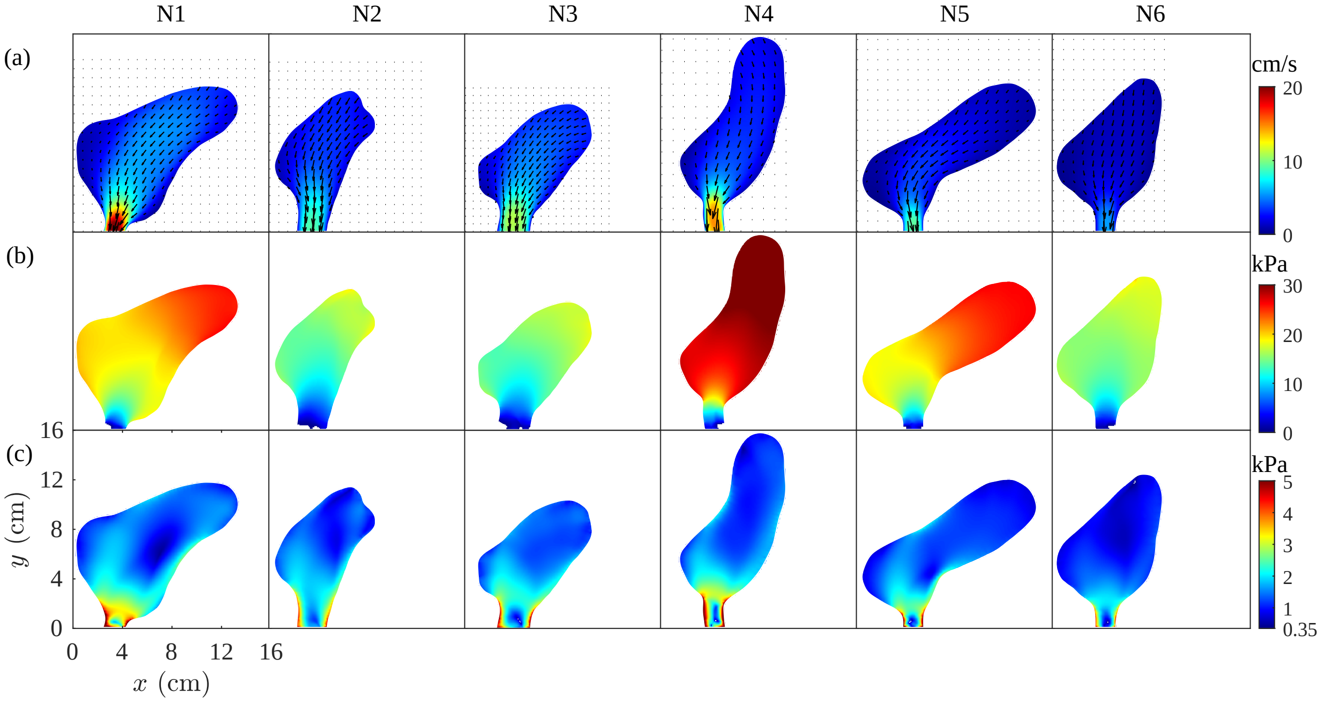

FIG. 3: Instantaneous *(a)* flow fields, *(b)* pressure fields and *(c)* viscous stress fields of 6 normal evacuations when the outlet velocity V_a was maximal.

(typically patient 5), the so-called 'clubbing', in which the velocity was minimal. The pressure was maximal in the rectal ampulla, Fig. 3-b. Its gradient was mainly orientated along the mean curvature of the rectum. There was no pressure gradient in the radial direction wether in the rectal ampulla or in the anal canal. However, there was a gradient in the radial direction in the ano-rectal junction that formed a converging channel. The viscous stress was also maximal in the anus and the anorectal junction, Fig. 3-c. Its magnitude was greater than the yield stress of the neostool ($\tau_0 = 350$ Pa).

Similarly to high resolution manometry [28], the spatio-temporal (ST) evolution of the pressure along a mid-line going from the anal to the proximal ends (black lines on Fig. 2-a, N5) is shown for one typical example in Fig. 2-c. The map can be divided spatially and temporally. Spatially, in the rectal ampulla, the pressure was homogeneous and maximal (between 5 and 15 cm in Fig. 2-d). The maximum was approximately 25 kPa, i.e. an order of magnitude in agreement with rectal manometry values [28]. Between the beginning of the ano-rectal junction (at 5 cm) and the end of the anal canal (at 0 cm), the pressure dropped from 20 to 0 kPa. Temporally, the pressure was increasing and propagating towards the ano-rectal junction up to 3 s. A 3 s, the same level of pressure was maintained.

In all patients (N1-N6), the evacuation force **F** followed also a bell-shaped curve which was synchronized with the outlet velocity V_a (black lines on Fig. 2-b, c), whereas its angle α was almost constant during the evacuation (20 ± 13 °), which corresponded to the anorectal angle.

B. Abnormal defecations

The two patients showing functional pathology of rectal evacuation were characterized by the absence of structural obstructive phenomena [1], Fig. 4-a. However, for the first pathologic patient P1, the anal canal was almost twice longer than in normal patients and the anorectal angle was fully open. Conversely, for the patient P2, the anorectal angle was closed and the diameter of the anal canal was normally dilated. During the full examination which lasted about 2 min, there were different attempts of evacuation. We simulated the sequence corresponding to a successful and partial evacuation (12 and 30 s, respectively). The maximal outlet velocity through the anal canal $V_a \simeq 1$ cm/s was one order of magnitude lower than for normal evacuation, Fig. 4-b, black plain lines.

Fig. 5 shows velocity, pressure and viscous stress fields at the time of maximum outflow velocity. The flow was also unidirectional along the middle axis of the rectum. The organisation of the pressure field was also similar to that of normal patients, although its amplitude was twice lower. The pressure was almost homogeneous in the rectal ampulla for both patients. For P1, the pressure drop was significant in the anorectal junction and the anal canal (square in Fig.5-b). It was combined with a high viscous stress localized at the walls. For P2, the pressure drop was mainly localized in the 90° bend formed by the ano-rectal junction and the anal canal. In the anal canal, the viscous stress was also maximal at the walls. For both

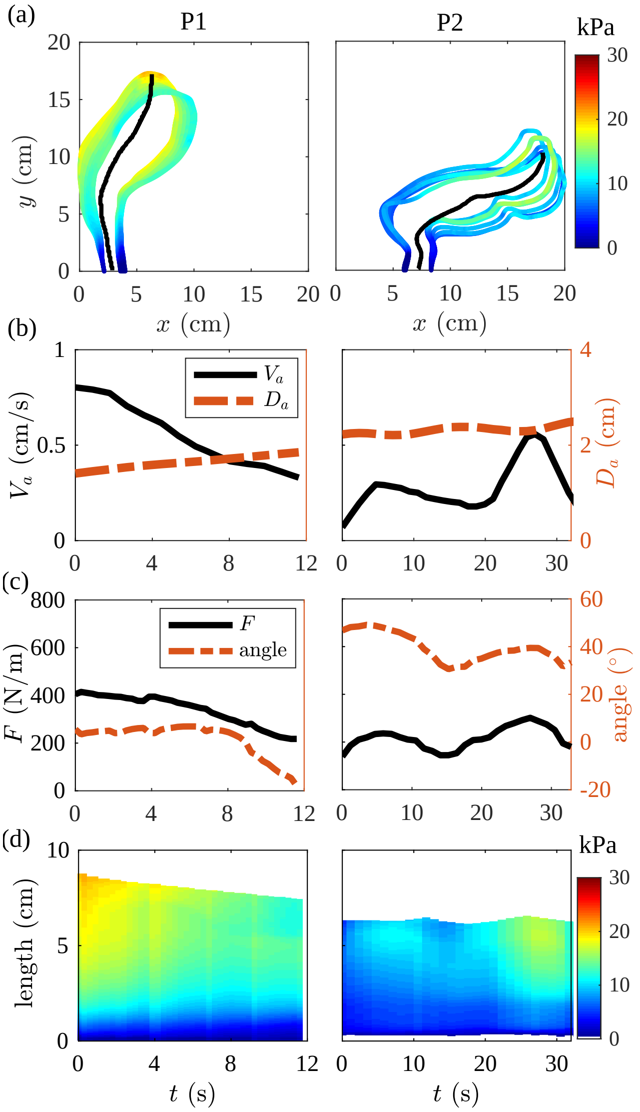

FIG. 4: Simulations of pathologic defecations showing abnormally slow evacuation. *(a)* Evolution of the boundaries of the rectum during the evacuation of the neostool for 2 patients. The color code shows the magnitude of the wall normal stress WNS. *(b)* Mean outlet velocity of the neostool through the anal canal V_a (plain lines, left axis) and diameter of the anal canal D_a (dashed lines, right axis) as a function of time. *(c)* The evacuation force F (plain lines, left axis) and its angle with the y axis (dashed lines, right axis) as a function of time. *(d)* Spatio-temporal map of the pressure variation along the length of mid-lines going from the anal canal (0 cm) to the proximal end (black lines in a).

patients, the maximal viscous stress (2 kPa) was 3 times lower than for normal patients, Fig.5-c.

As for normal patients, the WNS was also maximal at the proximal part, Fig. 4-a. However, the movement of the boundaries was clearly limited. Fig. 4-c shows the ST-maps of pressure along the black lines displayed in Fig. 4-a. Again, there was a proximal to distal gradient. Lastly, the evacuation force F was coordinated with the outlet velocity V_a (black lines in Fig. 4-b, c). The maximal value ranged from 200 to 400 N/m which was to 2 to 3 times lower than for normal evacuation. The orientation of the force (dashed red lines in 4-c) was around 0° for P1 and 40° for P2.

IV. DISCUSSION

The first attempts to model the fluid mechanics of human defecation were made by Farag [29, 30], who used the Hagen-Poiseuille law of purely viscous Newtonian fluids to deduce the intra-rectal pressure. Bush *et al.* [31] used a more realistic geometry by modeling the anorectal junction as a converging channel in the limit of purely plastic materials. In this asymptotic limit of the rheological behaviour of feces, the minimal pressure required to evacuate the feces is proportional to the yield stress [21] and a small change in the ratio of the diameters between the rectal ampulla and the anal canal can have a disproportionate effect on the flow resistance [21, 31]. Conversely, Yang *et al.* [24] considered that the flow of feces was solely governed by the rheology of the mucus layer and associated lubrication in a straight channel. This analysis was based on an observational study of defecation time across several animal species. To go beyond these speculations about the physical mechanisms that control rectal evacuation, we based our simulations on real anorectal kinetic data extracted from X-ray video defecographies and a full rheological model of the neostool. These simulations related pressure, stress and flow fields; these are fundamental quantities to understand flow phenomena and are impossible to obtain under physiological conditions with contemporary clinical investigation tests. Simulations give new insights into the fluid mechanics of human defecation, that we detailed below. Finally, we discuss how the assessment of pressure fields aid and guide the diagnosis of rectal evacuation disorders.

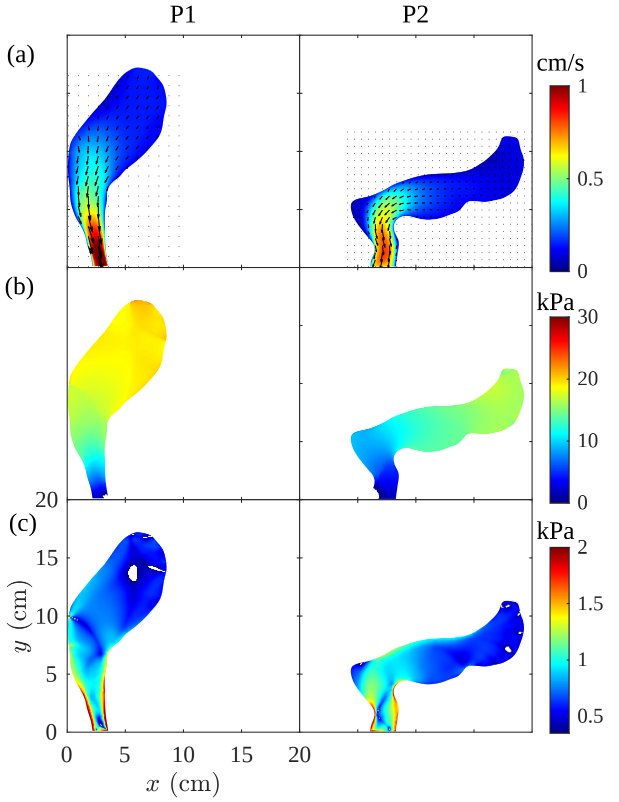

FIG. 5: Flow fields *(a)*, pressure fields *(b)* and viscous stress fields *(c)* of 2 pathologic evacuations when the mean outlet velocity of the neostool through the anal canal V_a was maximal. White color in *(c)* corresponds to regions where the viscous stress is lower than the yield stress of the neostool.

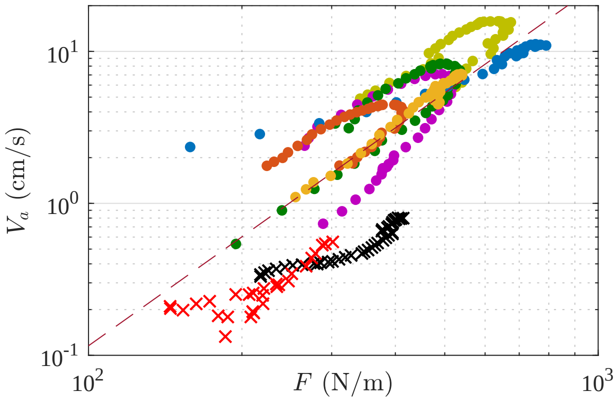

FIG. 6: Outlet velocity of the neostool through the anal canal V_a as a function of the force exerted by the rectum wall F for 6 normal (N1-N6, plain circles) and 2 pathologic (crosses and squares, P1-P2) evacuations. Dashed line is $V_a \sim F^{2.4}$.

A. Fluid dynamics of normal defecation

Simulations of normal defecation showed that the viscous stress was always much larger than the yield stress of the neostool in the anal canal and the anorectal junction, by a factor of almost 10, Fig. 3-c. Moreover, pressure drops were also significant in these anatomical regions and negligible in the rectal ampulla, Fig. 2-d and 3-b, c. Consequently, the flow of the neostool was restricted by the anorectal junction and the anal canal and governed by its shear-thinning properties, rather than by its yield stress. Indeed, the Bingham number Bn, which is the ratio of yield stress to viscous stress, was of the order of 0.1 for normal evacuations;

$$Bn = \frac{\tau_0}{k}\left(\frac{R_a}{V_a^{max}}\right)^n \tag{5}$$

The pressure gradient was about 10 kPa/cm in both anatomical parts, Fig. 2-d and 3-a. We calculated analytically the pressure loss associated with both anatomical parts by considering that the neostool behaves as a shear-thinning fluid (i.e. $\tau_{ij} = k\dot{\gamma}_{ij}^n$, Appendix D). Pressure losses were $\simeq$ 15 kPa and $\simeq$ 6 kPa for the anus and the anorectal junction, respectively. These values were consistent with our simulations, and confirmed that both anatomical parts had a significant role on pressure losses. However, we assumed a 2D flow in our calculations. Based on analytical solutions of pressure loss in asymmetric converging channel [32], we expect that the pressure was underestimated by a factor 2 to 4 in our simulations. A fully quantitative evaluation of hydrodynamic parameters requires three dimensional modeling. These findings confirm the relevance of the simplified representation of the rectum introduced by Bush *et al.* [21, 31], who modelled the recto-anal junction as a converging channel.

Because of the shear-thinning properties of the neostool and human feces [21, 33], the relationship between the outlet velocity through the anal canal V_a and the evacuation force F was strongly non-linear. Based on the analytical solutions given in Appendix D for shear-thinning fluids, we expected that $V_a \sim F^{1/n}$. Fig. 6 shows V_a as a function of F for the six normal patients. Although the ascending part of defecation did not overlap with the descending part as the geometry was changing, the data was well fitted with a power law with $1/n = 2.4$, in agreement with the rheological properties of the neostool. This strongly non-linear relationship has an important consequence: small variations in force (pressure) lead to large variations in flow. When the force was multiplied by 3, the flow rate increased by a factor 10. Another important consequence of the shear-thinning behaviour is the weak variations in the pressure loss with the ratio of diameter between the rectal ampulla and the anal canal ($F \sim 1 - (D_r/D_a)^{-3n}$ in 3D, [32]). For example, if the ratio D_r/D_a is increased from 2 to 6, the pressure loss is multiplied by 1.6. Conversely, in the regime dominated by the yield stress, i.e. low velocity and/or high yield stress ($Bn >>1$), F is very sensitive to the ratio of diameters ($F \sim \ln(D_r/D_a)$, [31]) and the pressure loss is multiplied by 2.5 if D_r/D_a increased from 2 to 6. As feces yield stress can be 22 times larger than the yield stress of the neostool [21], we can reasonably extrapolate that this asymptotic limit should be reached for hard feces, such as fecalom. In this case, the limiting factor would be the capacity of the anorectal musculature to dilate to a sufficient degree to allow defecation.

B. Towards a quantitative evaluation of pathophysiology of defecation

In the clinical practice, the prevalence of patients with functional and/or anatomical abnormalities is much higher than that of patients with normal defecography (85 vs. 15 %) [10]. We hypothesize that CFD modeling should help to find the origins of defecation disorders for patients showing anatomical and/or functional abnormalities, as it can measure simultaneously flow an pressure during defecation.

We illustrated how this data could be analyzed with two patients showing impaired defecations.

Patient P1, as a significant proportion of patients with impaired defecation [8, 9], had no well-defined anatomic disorders, Fig. 4-a. Simulated maximal pressure and forces were about 15 kPa and 300 N/m, almost twice smaller than in normal patients. Due to the non-linear pressure-flow relationship, the outlet velocity was 10 times lower than in normal patients. Red crosses in Fig. 6 show that this relationship for P1 followed the same power law than in normal patients at large forces ($F \sim V_a^{2.4}$) and was almost linear at small forces due to variations in the diameter of the anal canal. However, for the same F, V_a was twice smaller than in normal patients. This resulted from the fact that the anal canal was twice longer than for normal patients, and multiplying by 2 the pressure loss. The angle of the force was around 0 as the rectal ampulla and the anal canal were almost aligned. The Bingham number Bn was about 0.4, meaning that both the yield stress and the viscous effect control the dynamics of evacuation. This was also shown on the viscous stress field, which was of the same order of magnitude as the yield stress in the rectal ampulla and the anal canal. In conclusion, the main limited factor for this patient was an excessively weak applied pressure / force. This is in line with the concept of 'rectal akinesia'; the pathogenesis of which is a problem of rectal wall contractility [8, 9, 34]. Extending CFD simulations to video defecographies of patients showing impaired defecation in the absence of obvious obstructive phenomena should lead to a much better description of 'rectal akinesia'.

The second patient P2 did not present any obstructive phenomena, except an absence of variations in the anorectal angle which could be interpreted as a sign of anismus, also called dissynergic defecation. Anismus, a controversial topic [19, 35], is defined as inappropriate contraction of the pelvic floor during attempted evacuation. The fluid mechanics parameters extracted from the simulations are similar to those of patient P1: maximal pressure (15 kPa) and force (400 N/m) twice smaller than in normal patients, Fig. 4 and black squares in Fig. 6. For both pathologic cases, we did not observe hysteresis in Fig. 6, contrarily to normal cases. It could be attributed to the fact that the shape of the recto-anal junction changed little over the course of defecation. The pressure drop was clearly associated with the flow of the neostool through the bend anorectal junction, Fig. 5-b.

Consequently, the angle of the force was larger than for normal patients. However, as the pressure generated was smaller than in normal patients, we could postulate that the closed anorectal angle was not a cause of anorectal outlet obstruction. Thus, the existence of a dysfunction in the rectal wall contractility could be considered as a triggering factor of impaired defecation.

V. CONCLUSION

We introduced a fluid mechanics analysis of video defecography, which might be used to complete clinical investigations. Once applied to a large cohort of different types of patients, it should help physicians to better characterize the anorectal function and therefore, refresh our understanding of normal and pathologic defecation. In regard to the large overlap between functional and structural abnormalities in patients with defecation disorders [10], patient specific fluid mechanical simulations should help to identify the origin of these disorders. Specifically, they could help to identify reactoanal discoordination during excessive straining [36]. Finally, coupling medical imaging and complex fluid dynamics should contribute to a pathophysiological classification of evacuation disorders.

SUPPLEMENTAL MATERIALS

Digitized raw X-ray video defecographies for each patient are given in Supplemental Materials **DOI:** https://doi.org/10.6084/m9.figshare.c.6174462.v1.

ACKNOWLEDGMENTS

LRP is part of the LabEx Tec21 (ANR-11-LABX-0030) and of the PolyNat Carnot Institute (ANR-11-CARN-007-01). The authors thank Agence Nationale de la Recherche for its financial support of the TransportGut project, ANR-21-CE45-0015.

---

[1] P. T. Heitmann, P. F. Vollebregt, C. H. Knowles, P. J. Lunniss, P. G. Dinning, and S. M. Scott, Understanding the physiology of human defaecation and disorders of continence and evacuation, Nature Reviews Gastroenterology & Hepatology **18**, 751 (2021).

[2] A. E. Bharucha and S. S. Rao, An update on anorectal disorders for gastroenterologists, Gastroenterology **146**, 37 (2014).

[3] P. D. Higgins and J. F. Johanson, Epidemiology of constipation in north america: a systematic review, Official journal of the American College of Gastroenterology—ACG **99**, 750 (2004).

[4] I. Ditah, P. Devaki, H. N. Luma, C. Ditah, B. Njei, C. Jaiyeoba, A. Salami, C. Ditah, O. Ewelukwa, and L. Szarka, Prevalence, trends, and risk factors for fecal incontinence in united states adults, 2005–2010, Clinical Gastroenterology and Hepatology **12**, 636 (2014).

[5] S. Perry, C. Shaw, C. McGrother, R. Matthews, R. Assassa, H. Dallosso, K. Williams, K. Brittain, U. Azam, M. Clarke, *et al.*, Prevalence of faecal incontinence in adults aged 40 years or more living in the community, Gut **50**, 480 (2002).

[6] S. M. Scott and M. A. Gladman, Manometric, sensorimotor, and neurophysiologic evaluation of anorectal function, Gastroenterology clinics of North America **37**, 511 (2008).

[7] A. E. Bharucha and B. E. Lacy, Mechanisms, evaluation, and management of chronic constipation, Gastroenterology **158**, 1232 (2020).

[8] J.-L. Faucheron and A. Dubreuil, Rectal akinesia as a new cause of impaired defecation, Diseases of the colon & rectum **43**, 1545 (2000).

[9] C. Morandi, J. Martellucci, M. Genovese, and P. Torricelli, Defecographic functional evaluation of rectal akinesia, Techniques in coloproctology **19**, 437 (2015).

[10] U. Grossi, H. Heinrich, G. L. Di Tanna, S. A. Taylor, P. F. Vollebregt, C. H. Knowles, and S. M. Scott, Systematic characterization of defecographic abnormalities in a consecutive series of 827 patients with chronic constipation, Diseases of the Colon & Rectum **64**, 1385 (2021).

[11] E. V. Carrington, S. M. Scott, A. Bharucha, F. Mion, J. M. Remes-Troche, A. Malcolm, H. Heinrich, M. Fox, and S. S. Rao, Advances in the evaluation of anorectal function, Nature reviews Gastroenterology & hepatology **15**, 309 (2018).

[12] S. Palit, N. Thin, C. H. Knowles, P. J. Lunniss, A. E. Bharucha, and S. M. Scott, Diagnostic disagreement between tests of evacuatory function: a prospective study of 100 constipated patients, Neurogastroenterology & Motility **28**, 1589 (2016).

[13] B. Deb, M. Sharma, J. G. Fletcher, S. G. Srinivasan, A. Chronopoulou, J. Chen, K. R. Bailey, K. J. Feuerhak, and A. E. Bharucha, Inadequate rectal pressure and insufficient relaxation and abdominopelvic coordination in defecatory disorders, Gastroenterology **162**, 1111 (2022).

[14] K. Futaba, S.-C. Chen, W. W. Leung, C. Wong, T. Mak, S. Ng, and H. Gregersen, Fecobionics characterization of female patients with fecal incontinence, Scientific reports **12**, 10602 (2022).

[15] H. Gregersen, K. Krogh, and D. Liao, Fecobionics: integrating anorectal function measurements, Clinical Gastroenterology and Hepatology **16**, 981 (2018).

[16] S. Palit, C. Bhan, P. Lunniss, D. Boyle, M. Gladman, C. Knowles, and S. Scott, Evacuation proctography: a reappraisal of normal variability, Colorectal Disease **16**, 538 (2014).

[17] A. Zbar, M. Guo, and M. Pescatori, Anorectal morphology and function: analysis of the shafik legacy, Techniques in coloproctology **12**, 191 (2008).

[18] R. Lentle and P. Janssen, Physical characteristics of digesta and their influence on flow and mixing in the mam-

malian intestine: a review, Journal of Comparative Physiology B **178**, 673 (2008).

[19] W. Schouten, J. Briel, J. Auwerda, J. Van Dam, M. Gosselink, A. Ginai, and W. Hop, Anismus: fact or fiction?, Diseases of the colon & rectum **40**, 1033 (1997).

[20] N. J. Balmforth, I. A. Frigaard, and G. Ovarlez, Yielding to stress: recent developments in viscoplastic fluid mechanics, Annual Review of Fluid Mechanics **46**, 121 (2014).

[21] C. De Loubens, A. Dubreuil, R. Lentle, N. Kissi, and J.-L. Faucheron, Rheology of human faeces and pathophysiology of defaecation, Techniques in Coloproctology (2020).

[22] P. Patel, B. Picologlou, and P. Lykoudis, Biorheological aspects of colonic activity, Biorheology **10**, 441 (1973).

[23] S. Woolley, R. Cottingham, J. Pocock, and C. Buckley, Shear rheological properties of fresh human faeces with different moisture content, Water sa **40**, 273 (2014).

[24] P. Yang, M. Lamarca, C. Kaminski, D. Chu, and D. Hu, Hydrodynamics of defecation., Soft matter **13 29**, 4960 (2017).

[25] P. Mahieu, J. Pringot, and P. Bodart, Defecography: I. description of a new procedure and results in normal patients, Gastrointestinal radiology **9**, 247 (1984).

[26] J. Faucheron, S. Barot, D. Collomb, N. Hohn, D. Anglade, and A. Dubreuil, Dynamic cystocolpoproctography is superior to functional pelvic magnetic resonance imaging in the diagnosis of posterior pelvic floor disorders: results of a prospective study, Colorectal Dis **16**, 240 (2014).

[27] V. Ratz, T. Wech, A. Schindele, A. Dierks, A. Sauer, J. Reibetanz, A. Borzi, T. Bley, and H. Köstler, Dynamic 3d mr-defecography, in *RöFo-Fortschritte auf dem Gebiet der Röntgenstrahlen und der bildgebenden Verfahren*, Vol. 188 (© Georg Thieme Verlag KG, 2016) pp. 859–863.

[28] E. V. Carrington, A. Brokjaer, H. Craven, N. Zarate, E. Horrocks, S. Palit, W. Jackson, G. Duthie, C. Knowles, P. Lunniss, *et al.*, Traditional measures of normal anal sphincter function using high-resolution anorectal manometry (hram) in 115 healthy volunteers, Neurogastroenterology & Motility **26**, 625 (2014).

[29] A. Farag, Use of the hagen-poiseuille law: A new mathematical approach for the integration and evaluation of anorectal physiological testing in patients with faecal incontinence and pelvic dyschezia and in normal controls, European Surgical Research **30**, 279 (1998).

[30] A. Farag, The use of flow equation in functional coloproctology: a new theory in anorectal physiology (2009).

[31] M. Bush, P. Petros, M. Swash, M. Fernandez, and A. Gunnemann, Defecation 2: Internal anorectal resistance is a critical factor in defecatory disorders, Techniques in coloproctology **16** (2012).

[32] R. Lenk, Pressure drop through tapered dies, Journal of Applied Polymer Science **22**, 1775 (1978).

[33] R. Penn, B. J. Ward, L. Strande, and M. Maurer, Review of synthetic human faeces and faecal sludge for sanitation and wastewater research, Water research **132**, 222 (2018).

[34] R. L. Grotz, J. H. Pembérton, K. E. Levin, A. M. Bell, and R. B. Hanson, Rectal wall contractility in healthy subjects and in patients with chronic severe constipation., Annals of surgery **218**, 761 (1993).

[35] L. Gottesman, Anismus through surgical eyes, Diseases of the Colon & Rectum **65**, 137 (2022).

[36] A. Picciariello, P. O'Connell, D. Hahnloser, G. Gallo, A. Munoz-Duyos, O. Schwandner, P. Sileri, G. Milito, S. Riss, P. Boccasanta, *et al.*, Obstructed defaecation syndrome: European consensus guidelines on the surgical management, British Journal of Surgery **108**, 1149 (2021).

[37] S. Chaussade, A. Khyari, H. Roche, M. Garret, M. Gaudric, D. Couturier, and J. Guerre, Determination of total and segmental colonic transit time in constipated patients: results in 91 patients with a new simplified method, Digestive diseases and sciences **34**, 1168 (1989).

[38] I. Ginzburg, F. Verhaeghe, and D. d'Humieres, Two-relaxation-time lattice boltzmann scheme: About parametrization, velocity, pressure and mixed boundary conditions, Communications in computational physics **3**, 427 (2008).

[39] D. Rui and B.-c. Shi, Incompressible multi-relaxation-time lattice boltzmann model in 3-d space, Journal of Hydrodynamics, Ser. B **22**, 782 (2010).

[40] L. Talon and D. Bauer, On the determination of a generalized darcy equation for yield-stress fluid in porous media using a lattice-boltzmann trt scheme, The European Physical Journal E **36**, 139 (2013).

[41] T. Papanastasiou and A. Boudouvis, Flows of viscoplastic materials: models and computations, Computers & Structures **64**, 677 (1997).

[42] D. d'Humières and I. Ginzburg, Viscosity independent numerical errors for lattice boltzmann models: From recurrence equations to "magic" collision numbers, Computers & Mathematics with Applications **58**, 823 (2009).

[43] S. Gsell, U. D'Ortona, and J. Favier, Lattice-boltzmann simulation of creeping generalized newtonian flows: Theory and guidelines, Journal of Computational Physics , 109943 (2020).

[44] P. Lallemand and L.-S. Luo, Lattice boltzmann method for moving boundaries. j comput phys 184(2): 406-421, Journal of Computational Physics **184**, 406 (2003).

[45] S. Gsell, U. d'Ortona, and J. Favier, Lattice-boltzmann simulation of creeping generalized newtonian flows: theory and guidelines, Journal of Computational Physics **429**, 109943 (2021).

[46] Y. Wang, J. G. Brasseur, G. G. Banco, A. G. Webb, A. C. Ailiani, and T. Neuberger, Development of a lattice-boltzmann method for multiscale transport and absorption with application to intestinal function, Computational modeling in biomechanics , 69 (2010).

Appendix A: Video defecographies

All the patients with normal radiologic evacuation had no particular severe medical or surgical history except a nervous breakdown treated by anti-depressive drugs in a female patient aged 67 who also had anal incontinence, a hysterectomy for benign disease in a patient aged 64, and an anal incontinence in a female patient aged 61. These 6 patients presented with transit time constipation confirmed by a transit time examination [37] that responded to laxatives in 4 days; and all were referred to the radiologist (AD) for suspicion of pelvic floor disorder because they complained from dyschesia that responded to suppositories, enemas, and/or digital maneuvers for rectal evacuation. At that time, no specific obstructive defecation syndrome had been published [36].

Two further patients (one female and one male) with no particular past medical or surgical history presented with absence of pelvic organ deformity during defecation, but were suspected to suffer from rectal akinesia [26] in one and anismus (also called recto-anal dyssynergia) in the other [19].

Appendix B: Video processing

X-ray analog images (HI-8) were first digitized using VLC media player software and then processed with the Image Processing Toolbox of Matlab R2019b (Mathworks). The boundaries of the rectum and the anus were manually segmented with at least 40 points for each image. The coordinates of the boundary were interpolated with a Piecewise Cubic Hermite Interpolating Polynomial (PCHIP) method to increase the spatial resolution. Boundary nodes with equal arc-length distance were sampled from the interpolated boundary. The coordinates of these extracted nodes were spatially and temporally smoothed with a 2D Gaussian filter. This step permitted also to remove mass movements of the rectum when the patient was moving. The smoothed set of data was linearly interpolated for subsequent CFD simulations and differentiateed to deduce the velocity of each node of the boundary. In order to validate the image processing algorithm, for each patient, the variations in the surface area bounded by the smoothed boundaries were compared to the one bounded by the raw data, Fig. 1-e.

Appendix C: Lattice-Boltzmann methods

D2Q9 incompressible BGK lattice-Boltzmann methods with two relaxation times were used to simulate the creeping flow of a yield stress fluid with the Herschel-Bulkley constitutive equation during rectal emptying [38–40]. The nine discrete velocities are defined by,

$$\mathbf{e}_\alpha = (0,0)\,, \text{ for } \alpha = 0$$

$$\mathbf{e}_\alpha = (\pm c, 0)\,, (0, \pm c)\,, \text{ for } \alpha = 1-4$$

$$\mathbf{e}_\alpha = (\pm c, \pm c)\,, (\pm c, \pm c)\,, \text{ for } \alpha = 5-8$$

where $c = \Delta x/\Delta t$, Δx and Δt are the lattice grid spacing and lattice time step respectively. The evolution equation of the model is divided into two steps, the propagation,

$$f_\alpha\left(\mathbf{x} + \mathbf{e}_\alpha \Delta t, t + \Delta t\right) = \hat{f}_\alpha$$

and the collision,

$$\begin{aligned}\hat{f}_\alpha\left(\mathbf{x}, t\right) = {} & \frac{1}{\tau_+}\left[f_\alpha^+\left(\mathbf{x}, t\right) - f_\alpha^{+,eq}\left(\mathbf{x}, t\right)\right] \\ & + \frac{1}{\tau_-}\left[f_\alpha^-\left(\mathbf{x}, t\right) - f_\alpha^{-,eq}\left(\mathbf{x}, t\right)\right]\end{aligned}$$

$$f_\alpha^+ = \frac{1}{2}\left(f_\alpha + f_{\bar{\alpha}}\right), \, f_\alpha^- = \frac{1}{2}\left(f_\alpha - f_{\bar{\alpha}}\right)$$

$$f_\alpha^{+,eq} = \frac{1}{2}\left(f_\alpha^{eq} + f_{\bar{\alpha}}^{eq}\right), \, f_\alpha^{-,eq} = \frac{1}{2}\left(f_\alpha^{eq} - f_{\bar{\alpha}}^{eq}\right)$$

where f_α is the density distribution function, f_α^{eq} is the equilibrium distribution function, symbols '+' and '−' refer to the symmetric and anti-symmetric part of both functions, $\bar{\alpha}$ is the opposite direction to α (i.e $\mathbf{e}_\alpha = -\mathbf{e}_{\bar{\alpha}}$), τ_+ and τ_- are the two relaxation parameters, $\hat{f}$ is the density distribution function after collision and before propagation. f_α^{eq} is defined as

$$f_\alpha^{eq} = \begin{cases} 1 - (1-\omega_0)\frac{p}{c_s^2} + s_0(u), & \alpha = 0 \\ \omega_\alpha \frac{p}{c_s^2} + s_\alpha(\mathbf{u}), & \alpha = 1-8 \end{cases}$$

where $s_\alpha(\mathbf{u}) = 3\omega_\alpha e_\alpha \cdot \mathbf{u}$, for Stokes flow, $c_s = 1/\sqrt{3}$ is the speed of sound. The weight coefficients are given by

$$w_\alpha = \begin{cases} 4/9, & \alpha = 0 \\ 1/9, & \alpha = 1,2,3,4 \\ 1/36, & \alpha = 5,6,7,8 \end{cases}$$

The macroscopic flow velocity and pressure are computed from the distribution functions,

$$\mathbf{u} = \sum_{\alpha=1}^{8} e_\alpha f_\alpha$$

$$p = \frac{c_s^2}{1-\omega_0}\left[\sum_{\alpha=1}^{8} f_\alpha + s_0(\mathbf{u})\right]$$

The rate-of-strain ($\dot{\gamma}_{ij}$) tensor is given by

$$\dot{\gamma}_{ij} = -\frac{1}{2c_s^2\tau_+\Delta t}\sum_{i=0}^{18}\mathbf{e}_{i\alpha}\mathbf{e}_{i\beta}\left[f_i^+\left(\mathbf{x}, t\right) - f_i^{+,eq}\left(\mathbf{x}, t\right)\right]$$

The local viscosity was calculated with the Papanastasiou regularization of the Herschel-Bulkley consitutive equation by [40, 41]

$$\eta = \frac{\tau_0}{|\dot{\gamma}|}\left[1 - \exp\left(-m|\dot{\gamma}|\right)\right] + k|\dot{\gamma}|^{n-1}$$

where $|\dot{\gamma}| = \sqrt{\dot{\gamma}_{ij}\dot{\gamma}_{ij}}$ is the second invariant of the rate-of-strain tensor and m the regularization coefficient. The symmetric relaxation time (τ_+) was calculated using

$$\tau_+ = \frac{6\eta + 1}{2}$$

The anti-symmetric relaxation parameter is defined by

$$\tau_- = \frac{\Lambda}{\tau_+ - 0.5} + 0.5$$

where Λ is the magic collision parameter and taken to 1/4 in order to optimize the accuracy of the numerical scheme [42]. The TRT-LBM scheme was used as it is superior to the standard single relaxation time LBM scheme because it avoids strong numerical errors for non-Newtonian flows with large variations in viscosity [40, 43].

No-slip and moving boundary conditions were treated with a combination of the bounce-back scheme and the transfer of momentum to the fluid due the velocity of moving boundary ($\mathbf{u_w}$), see [44] for details. Outlet velocity was also imposed at the end of the anus. For each time step, the mean flow rate was known from image analysis and the flow profile was given by the analytical solution of the 2D Poiseuille flow for a Herschel-Bulkley fluid [40].

To solve the flow, we used the time-independent property of Stokes flow equations (Eq. 2) to speed-up the algorithm. For each movie, the time sequence of rectal emptying was divided into 40 time steps. For each time step, the corresponding boundary conditions were applied. The collision and streaming operations were computed. The local effective viscosity was updated. The iteration was pursued until convergence of the flow field was reached. It was repeated for each of the 40 time steps.

This methodology was already validated to solve flow of yield stress fluids [40, 45]. We validated the code with benchmarks, such as Poiseuille flow [40] or flow past a fixed/moving cylinder [46]. The grid to solve the flow consisted of about 4000 lattices. The value of m was chosen after preliminary tests and is a compromise between precision and speed of convergence. Excessively low values of m result in poor consideration of yield stress effects in the simulation, while excessively high values result in the code taking too long to converge.

Appendix D: Pressure loss in simplified geometries

Analytical solutions used to calculate the pressure loss for shear-thinning fluids in a 2D converging channel and in a straight channel were developed by Lenk [32] which read

$$\Delta P1 = \frac{k \cot\theta}{n} \left(Q\left(4n+2\right)\right)^n H_2^{-2n} \left[1 - \left(\frac{H_1}{H_2}\right)^{-2n}\right]$$

for the converging channel, where θ is the vertical taper angle, Q is the flow rate, H_1 and H_2 are the width at inlet and outlet of the converging channel and

$$\Delta P2 = \frac{2Lk}{h^{2n+1}} \left(Q\frac{4n+2}{n}\right)^n$$

for the straight channel, with h its width. Note that the analytical solution for the converging channel is valid for small angles θ ($< 15°$) and we extrapolated the formula to a larger angle ($45°$) so as to calculate orders of magnitude of pressure loss in the anorectal junction.

3.4 Application to Patients Showing Anatomical Abnormalities

3.4.1 Introduction

In the previous Section 3.3, we utilized the patient-specific 2D model 6 normal and 2 pathologic patients in the absence of anatomical abnormalities. We found that the magnitude of the pressure and the evacuation force in the case of normal patients was twice as high as that of pathological patients. The spatiotemporal (ST) mapping of the anorectal cavity of the normal patients also showed two times more positive pressure gradient than pathologic patients. In regard to the relationship between evacuation force and feces neostool outlet velocity curve, we observed hysteresis in the curve only for normal patients.

This section is again an extension of the model where we look into the cases of five patients with obvious anatomical obstructive phenomena. The influence of a rectocele on defecation and how the size of the rectocele can affect rectal function are subjects of investigation. Each patient will be discussed individually by presenting their results. In the discussion section, we will integrate all the results and highlight the differences between them.

Among obstructive phenomena, rectocele is a common condition in women where the anterior rectal wall herniates into the vaginal lumen. Rectoceles are an indication of structural deficits, such as weakening of the pelvic floor, particularly the perineal body. They can also result in pelvic floor dysfunction, leading to excessive straining and difficulty with rectal evacuation during defecation [53]. It can be present not only in women with pelvic floor disorders but also in asymptomatic individuals [109]. In a clinical study of 505 women, two groups [29, 109] found that rectocele formation is linked with preexisting pelvic floor disorders. Patients with symptomatic rectoceles often experience a continuous urge to defecate, leading to chronic straining and a feeling of incomplete evacuation. In some cases, patients may even need to remove feces manually. While most patients have a daily bowel movement, infrequent defecation is a common symptom. Large rectoceles (> 4 cm) and retention of contrast in the rectocele during defecography are frequently observed in patients with symptomatic rectoceles [109]. Therefore, defecography has been considered the "gold standard" for diagnosing rectocele since the beginning of the diagnosis of defecation-related disorders. Structural abnormalities, such as intussusception, excessive perineal descent, and obstructing rectoceles, are secondary causes of constipation in many patients [99].

Therefore, our interest was also to include structural abnormality of the rectum and then analyze the behavior of flow parameters, which will again give more information to the physicians to investigate and classify defecation disorders.

3.4.2 Materials and methods

We analyzed 5 defecography videos of patients with diagnosed structural abnormalities that were clearly visible during rectal examination conducted by the coloproctologist (as shown in Fig. 3.1). Additionally, we utilized the same 2D patient-specific fluid model that was applied in Paper 1 and Paper 2.

3.4.3 Results

The six patients showed obvious abnormal geometry in the form of rectocele in the defecography videos. The rectum with rectocele can be seen in Figures 3.2 3.3 3.4 a,b, with almost equal diameters ($D_a = 2 \pm 0.5$ cm) throughout the defecation period with different maximum mean outlet velocity ($V_a^{max} = 8.3 \pm 5$ cm/s). The figures also showed the evolution of the rectum boundary over time with the magnitude of the wall normal stress (WNS). Moreover, it was worth noting that at the end of defecation, the maximum value of WNS changed from the right proximal of the rectum to the left proximal, whereas the evacuation force showed a bell

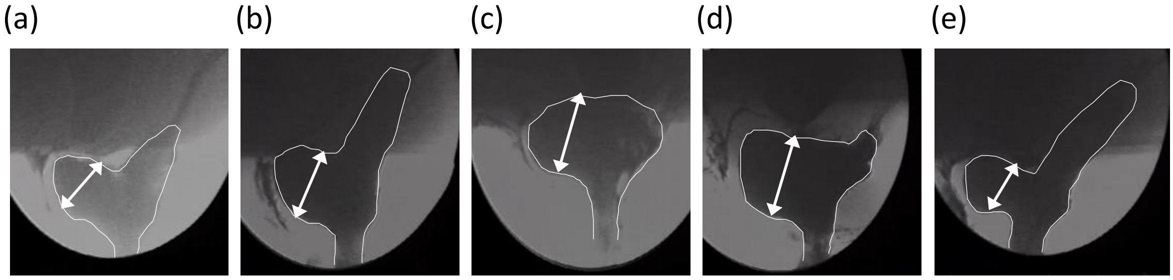

FIGURE 3.1: (a–e) Examples of one of the frames from X–ray defecography videos of 5 patients. The arrows in the left parts correspond to the rectocele and the white curves show the rectum boundaries. Length of the rectoceles from left to right 4.24 cm, 5.18 cm, 5.35 cm, 5.86 cm, 3.7 cm.

shape except for patient 1, and its angle underwent a change in value from positive degrees to negative degrees (Figures 3.2 3.3 3.4a,c).

At the maximum mean outlet velocity (V_a), the flow field in the fields diagram was directed towards the anal canal, with the exception of another direction formed due to the presence of the rectocele at the left part of the rectum, Figures 3.2 3.3 3.4d. The pressure field in the rectal ampulla was homogeneous, but there was a significant pressure drop between the anorectal junction and the anal canal, as shown in Figures 3.2 3.3 3.4 e, from 30 to 10 kPa for patient 1 and 20 to 10 kPa for other four patients. The stress field from Figures 3.2 3.3 3.4 e showed that the viscous stress was localized at the anal canal, with a maximum value of 5 kPa. The blue area in these figures indicated that the neostool formed a plaque because it had a stress level equal to its yield stress (350 Pa), which led to plaque flow.

The values of the WNS, pressure, and stress were almost two times higher for patient 1 than the other four patients. It can also be seen from Figures 3.2 3.3 3.4 b,c that the force and velocity were low at the end of defecation. In fact, the force was not sustained after half of the defecation time when formation of the rectoceles took place. Consequently, the angle of the force also varied around 100 ° between positive and negative values. Moreover, the stress field showed that the neostool stress was near to the yield stress ($\tau_0 = 350$) kPa which meant that the neostool was not moving as there was no deformation. That led to incomplete defecation, 10 %, 20 %, 15 %, and 10 % neostool residue for patient 2, patient 3, patient 4, and patient 5 respectively.

Patient 4 showed very small WNS (maximum 12 kPa), viscous stress almost equal to the yield stress (τ_0), and the presence of a big rectocele (5.86 cm), with two peaks in force versus time curve, Figures 3.3 a,c,e. After 10 s of defecation time, the patient had to use her finger to do a vaginal maneuver in order to push the remaining neostool from the rectocele. This suggested that she was experiencing difficulty with the normal process of defecation and the bigger rectocele (> 5.5 cm) was not active by itself in her case.

3.4.4 Discussions

Analysis of the wall normal stress (WNS) and force-time diagrams in patients with rectocele revealed significantly lower magnitudes of WNS and force, including a secondary velocity direction, compared to patients without rectocele. Notably, during defecation, patients with rectocele exhibited force variation that peaked but was not sustained throughout the entire process, ultimately leading to incomplete expulsion of stool. Additionally, these patients demonstrated significantly wider angles (-100° to 100°) throughout the defecation process, indicating the directional change of the force due to the rectocele.

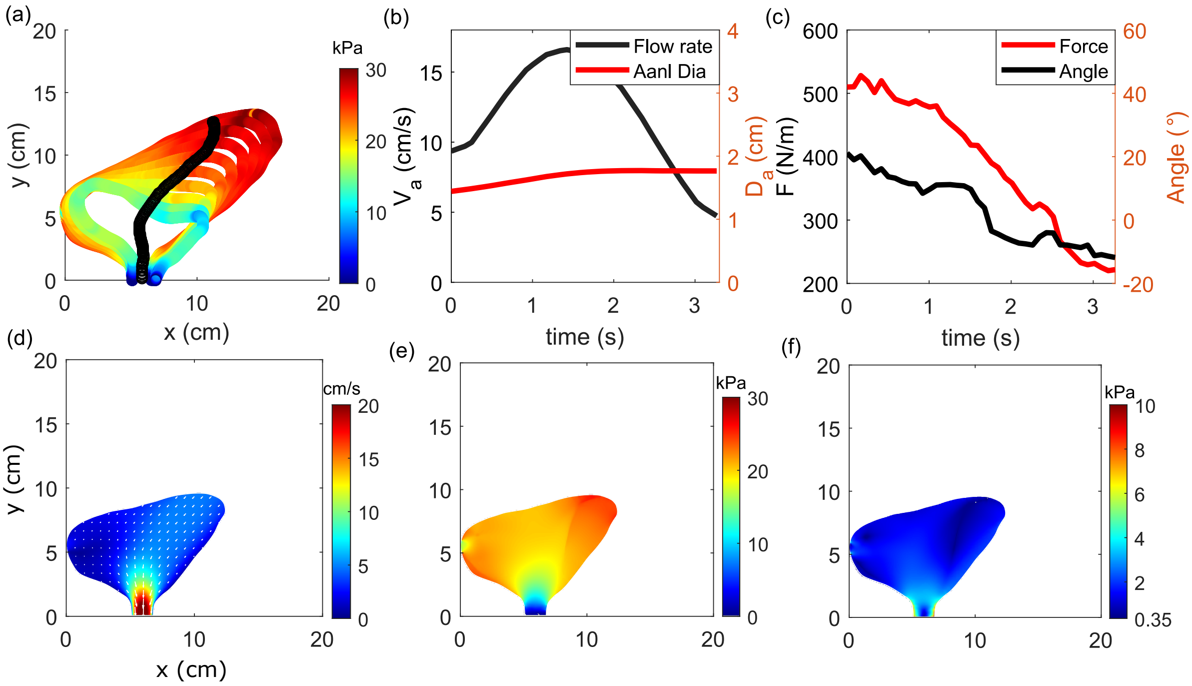

(A) Patient 1

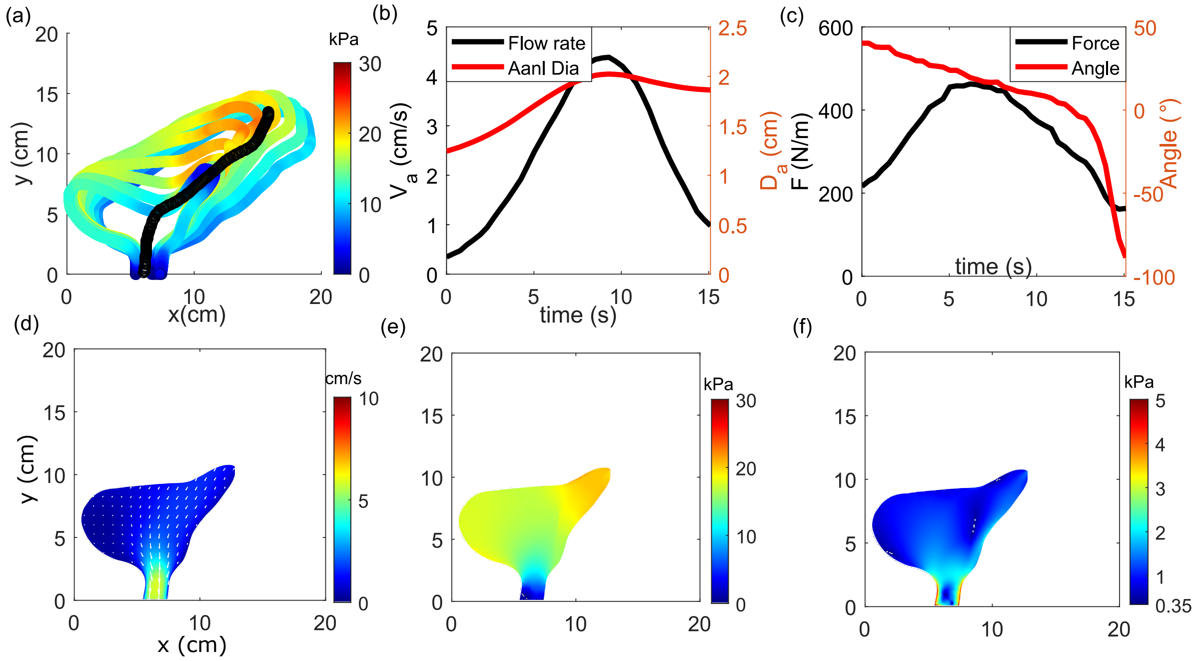

(B) Patient 2

Figure 3.2: (a) Evolution of the boundaries of the rectum during the evacuation of the neostool. The colour code shows the magnitude of the WNS. (b) Mean outlet velocity of the neostool through the anal canal (V_a) (black curve, left axis) and diameter of the anal canal D_a (red curve, right axis) as a function of time. (c) The evacuation force F (red curve, left axis) and its angle with the y-axis (black curve, right axis) as a function of time. Flow fields (d), pressure fields (e), and viscous stress fields (f) when the mean outlet velocity of the neostool through the anal canal (V_a) was maximal. Dark blue colour in (f) corresponds to regions where the viscous stress is lower than the yield stress of the neostool.

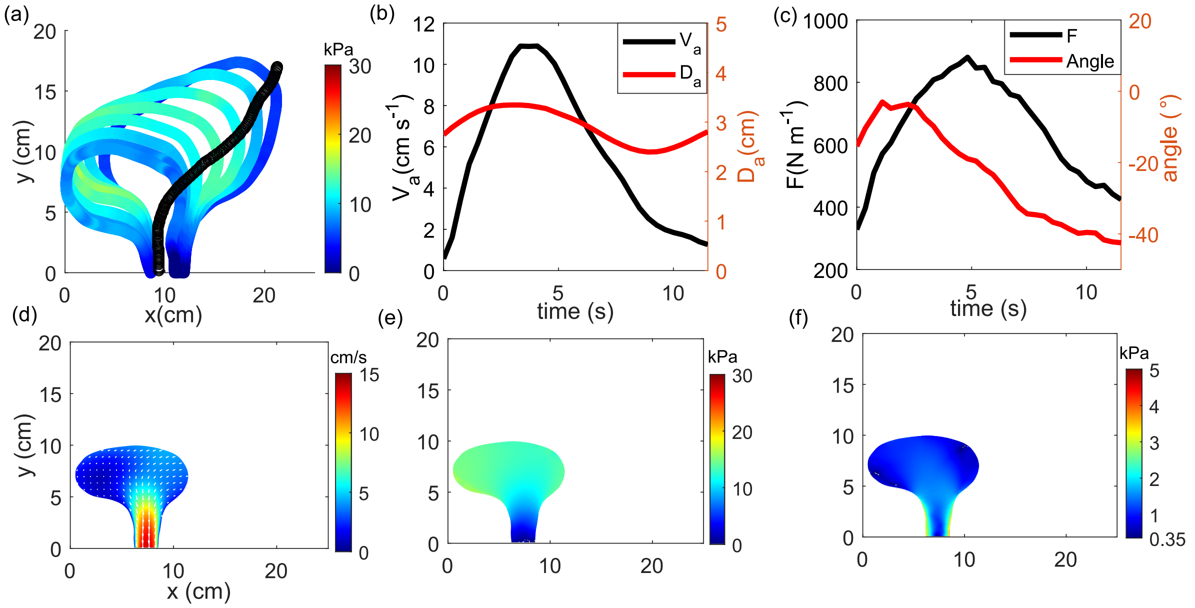

(A) Patient 3

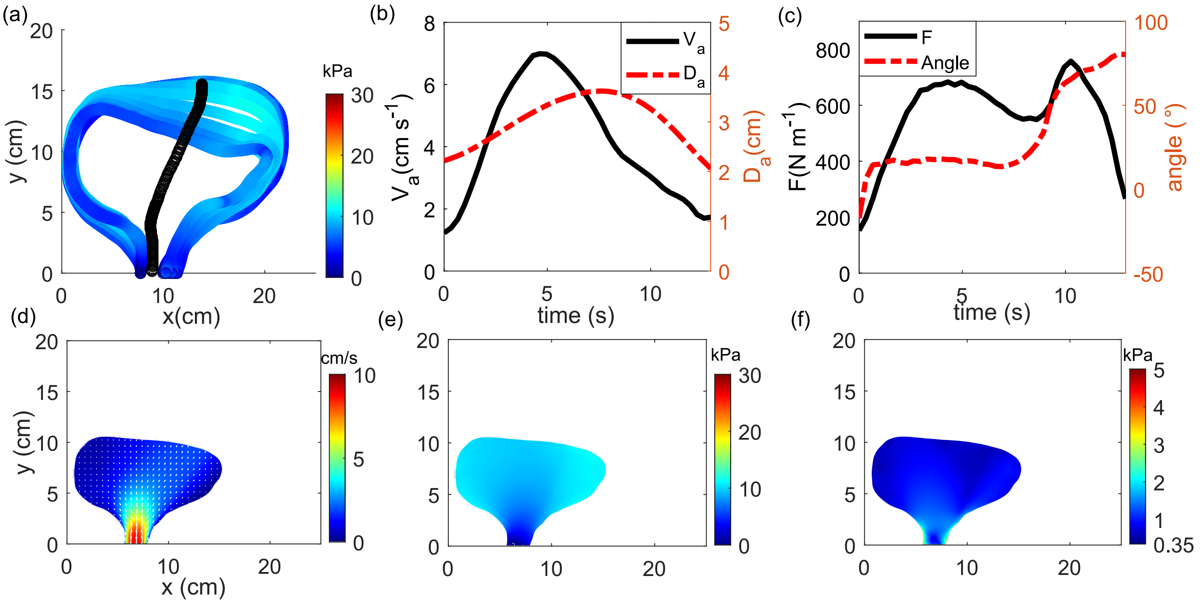

(B) Patient 4

FIGURE 3.3: (a) Evolution of the boundaries of the rectum during the evacuation of the neostool. The colour code shows the magnitude of the WNS. (b) Mean outlet velocity of the neostool through the anal canal (V_a) (black curve, left axis) and diameter of the anal canal D_a (red curve, right axis) as a function of time. (c) The evacuation force F (red curve, left axis) and its angle with the y-axis (black curve, right axis) as a function of time. Flow fields (d), pressure fields (e), and viscous stress fields (f) when the mean outlet velocity of the neostool through the anal canal (V_a) was maximal. Dark blue colour in (f) corresponds to regions where the viscous stress is lower than the yield stress of the neostool.

The organization of the pressure fields was similar to that of normal patients, although its amplitude was three−fourth (patients 1 and 2) or half lower (patients 3,4 and 5), Figures 3.2-3.4e. In the anal canal, the maximum viscous stress (5 kPa) was also lower than the normal evacuations and near to yeild stress (τ_0), Figures 3.2-3.4f.

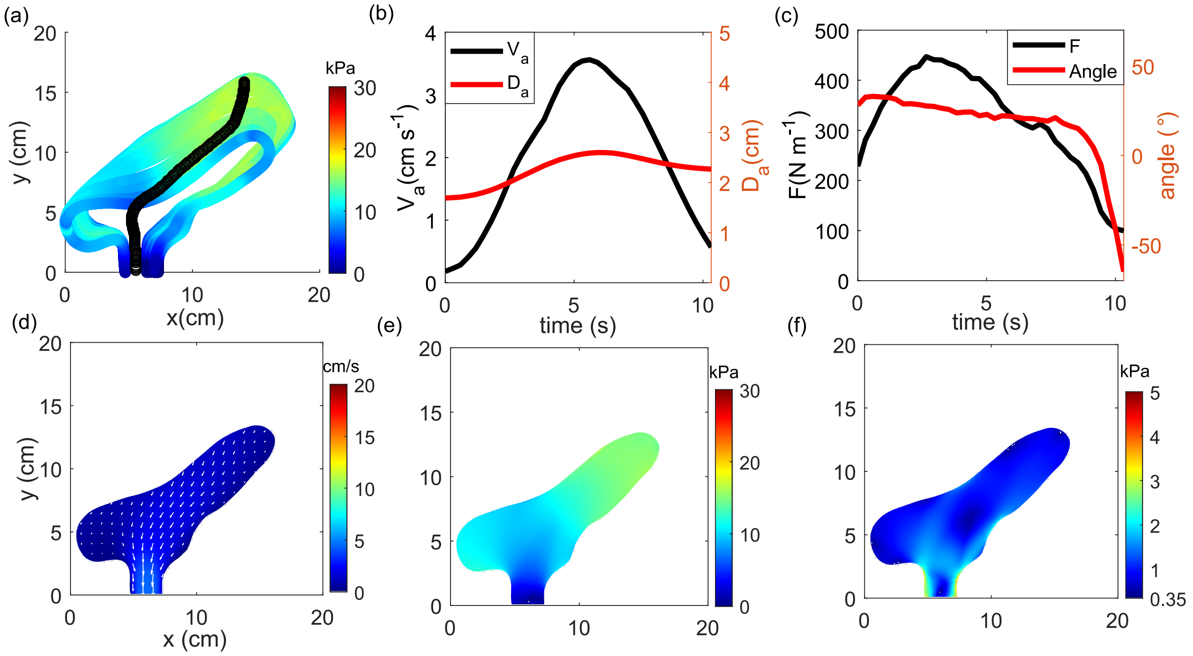

Figure 3.4: (a) Evolution of the boundaries of the rectum during the evacuation of the neostool for patient 5. The colour code shows the magnitude of the WNS. (b) Mean outlet velocity of the neostool through the anal canal (V_a) (black curve, left axis) and diameter of the anal canal D_a (red curve, right axis) as a function of time. (c) The evacuation force F (red curve, left axis) and its angle with the y-axis (black curve, right axis) as a function of time. Flow fields (d), pressure fields (e), and viscous stress fields (f) when the mean outlet velocity of the neostool through the anal canal (V_a) was maximal. Dark blue colour in (f) corresponds to regions where the viscous stress is lower than the yield stress of the neostool.

Figures 3.5a-d show the spatiotemporal evolution of pressure along the midline (black line in Figures 3.2-3.4a). In space, the pressure was homogeneous with maximum values ranging between approximately 12 and 25 kPa at the rectal ampulla, consistent with previous rectal manometry values [21, 46]. With time, the pressure was only maximum at the beginning for patient 1 (Fig. 3.5a) and propagated towards the anorectal junction. However, for the other 4 patients, the pressure increased around half of the defecation time and then decreased.

Similar to normal defecation, the flow of neostool was also limited by the anorectal junction and the anal canal, and influenced by its shear-thinning properties rather than its yield stress. The Bingham number (Bn), which represents the ratio of yield stress to viscous stress, was found to be on the order of 0.1 during the defecation of neostool. The simulated forces during neostool defecation were found to be approximately 700 N/m, which was similar to that of normal patients, with patients 4 and 5 exhibiting a wider range of forces, shown in Fig.3.5f. Just before the end of defecation, we observed that the evacuation force was half of the normal defecation for patients with rectocele and they were not able to maintain the same level of force during defecation. Due to the non-linear pressure-flow relationship, the outlet velocity was nearly two times lower than that of normal patients. The diamond markers in Fig. 3.5 f demonstrate that this relationship followed the same power law as normal patients at large forces ($V \approx F^{2.4}$). This implies that when the force was decreased after half of the defecation time, the outlet velocity decreased more than two times, resulting in a blockage of the neostool flow. Unlike normal patients, the ascending and descending parts of the velocity-force curve did not overlap due to changes in the rectum geometry. The angle of the force was around

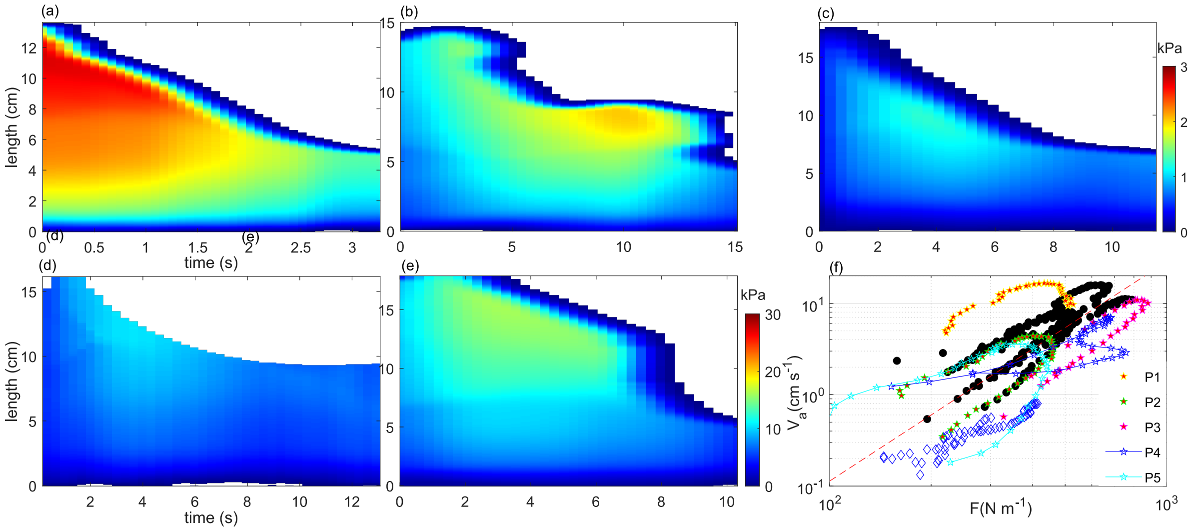

FIGURE 3.5: (a to e) Spatio-temporal map of the pressure variation along the length of a mid-line going from the anal canal (0 cm) to the proximal end at time 0 (black lines in Figures (3.2,3.3,3.4)a. (f) Outlet velocity of the neostool through the anal canal V_a as a function of the force exerted by the rectum wall F for 6 normal (black circles), 2 pathologic (blue squares), and 5 structural abnormal (legends are mentioned with five different colours) evacuations. Dashed line is $V_a \sim F^{2.4}$

30° and remained constant, similar to normal patients, but exhibited a range of -70° to 50° just before the end of defecation, indicating an additional force vector caused by the secondary pressure gradient at the rectoceles. This demonstrated that rectocele was not entirely passive, as it was unable to generate enough force to prevent its deformation when the rectal wall was under pressure. However, in the case of patient 4, a manual maneuver was needed to defecate the remaining neostool, indicating that the rectocele is not active in all cases. This could potentially be attributed to the size of the rectocele, which measured 5.86 cm for patient 4.

3.4.5 Conclusions

The 2D simulation model provides a valuable tool for understanding the mechanics of defecation in patients with rectoceles and identifying the underlying causes of their symptoms. We observed that the size of the rectocele influenced the degree of defecation (% residue of neostool). In most rectocele cases, the magnitude of evacuation force (600 N/m) resembled that of normal defecation, but it was not sustained. Due to the shear-thinning properties of the fluid flow in the rectum (neostool), resulting in a non−linear relationship between the outlet velocity of neostool and the evacuation force ($V \approx F^{2.4}$). Consequently, there was a very small outlet velocity before the end of defecation, leading to incomplete evacuation. Additionally, unlike in normal patients, the ascending and descending portions of the velocity−force curve did not overlap due to changes in rectal geometry.

Moreover, angle of the evacuation force with the vertical axis during defecation remained constant at around 30 °, similar to normal patients. However, just before the end of defecation, there was a range of -70 ° to 50 °, indicating an additional force vector caused by the secondary pressure gradient at the rectoceles. This demonstrated that rectoceles were not entirely passive, as they were unable to generate sufficient force to prevent deformation when the rectal wall was under pressure. Additionally, the pressure and wall normal stress (WNS) diagrams exhibited magnitudes approximately half (15 kPa) of those observed in normal cases (30 kPa).

Rectoceles can be categorized as active or passive, depending on their size. They were not solely morphological issues resulting from weakened pelvic floor muscles and connective tissues, but also functional problems that can disrupt the normal functioning of the pelvic floor muscles and lead to difficulties in achieving effective bowel movements. These findings were consistent with studies that have shown that patients with rectoceles may experience impaired rectal emptying due to the obstructive effect of the prolapse [53, 54].

By utilizing the additional information acquired from the simulation model, healthcare providers can assess the efficacy of various treatment strategies [114] and make informed decisions regarding the choice of therapy for patients with rectocele. Ultimately, this model can prove to be a valuable tool in the management of patients experiencing defecation disorders, including those with anatomical abnormalities.

3.5 Summary

Overall Summary

We developed a patient-specific two−dimensional CFD model of rectal evacuation for 6 normal patients, 2 patients with weak muscle problems, and 5 patients with structural abnormalities. The main aim of the model was to be able to simulate the pressure and velocity of the rectum in physiological conditions such as the geometry of the rectum obtained from the video defecography made using neostool which has the same rheology as the normal feces (yield stress fluid). This approach allowed us to study the mechanics of defecation in a realistic and patient-specific manner, providing valuable insights into the underlying causes of defecation disorders.

- In Section 3.2, We developed a 2D model and concluded its success in simulating rheological fluid flow in the complex rectum geometry. New insights emerged regarding crucial parameters (feces outlet velocity, pressure, and force) that varied with defecation period and location in the rectum. Thus, extending this model to a larger cohort is necessary for a comprehensive understanding of rectal function.

- In Section 3.3, We applied the developed model to six normal and two pathological patients and identified significant differences in the factors affecting rectal function between the two groups. Patients with pathologies (such as akinesia and anismus) showed almost half the magnitudes of the evacuation force and pressure than normal patients.

- Further, in this Section 3.4, we applied the model to five patients with evident structural abnormalities and observed a secondary pressure field where the rectocele was present, resulting in incomplete defecation. Additionally, the formation of the rectocele and its size after almost half of the defecation time lowered the evacuation force resulting in a very small outlet velocity (non-linear relationship between the velocity and the force, $V_a \sim F^{2.4}$).

- Our model can be applied to defecography videos for further understanding of defecation disorders (DDs) and aiding in their classification. This information may assist coloproctologists in guiding appropriate therapy for patients, enhancing treatment strategies, and classification of the DDs.

- The idea of extending the 2D model to a 3D model to better simulate the real 3D geometry of the rectum is an interesting perspective. It is true that obtaining well-defined 3D data for the rectum can be challenging, even with advanced imaging techniques such as MRI or magnetic marker tracing. However, there are ongoing advancements in imaging technologies, and it is possible that more accurate 3D data for the rectum will become available in the future. Overall, the idea of extending the model to a 3D model is promising, but there are limitations to consider, including the availability of well-defined 3D data and the computational resources needed for simulation.

Chapter 4

Computational Fluid Dynamics and Experimental Set-up: Investigating Villi Motility

In previous Chapter 3, we developed and applied a patient-specific 2D CFD model to multiple individuals. Likewise, in this chapter, we investigated villi movement in the small intestine of a rat using a fluid dynamics approach. Consequently, a two-dimensional (2D) domain of the small intestine with villi was considered, with Newtonian fluid flow taken into account. The model incorporated the pendular motion of the villi, incorporating a phase lag between the adjacent villi. The findings of this study are summarized in the form of a journal paper, which is still pending submission, Section 4.1.

Moreover, due to the lack of ex-vivo experimental set-up that can observe and record small intestinal motility in live tissue at both macro and micro scales, we have designed a new set-up. A systematic description of the design, validation, and future scope of the set-up is summarized in Section 4.2.

4.1 Role of Propagating Pendular Villi Motility in Intestinal Advective Transport and Mixing

The flow in the gastrointestinal (GI) tract or gut is a complex system characterized by multiple scales and complex rheology, primarily influenced by active boundaries. The coordination and interaction between GI motility and the movement of digesta play a vital role in digestion and the elimination of undigested waste. In this section, we aim to explore this phenomenon using a two-dimensional (2D) computational fluid dynamics (CFD) model that focuses on the villi movements in a rat small intestine.

While previous studies have examined villi movements induced by intestinal motility at the microscopic level, a comprehensive review of the literature has revealed that the presence of villi and their pendular motions contribute significantly to mixing and absorption processes. However, the extent to which villi oscillate with a consistent phase difference compared to their neighboring villi remains relatively unknown. Therefore, a comparative study was necessary to investigate the pumping effect generated by the mobile villi and the influence of fluid inertia in the small intestine on the transport and mixing phenomena. This work has been submitted in Physical Review Fluids.

My contributions

I wrote the first version of the paper. I performed the CFD simulation and prepared all the figures.

Role of propagating pendular villi motility in intestinal advective transport and mixing

Faisal Ahmad,[1,2] Rohan Vernekar,[1,*] Stéphane Tanguy,[2] and Clément de Loubens[1]
[1] *Univ. Grenoble Alpes, CNRS, Grenoble INP, LRP, 38000 Grenoble, France*
[2] *Univ. Grenoble Alpes, CNRS, UMR 5525, VetAgro Sup, Grenoble INP, TIMC, 38000 Grenoble, France*

(Dated: June 29, 2023)

The small intestine is a complex organ with a dense neural feedback network to drive motility of smooth muscles in its walls for mixing, digesting and absorbing food. On its inner mucosa it posses a dense layer of elongated micron-sized structures called the villi well known to significantly increase the surface area of the intestinal lumen for enhanced absorption. The villi also undergo complex patterns of motion due to the contraction of smooth longitudinal muscles, termed pendular motion, whose purpose is not well understood.

We conducted numerical simulations to analyze the impact of various longitudinal motility patterns on flow and mass transfer within the small intestine, taking into account the mechanical forcing exerted by the villi at micro-scales. Two-dimensional lattice-Boltzmann methods were employed to simulate reversible and irreversible flow fields focusing on cyclic propagating and non-propagating longitudinal contractions, as described in the duodenum of the rat. In the case of propagating contractions, each villus exhibited asynchronous oscillation with a specific phase lag relative to adjacent villi. On the other hand, for non-propagating longitudinal contractions, adjacent groups of villi moved out-of-phase, with each group characterized by cyclic approximation and separation.

In both scenarios, the motion of the villi induced cyclic radial pumping, primarily controlled by the variations in volume within the inter-villus space. For propagating contractions, the irreversible flow exhibited a similar magnitude to the reversible flow and induced a net axial flow in the center of the lumen and around the villi. Both phenomena reached their maximum for an optimal phase lag. In contrast, in the case of non-propagating contractions, irreversible flow was approximately two orders of magnitude lower compared to the reversible flow. The flow was organized into non-interchanging cells, inducing mixing *'in situ'* on long time scales.

Overall, our findings suggest that different patterns of small intestine motility, in addition to the presence of villi, play a crucial role in regulating the intensity, location, and direction of mass transfers.

I. INTRODUCTION

The gastro-intestinal tract is a tubular organ which transport and mix complex fluids by different patterns of contractions. At the scale of the organ, these patterns control food breakdown [1], mixing and propulsion of chyme along the GI tract [2]. Investigations of the fluid mechanical consequences of these patterns have primarily relied on numerical simulations [3–7], complemented by a limited number of experiments [8–10]. The understanding of gastro-intestinal fluid dynamics has led to the development of simplified mass transport models, aiding predictions regarding mass transfer and absorption of drug and nutrients [11], as well as the spatio-temporal organization of the microbiota [12–14].

Moreover, similarly to other organs, the small intestine mucosa is lined by microcsocopic finger-like or leaf-like structures, the so-called villi, Fig. 1-a. Spontaneous activity of small intestine villi was first described by Gruby and Delafond in 1843 [15] and in-depth investigations were carried out one century later in *ex-vivo* organs [16–19] leading to the conclusion that these microsctructures should have an active role in the enhancement of absorption [20–22].

At first sight, these considerations are in line with our understanding of the role of ciliated cells that decorate the mucosa of various organs such as the airways, cerebral ventricles, and female reproductive tract to transport complex fluids, such as mucus or seminal fluid [23]. The main difference between small intestinal villi and ciliated cells, are the scales. Whereas ciliated cells are structure of few tens of micrometers, small intestinal villi are ten times larger. The flow around the ciliated cells is characterized by a low Reynolds number (Re), where the inertial forces are negligible compared to the viscous forces. It has been firmly established that the non-reciprocal beating of these cilia, along with their coordination, enables the net movement of fluid in a specific direction to counteract the reversible nature of creeping flows [24–28].

---

[*] rohan.vernekar@univ-grenoble-alpes.fr

Conversely, recent studies on villi motility have demonstrated that they behave as rigid structures within the physiological range of shear stress [29]. Their movement is rather controlled by fast phasic contractions of the muscularis mucosae [30] than by their own motility [15–17, 19]. Longitudinal and radial muscle layers have the ability to adjust their tone and motility in response to external stimuli such as mechanical, chemical, or hormonal signals [31–34], which, in turn, modify the motion of the villi [30]. For instance, in rats, the motility of the proximal duodenum is primarily characterized by phasic longitudinal contractions that are organized into fixed domains at low intra-luminal pressure. When the pressure increases, phasic contractions propagate in one direction [35].

These findings have prompted the development of fluid dynamics models which aimed at understanding the role of small intestine motility and villi motion on flow, mixing and mass transfers [6, 11, 30, 36–42]. These studies reveal the intricate nature of fluid dynamics at small scale in the small intestine. More specifically, two main physical mechanisms have been identified, one relying on purely geometric pumping effects, and the other on fluid inertia.

Firstly, the relative movement of two adjacent villi creates volume variations that generates radial fluid transfers. This phenomenon is particularly relevant when groups of adjacent villi are forced to move in opposition of phase [41] due to phasic longitudinal contractions organized into fixed domains [30, 37, 39]. These contractions generate cyclic approximation and separation of groups of villi. This phenomenon is solely based on a geometrical concept making it efficient regardless of the rheological properties of the fluid [37].

Secondly, at non-vanishing and moderate Reynolds numbers, the alternative motion of the villi mechanically enforces a secondary flow phenomenon, called steady streaming flow (SSF) [43]. This flow creates a micro-mixing layer (MML) at the periphery of the lumen [36] and can be coupled with the bulk flow in the lumen at a larger scale [38, 40]. The flow is characterized by steady vortices at the tip of the villi [40, 41], which induces mass transfers between the bulk and the periphery of the lumen. Orders of magnitude showed that the transport of non-brownian particles, such as bacteria or nano-particles should be driven by the MML on long time scales (few min) [40]. The thickness of the MML is not solely governed by the Stokes boundary layer $\sqrt{\mu/\rho\omega}$, where μ is the fluid viscosity, ω is the pulsation of the forcing, and ρ is the fluid density; but also by the lateral confinement between the villi [40]. At high, but non-physiological Reynolds numbers, this description starts to be complexified by the shedding of vortices from the apex of the villi [41]. Moreover, MML can also be coupled to the pumping mechanism described above when villi do not move in phase [41].

The aforementioned outcomes raise an important issue regarding the relative influence of geometric pumping and SSF on transport and mixing in the small intestine, particularly in light of pertinent motility data in physiological scenarios.

Our objective is to identify flow phenomena that may be triggered by the motility of the small intestine villi. Based on the motility characterization of the rat duodenum [4, 35] and a dedicated lattice-Boltzaman flow solver [40], we investigated how the motility of the small intestine villi regulates the transfer of mass both radially and axially along its length. We analyzed both reversible and irreversible flow fields in two main scenarios. In the first scenario, villi movement was induced by longitudinal contractions propagated in the oral-distal direction, while in the second scenario, non-propagating longitudinal contractions. By examining these two situations, we aimed to understand how different modes of villi motility impact the flow patterns within the small intestine.

II. METHODS

A. Geometry and villi motility model

The 2D geometry under consideration is an infinite array of leaf-like villi, representative of those found in the small intestines of the rat, Fig. 1-a. The simulated domain with a finite number of villi undergoing periodic motion is illustrated in Fig. 1-b. Periodic boundary conditions are considered at the domain boundaries along the z direction. Symmetry condition is imposed at the center of the lumen.

The villi are modelled as a moving rigid structure [29]. Each villus has an equal height l_v and diameter d_v. The pitch p is the distance between the centres of two adjacent villi in the unstrained state, and thus the intervillous gap is $p - d_v$. ρ and μ are the density and dynamic viscosity of the fluid. Table I gives typical geometrical values of villi dimensions in the duodenum of the rat. We consider that each individual villus, indexed i, is put into axial translation by propagating or standing contractions of the duodenal musculature [35]. Consequently, the velocity $\mathbf{U}_i$ of the i^{th} villi is given by,

$$\mathbf{U}_i(t) = 2\pi f a_i \sin(2\pi f t + \phi_i)\, \mathbf{e}_z, \tag{1}$$

where f is the frequency of oscillation, a_i and ϕ_i the maximum amplitude of translation and the phase-lag for the i^{th} villi, respectively. For propagating contractions (Fig. 1-c), the amplitude is independent of the villi position

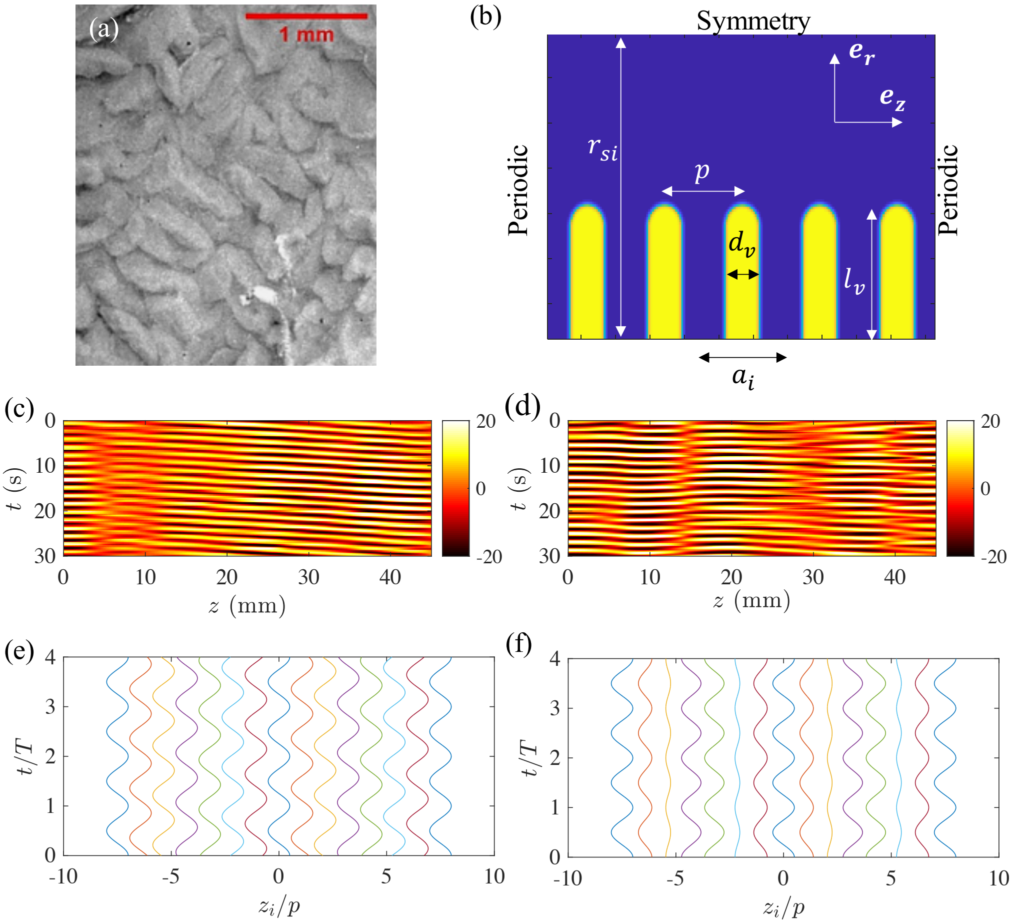

FIG. 1. **(a)** Image of small intestine villi in a *ex-vivo* preparation of the rat duodenum. **(b)** The 2D simulated domain with domain boundary conditions marked. Five vertical leaf-like villi seen in yellow, indexed i, oscillate with velocity $U_i\mathbf{e}_z$, covering a maximum amplitude a. The color field gradient shows the smoothed profiles for villi. Experimentally obtained spatio-temporal strain rate maps for **(c)** propagating and **(d)** non-propagating contractions of longitudinal smooth muscles in the duodenum of the rat from [35]. Examples for the temporal evolution of centre positions of the villi z_i, under propagating **(e)** and non-propagating **(f)** contractions, when using the simplified mathematical models in Eqs. 2 and 3, respectively.

TABLE I. Typical values of parameters characterizing villi geometry and the motility of the duodenum of the rat. Refs [4, 35, 44]

Radius of the small intestine	r_{si}	2.8 mm
Width of the villi	d_v	200 μm
Length of the villi	l_v	500 μm
Pitch	p	450 μm
Amplitude of translation	a	150 μm
Frequency	f	0.7 Hz
Length of a domain	l_d	10 mm
Amplitude of velocity	$U_0 = 2\pi f a$	0.66 mm/s
Fluid density	ρ	10^3 kg/m^3
Fluid viscosity	μ	0.7 mPa.s
Stokes layer	$\delta^{St} = \sqrt{\frac{\mu}{2\pi f \rho}}$	400 μm
Modified Reynolds number	$Re_m = d_v/\delta^{St}$	0.5−5

($a_i = a$) and the phase difference between two adjacent villi is taken as constant $\Delta\phi = \phi_i - \phi_{i-1} = 2\pi/N_v$, N_v is the number of villi. Whereas, for steady contractions (Fig. 1-d), all villi move in-phase but with a modulated amplitude $a_i = a\cos(2\pi z_i/l_d)$, where z_i is the position of the villi i, and $l_d = pN_v$ the length of the simulated domain of contraction. These two cases can be written respectively as,

$$\text{Propagating contractions:} \qquad \mathbf{U}_i(t) = 2\pi f a \sin\left(2\pi f t + i\Delta\phi\right)\mathbf{e}_z \tag{2}$$

$$\text{Standing contractions:} \qquad \mathbf{U}_i(t) = 2\pi f a \cos\left(2\pi z_i/l_d\right)\sin\left(2\pi f t\right)\mathbf{e}_z \tag{3}$$

B. Fluid flow solver

The fluid flow generated by propagating and non-propagating contractions of the villi is modelled by the incompressible Navier-Stokes equations for Newtonian fluids. By using the Stokes layer $\delta^{St} = \sqrt{\mu/2\pi f\rho}$ as the typical length scale and $\delta^{St}/2\pi f a$ as the typical time scale, the dimensionless Navier-Stokes equations for incompressible laminar flows are given by

$$\frac{\partial \tilde{u}_i}{\partial \tilde{x}_i} = 0 \tag{4}$$

$$\frac{\partial \tilde{u}_i}{\partial \tilde{t}} + \tilde{u}_j \frac{\partial \tilde{u}_i}{\partial \tilde{x}_j} = -\frac{\partial \tilde{p}}{\partial \tilde{x}_i} + \frac{d_v}{a}\frac{1}{Re_m^2}\frac{\partial^2 \tilde{u}_i}{\partial \tilde{x}_j \partial \tilde{x}_j} \tag{5}$$

where i, j (=1,2) are the indices of the system of coordinates. $\tilde{u}_i$, $\tilde{t}$, $\tilde{x}_i$, and $\tilde{p}$ are the dimensionless velocity, time, coordinate, and pressure, respectively. The problem allows us to form 6 dimensionless groups. The geometry is defined by three ratios, p/d_v, l_v/d_v, r_{si}/d_v which we do not vary in our simulations. The oscillatory motion gives us two more dimensionless parameters; the modified Reynolds number $Re_m = d_v\sqrt{2\pi f\rho/\mu}$, and the reduced oscillation amplitude a_0/d_v. Importantly, for the cases with propagating contractions, we have to consider the phase lag $\Delta\phi$ (Eq. 2), and for the ones with standing contractions we have the ratio l_d/d_v (Eq. 3). Setting these values determines the villi number N_v over the spatially periodic domain length l_d, in both the cases. However, an integer number of villi N_v need to be chosen in the simulated domain to ensure correct periodic boundary conditions along the z direction. Consequently, we can access only certain discrete values for the phase lag $\Delta\phi = 2\pi/N_v$ and the domain length $l_d = pN_v$.

The flow is solved in 2D by using the D3Q19 incompressible two relaxation time (TRT) lattice-Boltzmann methods (LBM) [45, 46], with one layer of nodes in the third direction. Moving rigid villi are modelled using the smoothed profile method (SPM), which was developed to simulate multi-body hydrodynamic interactions of solid particles [47]. The SPM models the villi by computing a force field that enforces the no-slip condition at the villi-fluid interface. Our coupled solver allows high accuracy computation of both the primary and secondary flow fields. See [40] for details on the solver and its validation.

C. Decomposition of the flow field and flow resolution

The villi periodic motion results in pulsatile shearing of the fluid, which reverses over half the time period $1/2f$. After simulating a number of time-periods of villi motion, the flow-field attains a steady time-periodic profile, i.e. the flow-field is invariant from one period fraction (ft) to the next $(ft+1)$. Periodically driven flows are known to generate steady secondary flows which are irreversible. We therefore extract two measures from the periodically pseudo-steady flow-field; irreversible field $\mathbf{u}_{\text{irrev}}$ and another reversible field $\mathbf{u}_{\text{rev}}$.

$$\mathbf{u}\left(\mathbf{x}, t\right) = \mathbf{u}_{\text{rev}}\left(\mathbf{x}, t\right) + \mathbf{u}_{\text{irrev}}\left(\mathbf{x}\right) \tag{6}$$

The irreversible part $\mathbf{u}_{\text{irrev}}$ is the mean value of $\mathbf{u}$ during one cycle $T = 1/f$,

$$\mathbf{u}_{\text{irrev}}(\mathbf{x}) = \frac{1}{T}\int_0^T \mathbf{u}(\mathbf{x}, t)dt. \tag{7}$$

whereas the reversible flow field oscillates around 0. Its amplitude $|\mathbf{u}_{\text{rev}}|$ is given by,

$$|\mathbf{u}_{\mathrm{rev}}| = \sqrt{|u^z_{rev}|^2 + |u^r_{rev}|^2} \tag{8}$$

with $|u^z_{rev}|$ and $|u^r_{rev}|$ the amplitudes of the reversible flow field in the axial (z) and radial (r) directions and defined by

$$|u^r_{rev}(\mathbf{x})| = \frac{1}{T}\int\limits_0^T |u^r(\mathbf{x},t) - u^r_{irrev}(\mathbf{x})|dt \tag{9}$$

$$|u^z_{rev}(\mathbf{x})| = \frac{1}{T}\int\limits_0^T |u^z(\mathbf{x},t) - u^z_{irrev}(\mathbf{x})|dt \tag{10}$$

The pseudo-steady state of the flow was achieved by convergence of the L2-norm of $\mid \mathbf{u}_{\mathrm{irrev}}(\mathbf{x}, t+T) - \mathbf{u}_{\mathrm{irrev}}(\mathbf{x}, t) \mid$ ($< 10^{-4}$). Typically, the small lattice grid consisted of a mesh of at least 40 $\times$ 120 nodes. One cycle of activity was divided into at least 10^4 time steps.

The amplitude of the reversible flow field $|\mathbf{u_{rev}}|$ was then averaged along the z direction to calculate the amplitude of the reversible flux density in the radial and axial direction, $|\varphi^r_{\mathrm{rev}}|$ and $|\varphi^z_{\mathrm{rev}}|$ respectively, i.e.

$$|\varphi^r_{\mathrm{rev}}(r)| = \frac{1}{l_d}\int\limits_0^{l_d} |u^r_{\mathrm{rev}}(r,z)|dz \tag{11}$$

$$|\varphi^z_{\mathrm{rev}}(r)| = \frac{1}{l_d}\int\limits_0^{l_d} |u^z_{\mathrm{rev}}(r,z)|dz \tag{12}$$

Similarly, the absolute value of the components of the irreversible flow-field $\mathbf{u}_{\mathrm{irrev}}$ are also averaged along the r and z direction to calculate the amplitude of the irreversible flux density in the radial and axial direction, $|\varphi^r_{\mathrm{rev}}|$ and $|\varphi^z_{\mathrm{irrev}}|$ respectively, i.e.

$$|\varphi^r_{\mathrm{irrev}}(r)| = \frac{1}{l_d}\int\limits_0^{l_d} |u^r_{irrev}(r,z)|\mathrm{d}z \tag{13}$$

$$|\varphi^z_{\mathrm{irrev}}(r)| = \frac{1}{l_d}\int\limits_0^{l_d} |u^z_{irrev}(r,z)|\mathrm{d}z \tag{14}$$

III. RESULTS

A. Propagating contractions

Firstly, we analyse the flow generated by propagating contractions, illustrated in the left panel in the spatio-temporal (ST) map in the Fig. 1-c. The colour code in ST map shows the amplitude of the strain rate in the longitudinal direction of the proximal duodenum of the rat [35]. At a given location z, the strain rate oscillates, which is characteristic of cyclic contraction and relaxation of smooth muscles at $f \sim 0.57$ Hz. The slopes of the white lines illustrate that the longitudinal contractions propagate along the length of the duodenum with a wave speed c of about 10 mm/s. At the scale of the villi, we assume that this pattern of propagating contractions induces an oscillation of the villi with constant amplitude a_0 and with a constant phase lag $\Delta\phi$ between two adjacent villi (Eq. 2).

$\Delta\phi$ can be estimated from these physiological readings by computing the modulo of $2\pi pf/c$ by π. This means that $\Delta\phi$ increases linearly between 0 and π if the ratio pf/c is smaller than 1/2. Any increase of this ratio when it is larger than 1/2 can lead to random variations of $\Delta\phi$. With a pitch p of about 0.5 mm, $pf/c \sim 0.028$ and we can estimate $\Delta\phi \sim \pi/18$. Therefore, under the physiological conditions typically encountered in the rat, the phase lag $\Delta\phi$ is finite but small, and would increases continuously with ratio pf/c. It is thus an important parameter to understand.

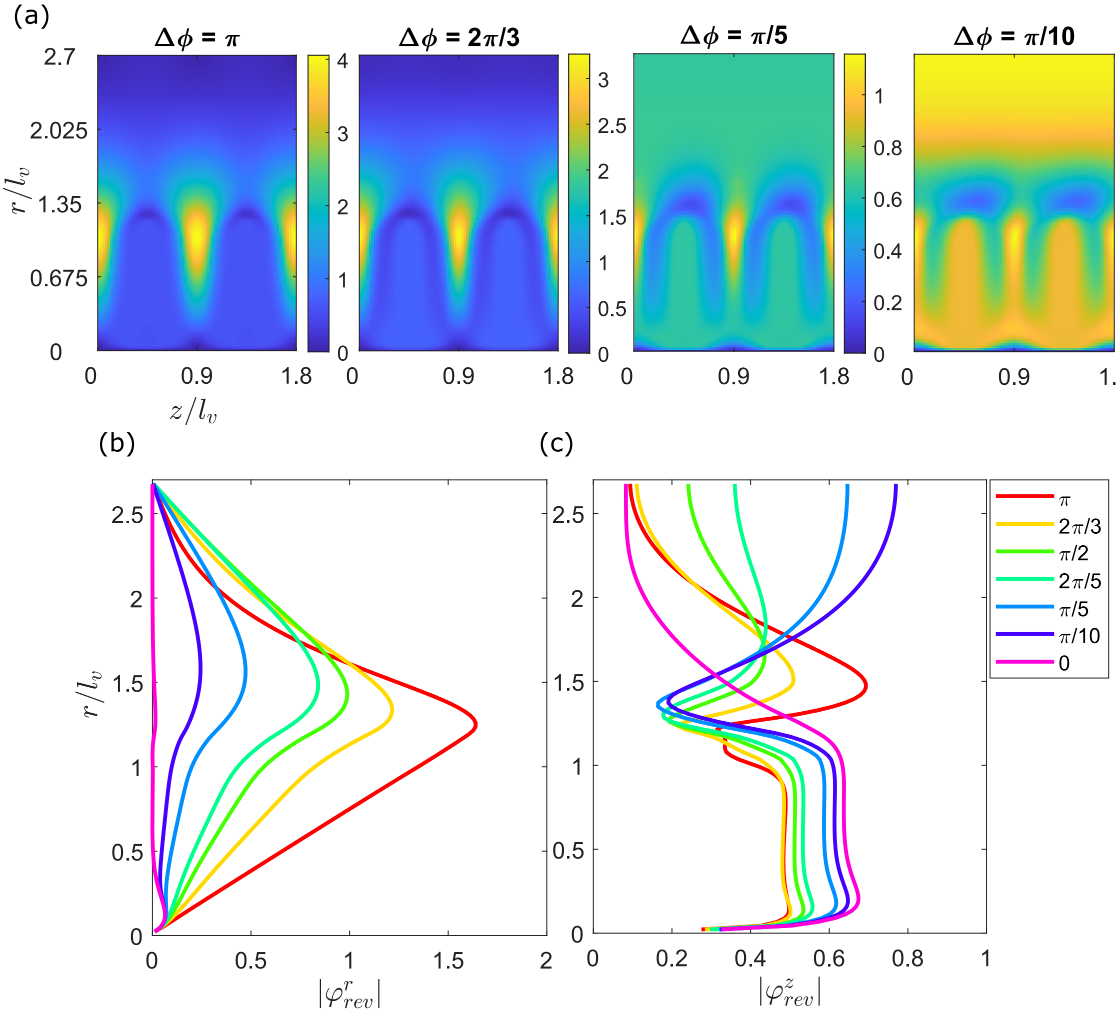

FIG. 2. Influence of the phase-lag $\Delta\phi$ on the reversible flow field due to propagating longitudinal contractions. **(a)** Magnitude of the reversible flow field $|\mathbf{u_{rev}}|$ for decreasing phase lag $\Delta\phi$. From left to right: π, $2\pi/3$, $\pi/5$, $\pi/10$ and 0. Amplitude of the reversible flux density in the **(b)** radial $|\varphi^r_{rev}(r)|$ and **(c)** axial $|\varphi^z_{rev}(r)|$ direction as a function of the radial position r for different $\Delta\phi$. $Re_m = 1$, $a/d_v = 0.3$, $p/d_v = 2.25$.

Reversible flow field

In this section we discuss the spatial organization of the reversible (oscillating) flow field, Fig. 2 and 3. The amplitude of the reversible flow field $|\mathbf{u}_{\text{rev}}|$ is shown in Fig. 2-a for $\Delta\phi$ decreasing from π to $\pi/10$. When the villi moved in out of phase ($\Delta\phi \to \pi$), the reversible flow was dominated by an oscillating axial flux in the inter-villus space. The amplitude of the reversible flux density in the radial direction $|\varphi^r_{rev}(r)|$ shows a maximum above the tip ($r/l_v = 1$) of the villi and decay up to 0 in the middle of the lumen, Fig. 2-b . $|\varphi^r_{rev}(r)|$ decreased when $\Delta\phi$ increased. This is coherent with the fact that the volume variation between two villi is maximal when $\Delta\phi = \pi$. Moreover, the amplitude of the flow in the middle of the lumen ($r/l_v = 2.6$) is maximal when the villi move out of phase ($\Delta\phi = \pi$) and minimal when moving in unison ($\Delta\phi = 0$), Fig. 2-a, c. The reversible axial flow is localized in the center of the lumen at low $\Delta\phi$, whereas it is adjacent to the villi ($1 < r/l_v < 2$) when $\Delta\phi$ tend to π.

The instantaneous flow field for different phase lag $\Delta\phi$ ($\pi, \pi/2, \pi/5$) is shown in Supp. Mat. S1.1 (at then end of this paper) for $Re_m = 1$. When $\Delta\phi = \pi$, there are two vortices concentrated near the tip of the villi throughout the oscillation period with an instantaneous velocity of magnitude 7. When the value of $\Delta\phi$ is less than $\pi/2$, two unsteady counter-rotating vortices are formed between the apex of the villi and the center of the lumen. The vortices propagate in the opposite direction of the contraction wave. Fluid is alternately ejected and pumped into the intervillous space, which corresponds to the influence of geometric pumping induced by the varying phase difference between the adjacent

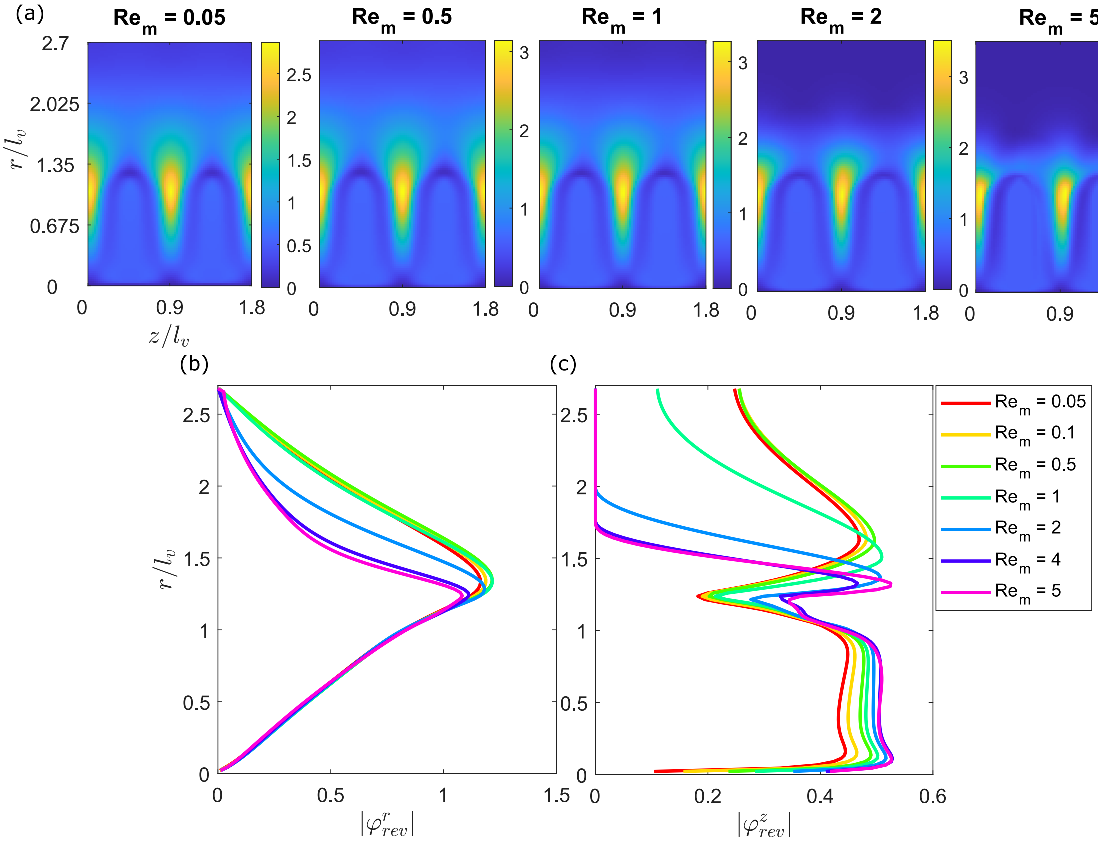

FIG. 3. Influence of the modified Reynolds number Re_m on the reversible flow field due to propagating longitudinal contractions. **(a)** Magnitude of the reversible flow field $|\mathbf{u_{rev}}|$ for increasing Re_m. From left to right: 0.1, 0.5, 1, 2 and 4. Amplitude of the reversible flux density in the **(b)** radial $|\varphi^r_{rev}(r)|$ and **(c)** axial $|\varphi^z_{rev}(r)|$ direction as a function of the radial position r for different $\Re_m$. $Delta\phi = 2\pi/3$, $a/d_v = 0.3$, $p/d_v = 2.25$.

villi.

Fig. 3 shows the influence of the modified Reynolds number Re_m on the reversible flow field for a fixed phase lag of $2\pi/3$. Increasing the modified Reynolds number Re_m from 0.05 to 5 tended to localize the reversible flow in a layer adjacent to the villi, Fig. 3-a. While the reversible flow propagated throughout the lumen at low Re_m, the amplitude of the reversible axial flux $|\varphi^z_{\mathrm{rev}}(r)|$ was maximal in a layer adjacent to the villi at high Re_m, Fig. 3-c. This result is in line with the phenomenon that periodic forcing leads to the development of an unsteady viscous boundary layer near the boundary, characterized by non-zero vorticity. Furthermore, this boundary layer scales with the Stokes layer δ^{St}. Finally, Re_m had a moderate effect on the radial flux $|\varphi^r_{\mathrm{rev}}(r)|$, confirming that the instantaneous radial flux is controlled by geometric effects.

From the supplementary data Supp. Mat. S1.2, we show the instantaneous flow with varying Re_m values of 1 and 5 when $\Delta\phi = 2\pi/3$. At $Re_m = 1$, the vortices near the tip of the villi were localized and exhibited changes in their rotation over the oscillation period T. Additionally, the effect of the vortices extended up to the center of the small intestine. On the other hand, at $Re_m = 5$, the localized vortices not only changed direction but also traveled from one villus to the adjacent villus. Furthermore, there was sustained flow at the center of the small intestine where the effect of the vortices was absent. When the vortices reached the adjacent villus, they interacted with the counter vortices formed by that villus.

Irreversible flow field

Secondly, we focus on the irreversible flow field generated by propagating longitudinal contractions, Fig. 4 and 5. It is first striking to observe the strong influence of $\Delta\phi$ on the amplitude of $\mathbf{u_{irrev}}$ in both radial and longitudinal directions. The amplitude was maximal for $\Delta\phi = 2\pi/5$ and was of the same order of magnitude than the amplitude

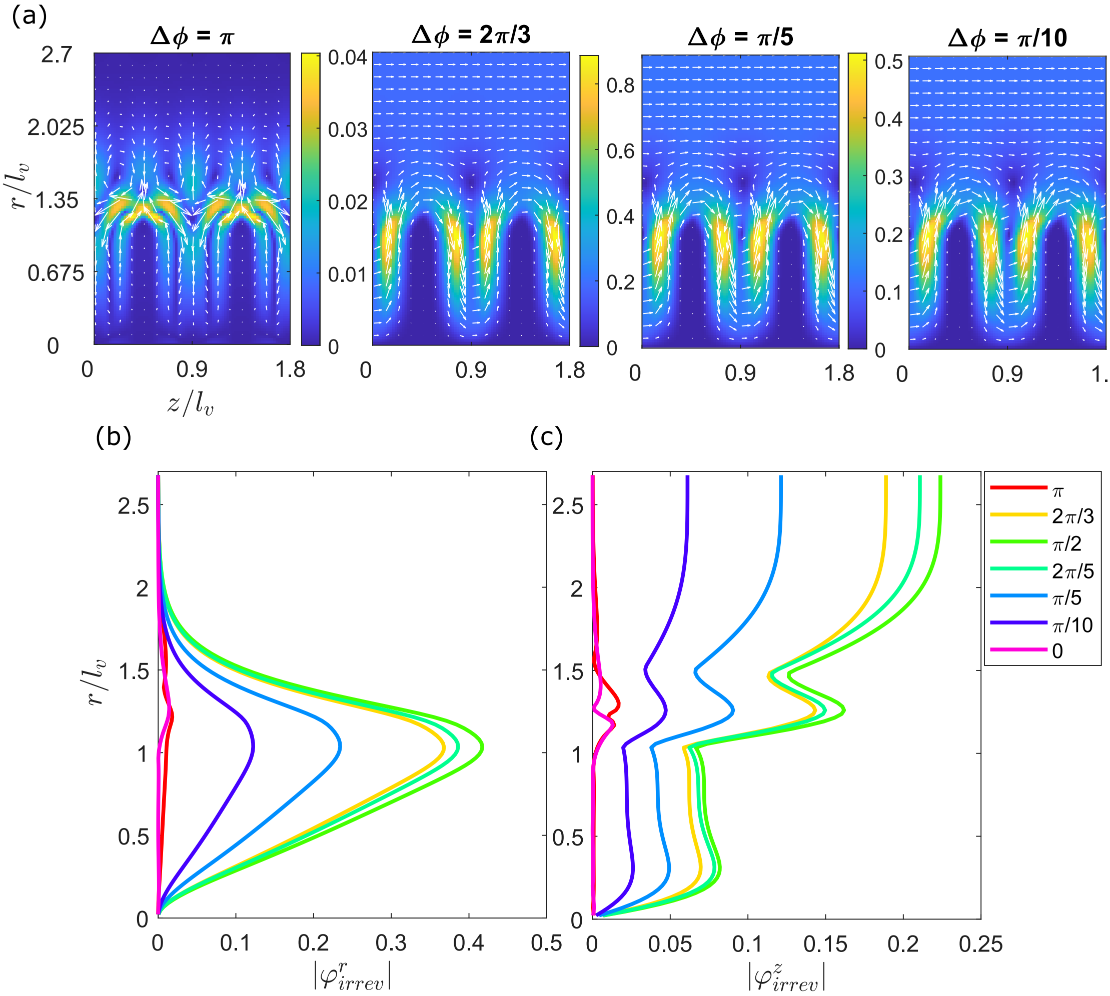

FIG. 4. Influence of the phase-lag $\Delta\phi$ on the irreversible flow field due to propagating longitudinal contractions. **(a)** Irreversible flow field $\mathbf{u_{irrev}}$ for decreasing phase lag $\Delta\phi$. From left to right: π, $2\pi/3$, $\pi/5$, $\pi/10$ and 0. Amplitude of the irreversible flux density in the **(b)** radial $|\varphi^r_{irrev}(r)|$ and **(c)** axial $|\varphi^z_{irrev}(r)|$ direction as a function of the radial position r for different $\Delta\phi$. $Re_m = 1$, $a/d_v = 0.3$, $p/d_v = 2.25$.

of the forcing velocity of the villi $U_0 = 2\pi f a$.

When adjacent villi moved in opposition of phase ($\Delta\phi = \pi$), the structure of the flow field was characterized by irreversible two vortices at the apex of the villi, and two additional vortices localized above the villi. There was an inflow and outflow in the inter-villus space. In the center of lumen, the irreversible flow was zero. For $\Delta\phi$ smaller than $2\pi/3$, there was a unidirectional permanent flow that swayed along the villi structure. Between two villi and at the level of their apex, there was a vortex and two other vortices above the villi. It was also noticeable that there was a unidirectional permanent axial flux in the center of the lumen see Supp. Mat. S1.2. Contrarily to its reversible counter part (Fig. 2-b), the irreversible radial flux $|\varphi^r_{irrev}(r)|$ was localized in a region near the villi and did not propagate up to the center of the lumen (Fig. 4-b).

For a fixed phase lag, $\Delta\phi = 2\pi/3$ in Fig. 3, Re_m had a weak influence of the radial flux $|\varphi^r_{\mathrm{irrev}}(r)|$ and the magnitude of the flow that swayed along the villi. However, the irreversible axial flux $|\varphi^z_{\mathrm{irrev}}(r)|$ increased both above the villi and in the center of the lumen as Re_m increased. The increase in the axial flux when $Re_m > 1$ shows that the dynamics in the centre of the lumen is now dominated by fluid inertia. The dominant flow here no longer reverses when the motion of the villi reverses (see corresponding figures for $\mathbf{u}_{\mathrm{rev}}$ in fig. 3-a), and the reversing flow is now confined to a small layer that scales with the Stokes length δ^{St}.

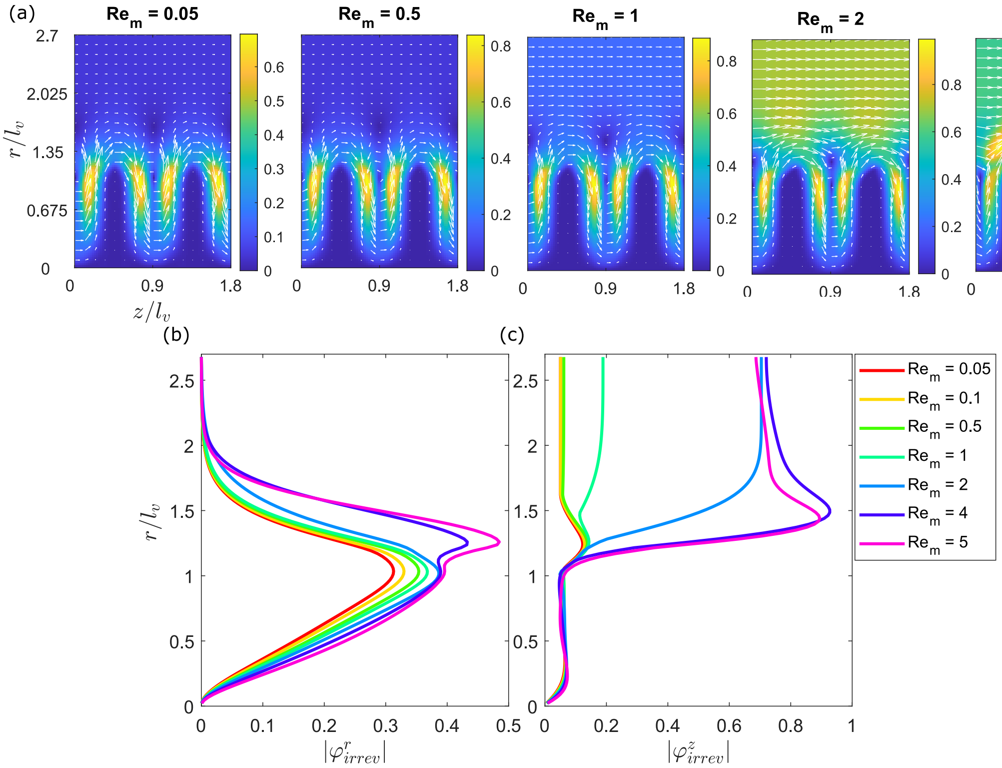

FIG. 5. Influence of the modified Reynolds number Re_m on the irreversible flow field due to propagating longitudinal contractions. **(a)** Irreversible flow field $\mathbf{u_{irrev}}$ for increasing Re_m. From left to right: 0.1, 0.5, 1, 2 and 4. Amplitude of the irreversible flux density in the **(b)** radial $|\varphi^r_{irrev}(r)|$ and **(c)** axial $|\varphi^z_{irrev}(r)|$ direction as a function of the radial position r for different $\Re_m$. $\Delta\phi = 2\pi/3$, $a/d_v = 0.3$, $p/d_v = 2.25$.

B. Non-propagating contractions

Secondly, we simulated the flow induced by non-propagating and pulsatile contractions, such as illustrated in Figure 1-d, f. In the duodenum of the rat, non-propagating longitudinal contractions are obtained when the intra-luminal pressure is low (< 1 cm H_20). The ST motility map shows that the strain rate is organized into several domains of about 10 mm long [35]. Roughly, when one domain is contracting, the adjacent domains are relaxing. Consequently, we modeled the velocity of the villi using Eq. 3, which provides a longitudinal displacement of the villi in an accordion-like manner. Fig. 1-f shows an example for 5 villi by domains of contractions. In the following sections, we varied the length of a domain l_d and the number of villi N_v per domain while keeping other geometric ratio constant.

Reversible flow field

Fig. 6 shows the amplitude of oscillation of the reversible flow field $|\mathbf{u_{rev}}|$, as well the reversible flux density in the radial $|\varphi^r_{rev}(r)|$ and axial directions $|\varphi^z_{rev}(r)|$. The oscillating radial flux occurs between the villi and propagates up to the center axis of the lumen. As the length of the domain l_d (or the number of villi N_v) increases, the radial flux decreases. However, increasing l_v promotes larger oscillating axial flow in the center of the lumen, due to the presence of localized vortices.

From the Supp. Mat. S2, we considered two cases: when the number of villi was 5 and 10. In both cases, vortices were formed near the tip of the villi, similar to the case of propagating contractions. The magnitude of the instantaneous velocity was almost two times higher for 5 villi compared to 10, as the oscillation of the villi depended on their position. Furthermore, the adjacent vortices collapsed and formed a larger vortex that propagated in the radial direction. Therefore, their effect can also be observed at the center of the small intestine.

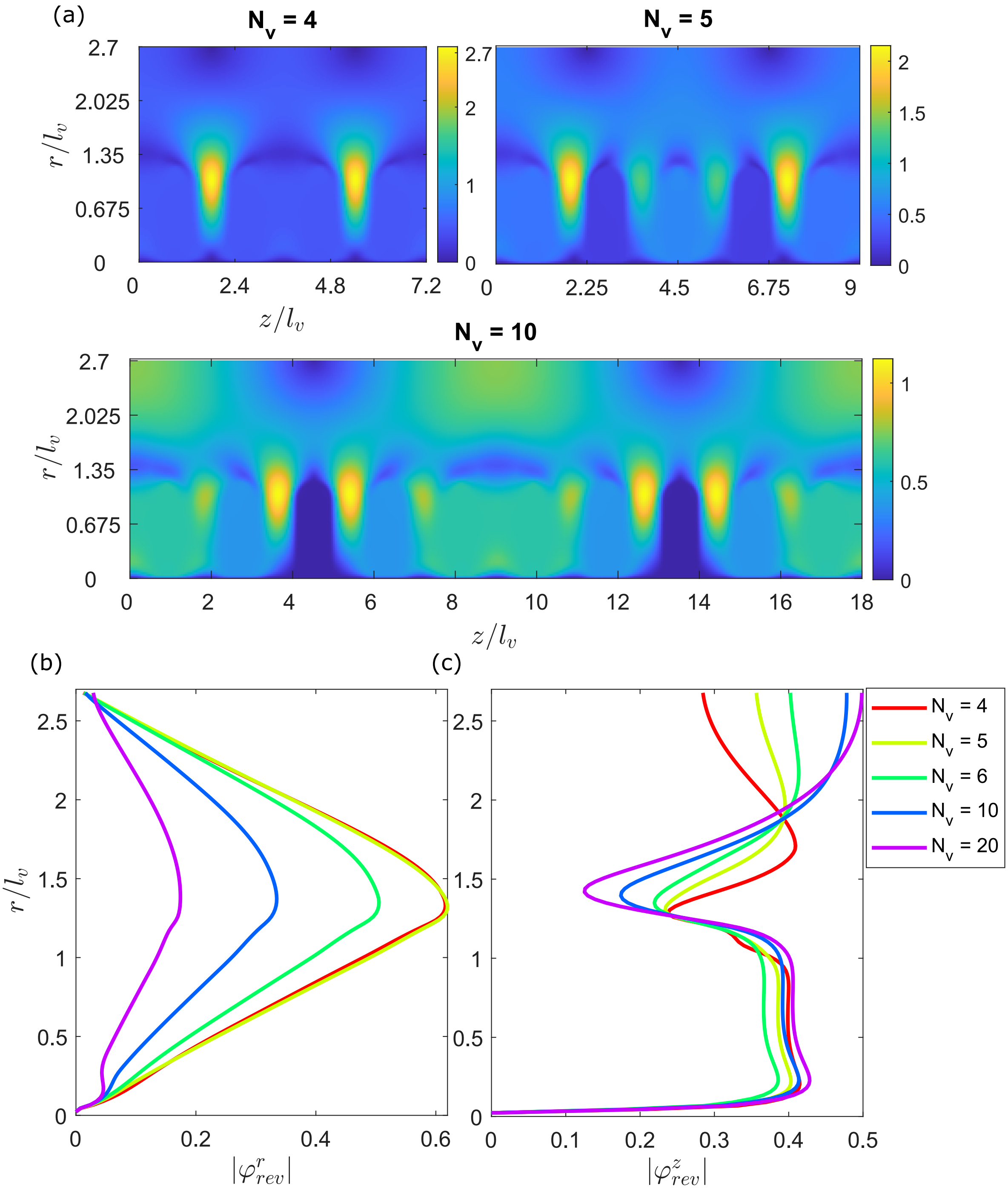

FIG. 6. Influence of the length of domain of contractions l_d on the reversible flow field due to non-propagating longitudinal contractions. **(a)** Magnitude of the reversible flow field $|\mathbf{u_{rev}}|$ for increasing l_d. From left to right: $l_d = 5p$, $10p$ Amplitude of the reversible flux density in the **(b)** radial $|\varphi^r_{rev}(r)|$ and **(c)** axial $|\varphi^z_{rev}(r)|$ direction as a function of the radial position r for different l_d. $Re_m = 1$, $a/d_v = 0.3$, $p/d_v = 2.25$.

Irreversible flow field

Non-propagating contractions induce irreversible radial exchange between the center of the lumen and the inter-villi space in fixed groups of villi, Fig. 7. Contrarily to propagating contractions, there is no net axial flux, and the flow is organized into domains that do not exchange matter between them. Moreover, the irreversible flow is approximately two orders of magnitude lower than the main flow.

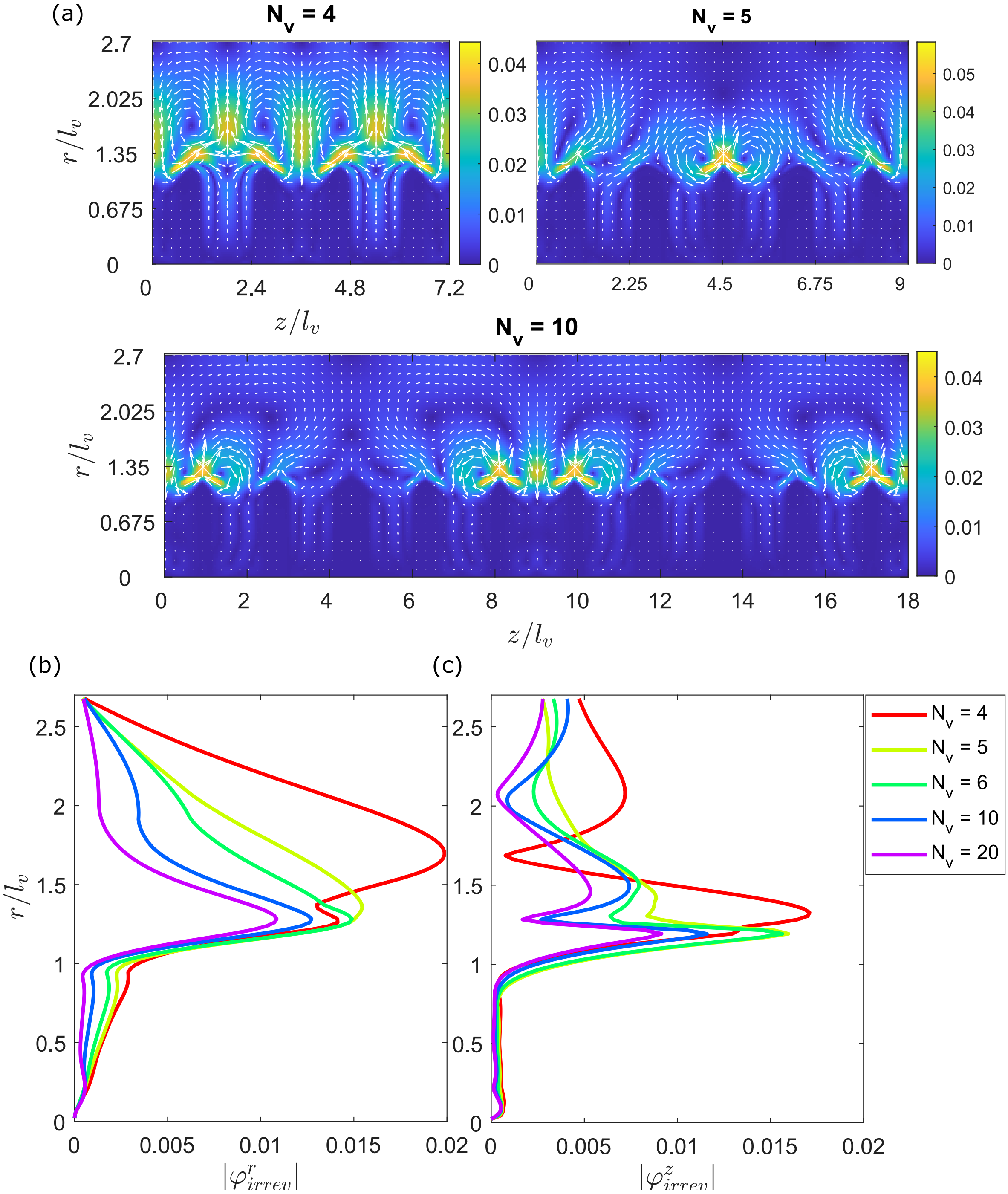

FIG. 7. Influence of the length of domain of contractions l_d on the irreversible flow field due to non-propagating longitudinal contractions. **(a)** Irreversible flow field $\mathbf{u_{irrev}}$ for increasing l_d. From left to right: $l_d = 5p$, $10p$ Amplitude of the irreversible flux density in the **(b)** radial $|\varphi^r_{irrev}(r)|$ and **(c)** axial $|\varphi^z_{irrev}(r)|$ direction as a function of the radial position r for different l_d. $Re_m = 1$, $a/d_v = 0.3$, $p/d_v = 2.25$.

IV. DISCUSSION

A. Villi, longitudinal contractions, and flow

The small intestine can regulate tone and motility in response to various chemical, physical, and hormonal stimuli [31–34]. This leads to different spatial organizations of the villi, such as variations in intervillus distance, and results in both propagating and non-propagating contractions of smooth muscles [30, 35]. In this study, we specifically focused on oscillating longitudinal contractions observed in the duodenum of rats [35]. We found that the activity pattern of smooth muscles and the spatial arrangement of the villi give rise to distinct spatiotemporal organization of pulsatile flow in the duodenal lumen.

For non-propagating contractions, the flow exhibits predominantly pulsatile behavior and forms unsteady vortices that facilitate mass transfer between the lumen's center and the intervillus space, Fig. 6, 7. The irreversible flow associated with this phenomenon is approximately two orders of magnitude lower than the main flow. One crucial feature is the organization of the flow into distinct domains, which prevents mass transfers between these domains and promotes mixing "in situ" [4].

Conversely, propagating contractions generate a net axial flow, which is irreversible, both adjacent to the villi, as well as in the centre of the lumen. This flow component is of similar magnitude to the main pulsatile flow and reaches its maximum intensity when there is a phase lag of $2\pi/4$. Propagating contractions also induce significant reversible radial flow. So, propagating contractions possess the capability to facilitate both radial mixing and axial transport of the digesta within the lumen.

B. Geometric scaling and role of inertia

We obtain scaling laws for the peak radial and axial fluxes generated by propagating contractions of the villi. These scaling terms give us an important insight into the mechanisms at play, and especially help understand the significant seen for the measured φ^z_{irrev} in comparison with the non-propagating contractions. We derive these scaling laws solely from geometric arguments, based on the propagating motion of the villi.

We first take a look at the contraction/relaxation process between adjacent villi during propagating contractions (with constant phase lag $\Delta\phi$). Here, we hypothesise that, in the limit of low Re_m, the radial flux should scale directly with changing this gap between adjacent villi. We can denote this gap between any adjacent villi, at positions z_i and z_{i+1}, as $g_{i+1} = z_{i+1} - z_i$. For the i^{th} villi, z_i can be easily computed by integrating the velocity given in eq. 2, and thus a time $t^\star = t/T$ and $\Delta\phi$ dependent equation for g_{i+1} is obtained. Solving for $\partial g_{i+1}/\partial t^\star = 0$, gives us the fractional times at which the gap is maximum or minimum as,

$$t^\star = \frac{1}{2}\left(m + \frac{1}{2} - \frac{(2i-1)\Delta\phi}{2\pi}\right), \tag{15}$$

where m takes integer values.

The maximum gap is given by $g^{\max}_{i+1} = p + 2a\sin(\Delta\phi/2)$ and the minimum gap is $g^{\min}_{i+1} = p - 2a\sin(\Delta\phi/2)$. Since, the gap goes from maximum to minimum, and *vice versa* in time $T/2$, the area swept by a single villus in this time would be $l_v|g^{\max}_{i+1} - g^{\min}_{i+1}|$. This now gives us the maximum volume of fluid "pumped" by two adjacent villi during propagating contractions as $4l_v a\sin(\Delta\phi/2)$. During the next $T/2$ part of the cycle, this flux should then return into the gap, in case the flow reverses entirely. When we measure φ_{rev} in our system, we measure this flux multiplied by N_v, averaged over the entire domain length $l_d = pN_v$, and over time $T = 1/f$. Thus, the non-dimensional radial reversible flux should scale as,

$$\varphi^r_{\text{rev}} \approx k_1 \sin\left(\frac{\Delta\phi}{2}\right), \tag{16}$$

where, the flux is non-dimentionalised using $2\pi fap$ (see eq. 11) to give the dimensionless prefactor $k_1 = \frac{4l_v}{p\pi}$. We plot the above scaling against the peak φ^r_{rev} values in fig. 8-a, where k_1 is treated as a free parameter.

We find an excellent match for $\Delta\phi$ dependence of φ^r_{rev}, and find that the prefactors k_1 only marginally depend on Re_m. Using the table I, the expected k_1 value is 1.4147, while those from the fits vary from 1.5 to 1.6. We suspect that the difference arises primarily because the scaling does not account for viscous effects, nor for the exact geometry of the individual villus that is simulated. Unsurprisingly, the scaling dependence tells us that the peak radial "pumping" will take place when $\Delta\phi = \pi$, i.e. when two adjacent villi move with velocities that are exactly opposing one another, and that this radial flux would also drop by approximately by an order when $\Delta\phi \approx \pi/10$. The flux will decay to zero when when all villi move in sync and $\Delta\phi \to 0$.

Understanding the geometric origins of the axial flux seen in figs. 2 and 4 is rather more subtle. The large values of $\varphi^z_{\mathrm{irrev}}$ seen in our simulations hint that, even at very low Re_m, the "pumped" out-flow due to contraction of the gap g_i during the half cycle $(0 \to T/2)$ does not return into the same gap when it undergoes expansion during the next half cycle $(T/2 \to 0)$. Here, we hypothesise that we need to take into account the relative dynamics of least two adjacent gaps in order to scale the irreversible part of the axial flux. If both adjacent gaps g_i and g_{i+1} are contracting (or expanding) at the same time, one expects, by conservation of fluid mass, that the fluid flux would have to travel further axially and would not be able to return completely into these two gaps.

For this analysis we consider what happens at the gaps adjacent to the i^{th} villi, relative to its evolving position. We first compute the relative velocities of the fore and aft villi as $V_{i+1} = U_{i+1} - U_i$ and $V_{i-1} = U_{i-1} - U_i$. We then obtain the evolution of the total gap $h_i = \int (V_{i+1} - V_{i-1})dt$, as observed from the i^{th} villus. We can simplify this expression using trigonometric identities to obtain a time $t^\star$ and $\Delta\phi$ dependent expression (with an integration constant), as done previously. Again, taking solving for $\partial h_i/\partial t^\star = 0$ gives us the fractional time for minimum and maximum values for h_i

$$t^\star = \frac{m}{2} + \frac{1}{4} - \frac{(i-1)\Delta\phi}{2\pi}, \tag{17}$$

where m again takes integer values.

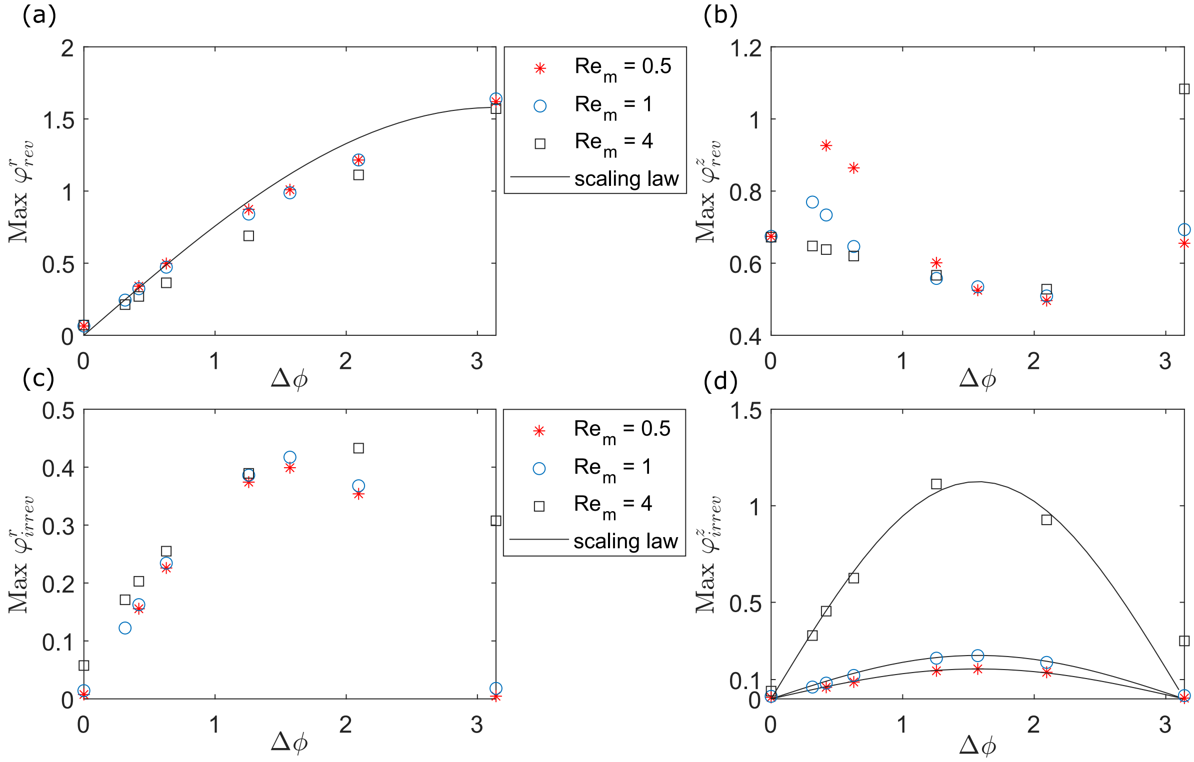

FIG. 8. Maximum values of **(a)** reversible radial, **(b)** irreversible axial, **(c)** irreversible radial, and **(d)** reversible axial flux as a function of the phase lag $\Delta\phi$ whne modified Reynolds number $Re_m = 0.5, 1, 4$, and $a/d_v = 0.3$, $p/d_v = 2.25$. Solid lines represent scaling laws, red (k1 = 1.6, k2 = 0.31), blue (k1 = 1.6, k2 = 0.45), black (k1 = 1.6, k2 = 2.35), k1 for maximum reversible radial flux, k2 maximum irreversible axial flux.

The maximum is given by $h_i^{\max} = 2aC\sin(\Delta\phi/2) + 4a\sin(\Delta\phi/2)\cos(\Delta\phi/2)$ and the minimum is $h_i^{\min} = 2aC\sin(\Delta\phi/2) - 4a\sin(\Delta\phi/2)\cos(\Delta\phi/2)$, where C is a constant of integration. We see that h_i goes from maximum to minimum in $(0 \to T/2)$, and *vice versa* in remaining half cycle. The relative area reduction (or expansion) in one half cycle by the two adjacent gaps would be $l_v|h_i^{\max} - h_i^{\min}| = 8al_v\sin(\Delta\phi/2)\cos(\Delta\phi/2)$. The a fraction of the fluid flux that is pushed by this contraction would not be return into its original gaps, as it must travel axially one gap further. We expect that the axial φ_{irrev} measured in the simulations, averaged over the entire domain length $l_d = pN_v$, would be N_v times the above scaling. The time scale here is over half cycle $T/2 = 1/2f$. Thus, the non-dimensional axial irreversible flux should scale as,

$$\varphi^a_{\text{rev}} \approx k_2 \sin\left(\frac{\Delta\phi}{2}\right) \cos\left(\frac{\Delta\phi}{2}\right), \tag{18}$$

where, the flux is non-dimentionalised using $2\pi fap$ as before. The geometric prefactor is $k_2 = \frac{8l_v}{p\pi}$. In the above analysis, we have not considered the actual axial flux that is irreversible but only the flux pumped in unison by two adjacent gaps between villi. We therefore do not expect k_2 to be meaningful when scaling φ^a_{irrev}.

We find an excellent match for the $\Delta\phi$ dependence of our scaling, as seen in fig. 8-d. We observe a strong dependence of Re_m on the prefactor k_2 which is used as a free parameter in the fits. The scaling predicts that the maximum axial flux occurs when $\Delta\phi = \pi/2$. It also shows us that the flux is zero when adjacent villi move exactly in phase $\Delta\phi \to 0$ or exactly out of phase $\Delta\phi \to \pi$.

We thus see that the radial reversible "pumping" is a direct consequence of pendular contractions and the rigid vertical geometry of the villi, and should aid in the localised mixing and absorption of the digesta in the neighbourhood of the villi. The irreversible axial flux however, is a consequence of a travelling wave effect of the propagating contractions, which does not allow for flow reversal into original intervillous gaps. The irreversible axial flux comes at a cost of the reversible part of the axial flow, as irreversible axial flux shows a minimum at $\Delta\phi = \pi/2$. The irreversible axial flux is strongly influenced by inertia, even at small Re_m, while the irreversible radial flux shows strong inertial effects only for larger $\Delta\phi$, and only after a critical Re_m value is crossed. We note that we cannot say much about the scaling for φ^z_{rev} and φ^r_{irrev} at this stage, due to their rather complex dependence on $\Delta\phi$ as well as Re_m.

Generally inertial is the sole driver for irreversibility in oscillating flows [48]. In our case we show though this scaling that even when inertial effects are not considered, irreversibility can arise solely through geometric considerations. Propagating contractions therefore create conditions for "geometric mixing" even in the Stokes limit $Re_m << 1$ [49], where a lagrangian tracer in the fluid would not return to its original position even after the flow driving motion of the boundaries undergoes reversible cyclic motion in a given time period. When small but finite fluid inertia come into play, these irreversibilities are significantly enhanced, such that a large section of the domain starts continuously flowing in the direction of the propagating contractile wave (see fig. 5). This is in direct contrast with the non-propagating contractions which are unable to generate irreversible axial flows and do not induce "geometric mixing".

V. CONCLUSION

In conclusion, our study highlights the significant impact of the coupling between smooth muscle motility and the presence of sub-millimeter structures on the mucosa of the small intestine, the villi, in tuning various flow patterns. These flow patterns can promote independently or not mass transfers between the mucosa and the center of the lumen and axial transport. Scaling laws show that purely geometric concepts can describe some aspects of these flows. However, these flow patterns are also dependent on inertia and viscous effects.

Our study contributes to a better understanding of the physical conditions faced by nano drug delivery systems at the vicinity of the mucosa [50] or which control the spatio-temporal organization of the microbiota which is sensitive to the competition between flow clearance and localized mixing conditions [12, 14, 34, 51, 52].

Growing efforts are required to better understand small intestine motility at the scales of the villi [29], as well as to study flow and mixing phenomena in physiological preparations [8–10, 37, 53, 54]. Understanding mixing phenomena in the small intestine can also promote the emergence of biomimetic active microscale flow reactors for chemical engineering [55, 56].

ACKNOWLEDGMENTS

LRP is part of the LabEx Tec21 (ANR-11-LABX-0030) and of the PolyNat Carnot Institute (ANR-11-CARN-007-01). The authors thank Agence Nationale de la Recherche for its financial support of the project TransportGut, ANR-21-CE45-0015.

---

[1] F. Kong and R. P. Singh, Disintegration of solid foods in human stomach, Journal of food science **73**, R67 (2008).

[2] R. Lentle and C. De Loubens, A review of mixing and propulsion of chyme in the small intestine: fresh insights from new methods, Journal of Comparative Physiology B **185**, 369 (2015).

[3] B. Jeffrey, H. S. Udaykumar, and K. S. Schulze, Flow fields generated by peristaltic reflex in isolated guinea pig ileum: impact of contraction depth and shoulders, American Journal of Physiology-Gastrointestinal and Liver Physiology **285**, G907 (2003).

[4] C. de Loubens, R. G. Lentle, R. J. Love, C. Hulls, and P. W. Janssen, Fluid mechanical consequences of pendular activity, segmentation and pyloric outflow in the proximal duodenum of the rat and the guinea pig, Journal of the Royal Society Interface **10**, 20130027 (2013).

[5] M. D. Sinnott, P. W. Cleary, and S. M. Harrison, Peristaltic transport of a particulate suspension in the small intestine, Applied Mathematical Modelling **44**, 143 (2017).

[6] J. Zha, S. Zou, J. Hao, X. Liu, G. Delaplace, R. Jeantet, D. Dupont, P. Wu, X. D. Chen, and J. Xiao, The role of circular folds in mixing intensification in the small intestine: A numerical study, Chemical Engineering Science **229**, 116079 (2021).

[7] R. J. A. Amedzrovi and N. R. Chevalier, Flow and mixing induced by single, colinear, and colliding contractile waves in the intestine, Physical Review Fluids **in Press** (2022).

[8] P. Janssen, R. Lentle, P. Asvarujanon, P. Chambers, K. Stafford, and Y. Hemar, Characterization of flow and mixing regimes within the ileum of the brushtail possum using residence time distribution analysis with simultaneous spatio-temporal mapping, The Journal of Physiology **582**, 1239 (2007).

[9] K. Schulze and E. Clark, Ink dispersion by sequential contractions in isolated segments of guinea pig ileum and duodenum, Neurogastroenterology & Motility **20**, 1317 (2008).

[10] C. de Loubens, R. G. Lentle, C. Hulls, P. W. Janssen, R. J. Love, and J. P. Chambers, Characterisation of mixing in the proximal duodenum of the rat during longitudinal contractions and comparison with a fluid mechanical model based on spatiotemporal motility data, PloS one **9**, e95000 (2014).

[11] Y. Qin, X. D. Chen, A. Yu, and J. Xiao, New understanding from intestinal absorption model: How physiological features influence mass transfer and absorption, AIChE Journal , e18099.

[12] J. Cremer, I. Segota, C.-y. Yang, M. Arnoldini, J. T. Sauls, Z. Zhang, E. Gutierrez, A. Groisman, and T. Hwa, Effect of flow and peristaltic mixing on bacterial growth in a gut-like channel, Proceedings of the National Academy of Sciences **113**, 11414 (2016).

[13] A. Codutti, J. Cremer, and K. Alim, Changing flows balance nutrient absorption and bacterial growth along the gut, Physical Review Letters **129**, 138101 (2022).

[14] D. Labavić, C. Loverdo, and A.-F. Bitbol, Hydrodynamic flow and concentration gradients in the gut enhance neutral bacterial diversity, Proceedings of the National Academy of Sciences **119** (2022).

[15] M. Gruby and M. Delafond, Resultats des recherches faites sur l'anatomie et les fonctions des villosites intestinales, l'absorption, la preparation et la composition organique du chyle dans les animaux, CR Acad Sci **16**, 1194 (1843).

[16] B. Hambleton, Note upon the movements of the intestinal villi, American Journal of Physiology-Legacy Content **34**, 446 (1914).

[17] E. Kokas, Intestinal villous motility and its regulation (1965).

[18] W. Joyner and E. Kokas, Effect of various gastrointestinal hormones and vasoactive substances on villous motility, Comparative Biochemistry and Physiology Part A: Physiology **46**, 171 (1973).

[19] W. A. Womack, J. A. Barrowman, W. H. Graham, J. N. Benoit, P. R. Kvietys, and D. N. Granger, Quantitative assessment of villous motility, American Journal of Physiology-Gastrointestinal and Liver Physiology **252**, G250 (1987).

[20] H. Westergaard, K. Holtermuller, and J. M. Dietschy, Measurement of resistance of barriers to solute transport in vivo in rat jejunum, American Journal of Physiology-Gastrointestinal and Liver Physiology **250**, G727 (1986).

[21] D. Mailman, W. A. Womack, P. R. Kvietys, and D. N. Granger, Villous motility and unstirred water layers in canine intestine, American Journal of Physiology-Gastrointestinal and Liver Physiology **258**, G238 (1990).

[22] M. D. Levitt, A. Strocchi, and D. G. Levitt, Human jejunal unstirred layer: evidence for extremely efficient luminal stirring, American Journal of Physiology-Gastrointestinal and Liver Physiology **262**, G593 (1992).

[23] W. F. Marshall and C. Kintner, Cilia orientation and the fluid mechanics of development, Current opinion in cell biology **20**, 48 (2008).

[24] C. Brennen and H. Winet, Fluid mechanics of propulsion by cilia and flagella, Annual Review of Fluid Mechanics **9**, 339 (1977).

[25] A. Dauptain, J. Favier, and A. Bottaro, Hydrodynamics of ciliary propulsion, Journal of Fluids and Structures **24**, 1156 (2008).

[26] B. Siyahhan, V. Knobloch, D. de Zélicourt, M. Asgari, M. Schmid Daners, D. Poulikakos, and V. Kurtcuoglu, Flow induced by ependymal cilia dominates near-wall cerebrospinal fluid dynamics in the lateral ventricles, Journal of the Royal Society Interface **11**, 20131189 (2014).

[27] D. J. Smith, T. D. Montenegro-Johnson, and S. S. Lopes, Symmetry-breaking cilia-driven flow in embryogenesis, Annual Review of Fluid Mechanics **51**, 105 (2019).

[28] E. Loiseau, S. Gsell, A. Nommick, C. Jomard, D. Gras, P. Chanez, U. D'ortona, L. Kodjabachian, J. Favier, and A. Viallat, Active mucus–cilia hydrodynamic coupling drives self-organization of human bronchial epithelium, Nature Physics **16**, 1158 (2020).

[29] Y. F. Lim, R. G. Lentle, P. W. Janssen, M. A. Williams, C. de Loubens, B. W. Mansel, and P. Chambers, Determination of villous rigidity in the distal ileum of the possum (trichosurus vulpecula), PloS one **9**, e100140 (2014).

[30] R. Lentle, P. Janssen, C. de Loubens, Y. Lim, C. Hulls, and P. Chambers, Mucosal microfolds augment mixing at the wall of the distal ileum of the brushtail possum, Neurogastroenterology & Motility **25**, 881 (2013).

[31] W. Kunze and J. Furness, The enteric nervous system and regulation of intestinal motility, Annual review of physiology **61**, 117 (1999).

[32] M. Hansen, Neurohumoral control of gastrointestinal motility, Physiological research **52**, 1 (2003).

[33] R. Lentle, G. Reynolds, and P. Janssen, Gastrointestinal tone; its genesis and contribution to the physical processes of digestion, Neurogastroenterology & Motility **25**, 931 (2013).

[34] B. Waclawiková, A. Codutti, K. Alim, and S. El Aidy, Gut microbiota-motility interregulation: insights from in vivo, ex vivo and in silico studies, Gut microbes **14**, 1997296 (2022).

[35] R. Lentle, C. De Loubens, C. Hulls, P. Janssen, M. Golding, and J. Chambers, A comparison of the organization of longitudinal and circular contractions during pendular and segmental activity in the duodenum of the rat and guinea pig, Neurogastroenterology & Motility **24**, 686 (2012).

[36] Y. Wang, J. G. Brasseur, G. G. Banco, A. G. Webb, A. C. Ailiani, and T. Neuberger, A multiscale lattice boltzmann model of macro-to micro-scale transport, with applications to gut function, Philosophical Transactions of the Royal Society A: Mathematical, Physical and Engineering Sciences **368**, 2863 (2010).

[37] Y. Lim, C. de Loubens, R. Love, R. Lentle, and P. Janssen, Flow and mixing by small intestine villi, Food & function **6**, 1787 (2015).

[38] Y. Wang and J. G. Brasseur, Three-dimensional mechanisms of macro-to-micro-scale transport and absorption enhancement by gut villi motions, Physical Review E **95**, 062412 (2017).

[39] Y. Zhang, P. Wu, R. Jeantet, D. Dupont, G. Delaplace, X. D. Chen, and J. Xiao, How motility can enhance mass transfer and absorption in the duodenum: Taking the structure of the villi into account, Chemical Engineering Science **213**, 115406 (2020).

[40] M. Puthumana Melepattu and C. de Loubens, Steady streaming flow induced by active biological microstructures; application to small intestine villi, Physics of Fluids **34**, 061905 (2022).

[41] A. Fishman, J. M. Rossiter, J. Leontini, and M. Homer, Mixing in arrays of villi-like actuators, Physics of Fluids **34**, 094112 (2022).

[42] S. Zhang, W. Liang, C. Li, P. Wu, X. D. Chen, B. Dai, R. Deng, and Z. Lei, Study on the effect of wall structures and peristalsis of bionic reactor on mixing, Chemical Engineering Science **267**, 118373 (2023).

[43] N. Riley, Steady Streaming, Annu. Rev. Fluid Mech. **33**, 43 (2001).

[44] Y. Hosoyamada and T. Sakai, Structural and mechanical architecture of the intestinal villi and crypts in the rat intestine: integrative reevaluation from ultrastructural analysis, Anatomy and embryology **210**, 1 (2005).

[45] I. Ginzburg, F. Verhaeghe, and D. d'Humieres, Two-relaxation-time lattice boltzmann scheme: About parametrization, velocity, pressure and mixed boundary conditions, Communications in computational physics **3**, 427 (2008).

[46] D. Rui and B.-c. Shi, Incompressible multi-relaxation-time lattice boltzmann model in 3-d space, Journal of Hydrodynamics, Ser. B **22**, 782 (2010).

[47] Y. Nakayama and R. Yamamoto, Simulation method to resolve hydrodynamic interactions in colloidal dispersions, Phys. Rev. E **71**, 036707 (2005).

[48] J. Lighthill, Acoustic streaming, Journal of sound and vibration **61**, 391 (1978).

[49] J. Arrieta, J. H. Cartwright, E. Gouillart, N. Piro, O. Piro, and I. Tuval, Geometric mixing, Philosophical Transactions of the Royal Society A **378**, 20200168 (2020).

[50] L. M. Ensign, R. Cone, and J. Hanes, Oral drug delivery with polymeric nanoparticles: the gastrointestinal mucus barriers, Advanced drug delivery reviews **64**, 557 (2012).

[51] S. Labarthe, B. Polizzi, T. Phan, T. Goudon, M. Ribot, and B. Laroche, A mathematical model to investigate the key drivers of the biogeography of the colon microbiota, Journal of theoretical biology **462**, 552 (2019).

[52] D. Hoces, M. Arnoldini, M. Diard, C. Loverdo, and E. Slack, Growing, evolving and sticking in a flowing environment: understanding iga interactions with bacteria in the gut, Immunology **159**, 52 (2020).

[53] S. Kuriu, N. Yamamoto, and T. Ishida, Microfluidic device using mouse small intestinal tissue for the observation of fluidic behavior in the lumen, Micromachines **12**, 692 (2021).

[54] S. Kuriu, N. Yamamoto, and T. Ishida, Development of a microfluidic device to observe dynamic flow around the villi generated by deformation of small intestinal tissue, Lab on a Chip (2023).

[55] M. Liu, J. Xiao, and X. D. Chen, A soft-elastic reactor inspired by the animal upper digestion tract, Chemical Engineering & Technology **41**, 1051 (2018).

[56] V. Hessel, H. Löwe, and F. Schönfeld, Micromixers—a review on passive and active mixing principles, Chemical engineering science **60**, 2479 (2005).

Supplementary Material of Role of propagating pendular villi motility in intestinal advective transport and mixing

Faisal Ahmad[1,2], Rohan Vernekar[1] [*], Stéphane Tanguy[2] and Clément de Loubens[1]
[1]Univ. Grenoble Alpes, CNRS, Grenoble INP, LRP, 38000 Grenoble, France
[2]Univ. Grenoble Alpes, CNRS, UMR 5525, VetAgro Sup, Grenoble INP,
TIMC, 38000 Grenoble, France

June 2023

In this supplementary, we provide a description of the attached villi motility using consecutive frames over the oscillating cycle period from simulated instantaneous velocity data. In these frames, instantaneous velocity vectors are overlayed on top of instantaneous velocity magnitude contours. The scale-bar is indicated in non-dimensional units as u/U_0, and is not normalized across videos in order to see the velocity field in greater detail.

In section S1, we detail 10 frames on the propagating contraction, for varying $\Delta\phi$ and Re_m. Here, we use a periodic domain, and vary the number of simulated villi $N_v = 2\pi/\Delta\phi$. And in section S2, we show 10 frames on non-propagating contractions for varying number of villi with constant intervillous spacing p at $Re_m = 1$.

S1: Frames on propagating contractions

S1.1: effect of phase

To observe the reversible and irreversible flow at different phases $(\pi, \pi/2, \pi/5)$ when $Re_m = 1$, three videos of the velocity field in the domain were made.

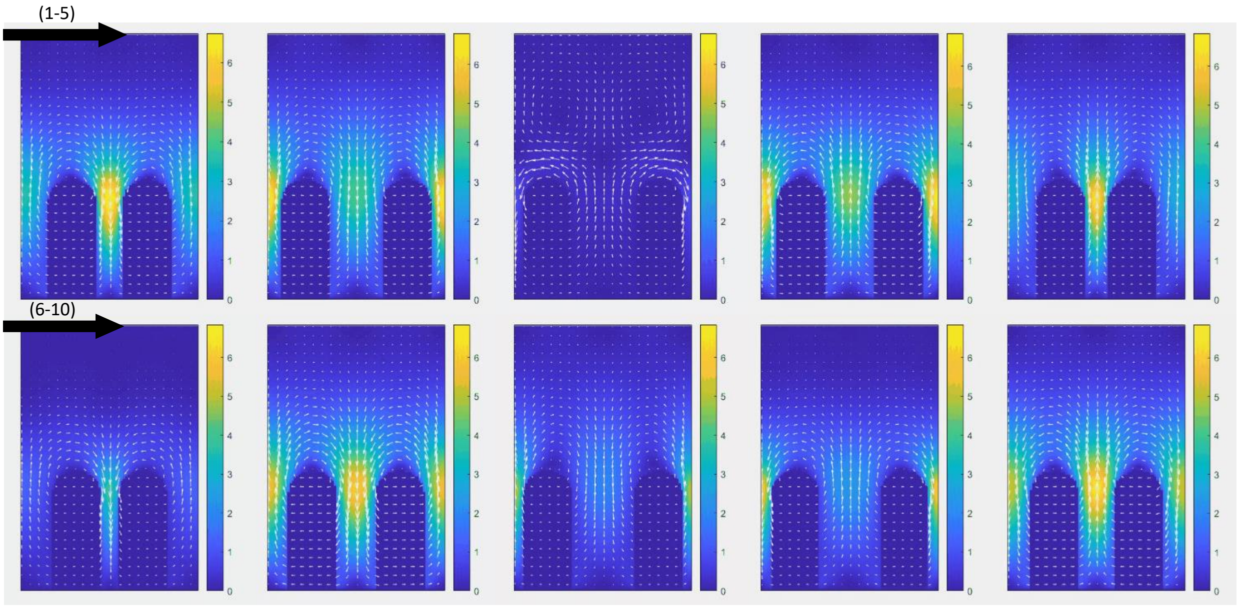

Figure 1: Example of the ten frames when $Re_m = 1$ and $\Delta\phi = \pi$.

---

[*] rohan.vernekar@univ-grenoble-alpes.fr

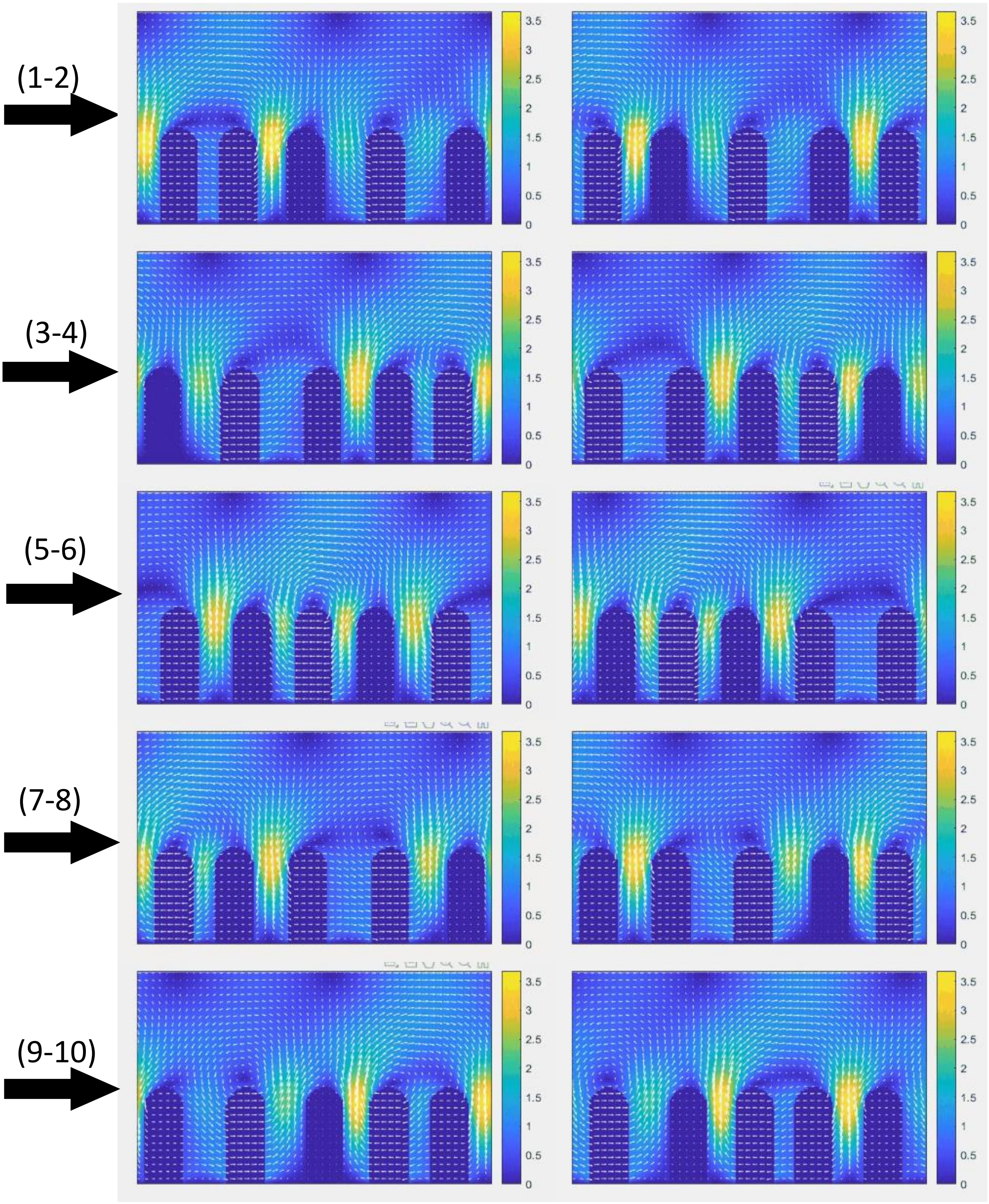

Figure 2: Example of the ten frames when $Re_m = 1$ and $\Delta\phi = 2\pi/5$.

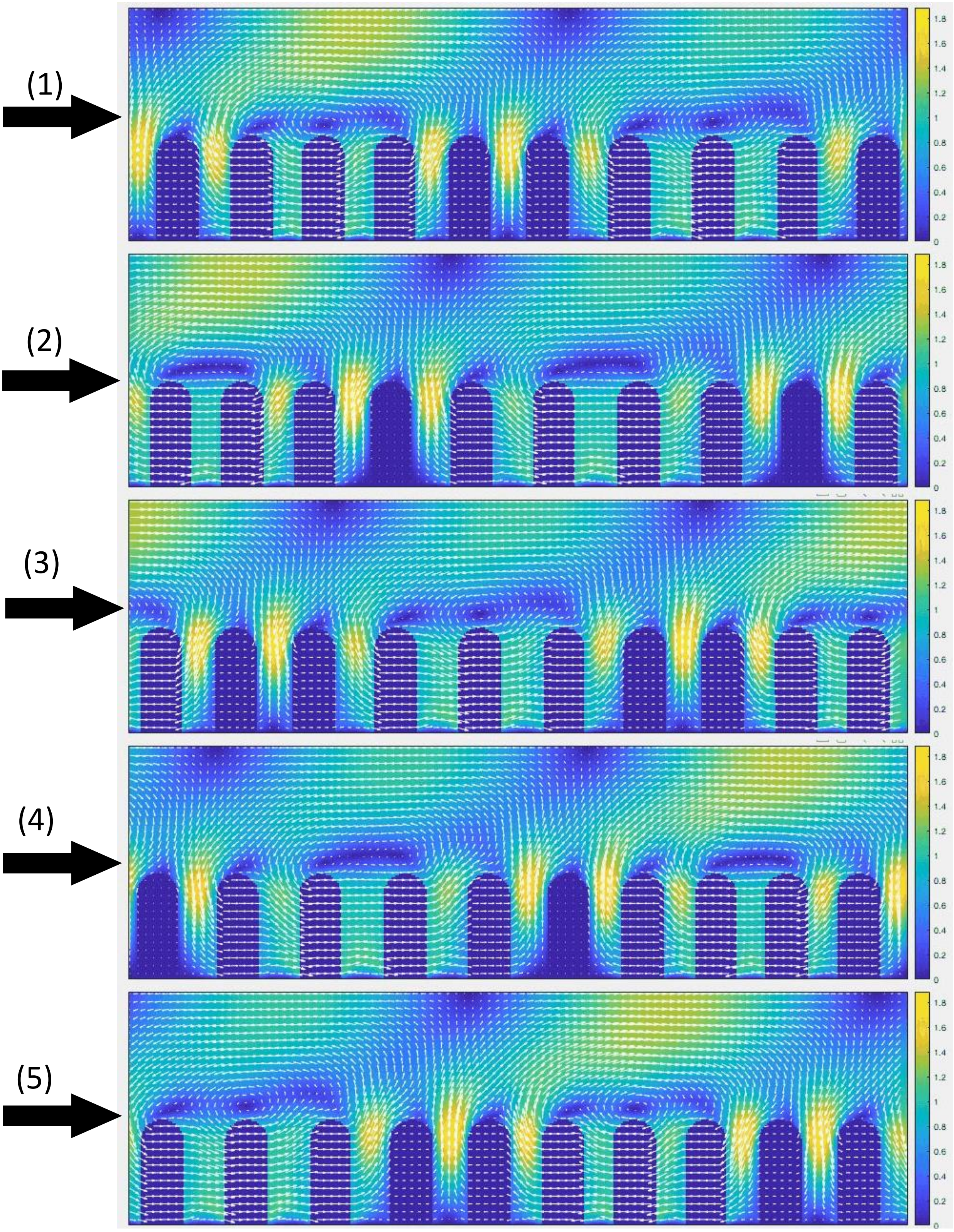

Figure 3: Examples of the first five frames when $Re_m = 1$ and $\Delta\phi = \pi/5$.

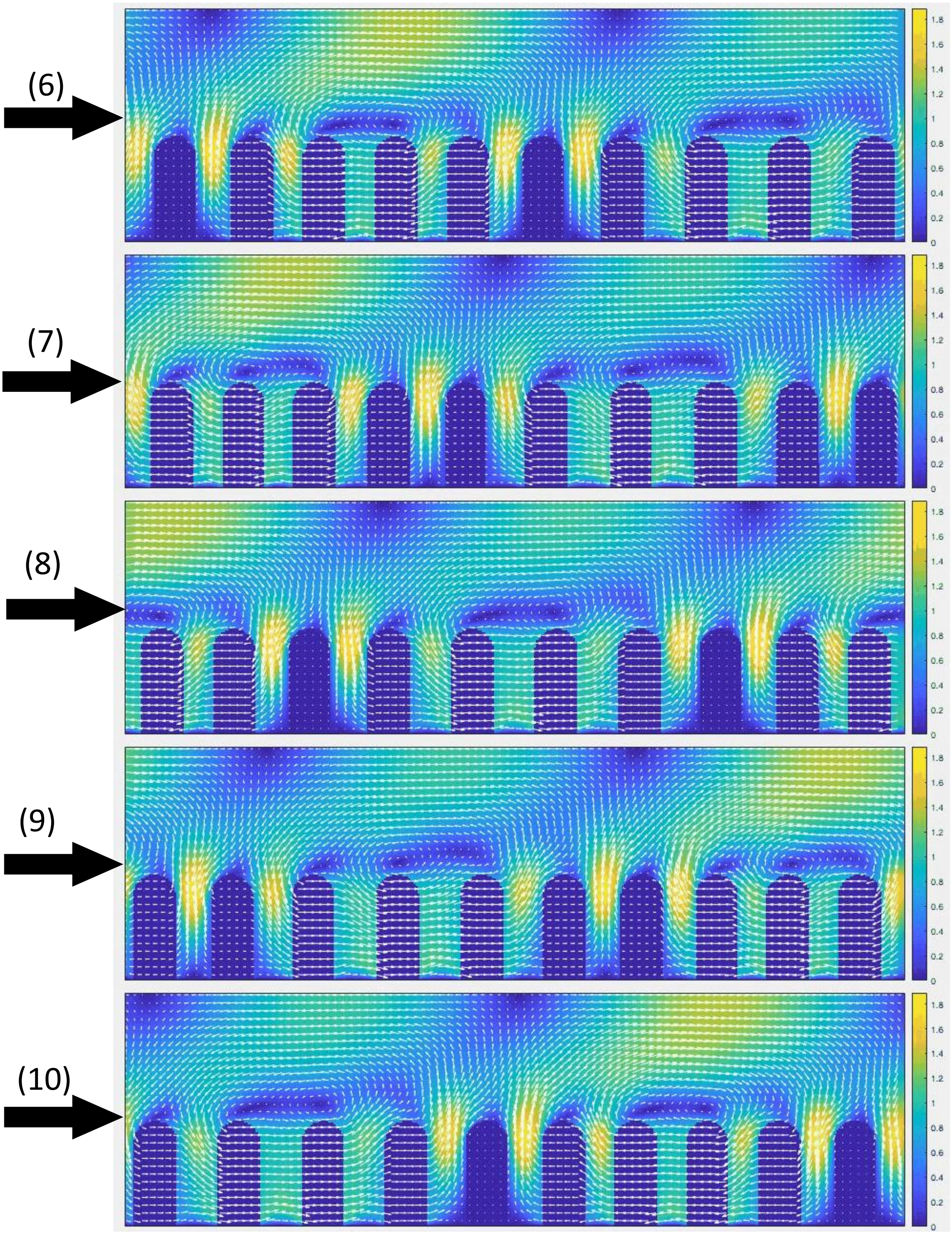

Figure 4: Example of the second five frames when $Re_m = 1$ and $\Delta\phi = \pi/5$.

S1.2: Effect of modified Reynolds number

We also created two additional frame sequences to observe the flow with varying Re_m values of 1 and 5 when $\Delta\phi = 2\pi/3$.

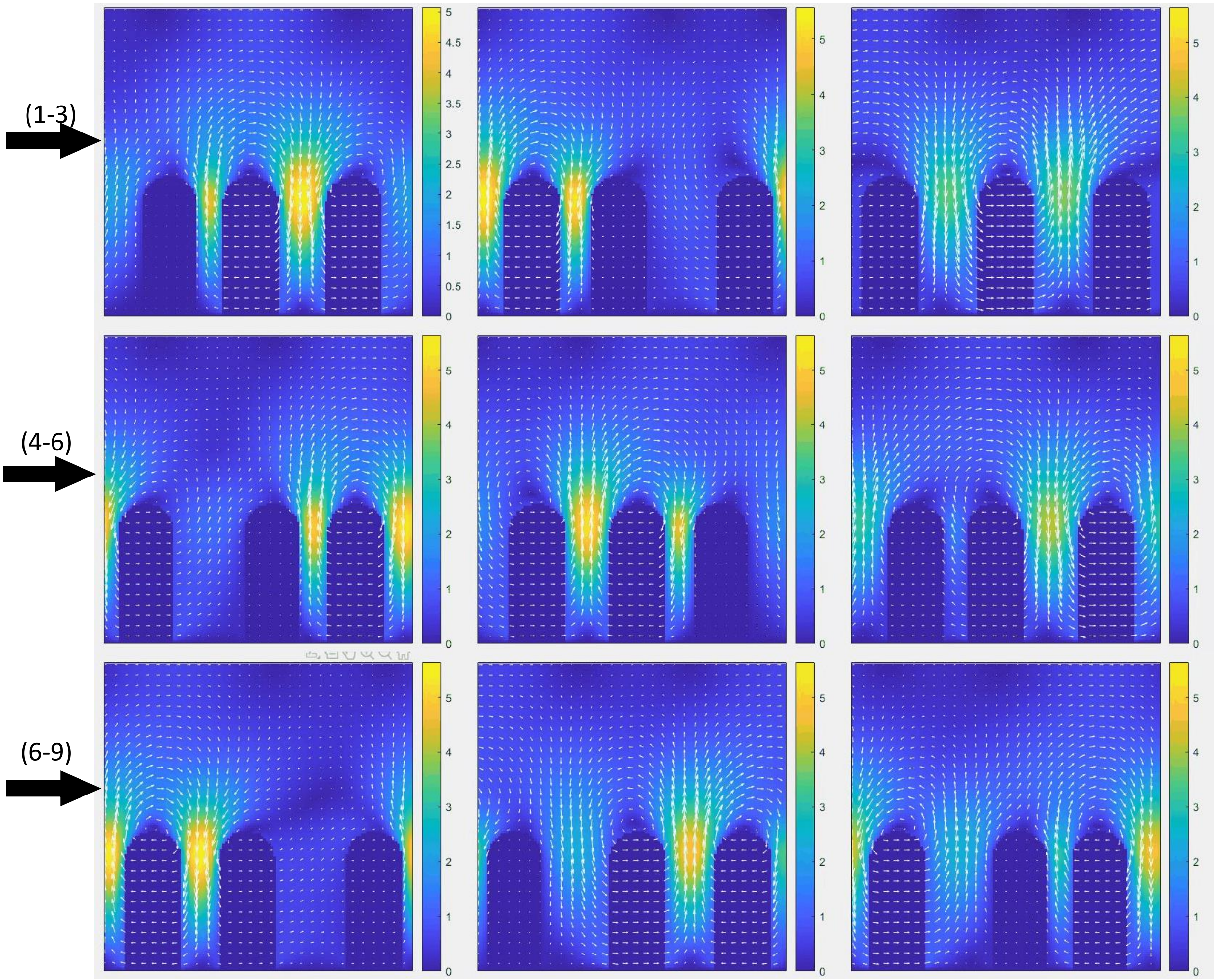

Figure 5: Example of the ten frames when $Re_m = 1$ and $\Delta\phi = 2\pi/3$.

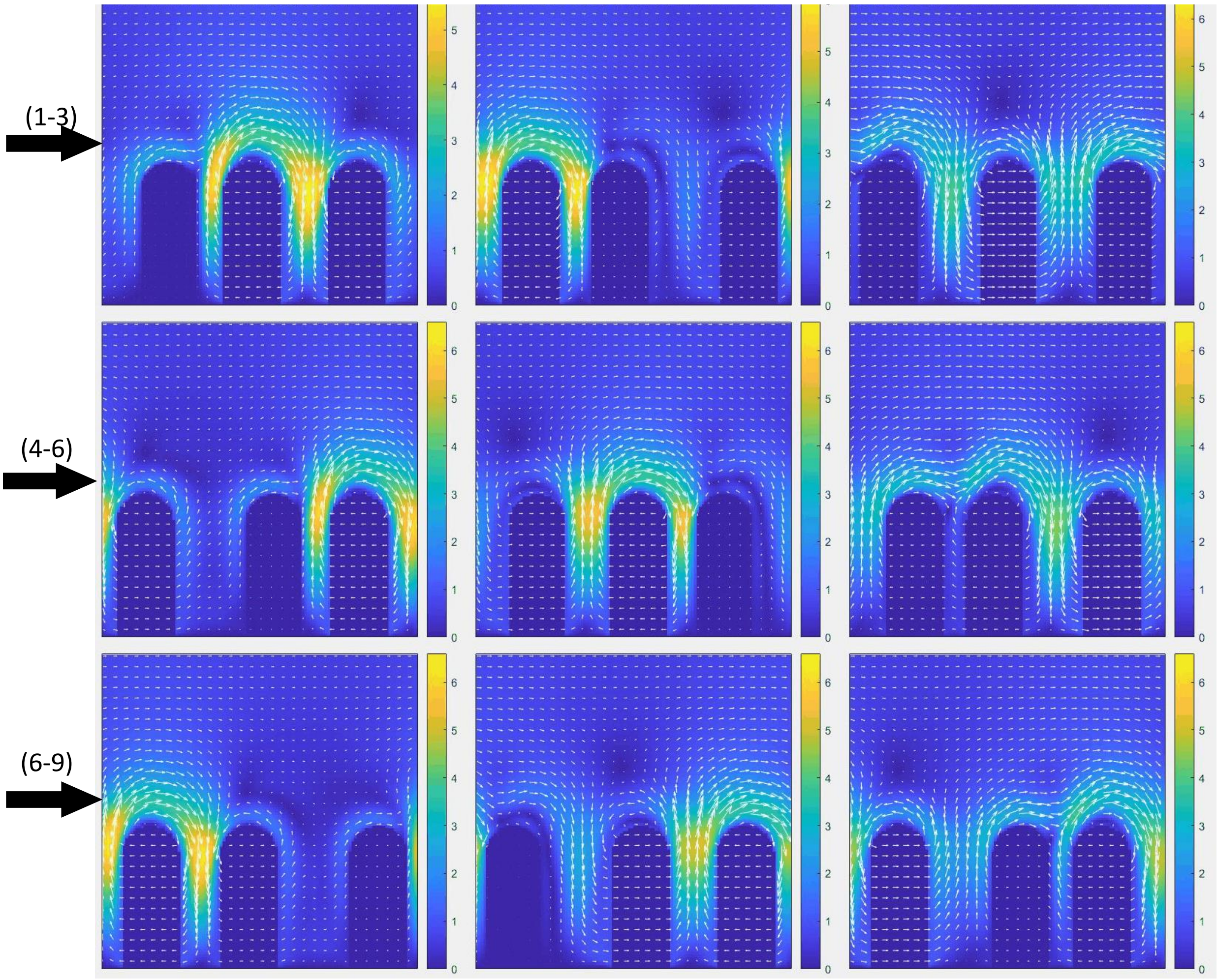

Figure 6: Example of the ten frames when $Re_m = 5$ and $\Delta\phi = 2\pi/3$.

S2: Frames on non-propagating contractions

Two image sequences were also created when the number of villi was 5 and 10.

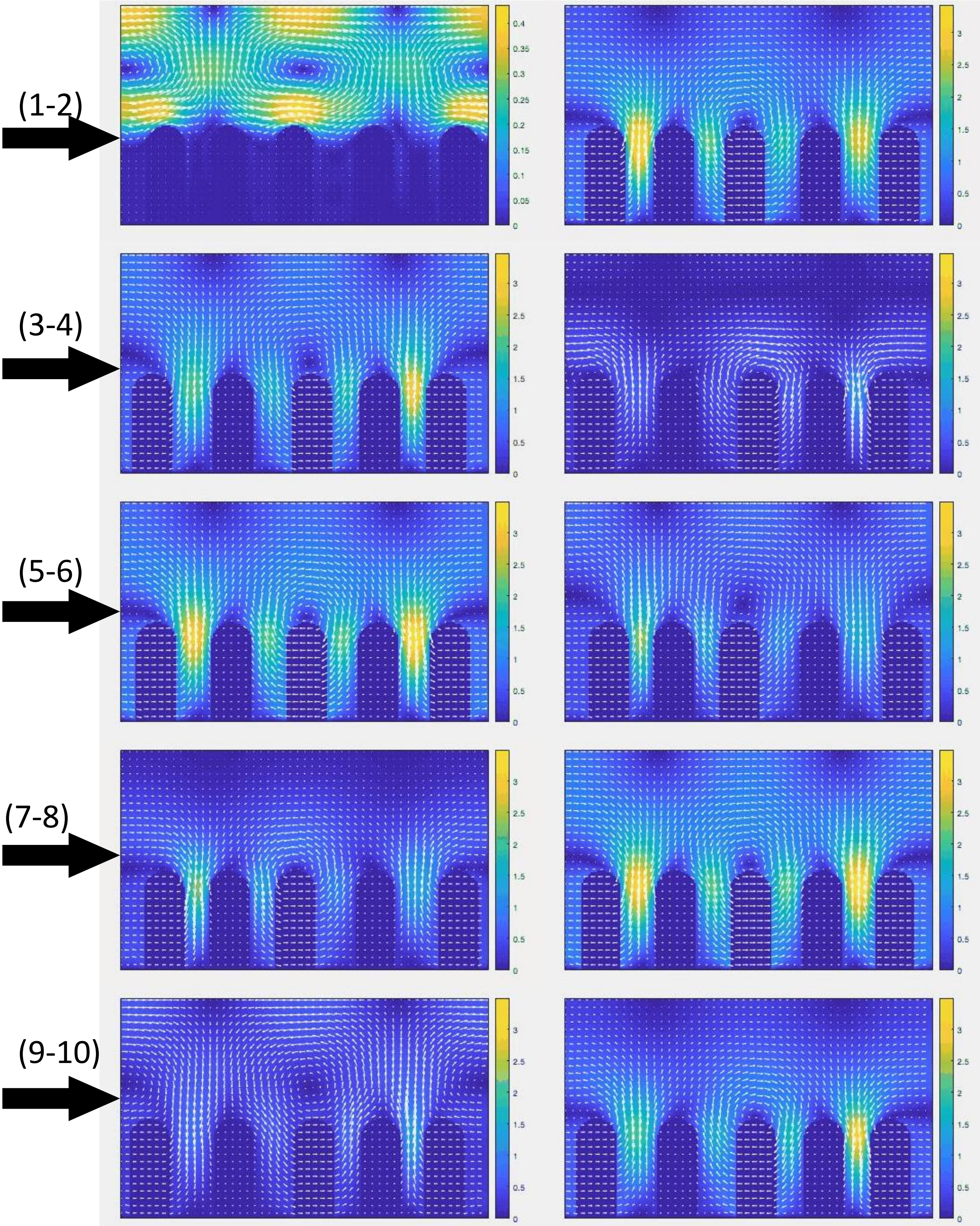

Figure 7: Example of the ten frames when $Re_m = 1$ and $N_v = 5$.

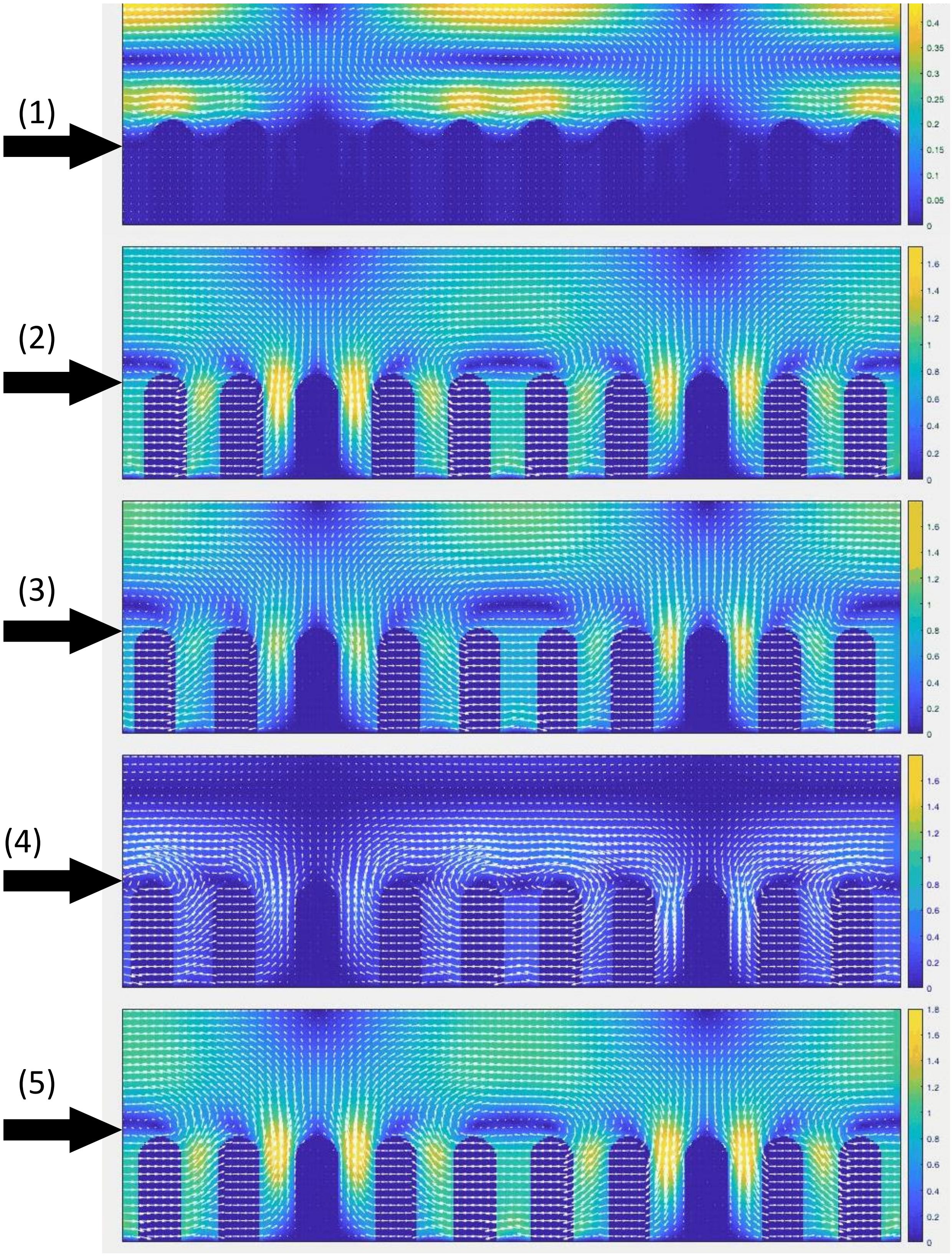

Figure 8: Example of the first five frames when $Re_m = 1$ and $N_v = 10$.

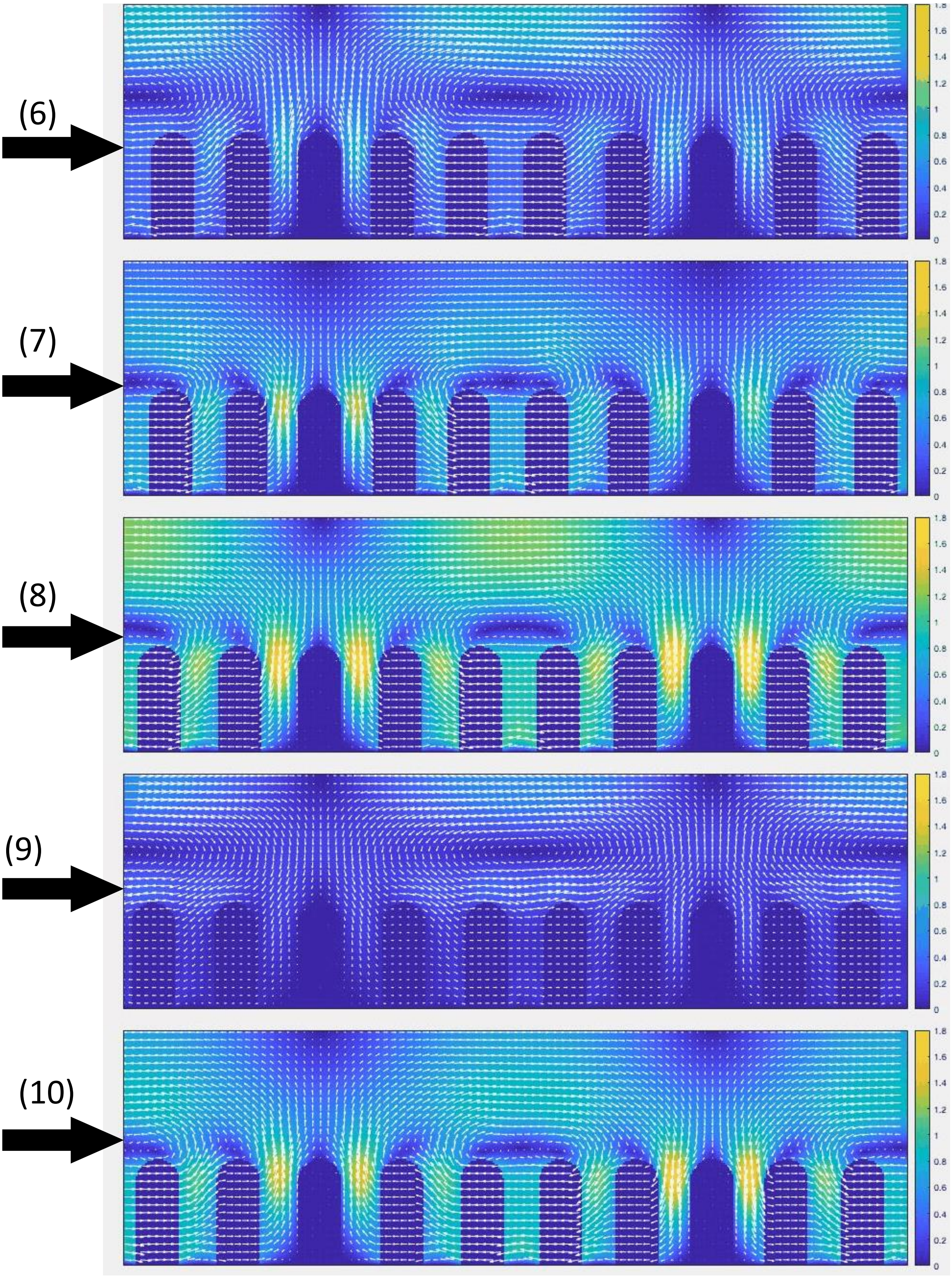

Figure 9: Examples of the second five frames when $Re_m = 1$ and $N_v = 10$.

4.2 Validation of a New Experimental Set-up for Investigating Duodenal Motility at Lumen and Villi Scales

4.2.1 Introduction

The small intestine (SI) is responsible for many crucial tasks, such as the absorption of nutrients and drugs, the mixing of food, and the transfer of digested materials to the blood vessels. The flow behavior and contraction of the muscles (segmentation, peristalsis, and pendular motion) along with the villi in the small intestine play a crucial role in maintaining the mixing, transport, and absorption of nutrients and, the overall well-being of the SI [71, 117]. Contrary to the previous belief that villi in the small intestine primarily serve to passively increase nutrient absorption by expanding the exchange surface between the mucosa and the lumen, several studies have now indicated an active role of these structures in enhancing the absorption process [74, 125].

Researchers have been able to quantify GI tract motility at macroscopic scales in isolated organs. Agnesi et al. experimentally observed bolus to-and-fro motion induced by shallow myogenic waves and used it in their fluid dynamics model [1]. While de Loubens compared the spatiotemporal data of the duodenum with a fluid model and found that mixing near the duodenum wall was enhanced by the longitudinal contraction of the duodenum wall [80]. However, there are very few studies have been conducted to observe fluid flow in the small intestine at microscopic scales while taking villi into consideration. For example, Lim et al. investigated villous rigidity and found that mixing and absorption were confined to the tips of villi under conditions where the villi and intestine were stationary [79]. Also, there are 'gut on chip' set−ups designed recently to observe flow around the villi. These set-ups utilized dead intestinal tissue with no natural motility, therefore, we would not have any information about the villi movement [68, 69].

To investigate the motility of the small intestine at macroscopic level, spatiotemporal (ST) studies have been widely used. Over the past two decades, researchers have utilized ST maps to analyze localized strain rate and mass movement in the closed stomach, small intestine (SI), and colon of rats and pigs [52]. These studies involved removing a portion of the lower GI tract and placing it on a platform with perfused saline water. High-resolution cameras were used to capture images of the organ's activities at a specific frame rate. Following this, strain rate maps as well as longitudinal (L), and diameter (D) maps were generated to aid in understanding tissue contractions and motility [52, 129]. In addition to ST maps analysis, Lentle et al. performed spectral analysis of the data using one-dimensional fast Fourier transformation (FFT) to quantify the propagating contractions along the tissue [71].

Our objectives were to develop a new experimental set-up to assess the overall function, specifically the macroscopic motility of the tissue, and to monitor the villi through video imaging. Since no existing set-up was available to study fluid flow in the small intestine at the level of villi, we designed a specialized experimental set-up within our laboratory. Our set-up is equipped with both signal and image recording tools, ensuring coherence between the results obtained from these two sources. This set-up enables us to visualize the motility of the villi in the isolated intestine under isotonic conditions. To validate our set-up and achieve our objectives, we will conduct a stepwise study. Initially, we will validate the set-up by comparing its results with available research data at the macroscopic level. Furthermore, the future scope of our set-up involves tracking the motion of individual villi and investigating fluid flow, mixing, and absorption at the scale of the villi.

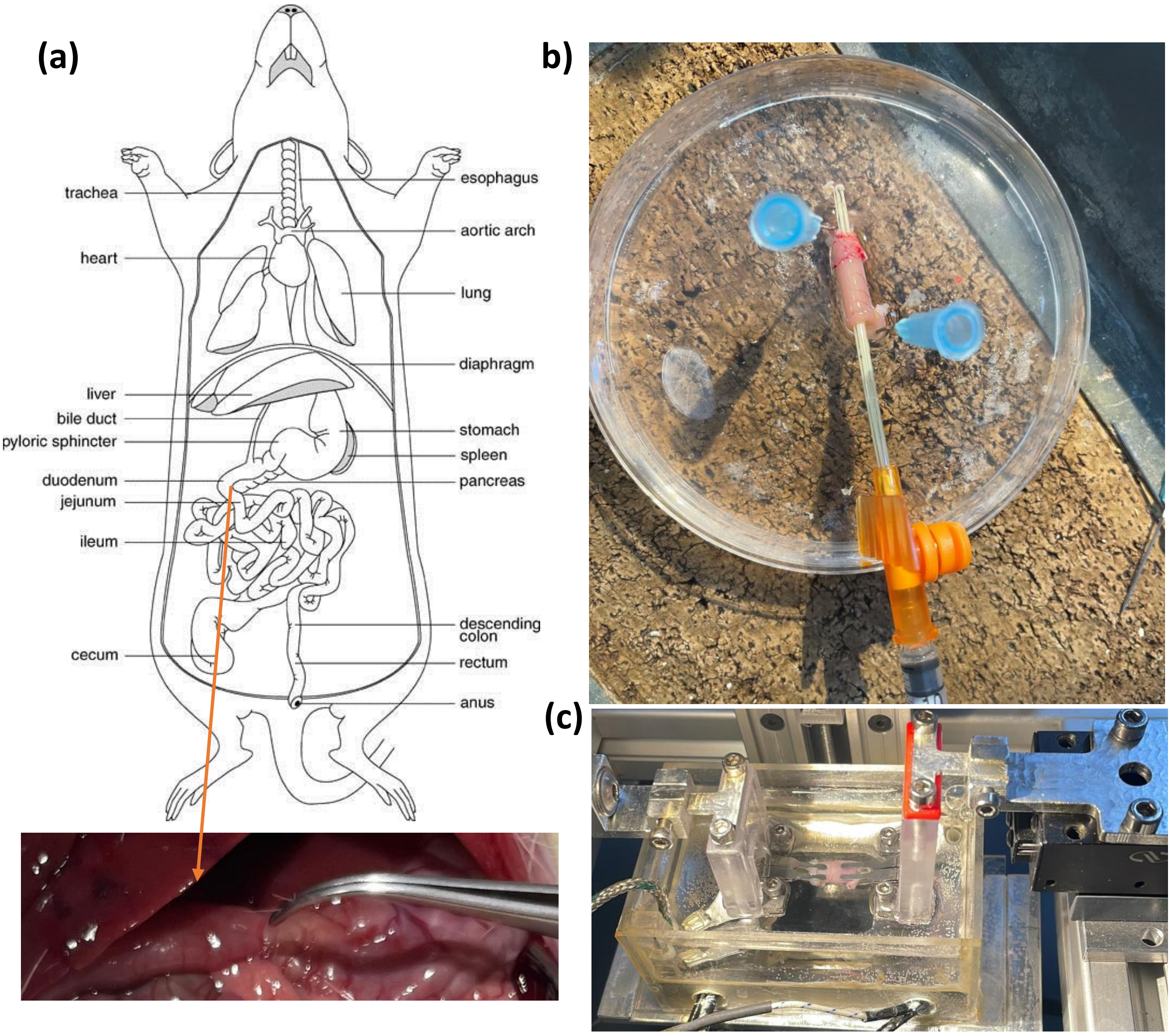

FIGURE 4.1: Tissue preparation before mounting it on motility set-up. (a) Schematic of the rat's organs with the duodenum used (bottom). (b) On the PDMS surface: Cleaning of the duodenum using a plastic needle and stretching it with two other needles to prepare for inserting the clips. (c) Duodenum mounted between the clips.

4.2.2 Materials and methods

Tissue preparation

Nine male Wistar rats (200 g to 300g, 4 months old) were used in this study. The rats were anesthetized with halothane and dissected. Fig. 4.1 illustrates the preparations involved before placing the duodenum in the organ bath. The peritoneal cavity was opened with a vertical incision. The isolated duodenum segments were cut into approximately 1 cm extending from the point just distal to the pyloric sphincter, Fig. 4.1a. The duodenum was then cleaned using a plastic needle and stretched using four needles placed on the Polydimethylsiloxane (PDMS) surface, Fig. 4.1b. Both clips were inserted into the duodenum, and it was then mounted in the organ bath using two screws at each end, Fig. 4.1c. The organ bath was filled with a Kreb's buffer solution (80 mL) with the following composition (in mmolL^{-1}) NaCl, 121; KCl, 4.75; MgSO$_4$·7H$_2$O, 1.19; KH$_2$PO$_4$, 0.4; NaHCO$_3$, 12; HEPES, 10; D$-$glucose, 5.5. To provide a physiological oxygen condition to the duodenal tissue, the organ bath was equipped with a narrow air supply pipe and thermal plates to regulate the temperature of the oxygenated bath at around 37°C before mounting the duodenum. This was critical for maintaining the stability of the small intestine tissue [8, 71].

Design of the experimental set-up

A schematic diagram of the set-up is shown in Fig. 4.2. It consists of a computer unit (connected to the LVDT sensor and the camera), two air bearings (1a, 2b), Variable Differential Transformer (LVDT) mounted on the moving rod (2), organ bath (3), camera (4), pulley (5) attached to a rod which is suspended by the air bearing (1b), weight (6), clips (7), thermal plate (8) with heating wires (9) and a thermocouple (10), and air pump (supply air into the organ bath). The major components were mounted on the main body and secured by three screws (Fig. 4.2), which enabled us to balance and keep the moving end in a free condition when there was no load. Thanks to the air bearings, the free-moving end was crucial to avoid any additional error due to the friction in the displacement data recorded by the LVDT sensor. Any external force or constraint (self-weight of the moving end) on the moving end could cause inaccurate readings and affect the overall accuracy of the experiment. The free end of the set-up also included a designated spot where a string was tied, passing through the pulley (which is mounted on the air bearing as shown in Fig. 4.2a (5). This string is used to apply tension forces on the tissue.

The set-up was designed to monitor tissue stretching in the horizontal plane and consists of a specialized assembly capable of applying a weight up to 1.5 g [8, 25]. To achieve this, the small intestine tissue was attached between two clips, Fig. 4.2b. One clip was fixed in place, while the other was free to move, allowing the tissue to be stretched horizontally for observation. Both clips were temporarily secured by screws on both sides. The movable slider was suspended in the air using a pressurized air bearing with minimal friction, and it was fitted with a linear variable differential transformer (LVDT) to measure the movement of the tissue, Fig. 4.2a (1a,1b,2). The LVDT output was recorded using the software installed on the computer. The movable slider also had a protrusion to which a string was connected and passed through a pulley to apply tensile loads to the tissue. The camera was positioned above the platform to capture videos of the tissue in motion. The camera, the fixed clip, and the organ bath were adjustable in both the horizontal and vertical directions, allowing for precise positioning as needed.

Finally, we used the set-up for two purposes, firstly, to quantify the motility of the tissue in terms of the change in length of the tissue, and secondly, to take pictures of the tissue from above which in turn quantified the motility of the tissue in depth using the strain rate map.

- **Technical descriptions:**
  a - **Air bearing** was used to suspend the moving rod, which was connected to one end of the duodenum using a clip. It comprised a pressure controller which was used to regulate the pressure by adjusting the purity and humidity before allowing it into the air bearing.
  b - **Linear Variable Differential Transformer(LVDT)**: Model number - SM-25-A-KA-G111.111, range - 25 mm, free core-axial cable output sensor with cable output for KAB. This set-up was connected to the moving rod and facilitated the conversion of the change in length of the duodenum into voltage.
  c - **Data acquisition form LVDT** NationalInstruments (NI), model number - USB-6002. It was connected to the computer and recorded the change in length data in millimeters with the help of LabVIEW software, which was developed by our technical team in our lab.
  d - **Temperature regulator**: To maintain the buffer solution at 37°C.
  e - **Camera:**(Basler a2A1920−160umpro, Ahrensburg, Germany) with **zoom lens:** Switar 10mm h16 rx.

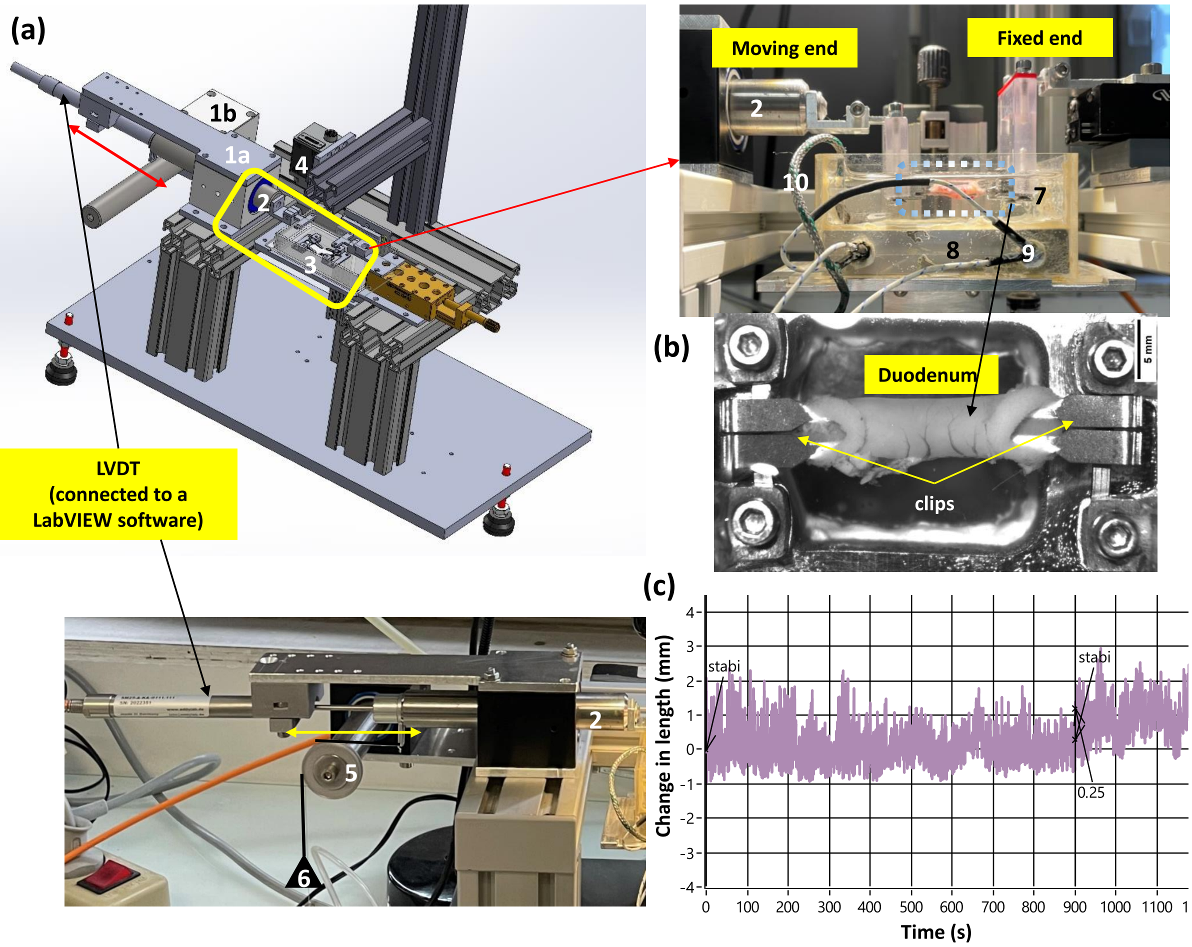

Figure 4.2: Set−up for ex-vivo experiments. **(a)** The set−up consists of an air bearing (1a) that supports a movable rod on the left side (2) inbuild with Linear Variable Differential Transformer (LVDT) is used to measure its displacement. Organ bath (3) consists of a temperature plate (7) with heating wires (9), thermocouple wires (10), and an overhead camera (4). A pulley (5) is mounted on the second air bearing (1b) and is used to apply weights (6). **(b)** An example image of the duodenum obtained under a 1g load is shown, displaying both clips with two screws at each end. Black spots are visible on the duodenum, which is due to the use of graphite powder to enhance contrast. **(c)** The LabVIEW software records the change in length (displacement) of the duodenum and the arrow shows where the stabilization period ends and we introduced 0.25 g weight.

Protocols

Before starting the experiments, we had to ensure the basic settings of the experimental set-up were taken care of, such as performing an accuracy test of the displacement sensor, checking the horizontality of the overall set-up to ensure a balanced moving end, regulating the temperature of the Kreb's solution, air supply, and positioning the camera.

The experiments were conducted under isotonic conditions, as shown in Fig. 4.3a in chronological order. Moreover, Fig. 4.3b shows an example of the displacement data obtained when the load was 0.25 g with mean contraction line, time period (T), and mean amplitude of oscillation (A). The small intestine tissue was carefully prepared and mounted in the organ bath. The movable end allowed it to have horizontal motion in one direction. The camera and displacement sensor were activated during the stabilization period. Due to the nature of the tissue, it was necessary to have a stabilization period of approximately 15 minutes before applying any loads. The duodenum was subjected to weights ranging from 0.25 g to 1.5 g, with increments of 0.25 g, resulting in six different loading conditions. The reason behind choosing weights between 0.25 g and 1.5 g was that we searched previous works in which researchers had conducted experiments in isometric conditions with loads ranging between 0.5 to 1 g [25, 57, 64, 66].

To ensure homogeneous data, the protocol involved recording for 5 minutes under each loading condition. During this period, the most stable spontaneous contraction observed in the last one minute was considered for further analysis.

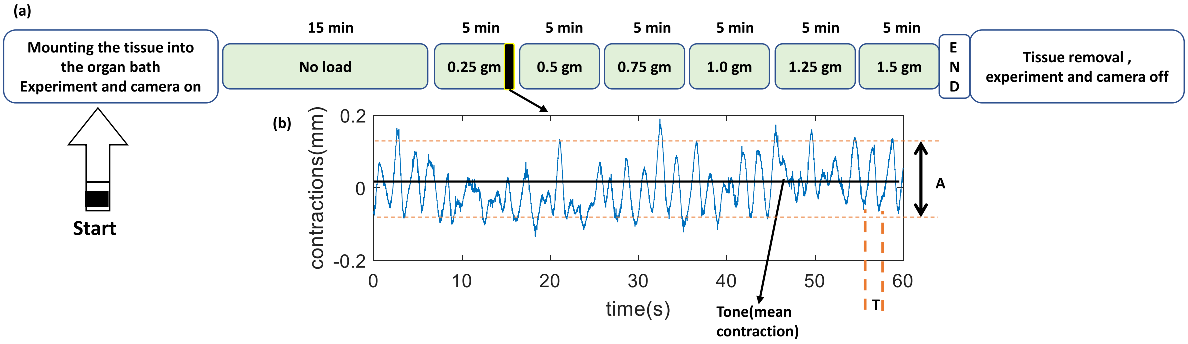

FIGURE 4.3: (a) Protocol: Duodenum under different loading conditions. (b) One-minute data on the spontaneous contractions of isolated rat duodenum just before the end of the 0.25g loading, were used to calculate tone (mean contraction), frequency (or time period (T) between two peaks or valleys), and mean of the amplitude (A).

Data acquisition

With the help of the experimental set-up, we obtained two different sets of data. One was obtained using the moving slider, which was connected to a displacement sensor, and the second was obtained using a fixed video camera situated just above the duodenum. The displacement sensor unit's data were acquired with the help of LabVIEW software that was made by the technical team in our lab (LRP lab). The data primarily consisted of changes in the length of the duodenum, which will be utilized to determine the values of mean contraction, mean amplitude (A), and frequency (measured in contractions per minute) under different loading conditions through data analysis, in the result section.

The movements of the duodenum were continuously monitored by a camera (model number: Basler a2A1920−160umpro, Ahrensburg, Germany) with a zoom lens (Cosmicar 12.5−75 mm) was mounted around 110 mm above the organ bath. The recording software, pylon Viewer, recorded monochrome images at the rate of 10 frames per second. The images had a size of 1920 × 1200 pixels and were saved in uncompressed **TIF** format on the computer. Through this procedure, we obtained high-quality images that were crucial for creating high−fidelity maps with a resolution of 0.033 mm per pixel. For each image sequence of approximately 600 frames, we used a custom MATLAB 2019b image processing code to generate multiple maps that visualized the motility and local strain rate of the duodenum.

Signal analysis

The displacement data consisted of the change in the length of the duodenum from the start to the end of the experiment. In our study, our focus was on analyzing the most stable spontaneous contractions, specifically the last one minute out of the five-minute recordings for each of the six loading conditions.

We used a well-known signal processing technique called peak detection or peak finding. To implement this method, we developed a MATLAB code that detected the minimum and maximum peaks of the signal. Prior to peak detection, we applied a Gaussian filter with a 0.25 smoothing factor to reduce noise in the data and prepare it for analysis. After identifying the peaks and valleys, we utilized standard signal processing techniques to compute the frequency and amplitude of the response. We determined the time interval between peaks and used the mean values of the signal at the peaks and valleys in our calculations. Fig. 4.4 shows a plot of the signal or spontaneous contraction versus time, indicating the location of peaks and valleys that were used to calculate the frequency, amplitude of the signal, and mean contraction or tone of the tissue.

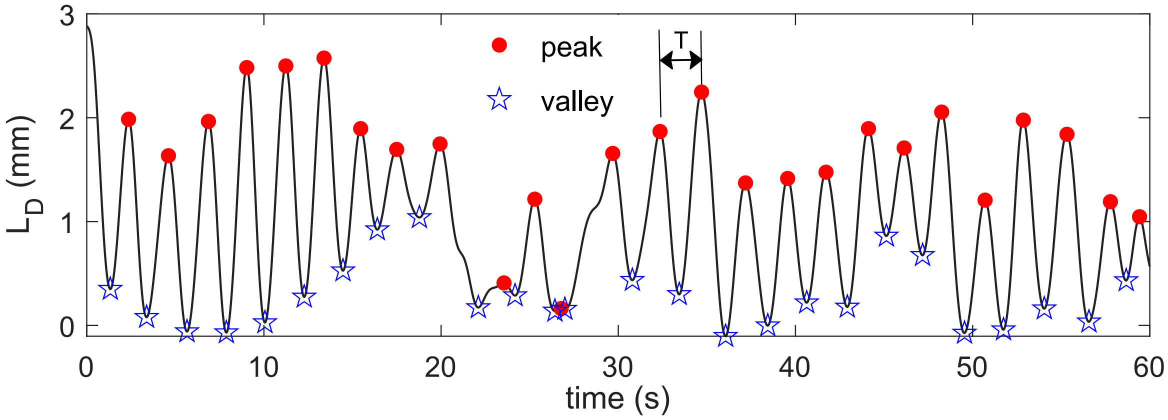

FIGURE 4.4: Signal analysis: change in length of the duodenum (L_d) with respect to time. The red dots and blue polygon show peaks and valleys respectively of the signal, with T representing the time interval between two consecutive peaks or valleys.

Image analysis

The camera captured the tissue (duodenum) movement at the rate of 10 frames per second. Therefore, the complete experiment on each rat consisted of 27000 images. Again, we considered only the last minute of the protocols of all the loading conditions. To enhance contrast along the length of the tissue and achieve clear pictures, we utilized simple fine graphite pieces taken from a pencil. This allowed us to track the movement of the live tissue using a cross-correlation function. To accomplish this, we developed a MATLAB code that divided the concerned domain of the tissue into pixels then we choose 20×20 pixels to track the tissue's movement. Using this method, we were able to obtain the displacement of each square relative to its initial position over a period of one minute. Fig. 4.5a shows the length and zone of the duodenum where we performed the image analysis. We only considered the rectangular region between the two clips and followed all the points in that zone. Fig. 4.5b illustrates the spatiotemporal variation of the length (L(t)) over time, where the ordinate represents the length divided which was divided into 12 squares. The abscissa shows the time axis. Additionally, in Fig. 4.5e, a bar graph displays the magnitude of variation of the points in millimeters (mm).

To calculate the strain rate of the tissue, a series of steps were taken. First, the coordinates of each square were smoothed both temporally and spatially using an image Gaussian filter, Fig. 4.5c. Next, to increase the spatial resolution, the coordinates were interpolated using a piecewise cubic Hermite interpolating polynomial (PCHIP) method, Fig. 4.5d. Then, the coordinates of these interpolated nodes were smoothed once again with an image Gaussian filter to remove any abrupt changes, Fig. 4.5e. This step was necessary to ensure accurate results. Finally, the smoothed data was differentiated to deduce the velocity of each square's length L(t). This led to the strain rate of the whole tissue by differentiating the velocity with respect to the length between two squares. The change in length of the duodenum (L_d) was measured using both an LVDT sensor and image analysis, and the results were compared to validate the image processing algorithm. The comparison is illustrated in Fig. 4.7c in the result Section 4.2.3.

Our algorithm, developed in MATLAB, was designed to process very small squares (Fig. 4.5a). However, it had certain limitations: when the square size was significantly reduced, the degree of cross−correlation ($\bar{r}$) would decrease as well, resulting in inaccurate data for the square position. For instance, when the grid size was 30×30, the value of $\bar{r}$ was 0.913, while it increased to 0.9911 for a grid size of 100×100. Therefore, we found that the algorithm produced reliable results up to the 20×20 dimensions of the square. Despite the limitations due to the contrast, the algorithm enabled us to generate spatiotemporal maps of the duodenum muscle, allowing us to study the tissue′s response to mechanical loading conditions in greater detail. This led to the calculation of the strain rate, which provided insights into the deformation properties (motility) of the tissue. The strain rate represents how quickly the tissue deforms or changes its shape over time in response to an applied load. Specifically, strain rate measures the rate of deformation or strain in the material per unit time. This parameter is important in understanding the mechanical behavior of biological tissues under different loading conditions.

To normalize the results, we used the mean initial length of the duodenum (L_0) at an applied load of 0.25 g which was the first loading condition. The L_0 was different for different duodenal segments, lying between 2.7−7.5 mm. Moving forward, whenever mentioned, the results pertaining to the change in length and amplitude of tissue oscillation will be presented in normalized values.

4.2.3 Results: Effect of loading on duodenal motility

Displacement data

When increasing loads are applied to the intestinal smooth muscle, the overall displacement or change in length of the muscle is expected to increase, as depicted in Fig. 4.6 1a. The first row of Fig. 4.6 (1a-1c) presents the results obtained from measuring the displacement data in the duodenum of nine different rats. The normalized length ($\overline{L_d}$), which indicates the length relative to each loading condition, is shown as the mean ± standard deviation (SD) calculated from the nine rat duodenum samples (Fig. 4.6 1a). The response of the mean length exhibited less variability up to a load of 0.75 g, beyond which the standard deviation ranged between ± 0.4.

Additionally, Fig. 4.6 1b illustrates the normalized amplitude ($\overline{A}$) of the oscillation, which represents the level of duodenal activity at each load. In comparison to the mean length, the mean amplitude displayed nearly the same level of variability (SD = ± 0.1) across all loading conditions, with the highest value observed when the load was 0.75 g.

Furthermore, the frequency (f) response of the duodenal tissues remained constant, with mean values of 25 contractions per minute (cpm) and standard deviations of SD = ± 5. The oscillation frequency, measured in terms of contractions per minute, is depicted in Fig. 4.6 1c.

Image data: Strain rate maps

The second row of Fig. 4.6 presents the results obtained from analyzing the image sequences of four rats, which had better contrast. Figures 4.6 2a-2b depict similar parameters as in Figures 4.6 1a-1b but utilizing the aforementioned image data. It is important to acknowledge that

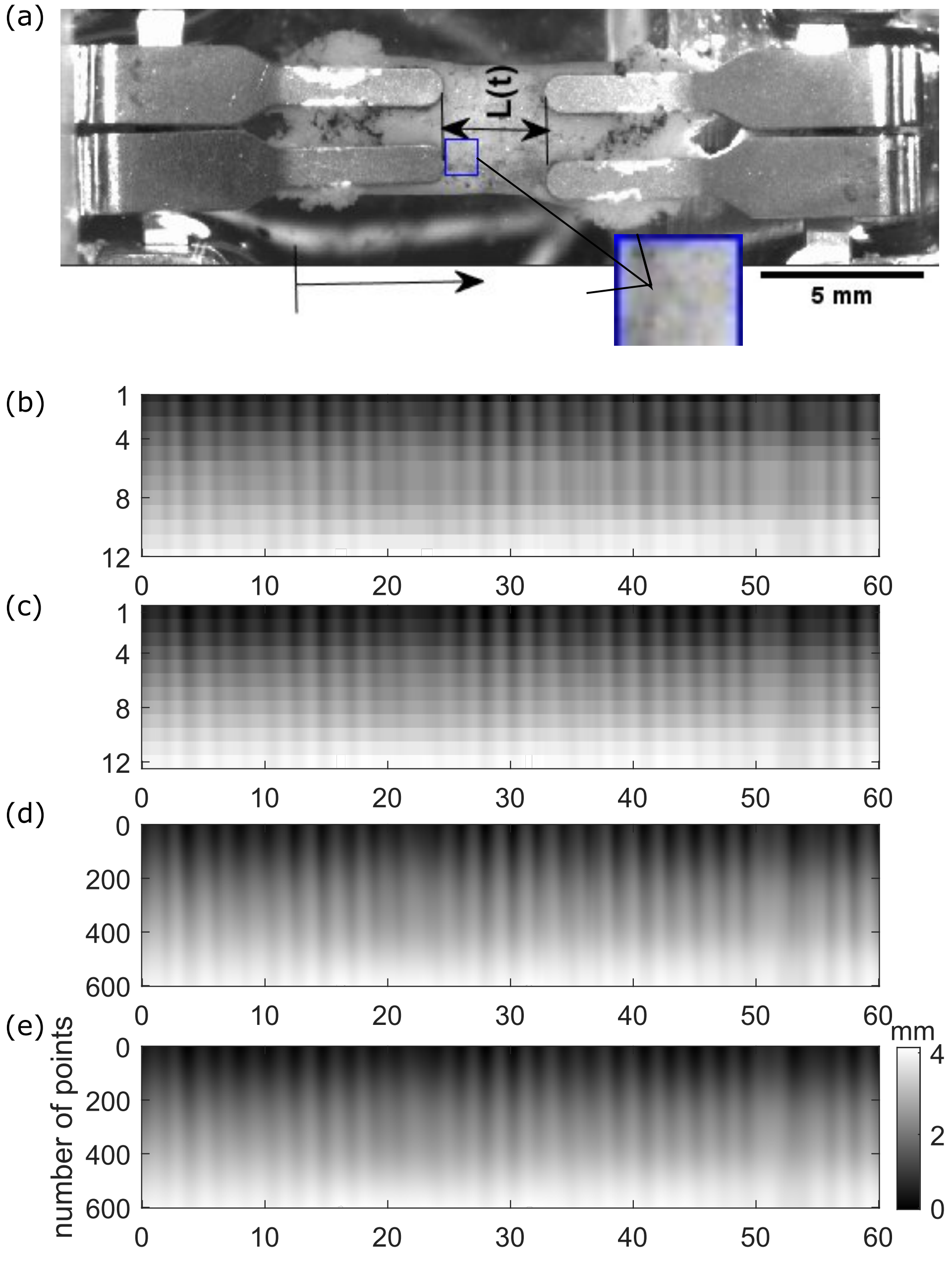

Figure 4.5: Spatiotemporal maps of the change in length (a) Example of the duodenum with the length considered over time, denoted as L(t). The blue zoomed square shows the minimum square dimensions (20×20) considered for the correlation analysis (b) The length was divided into 12 segments, and the changes in length (shown in the bar in mm) over time were graphed. (c) A Gaussian filter was then applied to smooth out any abruptness in the raw data. (d) The smoothed data were then interpolated into 600 points. (e) Again, the Gaussian filter was applied to further suppress any abrupt changes in the length data.

the figures derived from signal analysis and image analysis do not align perfectly due to the different number of rats used in each analysis. However, despite these variations, the patterns and magnitudes of the data displayed similarities between the two sets of analyses.

To visualize motility of tissue locally, strain rate (ST) maps have been used for more than 2 decades [8, 13, 71, 73]. Figures 4.7 1a-3a show the strain rate maps of two different rats at three different loading conditions 0.25 g, 1 g, and 1.5 g.

The ST maps created from duodenal preparations of two rats displayed transversely oriented "stripes", which corresponded to a high-frequency oscillation between a negative and positive strain rate. This phenomenon had previously been identified as fast phasic activity by Lentle et al. [73]. These stripes were either vertical (see Fig. 4.7 1a of both rats) or had a shallow slope (Fig. 4.7 3a of both rats), indicating that the contractions were either propagated instantaneously within a small domain or rapidly over a longer distance. The frequency of these fast phasic contractions was measured to be 30 ± 8 cycles per minute (cpm), and their amplitude was measured to be 35 ± 12 % s^{-1} (Figures 4.7 1b-3b). Although the frequencies of these fast phasic contractions varied somewhat between preparations, along the length of the duodenum, and with time, the overall frequency and amplitude of the contractions did not differ significantly between different loads.

In Fig. 4.7 (panels 1b-3b), we noticed that the strain rate amplitude decreased with loading for both rats. However, the amplitude of the oscillation remained almost constant for rat 1 (top panels 1c-3c), while for rat 2, it increased, which already had a higher magnitude of oscillation (bottom panels 1c-3c) than that of rat 1. This figure suggests that the variation in amplitude response could be attributed to the difference in duodenum length between the rats, with rat 1 having a length of 3.4 mm and rat 2 having a length of 5.8 mm. Figures 4.7 1c-2c show the change in the length of the duodenum obtained from the image analysis and Figures 4.7 1d-2d show the change in length obtained from the signal data. Moreover, the comparison between the responses obtained from the LVDT sensor and the image analysis approach solidified again our method for image analysis (Figures 4.7 c-d).

4.2.4 Discussions: To validate the set-up

Unlike traditional set-ups used to study smooth motility in isometric loading conditions [25, 118], which require the tissue to be fixed in a vertical direction, our set-up allows for stretching the tissue in the horizontal plane with a constant load, making it easier to observe the villi.

The frequency results we obtained were consistent with the findings of previous studies, despite those studies being conducted under isometric conditions [13, 34, 71]. The mean amplitude showed maximum activity when the load was 0.75 g or 1 g, which is consistent with the tension used in previous studies under isometric conditions. This indicates that our experimental set-up is consistent with existing research [57, 64, 66], gave us the confidence to proceed with further image analysis to study the local movement (motility) of the duodenum. Therefore, we used the image data to flow local movements of the tissue at the microscopic scale (Fig. 4.5 a). The image analysis code was able to follow the tissue and showed the results in terms of the ST maps (Fig. 4.7 1a-3a). Moreover, having two modes of data acquisition increase the robustness of the set-up. The displacement data show the global motility of the tissue while the image data record the motility locally. This makes the experimental set-up very useful with confidence to further use the experimental set-up to record villi movements.

In our experimental protocols, we utilized rats with varying lengths of the duodenum and observed diverse motility responses. Apart from the length, these variations might be influenced by certain factors, including the elapsed time between inserting the clips and mounting the tissue in the organ bath, potential excessive stretching during the mounting process, possible tissue erosion during cleaning with a plastic needle, and inherent physiological differences among the duodenum sourced from different rats. Therefore, we found that some rats had larger

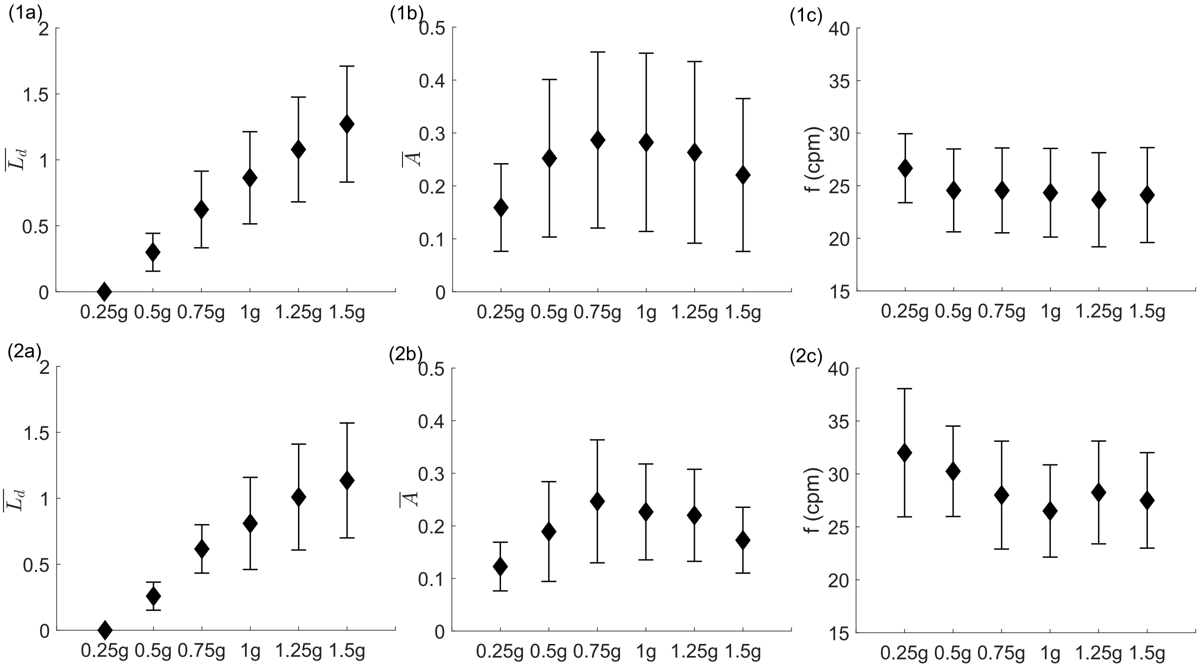

Figure 4.6: Motility response of the isolated duodenum under isotonic conditions. Data from nine different rats obtained from the signal analysis are presented in (a) Normalized change in length of the duodenum, (b) Normalized mean amplitude of the oscillation, and (c) Frequency of oscillation in terms of contractions per minute. The same parameters were analyzed from four rats using the image analysis and are displayed in (2a−2c). The mean value of the data is represented by a black diamond, and the two horizontal lines indicate the standard deviation about the mean value.

oscillating amplitudes than others, and some did not even have stable oscillating amplitudes during the 5−minute recording period at different loading conditions, so, it was important to carefully monitor and analyze the data obtained from each experiment.

4.2.5 Conclusion and perspectives

We have developed a new experimental set-up with the aim of gathering information on small intestinal motility at both macroscopic and validating it. Our study demonstrated the effectiveness of the experimental set-up for investigating duodenum motility. The set-up allowed us to observe tissue activities for an extended period of time (over 1 hour) by recording changes in the length of the entire duodenum and capturing image data that provided a microscopic view of the local movements. The obtained results, including changes in the length of the tissue, frequency (30 ± 8 cpm), and mean normalized amplitude (0.3 ± 0.15) with respect to the loading conditions, were coherent with previous studies [13, 34, 71]. The oscillating amplitude attributed to the degree of duodenal activity was maximum when the load was between 0.75 g and 1 g. Therefore, it inferred the idea behind the 1 g weight or 1 mN force used in isometric conditions by several groups [57, 64, 66].

Furthermore, the strain rate (ST) maps derived from the image analysis of the rat's duodenum offered valuable insights into both macroscopic or global motility and microscopic or localized motility of the tissue. These ST maps revealed distinct patterns at different loading conditions, indicating the occurrence of momentary or sustained propagation of contractions (changes in tissue length) over time and space. Remarkably, the data obtained from the ST

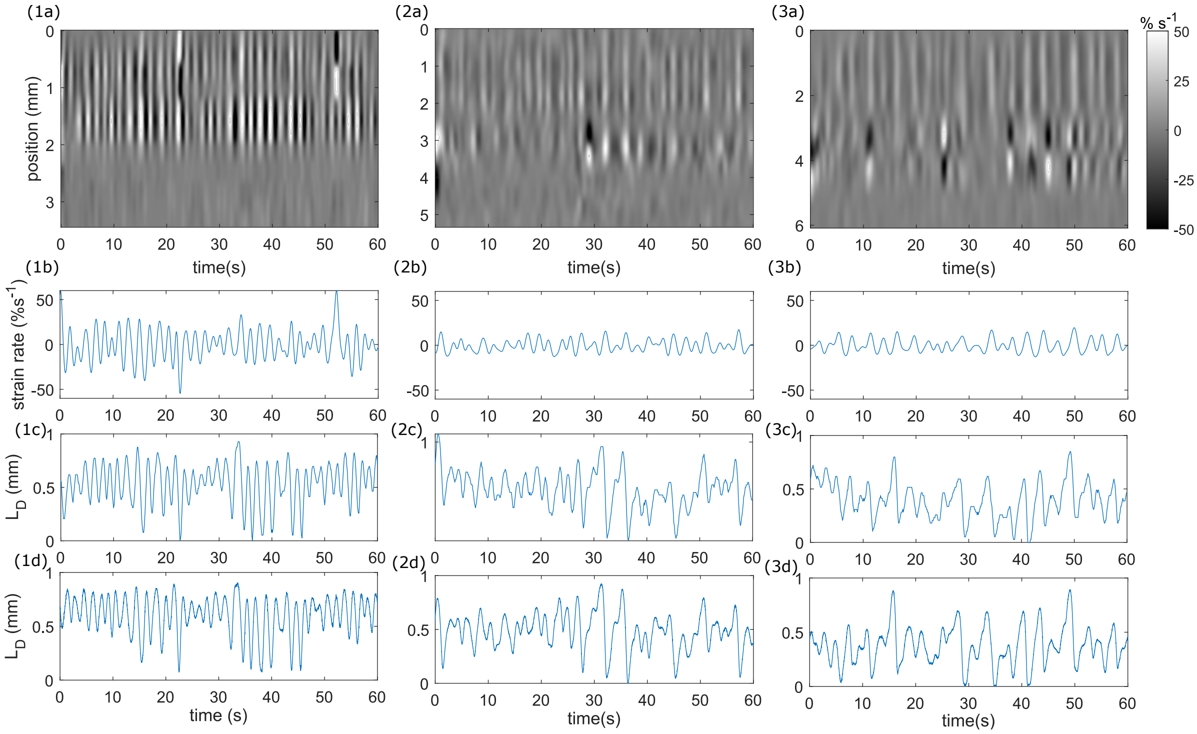

(A) Rat 1

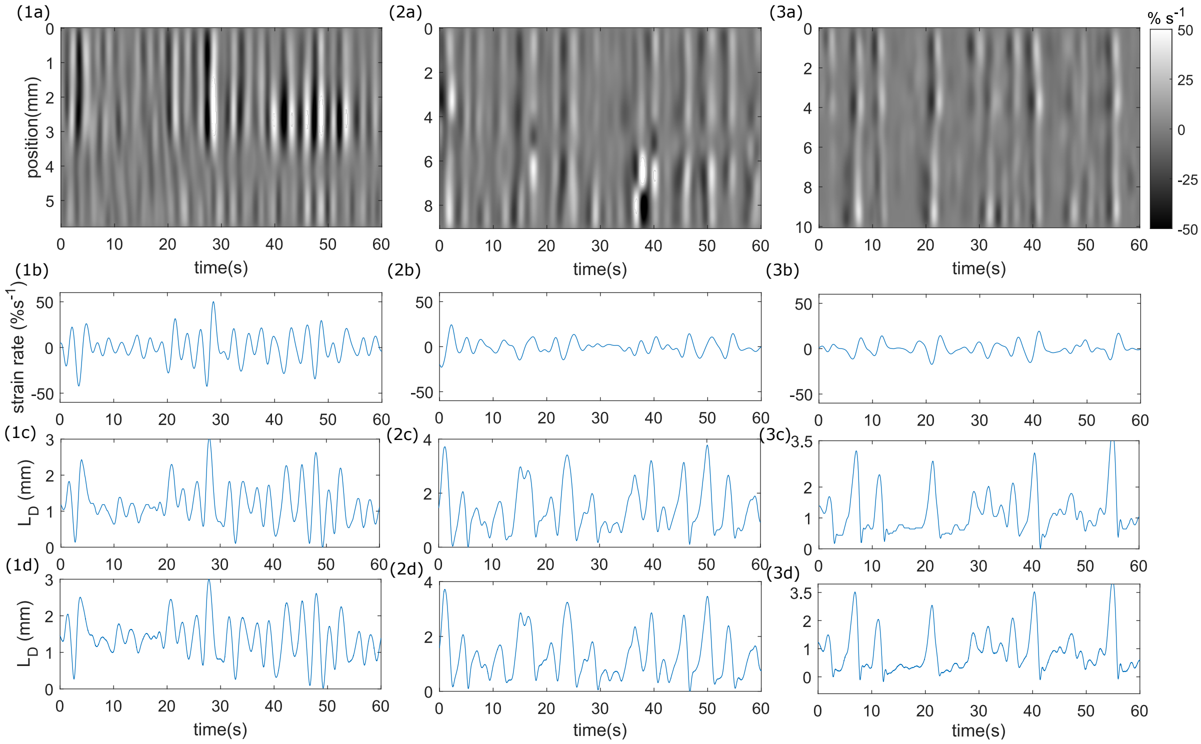

(B) Rat 2

FIGURE 4.7: Strain rate maps and change in length (a) Strain rate (% s^{-1}) maps, abscissa (time in seconds), ordinate (length of the duodenum from the distal pylorus), (b) Strain rate variation of the midpoint lying on the duodenum length, (c) The change in length (mm) obtained from the LVDT sensor, and (d) obtained from the image analysis. From left, three columns (1,2,&3) represent 3 different isotonic loadings 0.25 g, 1g, and 1.5 g.

maps exhibited patterns that were consistent with those found in previous studies conducted by Lentle et al. [71, 73].

The future scope of the set-up will involve performing microscopic-scale recordings of villi movements in open ex-vivo tissue. This will enable the creation of spatiotemporal (ST) maps that have the potential for direct integration into computational fluid dynamics (CFD) models of villi movement in the small intestine. The combination of experimental data with computational modeling has the capability to provide a comprehensive and detailed understanding of the complex mechanisms governing villi motility and its impact on digestion, mixing, and absorption processes. Additionally, this integration opens up avenues for exploring various physiological and pathological scenarios, allowing researchers to investigate the effects of different conditions or interventions on villus movement and optimize treatment strategies for gastrointestinal disorders.

Our set-up offered several advantages concerning the physiological environment for the tissue, the incorporation of its variable length ranging from 2 to 10 mm. Additionally, the set-up enabled the recording of data at both macro and micro scales. However, it is important to acknowledge that our set-up had certain limitations. These limitations included the potential for tissue erosion during the cleaning process, challenges associated with inserting clips into the tissue, and the process of mounting the tissue on the set-up. Overview of the set-up development, results, and, potential future scopes are mentioned below:

- The experimental set-up provided a favorable environment that allowed sufficient time to perform the protocols, keeping the tissue alive for over 1 hour in isotonic conditions.
- The image and the displacement data obtained from the experimental set-up were able to record the motility of the duodenum at both macro and microscopic scales.
- The signal data, which represented the change in length of the duodenum, provided us with the macroscopic amplitude and overall frequency under different isotonic loading conditions. We observed that the maximum amplitude occurred when the applied load ranged between 0.75 g and 1 g with frequency 30 ± 8 in contractions per minute.
- Along with the displacement, the strain rate maps gave information on the duodenum motility with the help of local magnitude and deformation. The results were consistent with the previous studies.
- Further, the experimental set-up can be used with the same protocols and the steps involved in the signal and image analysis tools on the open duodenum with the villi movement to record motility at the microscopic scale.
- By expanding the use of the set-up to include the open duodenum with villi movement, we anticipate the development of more comprehensive and accurate computational fluid dynamics (CFD) models in the future by incorporating the motility results. This will further enhance our understanding of mass transport and mixing in the digestive system.

4.3 Summary

Overall Summary

We developed a two-dimensional computational fluid dynamics (CFD) model to study the motility of villi in the small intestine and utilized a dedicated lattice-Boltzmann flow solver. Based on macroscopic motility data of the rat duodenum, we assigned two different motility patterns to the villi: first, non-propagating longitudinal contractions, and second, longitudinal contractions propagated in the oral-distal direction. Our investigation focused on understanding the impact of these motility patterns on the flow patterns and the transfer of mass both radially and axially within the small intestine. To accomplish this, we analyzed reversible and irreversible flow fields in both cases.
The CFD model of the villi provided us with motivation to observe and record duodenal motility at the villi scale. This enabled us to capture the movements of the villi and analyze the velocity field surrounding them. Consequently, we developed a new ex-vivo experimental set-up to record and study duodenal motility at both macro and micro scales.

- In Section 4.1, by examining two situations, we aimed to understand the impact of different modes of villi motility on flow patterns within the small intestine. Overall, our study highlights the significant impact of the coupling between smooth muscle motility and the presence of sub-millimeter structures (villi) on tuning various flow patterns. These flow patterns can either facilitate or hinder the transfer of mass between the mucosa and the central region of the lumen, as well as the axial transport. This understanding has implications for nano-drug delivery systems near the mucosa and the spatiotemporal organization of the microbiota. Further efforts are needed to enhance our understanding of small intestine motility at the villi scale and investigate flow and mixing phenomena in physiological preparations, which can contribute to the development of biomimetic active microscale flow reactors for chemical engineering.

- In Section 4.2, The experimental set-up created an optimal environment that allowed for sufficient time to conduct protocols while keeping the duodenal tissue alive under isotonic conditions for over an hour. Using this set-up, we were able to obtain image and displacement data, which provided insights into the motility of the duodenum at both macro and microscopic scales. Analyzing the signal data, we observed that the maximum amplitude of duodenal contractions occurred when the applied load ranged between 0.75 g and 1 g with a frequency of 30 ± 8 contractions per minute. Additionally, strain rate maps provided information on duodenum motility, aligning with previous studies. Furthermore, the experimental set-up can be utilized to record the microscopic scale motility of the duodenum with villi movement, utilizing the same protocols and signal and image analysis tools. By incorporating these motility results, we anticipate the future development of more comprehensive and accurate computational fluid dynamics (CFD) models, which will enhance our understanding of mass transport and mixing in the digestive system.

Chapter 5

Conclusion and Future Directions

5.1 General conclusion

The breakdown, mixing, and movement of food within the gastrointestinal (GI) tract occur at multiple scales, spanning from the macro-scale (organ level) to the micro-scale (villi and microvilli). Furthermore, the motility of the GI tract plays a crucial role in the absorption and transportation of nutrients, facilitated by the microscopic movements of the villi and microvilli, particularly in the small intestine. Taking motivation from the potential lying in the utilization of computational fluid dynamics (CFD) models to study the motility of the gastrointestinal (GI) tract, this thesis is mainly focused on the development and use of CFD models to study rectal function during defecation and analyze villi movements in the small intestine. The developed models considered the rheology of the digesta in the small intestine and the feces in the rectum, along with their respective geometries.

In regard to the **fluid mechanical modelling of human defecation**, first, we developed a patient-specific two-dimensional (2D) CFD model, second, we utilized the model on several individuals without any defecation disorder and patients with some pathology and rectal abnormal geometry. The main aim of the model was to be able to simulate the pressure and velocity of the rectum in physiological conditions such as the geometry of the rectum obtained from the video defecography made using neostool which has the same rheology as the normal feces (yield stress fluid). We have used the Lattice Boltzmann method (LBM) as the numerical solver. The model provided insights into defecation mechanics and the underlying causes of defecation disorders.

The model was applied to normal and pathological patients, revealing differences in rectal function. Patients with pathologies exhibited reduced evacuation force and pressure compared to normal patients. The magnitudes of the force (300 N/m) and the pressure (15 kPa) were almost half of the normal individuals. The case of structural abnormalities, such as rectocele, resulted in incomplete defecation depending on its length due to interrupted evacuation force (half of the normal defecation). Just before the end of defecation, one particular case (patient 4) even required the use of a manual maneuver involving the insertion of a finger to achieve complete evacuation of neostool. Unlike in normal patients, the ascending and descending portions of the velocity−force curve do not overlap due to changes in rectal geometry. Moreover, angle of the evacuation force with the vertical axis during defecation remained constant at around 30 °, similar to normal patients. However, just before the end of defecation, there was a range of -70 ° to 50 °, indicating an additional force vector caused by the secondary pressure gradient at the rectoceles. This demonstrated that rectoceles were not entirely passive, as they were unable to generate sufficient force to prevent deformation when the rectal wall was under pressure. Moreover, due to the shear−thinning properties of the fluid flow in the rectum (neostool), resulting in a non-linear relationship between the outlet velocity of neostool and the evacuation force ($V \approx F^{2.4}$). Consequently, the outlet velocity was decreasing fast (more than twice) when the force decreased slightly.

In conclusion, the 2D CFD model provides valuable insights into the mechanics of defecation in individuals with or without disorders, shedding light on both the morphological and functional aspects of the condition. By utilizing the information obtained from the simulation model, healthcare providers can evaluate the effectiveness of different treatment strategies and make informed decisions regarding therapy for patients. The model should serve as a valuable tool in the management of defecation disorders. Its patient-specific approach with physiological data enables a realistic and personalized understanding of rectal evacuation mechanics, facilitating the development of improved treatment strategies.

In the **2D CFD model of oscillating villi** in the duodenal part of the rat small intestine, our focus was on Newtonian fluid flow. We employed the LBM as the numerical method to solve the Navier-Stokes equations, similar to our approach in the rectal model except that we take the D3Q19 technique instead of the D2Q9.

We found from the literature the relative influence of geometric pumping and SSF (steady-streaming-flow) on transport and mixing in the small intestine, especially considering relevant motility data in physiological scenarios. Therefore, our objective was to identify flow phenomena that can be triggered by the motility of the small intestine villi. Utilizing the motility characterization of the rat duodenum and employing a dedicated lattice-Boltzmann flow solver, we conducted an investigation into how the motility of the small intestine villi regulates mass transfer both radially and axially along its length. We analyzed both reversible and irreversible flow fields in two main scenarios: the first scenario involved villi movement induced by longitudinal contractions propagated in the oral-distal direction, while the second scenario focused on non-propagating longitudinal contractions. Through the examination of these two situations, our aim was to gain an understanding of how different modes of villi motility impact the flow patterns within the small intestine.

In the case of propagating contractions, the reversible radial flux reached its maximum at the tip of the villi. It was also at its maximum when the villi were oscillating out of phase, and minimum when they were oscillating in unison. The reversible axial flow, on the other hand, was localized in the center of the lumen at low $\Delta\phi$, but it was adjacent to the villi $(1 < r/l_v < 2)$ as $\Delta\phi$ tended to π.

The reversible radial flux remained almost constant when the modified Reynolds number Re_m varied from 0.1 to 4. However, the reversible axial flux was localized and exhibited oscillatory behavior at the tip of the villi. Furthermore, the instantaneous flow field at $Re_m = 1$ for different phase lags $\Delta\phi$ $(\pi, \pi/2, \pi/5)$ revealed the formation of two unsteady counter-rotating vortices between the apex of the villi and the center of the lumen. These vortices propagated in the opposite direction of the contraction wave, resulting in the ejection and pumping of fluid into the intervillous space. This phenomenon corresponded to the influence of geometric pumping induced by the varying phase difference between adjacent villi. At $Re_m = 5$, the localized vortices not only changed direction but also traveled from one villus to the adjacent villus.

On the other hand, the irreversible radial flux was localized at the tip of the villi and remained almost constant regardless of $\Delta\phi$ and Re_m. However, the axial component increased up to $\pi/2$ $\Delta\phi$ at $Re_m = 1$, and it exhibited a fourfold increase at $Re_m > 1$ when $\Delta\phi = 2\pi/3$.

In contrast, for non-propagating contractions, the reversible radial flux decreased as the length of the domain l_d (or the number of villi N_v) increased, reaching approximately half its magnitude. Conversely, the axial flux increased within the lumen with respect to l_d. The irreversible component of the radial flux displayed variation with respect to the phase change, with its maximum value occurring at $\Delta\phi = \pi/2$. Unlike propagating contractions, there was no net axial flux, and the flow was organized into domains that did not exchange matter with each other. Moreover, the irreversible flow was approximately two orders of magnitude lower than the main flow.

To understand the geometric mixing, scaling laws were derived for the reversible radial and irreversible axial flux. These scaling laws demonstrated that irreversibility can arise solely from geometric considerations, even without considering inertial effects. Propagating contractions, therefore, create conditions for "geometric mixing" even in the Stokes limit ($Re_m << 1$).

In conclusion, our study emphasizes the significant impact of the coupling between smooth muscle motility and the presence of sub-millimeter structures, known as villi, on flow patterns in the small intestine. These flow patterns play a role in promoting mass transfers between the mucosa and the lumen center, as well as axial transport. While scaling laws demonstrate that geometric concepts can partially describe these flows, inertia and viscous effects also influence the observed patterns. Additionally, the absence of an established scale for the maximum values of irreversible radial and reversible axial fluxes is attributed to the combined effects of geometric mixing and fluid inertia.

Our findings contribute to a better understanding of the physical conditions experienced by nano drug delivery systems near the mucosa and the spatiotemporal organization of the microbiota, which is influenced by the competition between flow clearance and localized mixing conditions.

A **new experimental setup** was developed to investigate small intestinal motility at both macroscopic and microscopic scales. The setup allowed for extended observation of tissue activities in the duodenum, capturing changes in length and providing microscopic image data. The obtained results, including changes in tissue length, frequency, and mean normalized amplitude, were consistent with previous studies. Strain rate maps derived from image analysis revealed distinct patterns of motility under different loading conditions. The future scope of the setup involves microscopic-scale recordings of villi movements and their integration into computational fluid dynamics (CFD) models. This integration aims to enhance understanding of the complex mechanisms governing villi motility and its impact on digestion and absorption processes.

In conclusion, our experimental setup has proven to be effective in investigating duodenum motility at both macroscopic and microscopic scales. By recording changes in the length of the duodenum and capturing image data, we were able to observe tissue activities for an extended period of time and gain insights into the local movements. The obtained results, including changes in tissue length, frequency, and amplitude, were consistent with previous studies, validating the accuracy of our setup.

The strain rate (ST) maps derived from image analysis provided valuable information on both global and localized motility of the duodenal tissue. These maps revealed distinct patterns at different loading conditions, indicating the occurrence of contractions over time and space. The patterns observed in the ST maps were consistent with previous studies, further confirming the reliability of our findings.

While our setup offers several advantages, such as a favorable physiological environment and the ability to record data at both macro and micro scales, it is important to acknowledge its limitations. These include the potential for tissue erosion during the cleaning process, challenges associated with inserting clips into the tissue, and the process of mounting the tissue on the setup. These limitations should be taken into account when interpreting the results and planning future experiments.

By combining experimental data with computational modeling, we can gain a comprehensive understanding of the complex mechanisms governing villi motility and its impact on digestion, mixing, and absorption processes. This integration opens up opportunities to explore various physiological and pathological scenarios, enabling researchers to investigate the effects of different conditions or interventions on villus movement and optimize treatment strategies for gastrointestinal disorders.

5.2 Perspectives

Pour faire avancer davantage cette étude, nous pouvons envisager deux voies distinctes. Premièrement, passer de modèles 2D à des modèles 3D. Deuxièmement, les données utilisées dans cls modèles peuvent également être remplacées par des données plus physiologiques obtenues à l'aide de différentes techniques expérimentales. Le modèle de fonctionnement rectal s'est révélé être un outil essentiel pour aborder de nombreuses questions et a ouvert de nouvelles perspectives pour des explorations ultérieures.

- Le modèle rectal qui a été développé pourrait appliqué à une cohorte plus large, y compris des individus avec et sans troubles de la défécation. Cela permettra de collecter des données diverses, qui peuvent s'avérer utiles pour classer les troubles de la défécation et faire progresser les techniques de diagnostic. De plus, ces données seront cruciales pour évaluer l'efficacité du modèle.
- De plus, l'exploration de l'extension du modèle 2D à un modèle 3D, qui peut simuler avec précision la véritable géométrie 3D du rectum avec les propriétés viscoélastiques de la paroi rectale, présente un immense potentiel. Cependant, l'obtention de données 3D bien définies pour le rectum pose des défis et les avancées futures dans les technologies d'imagerie peuvent offrir des données 3D plus précises. Bien que des techniques d'imagerie telles que l'imagerie par résonance magnétique (IRM) et la tomodensitométrie (TDM) soient disponibles, elles présentent des limitations lors de la capture d'images rectales pendant la défécation. De plus, il est crucial de prendre en compte les limitations telles que la disponibilité des données physiologiques et les ressources informatiques nécessaires pour les simulations lors du développement d'un modèle 3D.

En ce qui concerne le modèle de CFD des mouvements des villosités induits par la motilité rectale et le nouveau dispositif expérimental, les travaux futurs suivants peuvent être intéressants à adopter.

- Les villosités ont une structure rigide et elles se déplacent en raison de la motilité intestinale. De plus, elles peuvent être assimilées à des poutres en porte-à-faux et peuvent présenter un mouvement tourbillonnaire par rapport à l'extrémité attachée à l'intestin. Par conséquent, il est possible d'incorporer l'élasticité dans notre modèle des villosités. On s'attend à ce que le transport radial et axial, influencé à la fois par le pompage géométrique et l'inertie du fluide, soit affecté en conséquence.
- Des efforts supplémentaires sont nécessaires pour approfondir notre compréhension de la motilité de l'intestin grêle à l'échelle des villosités et étudier les phénomènes d'écoulement et de mélange dans des préparations physiologiques à l'aide de dispositifs expérimentaux. Ces connaissances peuvent ouvrir la voie au développement de réacteurs d'écoulement microscopique actifs biomimétiques pour le génie chimique.

Bibliography

[1] Richard J Amedzrovi Agbesi and Nicolas R Chevalier. “Flow and mixing induced by single, colinear, and colliding contractile waves in the intestine”. In: *Physical Review Fluids* 7.4 (2022), p. 043101.

[2] Anuj G Agrawal, Ashok Kumar, and Paraag S Gide. “Self emulsifying drug delivery system for enhanced solubility and dissolution of glipizide”. In: *Colloids and Surfaces B: Biointerfaces* 126 (2015), pp. 553–560.

[3] Samad Ahadian et al. “Micro and nanoscale technologies in oral drug delivery”. In: *Advanced drug delivery reviews* 157 (2020), pp. 37–62.

[4] Faisal Ahmad et al. “Flow simulations of rectal evacuation: towards a quantitative evaluation from video defaecography”. In: *Interface Focus* 12.6 (2022), p. 20220033.

[5] Faisal Ahmad et al. “Towards an assessment of rectal function by coupling X-ray defecography and fluid mechanical modelling”. In: *2022 44th Annual International Conference of the IEEE Engineering in Medicine & Biology Society (EMBC)*. IEEE. 2022, pp. 4962–4965.

[6] Peter H Barry and JARED M Diamond. “Effects of unstirred layers on membrane phenomena.” In: *Physiological reviews* 64.3 (1984), pp. 763–872.

[7] Bart LH Bemelmans, Anthony R Mundy, and Michael D Craggs. “Neuromodulation by implant for treating lower urinary tract symptoms and dysfunction”. In: *European urology* 36.2 (1999), pp. 81–91.

[8] Thierry Benard et al. “In vitro analysis of rat intestinal wall movements at rest and during propagated contraction: a new method”. In: *American Journal of Physiology-Gastrointestinal and Liver Physiology* 273.4 (1997), G776–G784.

[9] Prabhu Lal Bhatnagar, Eugene P Gross, and Max Krook. “A model for collision processes in gases. I. Small amplitude processes in charged and neutral one-component systems”. In: *Physical review* 94.3 (1954), p. 511.

[10] Pierre-André Billat et al. “Models for drug absorption from the small intestine: where are we and where are we going?” In: *Drug Discovery Today* 22.5 (2017), pp. 761–775.

[11] L Billiauws et al. “Small intestine motility disorders: Chronic intestinal pseudo-obstruction”. In: *Journal of Visceral Surgery* (2022).

[12] Guy Boeckxstaens et al. “Fundamentals of neurogastroenterology: physiology/motility–sensation”. In: *Gastroenterology* 150.6 (2016), pp. 1292–1304.

[13] M Bouchoucha, T Benard, and M Dupres. “Temporal and spatial rhythmicity of jejunal wall motion in rats.” In: *Neurogastroenterology and motility: the official journal of the European Gastrointestinal Motility Society* 11.5 (1999), pp. 339–346.

[14] M’hamed Bouzidi, Mouaouia Firdaouss, and Pierre Lallemand. “Momentum transfer of a Boltzmann-lattice fluid with boundaries”. In: *Physics of fluids* 13.11 (2001), pp. 3452–3459.

[15] James G Brasseur et al. “Motility and absorption in the small intestines: integrating MRI with lattice Boltzmann models”. In: *2009 IEEE international symposium on biomedical imaging: From nano to macro*. IEEE. 2009, pp. 374–377.

[16] David J Brayden, Mark A Jepson, and Alan W Baird. “Keynote review: intestinal Peyer’s patch M cells and oral vaccine targeting”. In: *Drug discovery today* 10.17 (2005), pp. 1145–1157.

[17] Guillaume Bres, Franck Pérot, and David Freed. “Properties of the lattice Boltzmann method for acoustics”. In: *15th AIAA/CEAS aeroacoustics conference (30th AIAA aeroacoustics conference)*. 2009, p. 3395.

[18] Mark Bush et al. “Defecation 2: Internal anorectal resistance is a critical factor in defecatory disorders”. In: *Techniques in Coloproctology* 16.6 (2012), pp. 445–450.

[19] M Camilleri. “Pharmacology of the new treatments for lower gastrointestinal motility disorders and irritable bowel syndrome”. In: *Clinical Pharmacology & Therapeutics* 91.1 (2012), pp. 44–59.

[20] Jacob Campbell, James Berry, and Yu Liang. “Anatomy and physiology of the small intestine”. In: *Shackelford’s Surgery of the Alimentary Tract, 2 Volume Set*. Elsevier, 2019, pp. 817–841.

[21] Emma V Carrington et al. “Traditional measures of normal anal sphincter function using high-resolution anorectal manometry (HRAM) in 115 healthy volunteers”. In: *Neurogastroenterology & Motility* 26.5 (2014), pp. 625–635.

[22] Mohamad Chaaban, Yousef Heider, and Bernd Markert. “Upscaling LBM-TPM simulation approach of Darcy and non-Darcy fluid flow in deformable, heterogeneous porous media”. In: *International Journal of Heat and Fluid Flow* 83 (2020), p. 108566.

[23] Maria Chatzimina, Georgios Gerogiou, and Andreas Alexandrou. “Wall Shear Rates in Circular Couette Flow of a Herschel-BulkleyFluid”. In: *Applied Rheology* 19.3 (2009), p. 34288.

[24] Ji-Hong Chen et al. “Characterization of simultaneous pressure waves as biomarkers for colonic motility assessed by high-resolution colonic manometry”. In: *Frontiers in physiology* 9 (2018), p. 1248.

[25] Magdalena Chłopecka et al. “The effect of pyriproxyfen on the motoric activity of rat intestine-In vitro study”. In: *Environmental Pollution* 241 (2018), pp. 1146–1152.

[26] Cait M Costello et al. “Synthetic small intestinal scaffolds for improved studies of intestinal differentiation”. In: *Biotechnology and bioengineering* 111.6 (2014), pp. 1222–1232.

[27] David Dahlgren et al. “Direct in vivo human intestinal permeability (Peff) determined with different clinical perfusion and intubation methods”. In: *Journal of pharmaceutical sciences* 104.9 (2015), pp. 2702–2726.

[28] Clément De Loubens et al. “Fluid mechanical consequences of pendular activity, segmentation and pyloric outflow in the proximal duodenum of the rat and the guinea pig”. In: *Journal of the Royal Society Interface* 10.83 (2013), p. 20130027.

[29] Hans Peter Dietz and Andrew Korda. “Which bowel symptoms are most strongly associated with as rectocele?” In: *Australian and New Zealand journal of obstetrics and gynaecology* 45.6 (2005), pp. 505–508.

[30] PG Dinning et al. “Quantification of in vivo colonic motor patterns in healthy humans before and after a meal revealed by high-resolution fiber-optic manometry”. In: *Neurogastroenterology & Motility* 26.10 (2014), pp. 1443–1457.

[31] Ivo Ditah et al. "Prevalence, trends, and risk factors for fecal incontinence in United States adults, 2005–2010". In: *Clinical Gastroenterology and Hepatology* 12.4 (2014), pp. 636–643.

[32] Douglas A Drossman. "The functional gastrointestinal disorders and the Rome III process". In: *gastroenterology* 130.5 (2006), pp. 1377–1390.

[33] Dominique d'Humières and Irina Ginzburg. "Viscosity independent numerical errors for Lattice Boltzmann models: From recurrence equations to "magic" collision numbers". In: *Computers & Mathematics with Applications* 58.5 (2009), pp. 823–840.

[34] Ahmed F El-Yazbi, Richard Schulz, and Edwin E Daniel. "Differential inhibitory control of circular and longitudinal smooth muscle layers of Balb/C mouse small intestine". In: *Autonomic Neuroscience* 131.1-2 (2007), pp. 36–44.

[35] J Fallingborg et al. "pH-profile and regional transit times of the normal gut measured by a radiotelemetry device". In: *Alimentary pharmacology & therapeutics* 3.6 (1989), pp. 605–614.

[36] A Farag. "Use of the Hagen-Poiseuille law: a new mathematical approach for the integration and evaluation of anorectal physiological testing in patients with faecal incontinence and pelvic dyschezia and in normal controls". In: *European surgical research* 30.4 (1998), pp. 279–289.

[37] Ahmed Farag. "The use of flow equation in functional coloproctology: a new theory in anorectal physiology". In: *Pelviperineology* 28.1 (2009), p. 17.

[38] Ahmed Farag et al. "The Functional Luminal Imaging Probe (FLIP): A Good Tool for Adjustment of anal Canal Dimensions During Operative Management of Fecal Incontinence". In: *Surgical Innovation* (2023), p. 15533506231157438.

[39] Aaron Fishman et al. "Mixing in arrays of villi-like actuators". In: *Physics of Fluids* 34.9 (2022), p. 094112.

[40] John S Fordtran, Floyd C Rector, Norman W Carter, et al. "The mechanisms of sodium absorption in the human small intestine". In: *The Journal of clinical investigation* 47.4 (1968), pp. 884–900.

[41] LL Frase et al. "Enhanced glucose absorption in the jejunum of patients with cystic fibrosis". In: *Gastroenterology* 88.2 (1985), pp. 478–484.

[42] Leslie P Gartner and James L Hiatt. "Color textbook of histology (3rd)". In: *Ann Arbor, WB. Saunders Co. p* (2007), pp. 345–65.

[43] Irina Ginzbourg and D d'Humières. "Local second-order boundary methods for lattice Boltzmann models". In: *Journal of statistical physics* 84.5 (1996), pp. 927–971.

[44] Beverley Greenwood-Van Meerveld et al. "Long-term expression of corticotropin-releasing factor (CRF) in the paraventricular nucleus of the hypothalamus in response to an acute colonic inflammation". In: *Brain research* 1071.1 (2006), pp. 91–96.

[45] Hans Gregersen. "Fecobionics: a novel bionic test of anorectal function and defecation". In: *Gastroenterology* 152.5 (2017), S317.

[46] Hans Gregersen et al. "Anorectal volume–pressure relations, contraction work, and flow during defecation". In: *Biomechanics and Modeling in Mechanobiology* 21.5 (2022), pp. 1613–1621.

[47] D. Gruby and J. Delafond. "Recherches sur les animalcules se développant en grand nombre dans l'estomac et dans les intestines, pendant la digestion des animaux herbivores et carnivores". In: *Comptes rendus des séances de l'Académie des Sciences* 17 (1843), pp. 586–588.

[48] Simon Gsell, Umberto d'Ortona, and Julien Favier. "Lattice-Boltzmann simulation of creeping generalized Newtonian flows: Theory and guidelines". In: *Journal of Computational Physics* 429 (2021), p. 109943.

[49] BF Hambleton. "Note upon the movements of the intestinal villi". In: *American Journal of Physiology-Legacy Content* 34.4 (1914), pp. 446–447.

[50] Allan K Hardacre et al. "Predicting the viscosity of digesta from the physical characteristics of particle suspensions using existing rheological models". In: *Journal of The Royal Society Interface* 15.142 (2018), p. 20180092.

[51] Paul T Heitmann et al. "Understanding the physiology of human defaecation and disorders of continence and evacuation". In: *Nature Reviews Gastroenterology & Hepatology* 18.11 (2021), pp. 751–769.

[52] GW Hennig et al. "Quantitative analysis of peristalsis in the guinea-pig small intestine using spatio-temporal maps". In: *The Journal of physiology* 517.2 (1999), pp. 575–590.

[53] Caitlin W Hicks et al. "Are rectoceles the cause or the result of obstructed defaecation syndrome? A prospective anorectal physiology study". In: *Colorectal Disease* 15.8 (2013), pp. 993–999.

[54] Caitlin W Hicks et al. "In patients with rectoceles and obstructed defecation syndrome, surgery should be the option of last resort". In: *Surgery* 155.4 (2014), pp. 659–667.

[55] Corrin Hulls et al. "Spatiotemporal mapping of ex vivo motility in the caecum of the rabbit". In: *Journal of Comparative Physiology B* 182.2 (2012), pp. 287–297.

[56] Saeed Jafari, Ryoichi Yamamoto, and Mohamad Rahnama. "Lattice-Boltzmann method combined with smoothed-profile method for particulate suspensions". In: *Physical Review E* 83.2 (2011), p. 026702.

[57] Gaurav Jain et al. "Development of an ex vivo model for pharmacological experimentation on isolated tissue preparation". In: *Journal of Advanced Pharmaceutical Technology & Research* 3.3 (2012), p. 176.

[58] Sasan Jalili-Firoozinezhad et al. "A complex human gut microbiome cultured in an anaerobic intestine-on-a-chip". In: *Nature biomedical engineering* 3.7 (2019), pp. 520–531.

[59] P-H Kao and R-J Yang. "An investigation into curved and moving boundary treatments in the lattice Boltzmann method". In: *Journal of Computational Physics* 227.11 (2008), pp. 5671–5690.

[60] Tugrul T Kararli. "Comparison of the gastrointestinal anatomy, physiology, and biochemistry of humans and commonly used laboratory animals". In: *Biopharmaceutics & drug disposition* 16.5 (1995), pp. 351–380.

[61] GS Kassab et al. "Novel bionics developments in gastroenterology: fecobionics assessment of lower GI tract function". In: *Physiological Measurement* 42.6 (2021), 06TR01.

[62] Christopher Keating et al. "Ageing and gastrointestinal sensory function: altered colonic mechanosensory and chemosensory function in the aged mouse". In: *The Journal of Physiology* 594.16 (2016), pp. 4549–4564.

[63] Hyun Jung Kim et al. "Human gut-on-a-chip inhabited by microbial flora that experiences intestinal peristalsis-like motions and flow". In: *Lab on a Chip* 12.12 (2012), pp. 2165–2174.

[64] Timo Kirschstein et al. "Dopamine induces contraction in the proximal, but relaxation in the distal rat isolated small intestine". In: *Neuroscience letters* 465.1 (2009), pp. 21–26.

[65] Eszter Kokas. *Intestinal villous motility and its regulation.* 1965.

[66] Gokhan Koyluoglu et al. “Alterations in spontaneous contractions of rat ileum and jejunum after peritonitis”. In: *European journal of pharmacology* 580.1-2 (2008), pp. 250–255.

[67] Hiroyuki Kozu et al. “Analysis of flow phenomena in gastric contents induced by human gastric peristalsis using CFD”. In: *Food Biophysics* 5 (2010), pp. 330–336.

[68] Satoru Kuriu, Naoyuki Yamamoto, and Tadashi Ishida. “Development of a microfluidic device to observe dynamic flow around the villi generated by deformation of small intestinal tissue”. In: *Lab on a Chip* (2023).

[69] Satoru Kuriu, Naoyuki Yamamoto, and Tadashi Ishida. “Microfluidic device using mouse small intestinal tissue for the observation of fluidic behavior in the lumen”. In: *Micromachines* 12.6 (2021), p. 692.

[70] Hans Lennernaäs. “Human intestinal permeability”. In: *Journal of pharmaceutical sciences* 87.4 (1998), pp. 403–410.

[71] RG Lentle et al. “A comparison of the organization of longitudinal and circular contractions during pendular and segmental activity in the duodenum of the rat and guinea pig”. In: *Neurogastroenterology & Motility* 24.7 (2012), 686–e298.

[72] Roger Lentle and Janssen. *The Physical Processes of Digestion.* Jan. 2011. ISBN: 978-1-4419-9448-6. DOI: 10.1007/978-1-4419-9449-3.

[73] Roger G Lentle et al. “High definition mapping of circular and longitudinal motility in the terminal ileum of the brushtail possum Trichosurus vulpecula with watery and viscous perfusates”. In: *Journal of Comparative Physiology B* 177 (2007), pp. 543–556.

[74] Michael D Levitt, Alessandra Strocchi, and David G Levitt. “Human jejunal unstirred layer: evidence for extremely efficient luminal stirring”. In: *American Journal of Physiology-Gastrointestinal and Liver Physiology* 262.3 (1992), G593–G596.

[75] Simon J Lewis and Kenneth W Heaton. “Stool form scale as a useful guide to intestinal transit time”. In: *Scandinavian journal of gastroenterology* 32.9 (1997), pp. 920–924.

[76] Hewei Li et al. “Biopharmaceutics classification of puerarin and comparison of perfusion approaches in rats”. In: *International Journal of Pharmaceutics* 466.1-2 (2014), pp. 133–138.

[77] Xipeng Li et al. “GPU-based numerical simulation of multi-phase flow in porous media using multiple-relaxation-time lattice Boltzmann method”. In: *Chemical Engineering Science* 102 (2013), pp. 209–219.

[78] YF Lim et al. “Flow and mixing by small intestine villi”. In: *Food & function* 6.6 (2015), pp. 1787–1795.

[79] Yuen Feung Lim et al. “Determination of villous rigidity in the distal ileum of the possum (Trichosurus vulpecula)”. In: *PloS one* 9.6 (2014), e100140.

[80] Clément de Loubens et al. “Characterisation of mixing in the proximal duodenum of the rat during longitudinal contractions and comparison with a fluid mechanical model based on spatiotemporal motility data”. In: *PloS one* 9.4 (2014), e95000.

[81] Clément de Loubens et al. “Rheology of human faeces and pathophysiology of defaecation”. In: *Techniques in Coloproctology* 24.4 (2020), pp. 323–329.

[82] Catherine Loudon and Antoinette Tordesillas. “The use of the dimensionless Womersley number to characterize the unsteady nature of internal flow”. In: *Journal of theoretical biology* 191.1 (1998), pp. 63–78.

[83] Alan Mackie, Balazs Bajka, and Neil Rigby. “Roles for dietary fibre in the upper GI tract: The importance of viscosity”. In: *Food Research International* 88 (2016), pp. 234–238.

[84] Vishy Mahadevan. “Anatomy of the rectum and anal canal”. In: *Surgery (Oxford)* 32.4 (2014), pp. 159–164.

[85] Sébastien Marze. “Bioavailability of nutrients and micronutrients: advances in modeling and in vitro approaches”. In: *Annual review of food science and technology* 8 (2017), pp. 35–55.

[86] Guy R McNamara and Gianluigi Zanetti. “Use of the Boltzmann equation to simulate lattice-gas automata”. In: *Physical review letters* 61.20 (1988), p. 2332.

[87] Greenwood-Van Meerveld, Anthony C Johnson, David Grundy, et al. “Gastrointestinal physiology and function”. In: *Gastrointestinal pharmacology* (2017), pp. 1–16.

[88] Miguel Minguez et al. “Predictive value of the balloon expulsion test for excluding the diagnosis of pelvic floor dyssynergia in constipation”. In: *Gastroenterology* 126.1 (2004), pp. 57–62.

[89] Subhash C Mishra and Hillol K Roy. “Solving transient conduction and radiation heat transfer problems using the lattice Boltzmann method and the finite volume method”. In: *Journal of Computational Physics* 223.1 (2007), pp. 89–107.

[90] R Modigliani and JJ Bernier. “Absorption of glucose, sodium, and water by the human jejunum studied by intestinal perfusion with a proximal occluding balloon and at variable flow rates”. In: *Gut* 12.3 (1971), pp. 184–193.

[91] Yasuya Nakayama and Ryoichi Yamamoto. “Simulation method to resolve hydrodynamic interactions in colloidal dispersions”. In: *Physical Review E* 71.3 (2005), p. 036707.

[92] Ryozi Nanba, Seiko HIRAMATSU, and Katsushi MORIMOTO. “On the movements of the intestinal villi of the dog”. In: *The Japanese journal of physiology* 20.4 (1970), pp. 465–471.

[93] Denis O’Mahony, Paula O’Leary, and Eamonn MM Quigley. “Aging and intestinal motility”. In: *Drugs & aging* 19.7 (2002), pp. 515–527.

[94] S Palit et al. “Evacuation proctography: a reappraisal of normal variability”. In: *Colorectal Disease* 16.7 (2014), pp. 538–546.

[95] Somnath Palit, Peter J Lunniss, and S Mark Scott. “The physiology of human defecation”. In: *Digestive diseases and sciences* 57.6 (2012), pp. 1445–1464.

[96] Somnath Palit et al. “Diagnostic disagreement between tests of evacuatory function: a prospective study of 100 constipated patients”. In: *Neurogastroenterology & Motility* 28.10 (2016), pp. 1589–1598.

[97] K Sandy Pang. “Modeling of intestinal drug absorption: roles of transporters and metabolic enzymes (for the Gillette Review Series)”. In: *Drug metabolism and disposition* 31.12 (2003), pp. 1507–1519.

[98] TC Papanastasiou and AG Boudouvis. “Flows of viscoplastic materials: models and computations”. In: *Computers & Structures* 64.1-4 (1997), pp. 677–694.

[99] Pierre Paré et al. “Recommendations on chronic constipation (including constipation associated with irritable bowel syndrome) treatment”. In: *Canadian Journal of Gastroenterology* 21.Suppl B (2007), 3B–22B.

[100] D Arumuga Perumal and Anoop K Dass. “A Review on the development of lattice Boltzmann computation of macro fluid flows and heat transfer”. In: *Alexandria Engineering Journal* 54.4 (2015), pp. 955–971.

[101] Robert J Phillips and Terry L Powley. “Innervation of the gastrointestinal tract: patterns of aging”. In: *Autonomic Neuroscience* 136.1-2 (2007), pp. 1–19.

[102] SR Priyadarshini et al. “Predicting human glucose response curve using an engineered small intestine system in combination with mathematical modeling”. In: *Journal of Food Engineering* 293 (2021), p. 110395.

[103] Midhun Puthumana Melepattu and Clement de Loubens. “Steady streaming flow induced by active biological microstructures; application to small intestine villi”. In: *Physics of Fluids* (2022).

[104] Yue-Hong Qian, Dominique d’Humières, and Pierre Lallemand. “Lattice BGK models for Navier-Stokes equation”. In: *EPL (Europhysics Letters)* 17.6 (1992), p. 479.

[105] Yifan Qin et al. “New understanding from intestinal absorption model: How physiological features influence mass transfer and absorption”. In: *AIChE Journal* (2023), e18099.

[106] Yihong Qiu et al. *Developing solid oral dosage forms: pharmaceutical theory and practice.* Academic press, 2016.

[107] Satish SC Rao. “Advances in diagnostic assessment of fecal incontinence and dyssynergic defecation”. In: *Clinical gastroenterology and hepatology* 8.11 (2010), pp. 910–919.

[108] Muhammad Rehan et al. “Measurement of peristaltic forces exerted by living intestine on robotic capsule”. In: *IEEE/ASME Transactions on Mechatronics* 26.4 (2021), pp. 1803–1811.

[109] M Rentsch et al. “Dynamic magnetic resonance imaging defecography: a diagnostic alternative in the assessment of pelvic floor disorders in proctology”. In: *Diseases of the colon & rectum* 44 (2001), pp. 999–1007.

[110] Nikolay Repin, Steve W Cui, and H Douglas Goff. “Rheological behavior of dietary fibre in simulated small intestinal conditions”. In: *Food Hydrocolloids* 76 (2018), pp. 216–225.

[111] Gabriele Riegler and I Esposito. “Bristol scale stool form. A still valid help in medical practice and clinical research”. In: *Techniques in coloproctology* 5.3 (2001), pp. 163–164.

[112] Gustavo Ruiz-Pulido and Dora I Medina. “An overview of gastrointestinal mucus rheology under different pH conditions and introduction to pH-dependent rheological interactions with PLGA and chitosan nanoparticles”. In: *European Journal of Pharmaceutics and Biopharmaceutics* 159 (2021), pp. 123–136.

[113] Verney L Sallee and John M Dietschy. “Determinants of intestinal mucosal uptake of short-and medium-chain fatty acids and alcohols”. In: *Journal of lipid research* 14.4 (1973), pp. 475–484.

[114] Stephanie Sansone et al. “Role of Pessaries in the Treatment of Pelvic Organ Prolapse: A Systematic Review and Meta-analysis”. In: *Obstetrics & Gynecology* 140.4 (2022), pp. 613–622.

[115] Sitaraman Saraswati and Ramakrishnan Sitaraman. *Aging and the human gut microbiota—from correlation to causality.* 2015.

[116] Barbara O Schneeman. “Gastrointestinal physiology and functions”. In: *British Journal of Nutrition* 88.S2 (2002), S159–S163.

[117] K Schulze. “Imaging and modelling of digestion in the stomach and the duodenum”. In: *Neurogastroenterology & Motility* 18.3 (2006), pp. 172–183.

[118] Konrad Schulze-Delrieu. “Clearance patterns of the isolated guinea pig duodenum”. In: *Gastroenterology* 102.3 (1992), pp. 849–856.

[119] Inna Sekirov et al. “Gut microbiota in health and disease”. In: *Physiological reviews* (2010).

[120] M Sheikholeslami, Mofid Gorji-Bandpy, and D Domiri Ganji. “Lattice Boltzmann method for MHD natural convection heat transfer using nanofluid”. In: *Powder Technology* 254 (2014), pp. 82–93.

[121] Harjinder Singh, Aiqian Ye, and Maria J Ferrua. “Aspects of food structures in the digestive tract”. In: *Current Opinion in Food Science* 3 (2015), pp. 85–93.

[122] Figge F. H. J. Sobotta J. and Becher H. Hild W. J. *tlas of Human Anatomy 9Th English.* Hafner Press, 1974.

[123] Ami D Sperber et al. “Worldwide prevalence and burden of functional gastrointestinal disorders, results of Rome Foundation Global Study”. In: *Gastroenterology* 160.1 (2021), pp. 99–114.

[124] Alessandra Strocchi and Michael D Levitt. “A reappraisal of the magnitude and implications of the intestinal unstirred layer”. In: *Gastroenterology* 101.3 (1991), pp. 843–847.

[125] Alessandra Strocchi and Michael D Levitt. “Role of villous surface area in absorption science versus religion”. In: *Digestive diseases and sciences* 38 (1993), pp. 385–387.

[126] S Succi, E Foti, and F Higuera. “Three-dimensional flows in complex geometries with the lattice Boltzmann method”. In: *EPL (Europhysics Letters)* 10.5 (1989), p. 433.

[127] Daming Sun et al. “Mechanophysiological analysis of anorectal function using simulated feces in human subjects”. In: *Journal of Advanced Research* 28 (2021), pp. 245–254.

[128] Salvatore P Sutera and Richard Skalak. “The history of Poiseuille’s law”. In: *Annual review of fluid mechanics* 25.1 (1993), pp. 1–20.

[129] Mathusi Swaminathan et al. “Video imaging and spatiotemporal maps to analyze gastrointestinal motility in mice”. In: *JoVE (Journal of Visualized Experiments)* 108 (2016), e53828.

[130] Keith R Symon. *Mechanics. Addison.* 1971.

[131] Laurent Talon and Daniela Bauer. “On the determination of a generalized Darcy equation for yield-stress fluid in porous media using a Lattice-Boltzmann TRT scheme”. In: *The European Physical Journal E* 36.12 (2013), pp. 1–10.

[132] Masakazu Tatsuno. “Circulatory streaming around an oscillating circular cylinder at low Reynolds numbers”. In: *Journal of the Physical Society of Japan* 35.3 (1973), pp. 915–920.

[133] A Tharakan et al. “Mass transfer and nutrient absorption in a simulated model of small intestine”. In: *Journal of food science* 75.6 (2010), E339–E346.

[134] Patricia V Turner. “The role of the gut microbiota on animal model reproducibility”. In: *Animal models and experimental medicine* 1.2 (2018), pp. 109–115.

[135] KNET M VAN DE GRAAFF. “Anatomy and physiology of the gastrointestinal tract”. In: *The Pediatric Infectious Disease Journal* 5.1 (1986), pp. 11–16.

[136] CE Wagner, KM Wheeler, and K Ribbeck. “Mucins and their role in shaping the functions of mucus barriers”. In: *Annu. Rev. Cell Dev. Biol* 34.1 (2018), pp. 189–215.

[137] Yanxing Wang and James G Brasseur. “Three-dimensional mechanisms of macro-to-micro-scale transport and absorption enhancement by gut villi motions”. In: *Physical Review E* 95.6 (2017), p. 062412.

[138] Yanxing Wang et al. “A multiscale lattice Boltzmann model of macro-to micro-scale transport, with applications to gut function”. In: *Philosophical Transactions of the Royal Society A: Mathematical, Physical and Engineering Sciences* 368.1921 (2010), pp. 2863–2880.

[139] Yanxing Wang et al. “Development of a lattice-Boltzmann method for multiscale transport and absorption with application to intestinal function”. In: *Computational modeling in biomechanics* (2010), pp. 69–96.

[140] Henrik Westergaard, John M Dietschy, et al. “Delineation of the dimensions and permeability characteristics of the two major diffusion barriers to passive mucosal uptake in the rabbit intestine”. In: *The Journal of clinical investigation* 54.3 (1974), pp. 718–732.

[141] Dieter A Wolf-Gladrow. *Lattice-gas cellular automata and lattice Boltzmann models: an introduction.* Springer, 2004.

[142] WA Womack. “Barrowman JA, Graham WH, Benoit JN, Kvietys PR, Granger DN”. In: *Quantitative assessment of villous motility. Am J Physiol Gastrointest Liver Physiol* 252 (1987), G250–G256.

[143] William A Womack et al. “Villous motility: relationship to lymph flow and blood flow in the dog jejunum”. In: *Gastroenterology* 94.4 (1988), pp. 977–983.

[144] SM Woolley et al. “Shear rheological properties of fresh human faeces with different moisture content”. In: *Water sa* 40.2 (2014), pp. 273–276.

[145] Peng Wu and Xiao Dong Chen. “On designing biomimic in vitro human and animal digestion track models: ideas, current and future devices”. In: *Current Opinion in Food Science* 35 (2020), pp. 10–19.

[146] Patricia J Yang et al. “Hydrodynamics of defecation”. In: *Soft Matter* 13.29 (2017), pp. 4960–4970.

[147] Jinping Zha et al. “The role of circular folds in mixing intensification in the small intestine: A numerical study”. In: *Chemical Engineering Science* 229 (2021), p. 116079.

[148] Junfeng Zhang. “Lattice Boltzmann method for microfluidics: models and applications”. In: *Microfluidics and Nanofluidics* 10.1 (2011), pp. 1–28.

[149] Shuo Zhang et al. “Study on the effect of wall structures and peristalsis of bionic reactor on mixing”. In: *Chemical Engineering Science* 267 (2023), p. 118373.

[150] Yanan Zhang et al. “How motility can enhance mass transfer and absorption in the duodenum: Taking the structure of the villi into account”. In: *Chemical Engineering Science* 213 (2020), p. 115406.

[151] Fuzhang Zhao. “Optimal relaxation collisions for lattice Boltzmann methods”. In: *Computers & Mathematics with Applications* 65.2 (2013), pp. 172–185.